Multi-dimensional Analysis of Molecular Clusters in the Gas-phase

by

Tsun Hei Arthur Enoch Lee

A thesis

presented to the University of Waterloo

in fulfilment of the

thesis requirement for the degree of

Doctor of Philosophy

in

Chemistry

Waterloo, Ontario, Canada, 2024

© Tsun Hei Arthur Enoch Lee 2024

Examining Committee Membership

The following served on the Examining Committee for this thesis. The decision of the Examining Committee is by majority vote.

External Examiner	Jos Oomens Professor Radboud University
Supervisor	W. Scott Hopkins Professor Chemistry
Internal-External Examiner	Mark Servos Professor Biology
Internal Members	Marcel Nooijen Professor Chemistry
	Rick Marta Associate Professor Chemistry

Author's Declaration

This thesis consists of material all of which I authored or co-authored: see Statement of Contributions included in the thesis. This is a true copy of the thesis, including any required final revisions, as accepted by my examiners.

I understand that my thesis may be made electronically available to the public.

Statement of Contributions

This thesis contains works that are representative of my accomplishment which have been published in peer reviewed journals or in preparation for submission. Other works that I have contributed with my contributions are listed at the end of this statement. Each chapter contains the work of myself and other researchers, whose contributions are summarised below.

The contents of Chapter 3 are reproduced from the following publication:

Lee, A. E.; Featherstone, J.; Martens, J.; McMahon, T. B.; Hopkins, W. S. Fluorinated Propionic Acids Unmasked: Puzzling Fragmentation Phenomena of the Deprotonated Species. *J. Phys. Chem. Lett.* **2024**, *15* (11), 3029–3036. https://doi.org/10.1021/acs.jpclett.3c03400.

My contribution to the work in chapter 3 includes conducting the computational investigations, collision induced dissociation experiments, and writing of the manuscript. Dr. Featherstone performed the infrared multiple photon dissociation (IRMPD) experiments with the aid from Prof. Jonathan Martens. Prof. W. S. Hopkins and Prof. T. B. McMahon supervised the study and aided in the preparation of the manuscript for publication.

Contents of chapter 4 and 5 are written under the supervision of Prof. W. Scott Hopkins and is written for future publication. My contribution to chapter 4 includes conducting IRMPD experiments and computational studies on the different conformers. Cailum Stienstra aided in the conformation search process. Prof. W. S. Hopkins and Prof. T. B. McMahon supervised the study and aided in the preparation of the manuscript for publication.

My contribution to chapter 5 includes conducting the IRMPD experiments, ion mobility experiments, and computational study. Courtney Kates assisted with the differential ion mobility (DMS) experiments, and Patrick Thomas assisted with the IRMPD experiments. Prof. W. S. Hopkins and Prof. T. B. McMahon supervised the study and aided in the preparation of the manuscript for publication.

Other works I have contributed to:

1. Ieritano, C.; Lee, A.; Crouse, J.; Bowman, Z.; Mashmoushi, N.; Crossley, P. M.; Friebe, B. P.; Campbell, J. L.; Hopkins, W. S. Determining Collision Cross Sections from Differential Ion Mobility Spectrometry. *Anal. Chem.* **2021**, *93* (25), 8937–8944. https://doi.org/10.1021/acs.analchem.1c01420. – I created the multilayer perceptron model using pytorch to determine collision cross sections.

2. Ding, X.; Kumar, M.; Zheng, Z.; Lee, A.; Hopkins, W. S.; Attygalle, A. B. Evidence of Gas-Phase Attachment of Molecular Oxygen to Deprotonated Hydroquinone During Ion-Mobility Mass Spectrometry. *J. Am. Soc. Mass Spectrom.* **2022**, *33* (10), 1816–1824. https://doi.org/10.1021/jasms.1c00222. – I was responsible for determining MECP crossing point geometry between the triplet and the singlet state for the target analyte.

3. Stienstra, C. M. K.; Haack, A.; Lee, A. E.; Hopkins, W. S. Ion Core Switching during Photodissociation Dynamics via the Rydberg States of XeAr. *Chemical Physics* **2024**, *581*, 112254. https://doi.org/10.1016/j.chemphys.2024.112254. – I aided in the VMI experimentation by troubleshooting and aligning laser beam path.

Abstract

In this thesis, interactions and properties of novel gas-phase clusters are studied. These gas-phase clusters often possess unique geometries and unexpected properties, which are influenced by the forces and interactions between the moieties within the cluster. Spectroscopic methods and ion mobility methods are coupled with tandem mass spectrometry to elucidate the cluster properties and geometry. IRMPD provides insight toward the nature of the cluster by their IR fingerprints, which can be used in parallel with tandem mass spectrometry method such as CID to provide further information. In addition, ion mobility methods are used to differentiate conformational differences between isomeric clusters.

In chapter 3, IRMPD and CID of deprotonated fluorinated propionic acids are studied. In analytical studies of short chain per- and polyfluoroalkyl substances (PFAS), the quantification and the identification of these carboxylic acids are done by monitoring the carbanion signal after the loss of CO_2. The degree of fluorination influences fragmentation under IRMPD and CID, leading to fragmentation pathways such as formation of FCO_2^- and HF elimination. Fluorinated propionic acids with at least one fluorine atom bound to the terminal carbon yield FCO_2^-, whereas loss of HF is observed in polyfluorinated species with at least one fluorine bound to the α-carbon. The formation of FCO_2^- and HF elimination products occur through a four-membered ring transition state.

Chapter 4 describes the study of aromatic organometallic compounds such as cyclopentadienyl that are known to form sandwich complexes with counter cations, because the dominant interactions between the cation and the anion are Coulombic interactions and ion-induced dipole interactions. This work focuses on studying the influence on the geometry of the cluster by reducing the symmetry of the aromatic compound through clustering 1,2,3–triazolide and 1,2,4–triazolide with various alkali metal cations (with an excess of one cation to preserve cationic states). Through a combination of IRMPD and DFT calculations, the primary interaction between the alkali metal cations and the triazolide is found to be

dominantly ion-dipole interactions and lone-pair donation interactions. This results in the geometry of the 1,2,3–triazolide clusters to be a 3D compact structure, whereas the 1,2,4–triazolide analogues are found to be more open with longer distances between the cations. Potential overtone bands or combination bands associated with the C-H wagging motion and ring torsion motion are found between the 1500 – 1800 cm^{-1} region.

Chapter 5 is a study on the clusters of perfluorinated dodecaborate cages, $B_{12}F_{12}^{2-}$, with protonated diaminoalkanes $H_2N(CH_2)_nH_2N$ (n = 2 – 12) through a combination of IMRPD action spectroscopy and ion mobility spectrometry. I focus on characterizing the different singly-charged clusters of the form $[B_{12}F_{12} + H_2N(CH_2)_nNH_2 + H]^-$ and doubly-charged clusters of the form $[2(B_{12}F_{12}) + H_2N(CH_2)_nH_2N + 2H]^{2-}$ (n = 2 – 12). Three unique geometries are found for the singly-charged clusters, a low energy proton-bound ring geometry where intramolecular hydrogen bonding occurs between the two amine functional groups, a bidentate geometry (where both amine groups bind to the $B_{12}F_{12}^{2-}$ moiety), and a monodentate geometry. For the doubly-charged clusters, the doubly protonated diaminoalkane act as a tether between the $B_{12}F_{12}^{2-}$ cages. The major fragmentation channels of the singly-charged and doubly-charged clusters are found to be: (*i*) proton-transfer leading to production of $HB_{12}F_{12}^-$ and (*ii*) the loss of $B_{12}F_{12}^{2-}$. Formation of $HB_{12}F_{12}^-$ likely leads to further gas-phase reactions that can yield compounds such as $[B_{12}F_{11} + N_2]^-$. Travelling wave ion mobility spectrometry (TWIMS) analysis of $HB_{12}F_{12}^-$ finds $CCS_{TWIMS} = 142 \pm 6.7$ Å^2. IRMPD spectroscopy, aided by computational modelling, indicates that the bidentate conformation is the major sub-population in the gas-phase ensemble.

Acknowledgements

I want to thank my supervisors Prof. W. S. Hopkins and Prof. T. B. McMahon for their supervision over my graduate life at the University of Waterloo. I want to further extend my gratitude towards Prof. W. S. Hopkins for giving me the chance working at his lab as a second-year undergraduate student. I do not think I will be here without that opportunity. I also want to thank Prof. T. B. McMahon for his continue supervision after retirement and given me the chances to go to FELIX for performing IRMPD experiments. Thank you to my committee members, Prof. Rick Marta, Prof. Germán Sciaini, and Prof. Marcel Nooijen for their help over any little questions that I have. Thank you to Prof. Mark Servos for agreeing to be an internal-external committee member. I also want to thank my external committee member Prof. Jos Oomen for taking his time to be on my committee while being in a different time zone and country.

I want to thank all the current and previous Hopkins and McMahon group members that have guided me through my graduate school journey. Dr. Nour Mashmoushi is the silent workhorse that provides both emotional support and work support, including taking care of stuff around the lab. Dr. Christian Ieritano and Dr. Alex Haack were vital to the studies done in this thesis; I probably will not be able to finish any of the experimental work without their guidance. Dr. Josh Featherstone for his companionship across my university journey. Prof. Jonathan Martens at FELIX for his help and guidance so that I can complete the IRMPD experiments. Dr. Neville Coughlan for his support. Dr. Emir Nazdrajić for his time working on the different projects together and his help on this thesis. Also, honorary shout out to Courtney, Dawson, and Madi for being a cool undergraduate student to work with.

Finally, I want to give my gratitude towards my family members, especially my grandparents and my parents. I also want to shout out Henry, Ciaran, Kenta, Ryuta, Shoya, Kunio, and John for their friendship over the years. Lastly, I wish that my graduate school buddies, Nigel and Kevin, have a great defence and thesis.

Table of Contents

Examining Committee Membership II

Author's Declaration III

Statement of Contributions IV

Abstract VI

Acknowledgements VIII

List of Figures XII

List of Tables XVI

List of Abbreviations/Acronyms XVIII

– Chapter 1 – Introduction 1

– Chapter 2 – Methods 6

2.1 Experimental Methods 6

2.1.1 – Electrospray Ionization 6

2.1.2 – Collision Induced Dissociation 8

2.1.3 – Infrared Multiple Photon Dissociation 8

2.1.4 – Ion mobility 12

2.1.4.1 – Travelling Wave Ion Mobility Spectrometry 13

2.1.4.2 – Differential Ion Mobility Spectrometry 15

2.2 Computational Methods 20

2.2.1 – CREST 21

2.2.2 – Density Functional Theory 22

2.2.3 – Nudged Elastic Band 23

– Chapter 3 – Fluorinated Propionic Acids Unmasked 25
3.1 – Introduction 25
3.2 – Methods 26
3.3 – Results and Discussion 28
3.3.1 – IRMPD spectrum of the deprotonated 3,3,3,2-tetrafluoropropionic acid. 30
3.3.2 – Competition between FCO_2^- and CO_2 formation pathways. 37
3.3.3 – Competition between HF and CO_2 formation pathways 40
3.4 – Conclusions 44
– Chapter 4 – Gas-phase Triazolide Complexes 47
4.1 – Introduction 47
4.2 – Methods 50
4.3 – Results and Discussion 51
4.3.1 – 1,2,3-triazolide complexes 52
4.3.2 – 1,2,4-triazolide complexes 59
4.4 – Conclusions 64
– Chapter 5 – Gas-phase $B_{12}F_{12}^{2-}$ Diaminoalkane Clusters 66
5.1 – Introduction 66
5.2 – Experimental Methods 68
5.3 – Computational methods 69
5.4 – Results and Discussion 70
5.4.1 – Mass Spectrometry Results 70
5.4.2 – Computational Results 73
5.4.3 – Ion Mobility Results 80
5.4.4 – Infrared Ion Spectroscopy (IRIS) Results 84

5.5 – Conclusions 88
– Chapter 6 – Conclusions 90
References 94
Appendix A 112
Appendix B 146

List of Figures

Figure 2.1. Example of electrospraying positively charged ions into the mass spectrometer via an electrospray ionization (ESI) source. The ions are guided into the mass spectrometer by both gas flow and attracting Coulombic forces from the counter-electrode. 7

Figure 2.2. Schematic of the FEL at the FELIX laboratory. IR photons are generated via the synchrotron emission from the "wiggling" electron beam. 10

Figure 2.3. The IVR process. A photon excites the vibrational ground state ($\nu = 0$) of an ion to an excited state ($\nu = 1$). Energy transfer to the bath states de-excites the absorbing mode while maintaining the total internal energy of the ion. Repeated IR absorption followed by IVR raises the internal energy of the ion until a dissociation threshold is met and the ion fragments. 11

Figure 2.4. Schematic of a TWIMS cell. The large blue rings are the stacked ring electrod ion guide that confines the ions. The black lines across the image represents the travelling wave electric field. The purple circle represents an ion with a larger CCS than the red circle. (**Panel 1**) The ions introduction into the TWIMS cell. (**Panel 2**) The difference in CCSs (*viz.* mobility) causes the larger (purple) ion to lag in position compared to the smaller (red) ion. (**Panel 3**) The ions are fully separated as they exit the drift cell..... 14

Figure 2.5. Schematic of a DMS cell. (**Red**) The path of the analyte without any CV correction to an applied SV. (**Blue**) The path of the analyte following the application of an appropriate CV to correct the ion trajectory and steer it onto the transmission axis. 17

Figure 2.6. (**A**) Example of an ionogram at SV = 3800 V. (**B**) Common dispersion curve types observed in DMS experiments. 19

Figure 3.1. Experimental IRMPD spectra of the deprotonated 3,3,3,2-tetrafluoropropionic acid and the 3,3,2,2-tetrafluoropropionic acid. (A) 3,3,3,2-tetrafluoropropionic acid

with its signature IR region in red and (B) 3,3,2,2-tetrafluopropionic acid with its signature IR region in blue. 29

Figure 3.2. IRMPD and computed harmonic vibrational spectra for 3,3,3,2-tetrafluoropropionic acid. (A) total fragmentation efficiency, (B) CO_2 loss channel, (C) FCO_2^- channel, and (D) calculated spectra. The computed spectrum was scaled by a factor of 0.95. 31

Figure 3.3. (**A**) Computed transition state geometry for production of FCO_2^- from deprotonated 3,3,3,2-tetrafluoropropionic acid. (**B**) Computed dissociation pathways for deprotonated 3,3,3,2-tetrafluoropropionic acid. (Black trace) relative standard Gibbs energy, (red trace) relative zero-point corrected energy, and (blue trace) relative electronic energy. Calculations were conducted at the M06-2X/aug-cc-pVTZ level of theory with single point energy calculated with DLPNO-CCSD(T)/aug-cc-pVTZ. 39

Figure 3.4. (**A**) Computed transition state geometry for production of HF from deprotonated 2,2-difluoropropionic acid. (**B**) Computed dissociation pathway for HF loss from deprotonated 2,2-difluoropropionic acid. (Black trace) relative standard Gibbs energy, (red trace) relative zero-point corrected energy, and (blue trace) relative electronic energy. Calculations were conducted at the M06-2X/aug-cc-pVTZ level of theory with single point energy calculated with DLPNO-CCSD(T)/aug-cc-pVTZ. 42

Figure 4.3. IRMPD spectra for (**A**) $[Na_3(123T)_2]^+$, (**B**) $[Na_4(123T)_3]^+$, (**C**) $[K_3(123T)_2]^+$, and (**D**) $[K_3(123T)_3]^+$. Computed IR spectra for the lowest energy conformation, which are overlayed in red, are scaled by 0.95 in accordance with literature convention.[187,188] The inset green traces show a zoom of the 1500 – 1900 cm^{-1} region..... 53

Figure 4.4. The different isomeric forms of $[K_3(123T)_2]^+$ and their relative Gibbs energies. (**A**) is the lowest energy geometry, (**B**) is "drawbridge" like structure, and (**C**) is the extended structure that has the highest energy..... 55

Figure 4.5. The global minima and the first higher energy isomers of $[M_3(123T)_2]^+$ (M = Na, K). Calculations were conducted at the ωB97X-D3/def2-tzvpp level of theory. NBO interaction energies are summarized in **Table 4.2**..... 57

Figure 4.6. Computed global minima for the $[M_4(123T)_3]^+$ (M = Na, K) clusters. Calculations were conducted at the ωB97X-D3/def2-tzvpp level of theory..... 58

Figure 4.8. The lowest energy geometries of $[M_3(124T)_2]^+$, $[M_4(124T)_3]^+$, and $[M_5(124T)_4]^+$ (M = Na, K). Calculations were conducted at the ωB97X-D3/def2-tzvpp level of theory. The overlapping N lone pair and M^+ *s* orbitals, which give rise to C-T interactions, are plotted for the $[Na_4(124T)_3]^+$ cluster. NBO interaction energies are summarized in **Table 4.4**. 63

Figure 5.1. (**A**) The experimental mass spectrum recorded for the $[B_{12}F_{12} + H_2N(CH_2)_6NH_2 + H]^-$ cluster and (**B**) its theoretical isotopic distribution. Experimental *m/z* features associated with the various isotopologues of $[B_{12}F_{12} + H_2N(CH_2)_6NH_2 + H]^-$ are highlighted in blue. 71

Figure 5.2. Fragment mass spectra observed for $[B_{12}F_{12} + H_2N(CH_2)_6NH_2 + H]^-$ (*m/z* ~ 475) following (**A**) IRMPD and (**B**) CID. The parent ion is highlighted in blue at 3200 cm^{-1}. Tentative assignments are provided for the features at *m/z* ~ 394 and *m/z* ~ 399. The remaining mass features are assigned based on the reference 210. 73

Figure 5.4. (**Top**) Computed geometries of the $[B_{12}F_{12} + H_2N(CH_2)_6NH_2 + H]^-$ cluster: (**A**) proton-bound ring structure, (**B**) monodentate-bound structure, and (**C**) bidentate-bound structure. Calculated relative Gibbs energies for the three isomers are given in kJ mol^{-1}. (**Bottom**) Computed geometries of the $[2B_{12}F_{12} + H_2N(CH_2)_nNH_2 + 2H]^{2-}$ (n = 3, 4, 5) clusters. (**D**) The structure of the n = 3 doubly-charged cluster is representative of the ground state of those containing diaminopropane and diaminoethane species. (**E**) The structure of the n = 4 doubly-charged cluster. (**F**) The structure of the n = 5 doubly-charged cluster is representative of the ground state of those containing diaminopentane and longer chain species. 76

Figure 5.5. (**Black**) Measured CCSs for the $[B_{12}F_{12} + H_2N(CH_2)_nNH_2 + H]^-$ (n = 2 – 12) clusters. Error bars indicate the full width at half maximum for the arrival time distributions. The dashed line shows a linear trend that was fit to the n = 2 – 9 clusters. The dotted line shows a linear trend that was fit to the n = 10 – 12 clusters. Computed

CCS values for the (**green**) monodentate, (**red**) bidentate, and (**blue**) proton-bound ring structures..... 81

Figure 5.6. Ionograms of (**A, blue**) $[B_{12}F_{12} + H_2N(CH_2)_4NH_2 + H]^-$ and (**A, red**) $[2B_{12}F_{12} + H_2N(CH_2)_4NH_2 + 2H]^{2-}$ measured at SV = 3800 V in a pure N_2 environment. (**B, blue**) Ionograms of $[B_{12}F_{12} + H_2N(CH_2)_{10}NH_2 + H]^-$ and (**B, red**) $[2B_{12}F_{12} + H_2N(CH_2)_{10}NH_2 + 2H]^{2-}$ measured at SV = 3800 V in a pure N_2 environment. Ionograms for the other clusters measured at the same SV are provided in Appendix B(**Figure B24-34**)..... 83

Figure 5.7. (**A**) The experimental IRIS spectrum for the $[B_{12}F_{12} + H_2N(CH_2)NH_2 + H]^-$ cluster and the computed spectra of the (**B**) monodentate, (**C**) bidentate, and (**D**) proton-bound ring isomers. The intensity observed near 2,700 cm^{-1} demonstrates that the proton-bound-ring structure is present in the probed ensemble. 85

Figure 5.8. Comparisons of the IRMPD spectra for the (black) *m/z* 358 fragment and (red) *m/z* 339 fragment from the singly charged diaminoheptane cluster $[(B_{12}F_{12})\bullet H_3N\text{-}(CH_2)_7\text{-}NH_2]^-$. 87

List of Tables

Table 3.1. Product branching ratios observed following IRMPD of 2-monofluoropropionic acid (2-F), 3-monofluoropropionic acid (3-F), 2,2-difluoropropionic acid (2,2-F_2), 3,3,3-trifluoropropionic acid (3,3,3-F_3), 3,3,2,2-tetrafluoropropionic acid (3,3,2,2-F_4), 3,3,3,2-tetrafluoropropionic acid (3,3,3,2-F_4), and pentafluoropropionic acid (F_5). 32

Table 3.2. Product branching ratios observed following CID at Normalized collision energy of 22.5 eV of 2-monofluoropropionic acid (2-F), 3-monofluoropropionic acid (3-F), 2,2-difluoropropionic acid (2,2-F_2), 3,3-difluoropropionic acid (3,3-F_2), 3,2,2-trifluoropropionic acid (3,2,2-F_3), 3,3,3-trifluoropropionic acid (3,3,3-F_3), 3,3,2,2-tetrafluoropropionic acid (3,3,2,2-F_4), 3,3,3,2-tetrafluoropropionic acid (3,3,3,2-F_4), and pentafluoropropionic acid (F_5). 36

Table 3.3. Calculated thresholds for production of CO_2 and FCO_2^- for deprotonated 3-monofluoropropionic acid (3-F), 3,3-difluoropropionic acid (3,3-F_2), 3,2,2-trifluoropropionic acid (3,2,2-F_3), 3,3,3-trifluoropropionic acid (3,3,3-F_3), 3,3,2,2-tetrafluoropropionic acid (3,3,2,2-F_4), 3,3,3,2-tetrafluoropropionic acid (3,3,3,2-F_4), and pentafluoropropionic acid (F_5). Calculations were conducted at the M06-2X/aug-cc-pVTZ level of theory with single point energy calculated with DLPNO-CCSD(T)/aug-cc-pVTZ. Energies are given in kJ mol^{-1}. Other deprotonated fluorinated propionic acids with only computational results are provided in **Appendix A Table A8**. 40

Table 3.4. Calculated thresholds for production of CO_2 and HF for deprotonated 2-monofluoropropionic acid (2-F), 2,2-difluoropropionic acid (2,2-F_2), and 3,3,2,2-tetrafluoropropionic acid (3,3,2,2-F_4). Energies are given in kJ mol^{-1}. Calculations were conducted at the M06-2X/aug-cc-pVTZ level of theory with single point energy calculated with DLPNO-CCSD(T)/aug-cc-pVTZ. 42

Table 3.5. Summary for the result and method used to study the different deprotonated fluorinated propionic acids. 45

Figure 4.1. (**left**) deprotonated 1H-1,2,3-triazole and (**right**) deprotonated 1H-1,2,4-triazole. Molecular dipoles were computed at the ωB97X-D/def2-tzvpp level of theory. 49

Table 4.1. Assignments for the average observed IRMPD bands for the $[Na_x(123T)_y]^+$ and $[K_x(123T)_y]^+$ species (intensities; w = weak, m = medium, s = strong, vs = very strong). FT-IR band positions and symmetry assignments are those reported in reference 186 under a 0.5M NaOH environment.[186] 54

Table 4.2. Computed cluster binding energies and stabilization energies associated with charge-transfer (C-T) interactions between the 123T anions and alkali metal cations. NBO calculations were undertaken at the ωB97X-D3/def2-tzvpp level of theory. Gibbs binding energies, ΔG°, are calculated using standard temperature and pressure..... 59

Table 5.1. Computed binding energies for $[B_{12}F_{12} + H_2N(CH_2)_nNH_2 + H]^-$ dissociating to $H_2N(CH_2)_nNH_2 + HB_{12}F_{12}^-$ products for $n = 2, 6, 12$. Electronic energies (ΔE_{elec}), zero-point corrected energies (ΔE_{zpe}), enthalpies (ΔH), and standard Gibbs energies ($\Delta G°$) are reported in kJ mol^{-1}, and entropy (ΔS) is reported in units of kJ mol^{-1} K^{-1}..... 78

Table 5.2. Computed binding energies for $[2B_{12}F_{12} + H_2N(CH_2)_nNH_2 + 2H]^{2-}$ dissociating to: (I.) $[B_{12}F_{12} + H_2N(CH_2)_nNH_2 + H]^- + HB_{12}F_{12}^-$ and (II.) $[B_{12}F_{12} + H_2N(CH_2)_nNH_2 + 2H]^0 + B_{12}F_{12}^{2-}$ products for $n = 2, 6, 12$. Electronic energies (ΔE_{elec}), zero-point corrected energies (ΔE_{zpe}), enthalpies (ΔH), and standard Gibbs energies ($\Delta G°$) are reported in kJ mol^{-1} , and entropy (ΔS) is reported in units of kJ mol^{-1} K^{-1}..... 79

List of Abbreviations/Acronyms

CID	Collision Induced Dissociation
IRMPD	Infrared Multiple Photon Dissociation
PFAS	Per-/Polyfluoroalkyl Substance
PFCAs	Per-/Polyfluoroalkyl Carboxylic Acids
Cp^-	Cyclopentadienyl
ESI	Electrospray Ionization
FELIX	Free Electron Lasers for Infrared eXperiments
FEL	Free Electron Lasers
IVR	Intramolecular Vibrational energy Redistribution
IMS	Ion Mobility Spectrometry
DT	Drift Tube
CCS	Collision Cross-Section
TWIMS	Travelling Wave Ion Mobility Spectrometry
DMS	Differential Ion Mobility Spectrometry
SV	Separation Voltage
CV	Compensation Voltage
DFT	Density Functional Theory
CCSD(T)	Coupled Cluster Singles, Doubles, and Triples
RMSD	Root-Mean-Square-Deviation
MTD	Meta-Dynamic Algorithm
MD	Molecular Dynamic
MP2	Møller–Plesset perturbation theory of second order

M06-2x	Minnesota 06-2X method
ωB97X	Modified Becke 97 exchange-dipole moment method
NEB	Nudged Elastic band
MEP	Minimum Energy Path
PFOS	Perfluorooctanesulfonic acid
PFOA	Perfluorooctanoic acid
TS	Transition States
IRC	Intrinsic Reaction Coordinate
123T	1,2,3-triazolide
124T	1,2,4-triazolide
IRIS	Infrared Ion Spectroscopy

– Chapter 1 –
Introduction

The field of cluster science is a fascinating area of study because clusters systems lie in the grey area between bulk materials and smaller quantum systems. As an example, rhodium clusters containing up to *ca.* 30 atoms exhibit superparamagnetism, but bulk rhodium is non-magnetic and atomic rhodium has a small magnetic moment of 3 μ_B.[1] The fact that clusters can display drastically different properties relative to that of the bulk and atomic counterparts is one of the driving factors behind nanotechnology. Moreover, nanoclusters are excellent test systems to explore the interactions – covalent and non-covalent – that affect physicochemical properties and geometry.

Various types of clusters are studied to provide more insight to the transition from the molecular regime to the bulk condensed phase regime. As an example, organometallic clusters are often studied in the gas-phase to probe the catalytic properties without the influences from solvent effects and under high vacuum conditions to stabilize reactive intermediates.[2–4] This reasoning can be extended for studying ionic clusters in the gas-phase to distinguish the intrinsic ion chemistry from solvent effects.[5] However, it is not to say that all studies of clusters in the gas-phase are to be free from solvent effects. In the case of ion-solvent clusters, they are often studied as a mean to provide insights to the changes in properties of ions under the condensed phase and the gas-phase.[6–8]

Early studies of gaseous weakly bound ionic clusters were generated through supersonic jet expansion. In 1980s, Y.T. Lee and coworkers recorded infrared spectra of weakly bounded ionic clusters of protonated hydrogen and water clusters through a “messenger technique.” This technique is to tag the molecular ion of interest with a small molecule or rare gas atom to detect the absorption of infrared radiation via its dissociation.[9–11] With the development of more advanced laser systems such as IR free electron lasers (IR-FEL), infrared multiple photon dissociation (IRMPD) action spectroscopy allows for the dissociation of more

strongly bound species such as covalently bound molecules via absorbing multiple photons in succession to obtain IR action spectra for ion clusters.[12–14] These technological development allows for further work in studying ion clusters.

In this thesis, I aim to examine different clusters to elucidate how changes to a component within a cluster impacts its physicochemical properties. As an example, how do changes to the cluster composition or geometry impact its fragmentation behaviour? Thorough investigation of several different cluster systems is necessary to gain a deeper understanding in this regard. Hence, this thesis describes an exploration of gas phase ionic clusters, whereby mass spectrometry, ion mobility spectrometry, laser spectroscopy, and quantum chemical modelling were used to gain a deeper understanding of cluster structure and properties.

Chapter 2 describes the research methods used in chapters 3 – 5. The structure of an analyte can be indirectly elucidated by analysing the fragments generated from the precursor ion using tandem mass spectrometry techniques such as collision induced dissociation (CID).[15–17] However, this information is not always sufficient to determine molecular geometry, especially in cases where the target analyte is an ionic cluster that exhibits multiple conformations.[18] By coupling mass spectrometry with ion mobility or spectroscopic methods, additional complementary information can be measured. A key method employed in this research is infrared multiple photon dissociation (IRMPD) action spectroscopy.[19] IRMPD spectroscopy is a type of infrared ion spectroscopy (IRIS) that may be used to study the vibrational spectra (and hence geometric structures) of gas phase ionic clusters. This information can be used as a "vibrational fingerprint" for distinguishing analytes and is particularly useful for characterizing species that are difficult to distinguish via mass spectrometry alone (*e.g.*, isomers).[20,21] We also employ ion mobility spectrometry to separate ionic species prior to mass spectrometric characterization and, in some cases, to measure collision cross sections (CCSs) as an additional mean of determining molecular geometry.[22,23] To aid in the interpretation of experimental measurements, electronic structure calculations are conducted to predict cluster geometric structures, bond energies, and fragmentation pathways. Owing to the complexity of the systems studied and the need to balance

computational accuracy and efficiency, a variety of computational methods are used. In some cases, it was necessary to first employ conformational search algorithms to sample the cluster potential energy surface and identify energy minima corresponding to candidate structures.

Chapter 3 describes an investigation of a variety of per- and polyfluorinated propionic acids. These molecules belong to a class of environmental contaminants, per- and polyfluoroalkyl substances (PFAS), also known as "forever chemicals".[24] These species are common ingredients in various industrial, commercial, and household products.[25–27] Due to their links with long term detrimental impacts on human health, are now being regulated by governing bodies worldwide.[28,29] Concomitant with the introduction of regulations for long chain PFAS, short chain PFAS and fluoroethers were introduced as a substitute. Moreover, degradation of long chain PFAS often results in the formation of shorter chain species (such as per- and polyfluorinated propionic acids) for which chemical information and rigorous analytical methods of quantification are lacking.[30,31] Typically, short chain per- and polyfluoroalkyl carboxylic acids (PFCAs) are detected via multiple reaction monitoring (MRM) of the associated carboxylate anion and the carbanion produced following the loss of CO_2.[32] In this study, IRMPD is utilized to distinguish isomeric forms of PFCAs, and we observed unexpected fragmentation behaviour, such as formation of FCO_2^- and loss of HF, depending on the degree of fluorination and location of the F atoms. Computational mapping of the reaction pathways leading to the formation of FCO_2^- and loss of HF is conducted to gain further insight to the kinetics and thermodynamics of fragmentation.

In Chapter 4, the curious cases of sodiated and potassiated triazolide clusters are studied with IRMPD spectroscopy. Following the first synthesis of ferrocene in the early 1950s, significant effort was directed towards creating and characterizing aromatic organometallic complexes.[33–35] In the case of cyclopentadienyl (Cp^-) complexes, cluster structures depend on the nature of the cation; bonding within Cp^- complexes that contain relatively electropositive elements is mainly ionic (*e.g.*, Cs^+Cp^-), whereas bonding in clusters that contain *p*–block elements is highly covalent.[36] Previous studies by Kebarle *et al*. demonstrated that the binding energy of a potassium-benzene cationic cluster has a stronger

binding energy than a potassium-water cationic cluster.[37] Further investigations showed a trend of decreasing ion-benzene binding energy with increasing cation size. Recently, Featherstone *et al*. conducted a combined computational and experimental IRMPD spectroscopy study of the cationic $[Na_nCp_{n-1}]^+$ (n = 2-4) complexes.[38] They showed that the complexes exhibit inverse sandwich geometries wherein the sodium cations are located above and below the plane of the Cp^- anion. These complexes were found to be primarily bound by weak Coulombic interactions and charge-induced dipole interactions which, based on the negligible IR spectral shifts of the bound versus the free Cp^- ligands, resulted in very minor perturbation to the Cp^- moiety. An interesting open question regarding the structure of gas-phase aromatic organometallic complexes is the importance of the ring symmetry. What would be the result if the symmetry of the Cp^- moiety (D_{5h}) is reduced by substituting heteroatoms such as nitrogen in place of the carbon centres? Would such a substitution significantly impact cluster geometry and stability, given that relatively strong ion-dipole and charge-transfer interaction that might now be possible? These questions underpin our investigation of the sodiated and potassiated clusters of 1,2,3-triazolide and 1,2,4-triazolide. We show that these clusters systems do not exhibit inverse sandwich geometries like those observed for the analogous $[Na_nCp_{n-1}]^+$ clusters. However, as was observed for the $[Na_nCp_{n-1}]^+$ clusters, we observe combination bands in the spectra of the triazolide clusters, indicating a strong anharmonic coupling in the vibronic ground state or significant two-photon transition probability from the vibronic ground state.

In chapter 5 we investigate complexes of perfluorinated dodecaborate cages, $B_{12}F_{12}^{2-}$, with protonated diaminoalkanes, $H_2N(CH_2)H_2N$ (n = 2 – 12). Perhalogenated dodecaborate cages are interesting systems; they are "superweak" anions and have numerous condensed phase applications (*e.g.*, neutron capture, energy storage),[39–41] but exhibit strong and unexpected interactions when isolated in the gas phase. For example, in solution $B_{12}X_{12}^{2-}$ (X = H, Halogens) dianion are weakly coordinating compared to common anions such as SO_4^{2-} and HPO_4^{2-} because their electron density is distributed across the surface of the boron cage.[41,42] However, in the gas-phase, the $B_{12}F_{12}^{2-}$ anion was found to bind strongly with metal

cations, protonated trialkylamines all *cis*-hexafluorocyclohexane, predominantly through electrostatic interactions and incipient chemical bonding.[40,43–45] These works demonstrated that $B_{12}F_{12}^{2-}$ is prone to proton transfer and charge transfer reactions that can subsequently destabilize the dianion and result in a cascade of chemical reactions.[44] Experimentally, we employed mass spectrometry, travelling wave ion mobility spectrometry (TWIMS), differential mobility spectrometry (DMS), and IRMPD action spectroscopy to explore the structures and properties of $B_{12}F_{12}^{2-}$ complexes that contain increasingly flexible diaminoalkane chains, including systems wherein the diaminoalkane acts as a doubly-protonated tether between two dianion cages.[45]

Ultimately, this thesis describes three studies of gas-phase ions and ionic clusters wherein subtly different geometric structures are probed using mass spectrometry coupled with ion mobility spectrometry or IRMPD spectroscopy. In chapter 3, we show that subtle differences in fluorination patterns dramatically influence gas phase dissociation pathways. In chapter 4, we describe how slight differences in triazolide isomer geometries impacts cluster structure and stability. In chapter 5, we reveal that minor differences in the length of a (weakly interacting) alkyl chain significantly impacts the thermodynamically favoured cluster geometry. Collectively, this work represents a significant step towards understanding the interrelation between cluster structures and their physicochemical properties.

– Chapter 2 –

Methods

2.1 Experimental Methods

Multiple methods are used to probe and study gas-phase ionic clusters, an example being the use of mass spectrometry. Mass spectrometry can record mass-to-charge ratio (*m/z*) of a gas-phase cluster, giving information about the molecular weight of the cluster in the gas-phase ensemble. In addition, tandem mass spectrometry is typically used to give clues on the structure of the target cluster via unimolecular dissociation. However, mass spectrometry alone cannot give definitive clues pertaining to the structure of the cluster or differentiate isomers in the gas-phase ensemble and structural information of unknown species. Thus, we can couple tandem mass-spectrometry techniques with orthogonal measurements such as ion mobility and IR ion spectroscopy. These orthogonal techniques can provide further insight into the physicochemical properties of the targeted clusters within the gas-phase ensemble. In this chapter, details regarding the experimental details will be discussed.

2.1.1 – Electrospray Ionization

Electrospray ionization (ESI) is a technique commonly used to generate ions under atmospheric pressure for mass spectrometric analysis.[46–48] Prior to ESI, analytes are dissolved in a volatile polar solvent, such as methanol, acetonitrile, or a polar organic solvent that is miscible with water.[46] To this mixture, acids or bases are added to enhance ionization and generate protonated or deprotonated analytes, or species that are complexed with metal cations.[49,50] A sample schematic of ESI is provided in **Figure 2.1,** which shows that the ESI process can be thought of as a circuit containing a capacitor. The solution containing the analyte of choice is pumped through a charged capillary at voltages that typically range between 2–6 kV at a flow rate ranging from 1–1000 μL min^{-1}.[51,52] Ions within the solution will move under the influence of electric field within the charged capillary, creating an enrichment of charged ions near the surface on the solvent.[46,53] The increased concentration

of charged particles at the surface forms a Taylor cone that leads to the dispersal of charged droplets upon reaching the threshold for the applied field strength.[53] This results in a spray of charged droplets with the same polarity as the capillary voltage.[54] After the charged droplets are dispersed from the Taylor cone, they undergo evaporation with the aid of an inert nebulizing gas such as N_2 or He at high temperatures for thermal evaporation.[51,54]

Multiple models exist for ion generation after the droplet dispersal, but I will focus on the ion evaporation model as it is more relevant for low weight ions.[48,55,56] The ion evaporation model describes the ejection of small solvated ions from the surface of the charged droplet caused by the Coulombic repulsion between the charges on the surface of the droplet.[57] Upon reaching the Rayleigh stability limit, where the repulsive force of the charges on the droplet surface is greater than the surface tension of the droplet, the droplets undergo Columbic explosion to generate smaller ion-solvent clusters and the evaporation process continues.[57,58] When the ions have escaped from the solvent droplet, they are guided to the mass spectrometer via a counter-electrode with the opposite polarity of the target analyte.

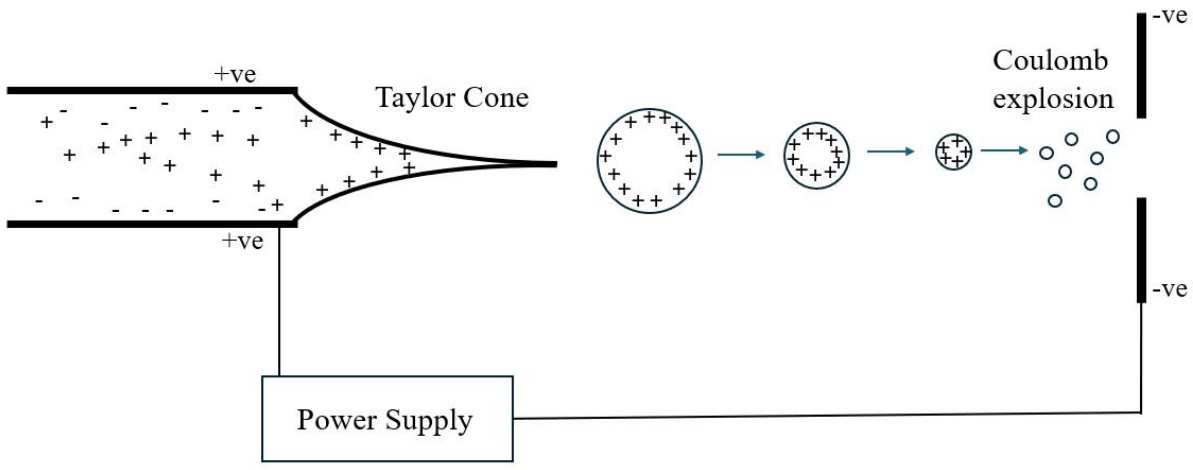


Figure 2.1. Example of electrospraying positively charged ions into the mass spectrometer via an electrospray ionization (ESI) source. The ions are guided into the mass spectrometer by both gas flow and attracting Coulombic forces from the counter-electrode.

After generating the ions, tandem mass spectrometry is often used to analyse the content of the ESI mixture. Various activation methods are used to energize the target analytes to promote a reaction that dissociates the precursor ions into smaller fragments.[59] By studying the relationship between the smaller fragments generated from the precursor analyte, structural differences and localized modifications between isomeric species can be elucidated. This is usually done by first mass-selecting the ions (*e.g.*, in an ion trap), then inducing fragmentation via collisions with an inert gas (*e.g.*, N_2, Ar) or via photodissociation (*e.g.*, by absorption of resonant photons).

2.1.2 – Collision Induced Dissociation

Collision induced dissociation (CID) is a tandem mass spectrometry technique that can aid in structural analysis for a wide range of analytes (*e.g.*, pharmaceutical drugs, peptides, and proteins).[60–62] The CID process begins by passing the target analyte through a collision cell containing an inert collision gas such as N_2 or Ar. As collisions occur, the internal energy of the analyte increases until the analyte ion dissociation threshold is reached, which results in a unimolecular dissociation.[63] Low energy CID usually consist of at least one collision with energy in the range of 1–100 eV.[54] The internal excitation caused by the collisions are initially vibrational in nature, with an interaction times on the order of picoseconds, prior to statistical distribution of energy across all accessible quantum states.[64] The redistribution of vibrational energy among all the internal modes of the ion leads to preferential cleavage at the weakest bond. Owing to this energy redistribution process, relatively large molecules (*i.e.*, those with a relatively large number of atoms) require more time and energy to dissociate than do small molecules.[65]

2.1.3 – Infrared Multiple Photon Dissociation

One can also induce dissociation of a target analyte via photodissociation (*i.e.*, photoexcitation followed by dissociation). An example of this process that is pertinent to this thesis is infrared multiple photon dissociation (IRMPD). IRMPD is a technique that can be used to measure the vibrational fingerprint of a gas phase ion by inducing dissociation *via* IR

photon absorption. The vibrational fingerprints region and functional group region of a molecule are the unique set of vibrational transitions that occur in the *ca*. 600 – 4000 cm^{-1} of the electromagnetic spectrum.[66–68] One can probe these transitions by monitoring the IRMPD efficiency as a function of probe laser wavenumber. Thus, the spectral intensity reflects the IR absorption cross section *and* the photodissociation efficiency of the analyte. IRMPD spectroscopy is a form of action spectroscopy that may be used to study a wide variety of molecular clusters, and this technique has been employed in targeted and untargeted proteomics, lipidomics, and metabolomics.[21,69–72] When conducted in tandem with computational simulations, IRMPD spectroscopy is a powerful tool for the elucidation of ionic structures. The IRMPD action spectra presented in this thesis were recorded at the Free Electron Lasers for Infrared eXperiments (FELIX) facility at Radboud University, Nijmegen, Netherlands.

For the IRMPD spectroscopy experiments described in this thesis, an IR free electron laser (FEL) is used to produce the necessary IR photons. A schematic of the main components of the IR-FEL is shown in **Figure 2.2**. A pulsed beam of electrons is generated by an electron gun and is accelerated to kinetic energies in the range 10 – 50 MeV before entering an undulator (*i.e.*, a stack of movable magnets that have alternating polarity). As the electron beam passes through the undulator, the alternating magnetic fields induce a sinusoidal beam path that generates coherent radiation (*viz*. photons) within the FEL optical cavity via the synchrotron effect.[73,74] The wavelength of the photons can be adjusted by changing the magnetic field and the kinetic energy of the electrons. For IR-FELs, specifically for the FELIX beamline, emission usually occurs over the spectral range of 66 – 3600 cm^{-1}. After the electron beam exits the undulator, the beam is directed to a beam dump and the photons are redirected to an experimental end-station (*e.g.*, a mass spectrometer). Additional details of free electron laser systems are available in references 74–77.[74–77]

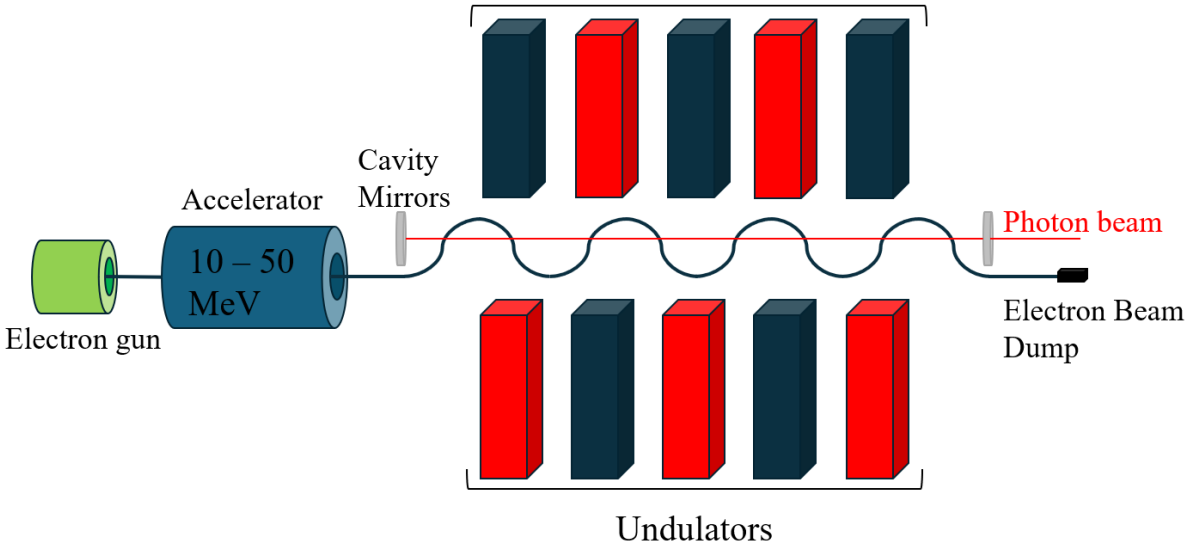


Figure 2.2. Schematic of the FEL at the FELIX laboratory. IR photons are generated via the synchrotron emission from the "wiggling" electron beam.

To acquire the IRMPD spectra described in this thesis, ions were generated by ESI at a voltage of 3-5 kV and a temperature of 453 K, with a typical flow rate of 4 μL sec^{-1} (can vary with experiment). The ions were then held in position in a Bruker Amazon ion trap mass spectrometer, which employs a radio-frequency field of 400 – 800 V_{pp} oscillating at 781 kHz, and they were cooled to approximately room temperature via collisional cooling in 10^{-3} mbar pressure of helium. The trapped ions were then irradiated with the tunable output the FELIX laser within the range of 600 – 3600 cm^{-1}.[14,78] When resonant with a vibrational transition, the FEL excites the ions to a higher vibrational energy state (*e.g.* $\nu = 0 \rightarrow 1$). This excited vibrational state couples to other 'quasi-continuum' vibrational energy states, known as bath states, resulting in a redistribution of energy via a process known as intramolecular vibrational energy redistribution (IVR). When IVR occurs, the ion is de-excited in the absorbing mode, enabling absorption of another photon of the same energy.[14,79,80] This process enables repeated absorption of IR photons until the ion's internal energy surpasses a dissociation threshold and it fragments. The depletion of the parent ion and appearance of the

fragment ions were monitored by the mass spectrometer as a signal of photon absorption. **Figure 2.3** provides a schematic of the IVR process, indicating how the process repeats until a thermodynamic dissociation threshold is met for the ion. Note that IRMPD is a stepwise multiple photon process, rather than a concerted multi-photon process; the $v = 2$ level is below the two-photon level associated with the $\nu = 0 \rightarrow 1$ resonance owing to vibrational anharmonicity, a situation that is exacerbated for higher vibrational levels.

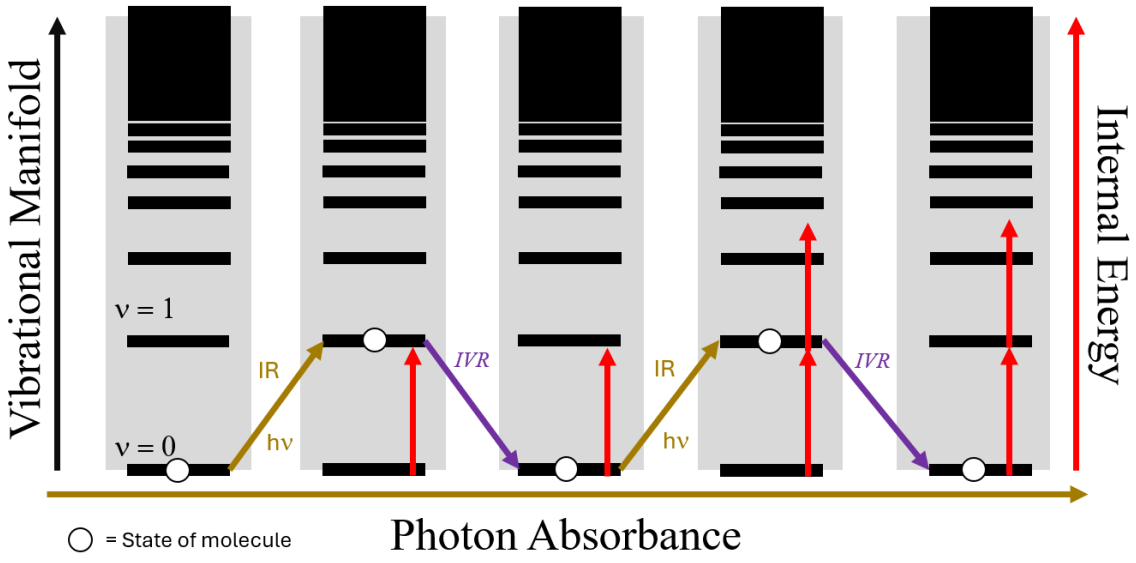


Figure 2.3. The IVR process. A photon excites the vibrational ground state ($\nu = 0$) of an ion to an excited state ($\nu = 1$). Energy transfer to the bath states de-excites the absorbing mode while maintaining the total internal energy of the ion. Repeated IR absorption followed by IVR raises the internal energy of the ion until a dissociation threshold is met and the ion fragments.

At FELIX, the IR photons are produced in 5-10 μs macropulses that are generated at a frequency of 10 Hz. The macropulses consist of a pulse train of 6 ps micropulses that are separated by 1 ns (*i.e.*, produced at 1 GHz). Each macropulse has an energy of 40 – 100 mJ.[78] The IRMPD spectrum is generated by plotting the fragmentation efficiency of the analyte ion

as a function of FEL wavenumber. The fragmentation efficiency, F_{eff}, is defined as the logarithmic ratio between the intensity of the precursor ion ($I_{precursor}$) and the total ion intensity (*i.e.*, sum of the precursor and fragment ion intensities $\{I_{fragments}\}$), as described **equation 2.1**.

$$F_{eff} = -\ln\left(\frac{\sum I_{precursor}}{\sum\left(I_{precursor} + I_{fragments}\right)}\right) \quad \textbf{(2.1)}$$

2.1.4 – Ion mobility

Ion mobility spectrometry (IMS) is a chromatographic technique often employed in conjunction with mass spectrometry to separate ions based on their mobilities through a gaseous environment prior to MS analysis. There are several variant of IMS, but most employ the same underlying principle – an ion's mobility in an inert gaseous environment, and is determined by its size/shape, mass, charge, and by the applied electric field.[81] For example, in drift-tube (DT) IMS experiments, ions are pulsed into a cell that contains an inert buffer gas (usually N_2 or He) and across which a low-field voltage ramp is applied. The electric field pushes the analyte ions through the buffer gas, and the ions will exit the drift-tube with arrival time distributions that depend on their respective mobilities.[82,83] The Mason-Schamp equation (**equation 2.2**) describes the relationship between an ion's mobility (**K**) and its collision cross-section (CCS, **Ω**) under low electric field conditions (< 10 Td; 1 Td = 10^{-21} V ·m^2). In **equation 2.2**, m_{ion} is the mass of the target analyte, the mass of the buffer gas is m_{gas}, *z* refers to the charge of the ion, *e* is the elementary charge, and k_bT is the Boltzmann constant multiplied by the temperature. Finally, *N* refers to the number density of the buffer gas. The CCS of an analyte is the orientationally averaged collision area between itself and a buffer gas particle. Ions with relatively large CCSs experience more collisions during transit through the mobility cell than do ions with relatively small CCS, which results in decreased mobility and longer drift times for the larger species. Thus, in instances where two isomers (or isobars)

are present in a gas phase ensemble of ions, the smaller of the two isomers elutes from the DT-IMS cell before the larger isomer.

$$K = \frac{\sqrt{18\pi}}{16} \cdot \sqrt{\frac{1}{m_{ion}} + \frac{1}{m_{gas}}} \cdot \frac{ze}{\sqrt{k_B T}} \cdot \frac{1}{\Omega N} \qquad \textbf{(2.2)}$$

2.1.4.1 – Travelling Wave Ion Mobility Spectrometry

In chapter 5, we employ travelling wave ion mobility spectrometry (TWIMS) to measure the mobilities of ion clusters that contain the $B_{12}F_{12}^{2-}$ dianion. TWIMS, like DT-IMS, can be used to determine CCSs, although in this case a set of calibration molecular are required. **Figure 2.4** shows a schematic of a TWIMS device. The TWIMS cell is made up of a stacked ring electrode ion guide, arranged in sequence with opposite RF phases applied to consecutive rings. This implementation radially confines ions within an effective potential well.[81] On top of the confining potential, a series of direct current waves are applied to push ions through the gas-filled ion guide. Ions above a certain mobility threshold will surf on a single wave through the TWIMS cell, whereas ions that are below the mobility threshold experience both forward and reverse field of the travelling DC pulse. As the waveform travels forward in the TWIMS cell, the ion species spends more time experiencing the forward field than the reverse field, and so is propelled to the exit of the drift cell. Thus, mobility separation in TWIMS is driven by the velocities of the ions as they surf the electric field through the collision cell; ions of relatively low mobility take longer to traverse the TWIMS cell than high mobility species.[84–86] The net drift velocity in TWIMS scales quadratically with mobility, whereas the drift velocity in DT-IMS scales linearly.[87] Moreover, because wave characteristics are tunable, TWIMS can manipulate ions into long path length separations without major signal loss or the need for high voltages.[81]

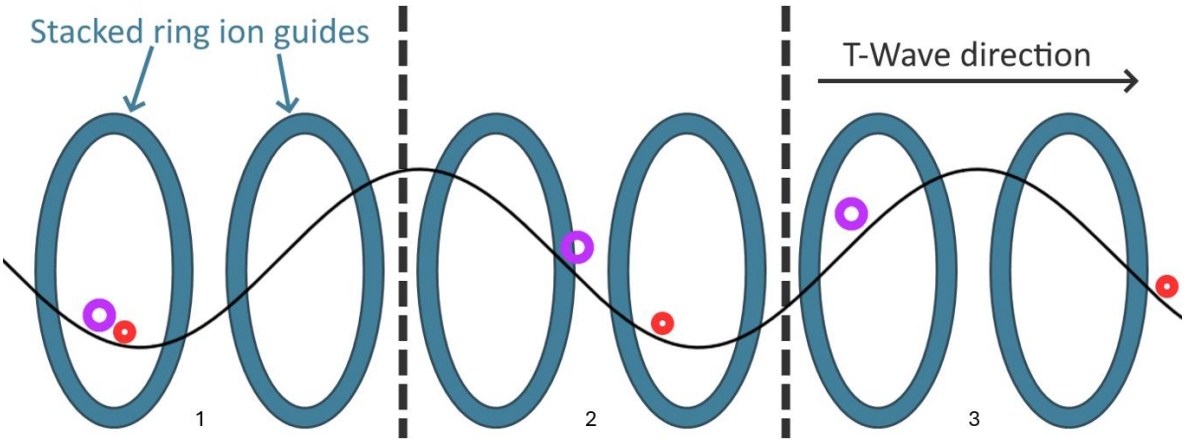


Figure 2.4. Schematic of a TWIMS cell. The large blue rings are the stacked ring electrod ion guide that confines the ions. The black lines across the image represents the travelling wave electric field. The purple circle represents an ion with a larger CCS than the red circle. (**Panel 1**) The ions introduction into the TWIMS cell. (**Panel 2**) The difference in CCSs (*viz.* mobility) causes the larger (purple) ion to lag in position compared to the smaller (red) ion. (**Panel 3**) The ions are fully separated as they exit the drift cell.

Because ions experience a changing electric field in the TWIMS cell, the Mason-Schamp relationship (**equation 2.2**) does not hold in this environment.[88,89] Following the recommendations by Gabelica *et al*.,[90] to determine the CCS of an analyte using TWIMS, a calibration curve must be generated using known CCSs that have been determined *via* DT-IMS measurements. To generate these CCS calibration curves, the DT-IMS CCS values of each ion in the set of calibration standards are converted to a CCS′ value by **equation 2.3**. Here, μ is the reduced mass of the buffer gas and target analyte system, and z is the charge of the analyte.

$$CCS' = \frac{CCS\sqrt{\mu}}{z} \qquad \textbf{(2.3)}$$

The CCS′ values are then plotted against a function t′ (given by **equation 2.4)** which is determined by subtracting the square root of the mass-to-charge ratio multiplied by the

constant c from the arrival time, t_A. The constant c is dependent on the voltage used by the transfer optics.

$$t' = t_A - c\sqrt{\frac{m}{z}} \tag{2.4}$$

With this treatment, we obtain a relationship for the calibration curve as shown in **equation 2.5.** An undetermined time offset, t_0, is used to account for systematic delays to the arrival time for improved accuracy. A and N is the fit parameter of the power function.

$$CCS' = A(t' - t_0)^N \tag{2.5}$$

2.1.4.2 – Differential Ion Mobility Spectrometry

Differential (ion) mobility spectrometry, referred to as DMS, DIMS, or FAIMS, can be used to separate regioisomers, conformers, and even tautomers prior to MS analysis.[91–96] For the SCIEX Selexion system used in this research, the DMS cell is at atmospheric pressure and the vacuum of the mass spectrometer (orifice positioned at the exit of the DMS cell) is used to create a carrier gas flow in which the analyte ions are entrained. Two parallel, planar electrodes are position on either side of the carrier gas flow axis and an asymmetric RF waveform, referred to as the separation voltage (SV) is applied across the electrodes. The waveform is a sum of sinusoids such that one-third of the period is at high-field and two-thirds is at low-field (see **Figure 2.5**). Because of the non-linear dependence of ion mobility on the electric field, ions exhibit different mobilities under the high- and low-field conditions. In an inert environment (*e.g.*, N_2, Ar, He) under the low-field limit, the ion temperature equilibrates to that of the carrier gas. Above the low-field limit, the ion's effective temperature is a sum of that of the carrier gas and the temperature induced by acceleration caused by the applied electric field. **Equation 2.6** describes the field-dependent mobility, $K(E/N)$, of the ion; the alpha function, $\alpha(E/N)$, scales the low-field mobility, K_0, as a function

of the reduced electric field strength of (*E/N*), where *E* is the electric field strength and *N* is the number density of the carrier gas.[97]

$$K\left(\frac{E}{N}\right) = K_0\,[1 + \alpha(\frac{E}{N})] \qquad \textbf{(2.6)}$$

To increase separation of ions in the DMS cell, a volatile solvent modifier is often introduced to the carrier to increase separation. For example, some commonly used protic modifiers such as isopropyl alcohol or methanol or aprotic modifiers such as acetonitrile are introduced at a 1.5 molar percent into the carrier gas.[98,99] The introduction of the modifiers changes the dynamic clustering behaviour of the target analyte in the DMS cell, as the analyte can interact with the modifiers through stronger intermolecular interactions such as charge-dipole interactions and hydrogen bonding interactions that are not possible in a pure nitrogen environment. The strength of the ion-solvent interaction for any ions can usually be approximated by the magnitude of the dipole moment of the solvent molecule. However, ion-solvent-cluster geometries and solvent-solvent interactions can influence this correlation. A simple example of this can be seen from a case of tetramethyl ammonium.[100] Doping the pure nitrogen environment with polar protic modifiers such as water, methanol, or isopropyl alcohol results in a weakly clustering type B clustering behaviour, whereas a polar aprotic modifier such as acetone or acetonitrile results in a strong clustering type A behaviour. Water is found to show the weakest clustering behaviour while having a larger dipole moment than isopropyl alcohol, which demonstrates that the magnitude of the dipole may not always be the dominant interaction influencing the clustering behaviour. This shows that the affinity of the microsolvation partner for a target analyte versus another depends on factors such as the number of solvent molecules accrete onto the analyte, the geometries of the microsolvated cluster, and the strength of the intermolecular interaction between the solvent molecule and the target analyte. The dissimilar clustering behaviours translate in the unique DMS behaviours that can be used to elucidate properties of the target analyte.

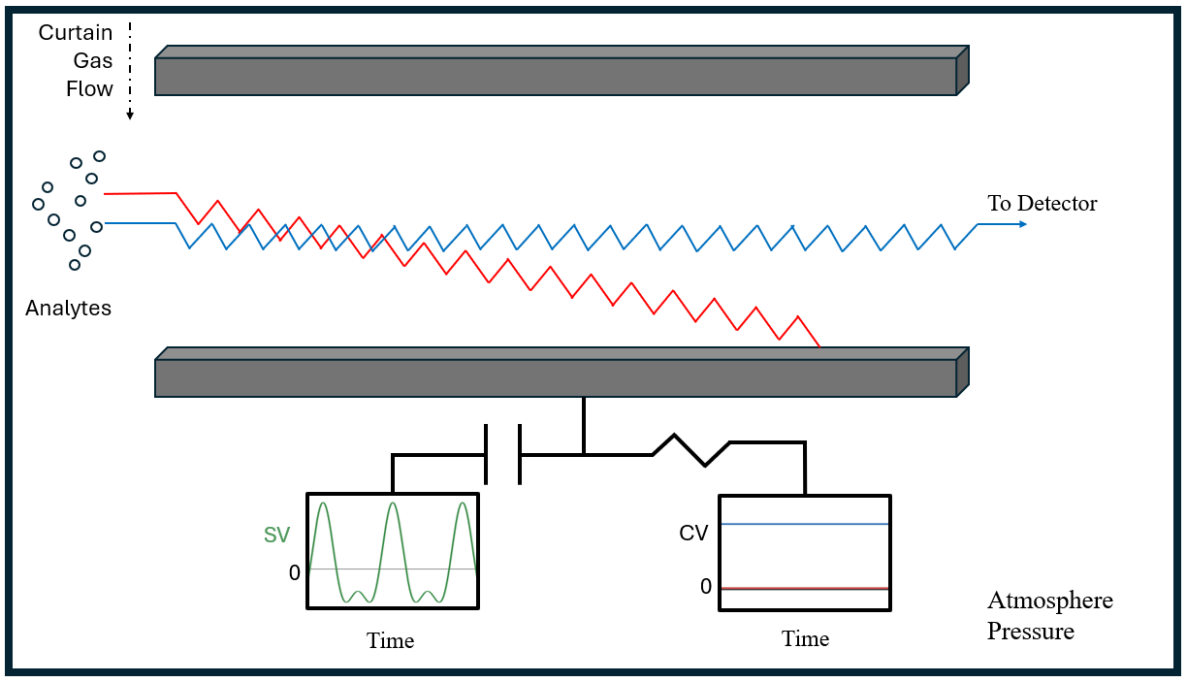


Figure 2.5. Schematic of a DMS cell. (**Red**) The path of the analyte without any CV correction to an applied SV. (**Blue**) The path of the analyte following the application of an appropriate CV to correct the ion trajectory and steer it onto the transmission axis.

As can be seen in **Figure 2.6**, the differential mobility between the high- and low-field portions of the DMS waveform causes the ions to migrate off-axis (*e.g.* away from the orifice of the mass spectrometer) in a zig-zag motion as they transit the DMS cell. To remedy the ion path, a DC static potential, referred to as the compensation voltage (CV), is applied to the electrodes. The CV necessary to steer the ion onto the transmission axis encodes the ion's differential mobility. In general, the CV required to correct the ion path depends on the ion's *m/z,* its field-dependent CCS, the magnitude of the SV, and the conditions within the DMS cell (*i.e.,* temperature, pressure, gas composition).

DMS instruments can be operated in one of three modes: (*i*) narrow-pass filter, (*ii*) CV scan, or (*iii*) full scan. By setting the SV and CV to optimal values for transmission of an analyte of interest, one creates a narrow-pass filter (mode *i*) that can exclude most other ions

from a complex matrix. Alternatively, one can fix the SV and scan the CV (mode *ii*) while monitoring a particular *m*/*z* to create an ionogram (see **Figure 2.6A**), which is a DMS measurement that is analogous to a TWIMS or DT-IMS arrival time distribution. In this case, though, rather than temporal separation, separation is spatial in nature. By plotting the optimal CV for ion transmission as a function of SV (mode *iii*), one generates a dispersion curve for the ion in the given DMS environment. In full scan mode, ions typically adopt one of three common behaviours, referred to as Types A, B, and C (see **Figure 2.6B**). Type A behaviour is associated with strong interactions (usually dynamic ion-solvent clustering behaviour) between the analyte and the collision gas. This behaviour leads to higher mobility at high-field compared to low-field conditions, requiring increasingly negative CVs with increasing SV to correct ion trajectories. In contrast, Type C behaviour is associated with 'hard sphere' scattering behaviour. Under these conditions, ions experience lower mobility at high-field than at low-field (as dictated by the kinetic theory of gases) and so increasingly positive CVs are required to correct ion trajectories as the SV increases. Type B behaviour is intermediate to Types A and C. In this case, ions require increasingly negative CV correction with increasing SV (like Type A) up to some critical point whereupon that trend reverses, and increasingly positive CVs are required (like Type C). This behaviour is normally associated with relatively weak dynamic ion-solvent clustering; at low SV values, dynamic clustering and de-clustering occurs as the ions experience the oscillating field-dependent heating and cooling, but when SVs are too high the ions experience so much heating that clustering cannot occur during the low-field portion of the waveform. Further details on the operations and theories on the DMS can be found in references 101 and 102.[101,102]

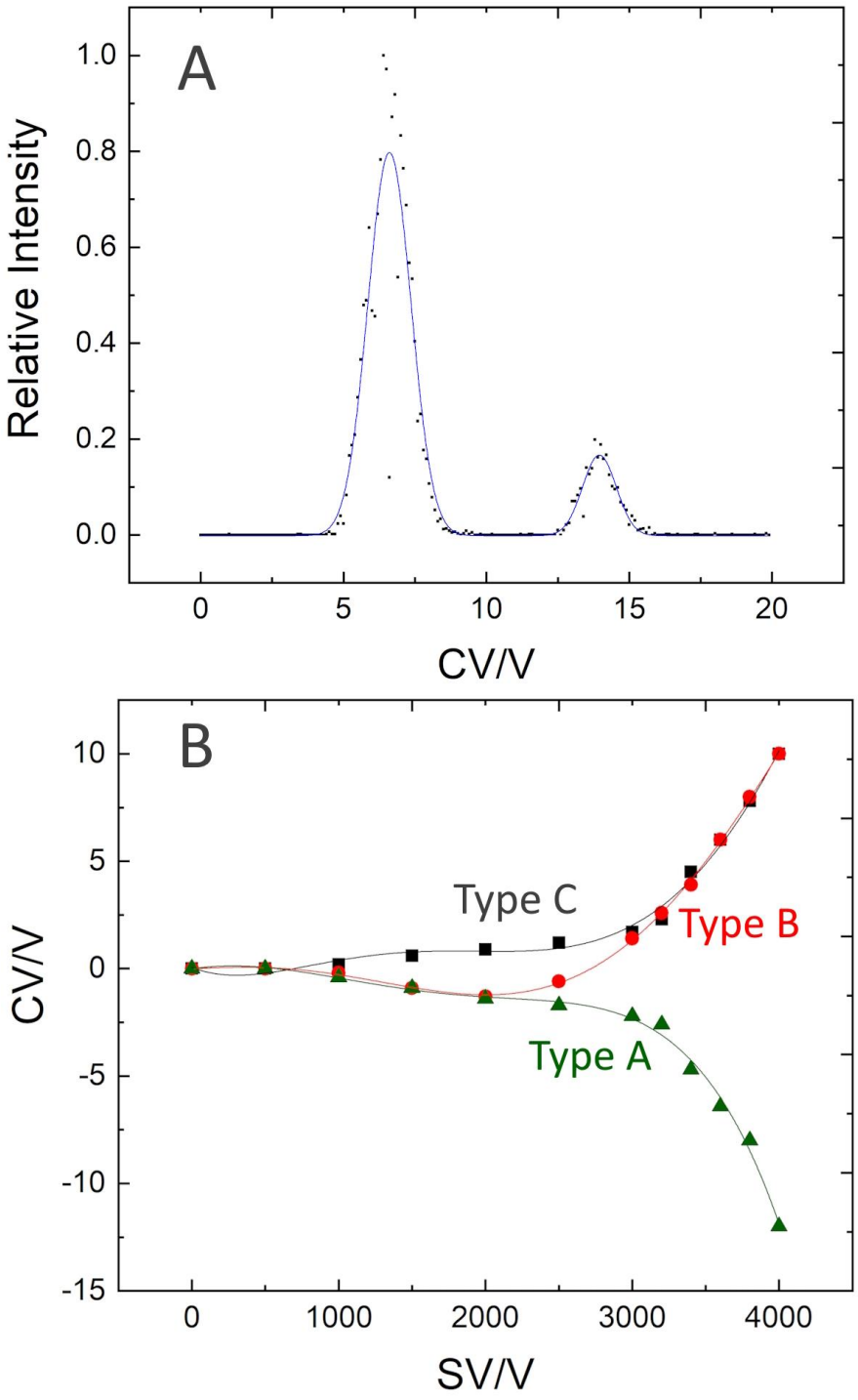


Figure 2.6. (**A**) Example of an ionogram at SV = 3800 V. (**B**) Common dispersion curve types observed in DMS experiments.

2.2 Computational Methods

To interpret the data obtained by ion mobility and spectroscopic measurements, computational modelling using electronic structure methods such as density functional theory (DFT) are often required. For molecular clusters in the gas-phase, multiple conformations may exist simultaneously within the ensemble.[103,104] Consequently, IRMPD spectra or ion mobility data may represent a convolution of multiple signals. These convolved signals can sometimes be disentangled by comparison with, for example, the computed vibrational spectra of geometry optimized cluster isomers. Moreover, identifying a reasonable match between experiment and theory can inspire confidence in additional computed properties such as bond dissociation energies geometric structures for the target analytes.

To study any analyte computationally, one typically begins with some intuitive "guess" structures for the analyte. These candidate structures are then treated with sampling algorithms such as CREST to identify possible local minima on the potential energy surface.[105] CREST output structures are sorted by their relative energies and pruned based on geometric similarity, and the lowest energy candidates (typically 5 – 10 structures) are re-optimized using higher level DFT methods. These computational methods are available in software such as ORCA or Gaussian 16.[106,107] If the energetics of the cluster are especially important, electronic energy calculations may be further refined at the coupled cluster level of theory (*i.e.* CCSD(T)), although this may be impractical for large species owing to the need to calculate correlation for all electron-electron pairs within the system. DLPNO-CCSD(T), a domain-based local pair natural orbital method that is available in ORCA may be able to address this limitation to some extent, but it still carries a significant computational cost.[108,109] Brief summaries of each of the above mentioned computational methods are provided in the following sections.

2.2.1 – CREST

The CREST algorithm is an iterative conformational searching algorithm created by Pracht, Bohle, and Grimme to generate unique conformers using meta dynamic simulations that are coupled with molecular dynamics (MD) calculations.[110] The algorithm uses a root-mean-square-deviation (RMSD) based meta-dynamic algorithm (MTD) employing a set of collective variables and presence of a history-dependent potential that fills the minima on the potential energy surface to overcome energy barriers. Further details of the MTD algorithm are provided in reference 111.[111] Multiple structures are generated by the MTD, which are sorted by their relative energies calculated by the GFN2-xTB semi-empirical method. In the case that a new minimum structure is found during the search, the new structure is re-introduced to the algorithm as a new starting point. MD simulations are then performed on the six lowest energy conformers to identify rotamers and to more extensively sample the local surroundings on the potential energy surface. The algorithm distinguishes conformers and rotamers based on their total energy, the rotational constants of the molecule, and the Cartesian RMSD between the conformations.

For the research performed in this thesis, the CREST algorithm is used along with the semi-empirical Extended Tight-Binding program package.[112] In Chapters 4 and 5, cluster geometries are generated by CREST algorithm using the "GFN2-xTB" keyword. In our study of triazolide clusters (described in Chapter 4), the "-nci" flag is used specifically to sample non-covalent interactions between the deprotonated triazolide and alkali metal cations within the clusters. This keyword enhances the identification of different conformations for non-covalently bound complexes, wherein the arrangement of the ions within the cluster is important. For this method, an ellipsoidal potential is used to counteract the minimized MTD bias potential that may lead to dissociation of the complex. After sorting the output from the CREST algorithm, the remaining geometries are optimized further with DFT.

2.2.2 – Density Functional Theory

Density Functional Theory (DFT) is a useful (and common) method for calculating electronic energies and thermochemical properties, and for determining molecular structures with accuracy that is comparable to higher levels of theory (*e.g.*, Møller–Plesset perturbation theory of second order; MP2).[113] Moreover, DFT can accomplish this performance at a relatively low computational cost. This speed increase stems from treatment of the spatially dependent electron density rather than the individual electron wavefunctions. In the basic form of DFT defined by Kohn and Sham, the electronic density is a universal density function described as the approximation of the summation of the kinetic energy, electron-nuclear interaction energy, Coulomb energy, and the exchange/correlation energy.[114] Modification of these energies and inclusion of additional terms such as damping functions or dispersion corrections have spawned a plethora of DFT functionals.

The Minnesota 06-2X (M06-2X) functional that we used in **Chapter 3** was chosen for its accuracy when treating simple fluorocarbon species;[115,116] significant accuracy is achieved for binding energy calculations without requiring more computationally expensive levels of theory as the dispersion is implicitly accounted for through parametrization and without an explicit empirical correction. In addition to this, the M06-2X functional yields relatively accurate harmonic vibrational spectrum predictions, which are useful for assigning vibrational modes in experimental IRMPD spectra.

In **Chapters 4** and **5,** we employed the Modified Becke 97 exchange-dipole moment (ωB97X-D3) functional with damping function.[117,118] The damping function is used to model the short-range behaviour of a dispersion interactions, avoiding near-singularities for small distances between atoms and double-counting effects of electron correlations at intermediate distances. This method was found to be one of the most accurate for calculating energies in a comparison of 5000 data points computing using 200 different DFT methods.[113] In **Chapter 5**, the ωB97X-D3BJ approach is used because it performs better than D3 damping for thermochemical problems that are sensitive to medium-range correlation effects.[119,120] This

is true for the $B_{12}F_{12}^{2-}$ dianion cages that we study in **Chapter 5**; in these systems, the negative charge density is delocalized about the surface of the cage. Computational results for **Chapter 3 – 5** are available on the iochem database.

It should be noted that the basis set used to represent the atomic orbitals also plays a large role in DFT calculation accuracy when computing optimized geometries and energies.[121] In general, if the target analyte is a protonated cation, a polarized basis set is used, such as the def2-TZVPP basis set.[122] This is to account for the change in polarization of the molecule after protonation. For an anion, a diffused augmented basis set, such as def2-TZVPPD,[123] should be used to account for wavefunctions that extend far beyond the nuclei (since the extra electron(s) is(are) usually relatively weakly bound compared to other valence electrons.[124]

2.2.3 – Nudged Elastic Band

The Nudged Elastic Band (NEB) method is an important computational tool for determining transition state (TS) geometries. We used NEB to identify TSs in the dissociation pathways of the deprotonated fluorinated propionic acid derivatives discussed in **Chapter 3**. NEB was first described by Henkelman *et al.*[125] and implemented in the ORCA computational suite.[126] The goal of NEB calculations is to determine the minimum energy path (MEP) connecting two local minima (*e.g.*, product and reactant) on the associated potential energy surface. For each point along the MEP, the energy is at a minimum with respect to all orthogonal directions, but at a maximum along the minimum energy path. Following the definition in transition state theory, the energy maximum on the MEP should be the energy barrier for the transition, *i.e.*, the TS. NEB is an iterative optimization method that generates a guess reaction path via discretized intermediate structures (usually referred as images) between the two linked minima. Multiple approaches can be used to generate this initial guess reaction path between the two minima. For example, one can utilize linear interpolation in the Cartesian coordinates between pairs of atoms in the starting and ending structure, while matching the distances between the pair as closely as possible in a least-square sense. The intermediate images iteratively converge toward the MEP by considering

the component of the atomic forces that are perpendicular to the current reaction path (estimated from the tangent to the path at each image with the end points of the path being fixed). This allows for parallelization of the calculation, where electronic structure computation can be distributed to different cores in the processor.

For the research reported in this thesis, the energy weighted NEB-TS method is used to determine the transition state geometry for the formation of FCO_2^- and the elimination of HF from fluoropropionic acids (see **Chapter 3**). For all energy weighted NEBs, the density of images is higher around the energy maximum on the MEP. Before initializing the NEB-TS calculation, a NEB-CI (*i.e.*, climbing image) calculation with looser convergence criteria is conducted. The NEB-CI calculation has its energy maximized with respect to one degree of freedom along the direction of the tangent, while minimizing the energy with respect to the other degrees of freedom. After finding the maximum point along that reaction path, it is then used as a guess structure for a TS optimization using the tangent at the CI to select the eigenvector that should be followed. As the tangent estimate provides an accurate approximation to the saddle point on the potential energy surface which guides the algorithm to determine the transition state of the MEP.

– Chapter 3 –

Fluorinated Propionic Acids Unmasked

Chapter 3 was published in the Journal of Physical Chemistry Letters. For the original publication, see Lee, A. E.; Featherstone, J.; Martens, J.; McMahon, T. B.; Hopkins, W. S. Fluorinated Propionic Acids Unmasked: Puzzling Fragmentation Phenomena of the Deprotonated Species. *J. Phys. Chem. Lett.* **2024**, *15* (11), 3029–3036. https://doi.org/10.1021/acs.jpclett.3c03400.

3.1 – Introduction

Per- and polyfluoroalkyl substances (PFAS) have emerged as a subject of concern in recent years due to their widespread usage and potential adverse effects on human health.[127,128] These man-made chemicals, which have some or all of the hydrogen atoms in their carbon chains replaced with fluorine atoms, possess exceptional stability and resistance to degradation. Consequently, PFAS have found extensive application in various industrial, commercial, and household products, ranging from firefighting foams to nonstick cookware.[25–27] As mounting evidence raises serious questions about the potential long-term consequences of PFAS exposure, long-chain PFAS such as perfluorooctanesulfonic acid (PFOS) and perfluorooctanoic acid (PFOA) are being phased out of production and many industries are shifting their focus to short chain PFAS and fluoroether replacements.

Legacy PFAS such as PFOS and PFOA have been extensively studied, and their structures and properties are well-characterized.[131] However, the PFAS class of compounds has more than 9000 members, and characterization of emerging short chain PFAS is limited.[132–134] Moreover, common degradation methods of long-chain PFAS often result in production of shorter chain species for which chemical information and rigorous analytical quantification methods are lacking.[135–137] Of pertinence to this study is the gas-phase fragmentation behaviour of short-chain per- and polyfluoroalkyl carboxylic acids (PFCAs). Typically,

PFCAs are detected via mass spectrometric multiple reaction monitoring of the carbanion produced following CO_2 loss from the deprotonated parent molecule.[138] This fragmentation behaviour is well documented for carboxylate anions and the energetics of decarboxylation have been thoroughly investigated for a variety of analytes.[139] However, the impact of fluorination on the gas-phase fragmentation behaviour of carboxylic acids is not well understood.

Here we investigate the fragmentation of fluorinated propionic acid derivatives using infrared multiple photon dissociation (IRMPD)[140] and collision induced dissociation (CID). In addition to the loss of CO_2, the presence of fluorine in PFCAs gives rise to the possibility of accessing additional product channels such as those associated with HF elimination and the formation of the fluoroformate anion, FCO_2^-, which is produced by the reductive derivatization of carbon dioxide. In spite of its well-known stability, FCO_2^- has only recently been characterized spectroscopically in an IRMPD study by von Helden and co-workers.[141] McMahon *et al.* first generated FCO_2^- via fluoride ion transfer and studied its thermochemistry in an ion cyclotron resonance instrument.[142,143] They determined a bond dissociation enthalpy of $\Delta H_{298} = 133 \pm 8$ kJ mol^{-1} which, although significantly weaker than typical C–F bonds (*ca.* $\Delta H_{298} > 400$ kJ mol^{-1}),[143,144] indicates that FCO_2^- could be a reasonably stable product of gas-phase dissociation of PFCAs. Such a process might be akin to the fluoride transfer mechanism that was observed in early attempts to deprotonate ethyl fluoride and determine its gas-phase acidity.[144]

3.2 – Methods

IRMPD spectra were recorded at the FELIX free electron laser (FEL) laboratory.[140] 2-monofluoropropionic acid, 3-monofluoropropionic acid, 3,3,3-trifluoropropionic acid, 3,3,2,2-tetrafluoropropionic acid, 3,3,3,2-tetrafluoropropionic acid, and pentafluoro-propionic acid were sourced from Oakwood Chemicals and Enanmine at greater than 95% purity. Each sample was prepared in a 50:50 methanol-water mixture at a concentration of 10 μM. Ions were generated using electrospray ionization and were mass selected using a

modified quadrupole ion trap mass spectrometer (Bruker Amazon) interfaced with the output of the FELIX IR beam. Following mass selection of the precursor ions, fragment ions were produced via IRMPD across the 600 – 1850 cm^{-1} region. Vibrational spectra were then generated by recording the precursor fragmentation efficiency as a function of the tuneable FEL output.

To complement IRMPD experiments, CID experiments were conducted using a Thermo Scientific LTQ Linear Ion Trap system at the University of Waterloo. 2-monofluoropropionic acid, 3-monofluoropropionic acid, 2,2-difluoropropionic acid, 3,3-difluoropropionic acid, 3,2,2 trifluoropropionic acid, 3,3,3-trifluoropropionic acid, 3,3,3,2-tetrafluoropropionic acid, 3,3,2,2-tetrafluoropropionic acid, and pentafluoropropionic acid were purchased from Enanmine at greater than 95% purity. Each sample was prepared in a 50:50 methanol-water mixture at a concentration of 10 μM. Ions were generated using electrospray ionization and were mass selected prior to interrogation. CID were monitored for collision energies of 10 – 20 eV with a step size of 5 eV between 20 eV to 30 eV with a step size of 2.5 eV to generate the breakdown curves.

Computational investigations were carried out with the ORCA computational suite, using the Minnesota 06-2X (M06-2X) functional with the def2-tzvp basis set.[145] This level of theory was selected due to its documented accuracy and efficiency for treating fluorinated species.[146–149] We have further supplemented the frequency calculation with M06-2X/aug-cc-pVTZ level of theory, and energy calculation with DLPNO-CCSD(T) /aug-cc-pVTZ level of theory with the corresponding auxiliary basis set.[150–153] In addition to computing energetic along reaction pathways, the nudged elastic band (NEB) method was used to identify transition states (TSs) associated with production of the fluoroformate anion and loss of hydrogen fluoride (HF).[154] The ORCA implemented NEB-TS method is utilized to generate transition states. In the case that the climbing image calculated by the NEB algorithm cannot optimize to a TS. Further TS optimization cycles are computed until a single negative frequency is achieved and verified by a frequency calculation. The initial guess structures for the TSs are required as inputs; structures were manually generated wherein the fluoroformate

anion was complexed with the associated fluoroethylene derivative via an anion–π interaction. All NEB calculations were energy weighted with 32 individual points along the potential energy surface and geometries located around the predicted TSs. The TSs identified via the NEB method were subsequently optimized at the M06-2X/def2-tzvp level of theory to ensure they were local maxima and to accurately compute relative energies. Intrinsic reaction coordinate calculations (IRC) are used to verify NEB results.

3.3 – Results and Discussion

Traditional mass spectrometry techniques have difficulties in separating isomeric analytes which can be solved by coupling to a spectroscopic technique such as IRMPD. Similar to identifying compounds with FT-IR by their IR fingerprints, IRMPD can serve a similar purpose for gas-phase ions. As an example, **Figure 3.1** shows the experimental IRMPD spectra of the deprotonated 3,3,3,2-tetrafluoropropioic acid and the 3,3,2,2-tetrafluoropropioic acid. Although the geometrical differences between the two propionic acids are small, the resulting IMRPD spectra are significantly different from each other. By inspection, the 3,3,2,2-tetrafluoro has IR signatures between 1000 – 1300 cm^{-1}, which is different from the location of the signature peak for the 3,3,3,2-tetrafluoro in the range of 1200 – 1500 cm^{-1}. In addition to differentiating the compounds *via* IR fingerprints, we can study the IRMPD spectrum of the individual product channels, as the fragmentation efficiency between the isomeric precursor ions are likely to be different.

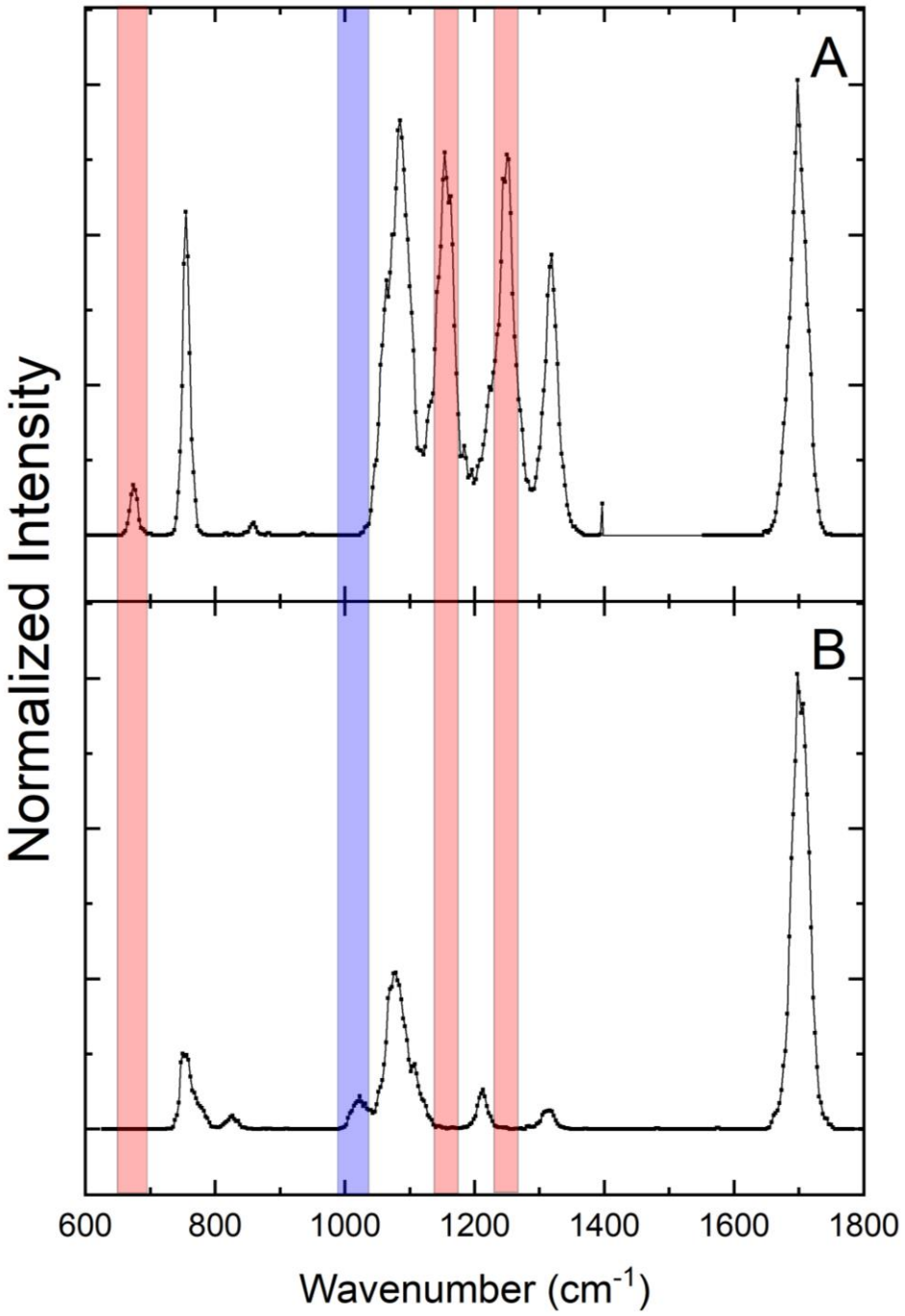


Figure 3.1. Experimental IRMPD spectra of the deprotonated 3,3,3,2-tetrafluoropropionic acid and the 3,3,2,2-tetrafluoropropionic acid. (A) 3,3,3,2-tetrafluoropropionic acid with its signature IR region in red and (B) 3,3,2,2-tetrafluopropionic acid with its signature IR region in blue.

3.3.1 – IRMPD spectrum of the deprotonated 3,3,3,2-tetrafluoropropionic acid.

The IRMPD spectrum of deprotonated 3,3,3,2-tetrafluoropropionic acid is shown in **Figure 3.2** along with the computed vibrational spectrum. The IRMPD and computed vibrational spectra for deprotonated 3-monofluoropropionic acid, 2-monofluoropropionic acid, 2,2-difluoropropionic acid, 3,3,3-trifluoropropionic acid, 3,3,2,2-tetrafluoropropionic acid, and pentafluoropropionic acid are provided in Appendix A (**Figure A1–A6**). Computed vibrational spectra employ a scaling factor of 0.95, in alignment with literature convention.[155,156] IRMPD of the various fluorinated derivatives yielded fragments associated with four product channels: (1) loss of CO_2, (2) loss of HF, (3) loss of HF + CO_2, and (4) production of FCO_2^-. Although the loss of CO_2 is typically the dominant product channel for carboxylate ions, it was observed for only the three most highly fluorinated propionic acid derivatives and was the major product channel only for the 3,3,2,2-tetrafluoro and pentafluoro species. Interestingly, the 3-monofluoro, 3,3,3-trifluoro, 3,3,2,2-tetrafluroro, and 3,3,3,2-tetrafluoro species all exhibited production of an ion at *m*/*z* 63, which we confirmed to be FCO_2^- by conducting IRMPD spectroscopy on the isolated product. The IRMPD spectrum of FCO_2^-, which is provided in **Figure A7** of Appendix A, agrees with that reported by von Helden.[141] In contrast with the other fluorinated derivatives, the 2-monofluoro and 2,2-difluoro species exhibited only HF loss via IRMPD. **Table 3.1** provides a summary of the product branching ratios observed for each parent ion.

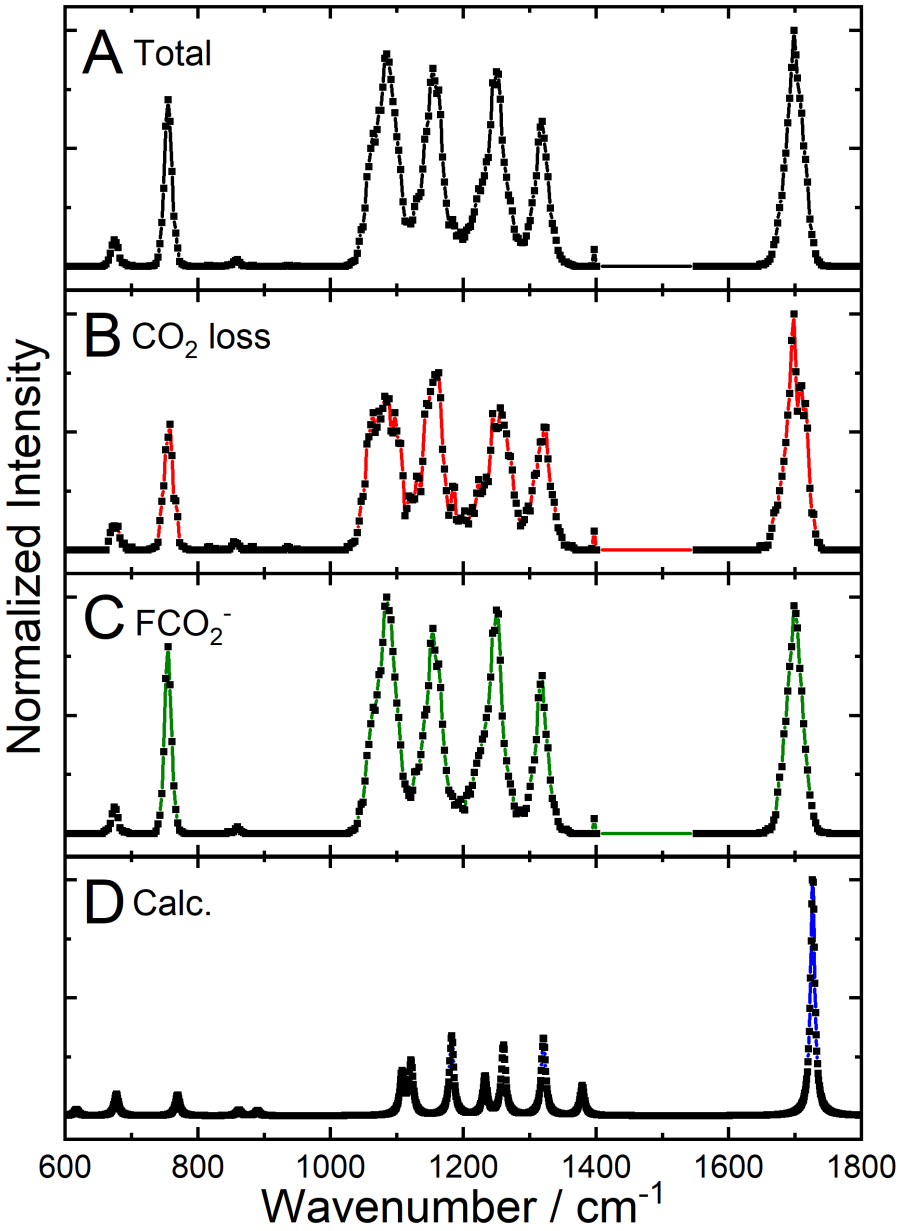


Figure 3.2. IRMPD and computed harmonic vibrational spectra for 3,3,3,2-tetrafluoropropionic acid. (A) total fragmentation efficiency, (B) CO_2 loss channel, (C) FCO_2^- channel, and (D) calculated spectra. The computed spectrum was scaled by a factor of 0.95.

Table 3.1. Product branching ratios observed following IRMPD of 2-monofluoropropionic acid (2-F), 3-monofluoropropionic acid (3-F), 2,2-difluoropropionic acid (2,2-F_2), 3,3,3-trifluoropropionic acid (3,3,3-F_3), 3,3,2,2-tetrafluoropropionic acid (3,3,2,2-F_4), 3,3,3,2-tetrafluoropropionic acid (3,3,3,2-F_4), and pentafluoropropionic acid (F_5).

Precursor Ion	IRMPD Product Branching Ratio			
	Loss HF	Loss CO_2	Loss HF + CO_2	Form. FCO_2^-
2-F	1	0	N/A*	0
3-F	0	0	N/A*	1
2,2-F_2	1	0	0	0
3,3,3-F_3	0	0	0	1
3,3,2,2-F_4	0	0.9997	0	0.0003
3,3,3,2-F_4	0	0.3333	0	0.6667
F_5	0	1	0	0

*The loss of HF + CO_2 from the 2-F and 3-F derivatives yields a product with *m*/*z* less than the lower detection limit of the Bruker Amazon mass spectrometer and so could not be quantified.

The IRMPD branching ratios given in **Table 3.1** suggest two interesting trends. First, it appears that HF elimination only occurs when a hydrogen atom is bound to the β-carbon and a fluorine atom is bound to the α-carbon. A notable exception to this trend is that HF elimination was not observed for the 3,3,2,2-tetrafluoro derivative. The second apparent trend is that FCO_2^- production is only possible when a fluorine atom is bound to the β-carbon. However, the fact that the fluoroformate ion is not produced via IRMPD of the pentafluoro derivative and only in minor quantities for the 3,3,2,2-tetrafluoro derivative indicates that a more detailed investigation of the thermodynamics and/or kinetics of the unimolecular decomposition reaction is warranted. For these reasons, we computed the various reaction pathways at the DFT level of theory, the results of which are discussed below.

The IRMPD spectra of the fluorinated propionic acid derivatives all exhibit intense bands associated with the asymmetric stretch of the carboxylate moiety at *ca*. 1700 cm^{-1}. As the degree of fluorination increases, this band shifts from 1644 cm^{-1} for the 3-monofluoro derivative up to 1729 cm^{-1} for the pentafluoro derivative. Vibrational bands associated with $\angle CCC$ bending of the alkyl chain, $\angle FCC$ and $\angle FCF$ bending motions, and C–F stretching motions are observed in the *ca*. 1000 cm^{-1} to 1350 cm^{-1} region. These vibrations, while formally associated with specific functional groups, are highly coupled and all exhibit displacements of the fluorine atoms. Like the carboxylate asymmetric stretch, these bands also exhibit blue shifts that correlate with increasing degrees of fluorination. In contrast, the $\angle OCO$ scissoring band at *ca*. 800 cm^{-1} shifts to lower wavenumber with increasing fluorination. DFT calculations show that removing electron density from the -CO_2 group reduces the vibrational mode force constant resulting in the observed shift. The observed bands for each fluorinated propionic acid derivative and their assignments are provided in the Appendix A **Table A1-A7**.

The IRMPD spectrum for the deprotonated 3,3,3,2-tetrafluoro derivative, which was the only species that exhibited appreciable competition between two dissociation pathways, could be extracted for each of the individual product channels (*i.e.*, loss of CO_2 *versus* formation of FCO_2^-). These spectra are plotted in **Figures 3.2B** and **3.2C**. Although the same vibrational bands are observed via both product channels, there are notable differences between the observed spectra with respect to band intensities. Specifically, the bands associated with displacement of the fluorine atoms are relatively more intense in the FCO_2^- product channel when compared to those observed in the CO_2 loss channel. Similar behaviour was also observed for the 3,3,2,2-tetrafluoro derivative but, because FCO_2^- production was observed in such minor quantities for this species, conclusions drawn based on relative intensities are more tenuous in this case. The observed differences in band intensities might indicate that exciting vibrations which bring a fluorine atom into closer proximity of the carboxylate moiety promotes formation of FCO_2^-. To explore further the possibility, a computational search for the transition state(s) leading to FCO_2^- production was conducted;

a transition state geometry resembling a fluorine transfer to the -CO_2 group would provide some evidence for this speculative notion. The results of our computational study are discussed below.

To compare with the fragmentation behaviour observed via IRMPD, the unimolecular decomposition of the fluorinated propionic acid derivatives was also investigated with CID. **Table 3.2** provides a summary of CID results. In general, the loss of CO_2 is more pronounced via CID than IRMPD. In our discussion of **Figure 3.2**, we hypothesized that exciting vibrational modes corresponding to the movement of fluorine atoms results in a higher yield of the FCO_2^- anion. In the case of CID, vibrational mode selection is not possible because the analyte is heated stochastically via collision. Interestingly, although the production of FCO_2^- is the dominant product channel for deprotonated 3,3,3,2-tetrafluoropropionic acid via IRMPD, FCO_2^- is only produced to a minor degree via CID (see **Table 3.2**). Moreover, at no collision energy does the production of FCO_2^- become the dominant product channel. CID breakdown curves are provided for all species studied in Appendix A **Figure A8–A16**.

The 2-monofluoro and 2,2-difluoro derivatives both exhibit a relatively high degree of HF loss via CID as was observed in IRMPD experiments. However, CO_2 loss is the dominant fragmentation pathway for the 2,2-difluoro derivative in CID experiments. Unfortunately, CO_2 loss from the 2-monofluoro derivative was below the low-mass threshold of our instrument and so could not be quantified. To explore further the impact of fluorination sites on the loss of HF, we expanded our study to include CID experiments on the 3,3-difluoro and 3,2,2-trifluoro derivatives, both of which exhibited detectable, but very minor, amounts of HF production. These results further support the hypothesis that HF elimination predominantly involves a fluorinated α-carbon and suggests that any degree of fluorination of the terminal methyl group effectively closes the HF product channel because the competition from the fluoroformate production.

Interestingly, FCO_2^- is the dominant product observed via CID for the 3-monofluoro, 3,3-difluoro, 3,2,2-trifluoro, and 3,3,3-trifluoro derivatives. However, for the tetrafluoro and

pentafluorinated species, FCO_2^- production is negligible and CO_2 loss dominates CID. This behaviour aligns with expectations based on IRMPD experiments with the notable exception of 3,3,3,2-tetrafluoropropionic acid. Considered collectively, CID results indicate that FCO_2^- production requires fluorination of the b-carbon and that higher degrees of fluorination close this product channel in favour of CO_2 loss. Electronic structure calculations were conducted to explore this behaviour in more detail.

Table 3.2. Product branching ratios observed following CID at Normalized collision energy of 22.5 eV of 2-monofluoropropionic acid (2-F), 3-monofluoropropionic acid (3-F), 2,2-difluoropropionic acid (2,2-F_2), 3,3-difluoropropionic acid (3,3-F_2), 3,2,2-trifluoropropionic acid (3,2,2-F_3), 3,3,3-trifluoropropionic acid (3,3,3-F_3), 3,3,2,2-tetrafluoropropionic acid (3,3,2,2-F_4), 3,3,3,2-tetrafluoropropionic acid (3,3,3,2-F_4), and pentafluoropropionic acid (F_5).

Precursor Ion	CID Product Branching Ratio			
	Loss HF	Loss CO_2	Loss HF + CO_2	Form. FCO_2^-
2-F	1	N/A*	N/A*	0
3-F	0	N/A*	N/A*	1
2,2-F_2	0.1536	0.8464	N/A*	0
3,3-F_2	0.0031	0.2313	N/A*	0.7655
3,2,2-F_3	0.0015	0.0908	0.0454**	0.8622**
3,3,3-F_3	0	0.2223	0**	0.7777**
3,3,2,2-F_4	0	0.9994	0.0002	0.0004
3,3,3,2-F_4	0	0.9840	0.0001	0.015
F_5	0	1	0	0

*The loss of CO_2 and the loss of HF + CO_2 from the 2-F and 3-F derivatives yields a product with *m/z* less than the lower detection limit of the Thermo LTQ mass spectrometer and so could not be quantified.

Fragment *m/z* for the loss of CO_2 + HF is equivalent to the *m/z* of FCO_2^-. A Waters Synapt G2-Si was used to verify the fragmentation as the two products differ in exact mass by 0.02 *m/z* (see **Appendix A figure **A17** and **A18**).

3.3.2 – Competition between FCO_2^- and CO_2 formation pathways.

To investigate the FCO_2^- formation mechanism, the nudge elastic band (NEB) algorithm was used to identify transition states along the reaction pathway of the various deprotonated fluorinated propionic acid derivatives. In all cases, NEB calculations identified a four-membered ring transition state formed between the carboxylate carbon atom and a fluorine atom bound to the β-carbon. **Figure 3.3A** shows the transition state *en route* to FCO_2^- formation for the deprotonated 3,3,3,2-tetrafluoro derivative. In general, the transition states associated with FCO_2^- production exhibit elongated C_a–CO_2^- bonds (*ca*. 3.0 Å) and C_b–F bonds (*ca*. 1.9 Å), and a F•••CO_2^- distance of *ca*. 2.2 Å compared to the equilibrium geometry of the intact parent (*ca*. 1.6 Å, *ca*. 1.3 Å, and *ca*. 3.0 Å, respectively). Concomitant with F•••CO_2^- bond formation, the F_2C_b–C_aHF moiety adopts a planar geometry and shortened C_b–C_a bond length expected for the fluorinated ethene co-fragment. Transition state structures and reaction pathways for all species studied are provided in **Appendix A Figure A17–A29**.

Figure 3.3B plots the computed dissociation pathway for deprotonated 3,3,3,2-tetrafluoropropionic acid. DFT calculations indicate an interesting competition between pathways leading to the formation of FCO_2^- and the loss of CO_2. Formation of CO_2 was found to proceed by barrierless dissociation of the C_a–CO_2^- bond. At standard temperature and pressure, Gibbs energy, zero-point corrected energy, and electronic energy calculations indicate that CO_2 loss is favoured. Note that the formation of FCO_2^- is thermodynamically favoured for both 3,3-difluoropropionic acid and 3,3,3-trifluoropropionic acid in most cases. For 3,3,3-trifluoro, the Gibbs energy for the formation of FCO_2^- calculated at standard room temperature and pressure are higher than the CO_2 loss threshold. The fact that the CO_2 loss is the dominant product channel observed for CID of the 3,3,3,2-tetrafluoro derivative suggests that the conditions in our mass spectrometer are such that the barrier along the reaction pathway leading to FCO_2^- is indeed higher than the CO_2 loss threshold.

Table 3.3 provides a comparison of the computed thresholds for CO_2 production and the barriers to FCO_2^- production for all species studied. In general, computational predictions of the preferred dissociation pathway align with CID experimental observations. We find that higher degrees of fluorination (*i.e.*, tetrafluoro and pentafluoro substitution) yields relatively high barriers to FCO_2^- production, thus favouring CO_2 production, and that lower degrees of fluorination yield relatively low barriers to FCO_2^- production. However, there are two notable exceptions to this trend: the 3-monofluoro and the 3,2,2-trifluoro derivatives. Calculations indicate that CO_2 production is strongly favoured for the 3-monofluoro derivative. This behaviour was not observed in IRMPD experiments and CID experiments were inconclusive in this regard because the CO_2 loss channel was below our lower mass limit. In the case of the 3,2,2-trifluoro derivative, FCO_2^- production was the predominant channel observed via CID, but calculations suggest a slight preference for CO_2 production. Whether the discrepancy between experiment and theory for these species is due to calculation accuracy, experimental conditions, or a combination of both is not clear. It is also worth noting that our computational results indicate that CO_2 production is favoured for the 3,3,3,2-tetrafluoro derivative, and that this behaviour is observed in CID, but not in IRMPD experiments (which yield a FCO_2^- to CO_2 branching ratio of *ca*. 2:1). This further supports the hypothesis that one can exert some control over the unimolecular dissociation process for the 3,3,3,2-tetrafluoro derivative via resonant IR photoexcitation. A detailed investigation of the photochemical dynamics associated with the IRMPD process for deprotonated 3,3,3,2-tetrafluoropropionic acid would certainly be interesting but is beyond the scope of this study.

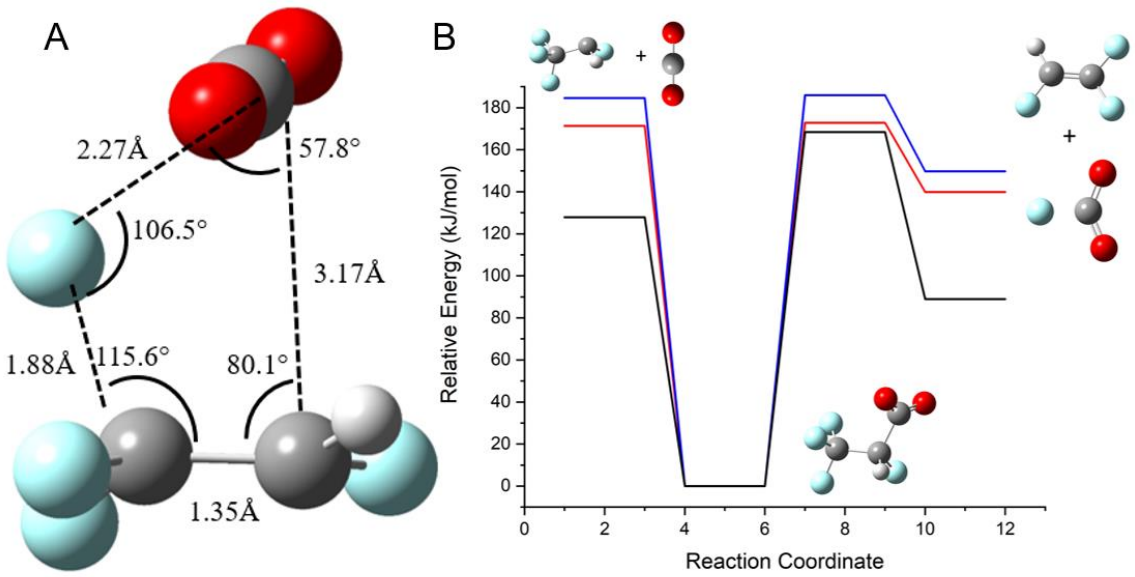


Figure 3.3. (**A**) Computed transition state geometry for production of FCO_2^- from deprotonated 3,3,3,2-tetrafluoropropionic acid. (**B**) Computed dissociation pathways for deprotonated 3,3,3,2-tetrafluoropropionic acid. (Black trace) relative standard Gibbs energy, (red trace) relative zero-point corrected energy, and (blue trace) relative electronic energy. Calculations were conducted at the M06-2X/aug-cc-pVTZ level of theory with single point energy calculated with DLPNO-CCSD(T)/aug-cc-pVTZ.

Table 3.3. Calculated thresholds for production of CO_2 and FCO_2^- for deprotonated 3-monofluoropropionic acid (3-F), 3,3-difluoropropionic acid (3,3-F_2), 3,2,2-trifluoropropionic acid (3,2,2-F_3), 3,3,3-trifluoropropionic acid (3,3,3-F_3), 3,3,2,2-tetrafluoropropionic acid (3,3,2,2-F_4), 3,3,3,2-tetrafluoropropionic acid (3,3,3,2-F_4), and pentafluoropropionic acid (F_5). Calculations were conducted at the M06-2X/aug-cc-pVTZ level of theory with single point energy calculated with DLPNO-CCSD(T)/aug-cc-pVTZ. Energies are given in kJ mol^{-1}. Other deprotonated fluorinated propionic acids with only computational results are provided in **Appendix A Table A8**.

Precursor Ion	CO_2 loss			FCO_2^- TS			FCO_2^- Production		
	ΔE_{elec}	ΔE_{zpe}	$\Delta G°$	$\Delta E_{elec‡}$	$\Delta E_{zpe‡}$	$\Delta G_{‡}°$	ΔE_{elec}	ΔE_{zpe}	$\Delta G°$
3-F	190	159	116	177	162	159	33.8	18.7	-24.6
3,3-F_2	198	181	139	142	126	122	47.8	35.1	-12.2
3,2,2-F_3	216	203	159	235	221	218	67.5	55.7	48.4
3,3,3-F_3	176	160	114	156	142	135	108	97.6	45.1
3,3,2,2-F_4	170	158	111	226	213	205	118	108	54.5
3,3,3,2-F_4	185	171	128	186	173	168	150	140	89.0
F_5	161	150	102	250	238	218	194	186	130

3.3.3 – Competition between HF and CO_2 formation pathways

The NEB algorithm was employed to investigate the HF formation mechanism for the deprotonated 2-monofluoro-, 2,2-difluoro-, and 3,3,2,2-tetrafluoropropionic acid derivatives. As expected, HF elimination proceeds via a four-membered ring transition state *en route* to generating the C_b–C_a double bond of the associated deprotonated propenoic acid derivative.[157] **Figure 3.4A** shows the calculated transition state for deprotonated 2,2-difluoropropionic acid. In general, the transition states along the HF formation pathway

exhibit elongated C_a–F bonds (*ca*. 2.0 Å) and C_b–H bonds (*ca*. 1.3 Å) for nuclei associated with the nascent HF moiety, and a shortened F•••H (*ca*. 1.4 Å) compared to the equilibrium geometry of the intact parent (*ca*. 1.4 Å, *ca*. 1.1Å, and *ca*. 2.6 Å, respectively). Transition state structures and reaction pathways for the deprotonated 2-monofluoro- and 3,3,2,2-tetrafluoropropionic acid derivatives are provided in **Appendix A**.

Figure 3.4B plots the computed dissociation pathway for deprotonated 2,2-difluoropropionic acid. DFT calculations suggest a competition between pathways leading to the formation of HF and the loss of CO_2; the CO_2 loss pathway is slightly favoured over the HF loss pathway. Although CO_2 loss is also favoured for the 3,3,2,2-tetrafluoro derivative, HF loss is favoured for the 2-monofluoro derivative. Thus, the trend that higher degrees of fluorination favour CO_2 production is again observed computationally (as was the case when investigating the FCO_2^- formation pathway). The energetics for HF and CO_2 production for the deprotonated 2-monofluoro-, 2,2-difluoro-, and 3,3,2,2-tetrafluoropropionic acid derivatives, all of which align with the results of CID experiments, are summarized in **Table 3.4**. Note, though, that for the deprotonated 2-monofluoro derivative, the CO_2 loss channel is below our instrument's lower mass limit. Consequently, we cannot make a definitive statement regarding CO_2 production via CID and its alignment with theoretical predictions. It is also worth noting that CO_2 production is favoured for the 2,2-difluoro derivative, and that although this behaviour is observed in CID, IRMPD exclusively yields HF. This apparent selectivity via resonant IR photoexcitation parallels our observations for production of FCO_2^- and further underscores the need for a detailed investigation of IR-induced photochemical dynamics in these systems.

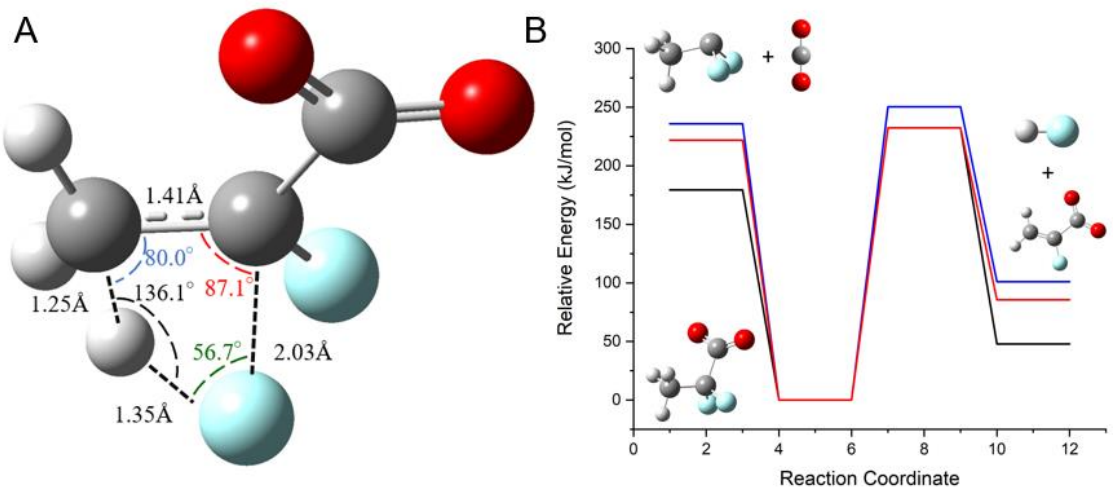


Figure 3.4. (**A**) Computed transition state geometry for production of HF from deprotonated 2,2-difluoropropionic acid. (**B**) Computed dissociation pathway for HF loss from deprotonated 2,2-difluoropropionic acid. (Black trace) relative standard Gibbs energy, (red trace) relative zero-point corrected energy, and (blue trace) relative electronic energy. Calculations were conducted at the M06-2X/aug-cc-pVTZ level of theory with single point energy calculated with DLPNO-CCSD(T)/aug-cc-pVTZ.

Table 3.4. Calculated thresholds for production of CO_2 and HF for deprotonated 2-monofluoropropionic acid (2-F), 2,2-difluoropropionic acid (2,2-F_2), and 3,3,2,2-tetrafluoropropionic acid (3,3,2,2-F_4). Energies are given in kJ mol^{-1}. Calculations were conducted at the M06-2X/aug-cc-pVTZ level of theory with single point energy calculated with DLPNO-CCSD(T)/aug-cc-pVTZ.

Precursor Ion	CO_2 loss			HF loss TS			HF loss product		
	ΔE_{elec}	ΔE_{zpe}	$\Delta G°$	$\Delta E_{elec‡}$	$\Delta E_{zpe‡}$	$\Delta G_{‡}°$	ΔE_{elec}	ΔE_{zpe}	$\Delta G°$
2-F	280	263	221	187	147	171	77.1	60.1	22.0
2,2-F_2	236	222	179	250	232	232	101	85.6	48.0
3,3,2,2-F_4	170	158	111	208	199	196	122	105	64.0

The loss of CO_2 to yield the associated fluorinated carbanion is the commonly known fragmentation pathway for per- and polyfluorinated carboxylic acids (*i.e.*, PFCAs), we find this to be the case only for fluorinated propanoic acids exhibiting a relatively high degree of fluorination. Mono-, di-, and tri-fluorinated species with fluorine atoms bound to the *beta*-carbon atom instead predominantly yield FCO_2^- via both CID and IRMPD. In further contrast, mono-, di-fluorinated species with fluorine atoms bound to the α-carbon atom exhibit HF loss.

Interestingly, significant differences in product branching ratios are observed for some fluorinated propionic acid derivatives depending on whether fragmentation occurs via CID or IRMPD. For example, the 2,2-difluoropropionic acid exhibits only HF loss via IRMPD, whereas via CID the loss of CO_2 is favoured over the loss of HF by nearly 6:1. Similarly, in the case of 3,3,3,2-tetrafluoropropionic acid, CID yields predominantly CO_2 (>99%) whereas IRMPD produces FCO_2^- and CO_2 with a branching ratio of approximately 2:1. Computational modelling of the reaction pathways revealed that the observed CID behaviour can be explained in terms of the barrier to HF (or FCO_2^-) production relative to the threshold for CO_2 loss. The cases for which IRMPD outcomes differ from those observed via CID suggests that resonant IR photoexcitation and the subsequent energy redistribution selectively accesses specific product channels via non-stochastic processes dissimilar from that of a thermal mechanism. Mode specific fragmentation ratios can be found in **Table A9 and A10** in Appendix A. It is also an interesting open question as to whether the degree of fluorination affects similar variability in fragmentation for other sub-classes of PFAS, such as per- and polyfluorinated sulfonic acids.

3.4 – Conclusions

A result summary for all the deprotonated propionic acids is in **Table 3.5**. All propionic acids access two product channels depending on its isomeric form, molecules with a higher degree of fluorination favour the CO_2 loss product channel in CID. The FCO_2^- product channel is hypothesized that a fluorine atom must be bonded to the β-carbon for the reaction to be accessible. Comparing the fragmentation results between CID and IRMPD of the 3,3,3,2-tetrafluoropropionic acid, the IRMPD facilitates the yield of FCO_2^- more than the loss of CO_2 compared to the CID fragmentation which primarily yields the loss of CO_2. Further computational investigations reveal that the transition state for the FCO_2^- formation to be a four-membered ring transition state comprised of the three carbon atoms and a fluorine atom bonded to the β-carbon. In contrast, the HF elimination pathway is only experimentally observed from the 2-monofluoro, 2,2-difluoro, and the 3,3,2,2-tetrafluoro species. Thus, we believed that a fluorine bonded to an α-carbon and hydrogen bonded β-carbon must be present. DFT calculations show that the transition state geometry for the HF elimination is comprised of the α- and β- carbon, the fluorine atom bonded to the α-carbon, and a hydrogen bonded to the β-carbon. Differences between CID and IRMPD can be seen again from the 2,2-difluoro, where HF elimination is the dominant fragmentation channel under IRMPD, but CO_2 loss is the dominant fragmentation channel under CID. The fragmentation differences between CID and IRMPD suggests that resonant IR excitation and the subsequent energy redistribution may not be stochastic in nature compared to a thermal mechanism.

Table 3.5. Summary for the result and method used to study the different deprotonated fluorinated propionic acids.

For Formation of FCO_2^-

Precursor Ion	Method used for studying			IRMPD Experiment Favours		CID Experiment Favours	
	IRMPD	CID	Computational	Loss of CO_2	Formation of FCO_2^-	Loss of CO_2	Formation of FCO_2^-
3-F	✓	✓	✓		✓	✓	
3,2-F_2			✓	N/A		N/A	
3,3-F_2		✓	✓		✓		✓
3,2,2-F_3		✓	✓	N/A			✓
3,3,2-F_3			✓	N/A		N/A	
3,3,3-F_3	✓	✓	✓		✓		✓
3,3,2,2-F_4	✓	✓	✓	✓		✓	
3,3,3,2-F_4	✓	✓	✓		✓	✓	
F_5	✓	✓	✓	✓		✓	

For HF Elimination

Precursor Ion	Method used for studying			IRMPD Experiment Favours		CID Experiment Favours	
	IRMPD	CID	Computational	Loss of CO_2	HF Elimination	Loss of CO_2	HF Elimination
2-F	✓	✓	✓		✓		✓
2,2-F_2	✓	✓	✓		✓	✓	
3,3,2,2-F_4	✓	✓	✓	✓		✓	

Although there are more than 9,000 unique PFAS listed in EPA CompTox database, standardized methods for detection and quantification exist for only a few dozen, and there is limited knowledge regarding the structures and properties of transformation products. Future studies of other short-chain PFAS and PFAS from other chemical classes such as fluorotelomers (*e.g.*, ADONA) and fluoroethers (*e.g.*, GenX) will help remedy these

shortcomings and may provide insights with respect to trends in reactivity, which in turn will guide the development of methods for treatment and analysis. This work highlights an important consideration for researchers interested in the treatment, detection, and quantification of PFAS. During treatment, it is expected that longer-chain PFAS are converted into shorter-chain species and that the degree of fluorination is reduced.[136,137,158] To assess treatment efficiency and elucidate reaction mechanisms, it is necessary to accurately quantify the contaminants and the transformation products. Owing to typical environmental concentrations for these species, quantification most often is achieved using mass spectrometry. However, the application of mass spectrometry alone can lead to ambiguous results when it comes to isomeric species. For example, as demonstrated above the deprotonated 3,3,3-trifluoro and 3,2,2-trifluoropropionic acid derivatives exhibit the same *m*/*z* ratio, and both yield FCO_2^- + 1,1-difluoroethene upon dissociation. Similarly, 2,2-difluoropropinoic acid yields predominantly the loss of CO_2 with minor production of HF. In contrast, 3,3-difluoro yields predominantly FCO_2^- via CID with minor loss in CO_2. If CO_2 loss is used in multiple reaction monitoring to monitor the difluoroproionic acid, much of the quantitation of the 3,3-difluorofluoropropionic acid isomer will be lost. Consequently, orthogonal separation and/or characterization techniques (*e.g.*, ion mobility, liquid chromatography) are required to unambiguously characterize these analytes. Moreover, as underscored by this study, even for a particular sub-class of PFAS (*e.g.*, PFCAs), chemistry can vary significantly with substitution pattern and degree of fluorination.

Computational Geometries are available through the following link:

http://dx.doi.org/10.19061/iochem-bd-6-431

– Chapter 4 –
Gas-phase Triazolide Complexes

4.1 – Introduction

Since ferrocene was first synthesized in the early 1950s,[33,159] much effort has gone into creating and characterizing aromatic organometallic complexes.[34,35] For example, heavy analogues of the cyclopropenyl cation,[160,161] benzene and its homologues,[162–164] and oxazole and thiazole have been reported.[165,166] Researchers have also explored the impact of the cationic moiety in cyclopentadienyl (Cp^-) complexes, and have found that a variety of structures arise depending on the nature of the cation;[36] bonding in Cp^- complexes containing relatively electropositive elements are considered to be mainly ionic (*e.g.*, Cs^+Cp^-), whereas bonding in complexes containing *p*-block elements is highly covalent. It is the degree of ionic versus covalent bonding, in conjunction with the nature of orbital overlap (referred to as "hapticity" for transition metals), that yields the observed structural diversity of these compounds.

Quantitative studies of aromatic complexes in the gas-phase were first reported by Kebarle *et al.*, who demonstrated that the binding energy of 80 kJ mol^{-1} for the potassium benzene cation, $K^+[C_6H_6]$, exceeds that of $K^+[H_2O]$ (~75 kJ mol^{-1}).[37] Armentrout and coworkers extended this work to study the series of alkali cation-benzene complexes, and observed the expected trend of decreasing binding energy with increasing cation size.[167] This trend can be satisfactorily explained in terms of cation-quadrupole and cation-induced dipole interactions

that dominate "cation-π" interactions. Many studies have since invoked cation-π interactions as driving forces in determining molecular and cluster geometries, particularly in the context of aromatic amino acids.[168–172]

There have been relatively few studies of gas-phase complexes containing metal ions and Cp^- ligands.[173–178] Foster and Beauchamp investigated ion-molecule reactions involving ferrocene and observed the $Fe_3Cp_3^+$ complex, which they suggested might exhibit a "triple decker sandwich" geometry.[173] Beauchamp and coworkers followed up on this by studying nickelocene via ion cyclotron resonance mass spectrometry, whereby they identified similar behaviour to ferrocene for these anologus nickel complexes.[174] More recently, Featherstone *et al*. conducted a combined computational and experimental infrared multiple photon dissociation (IRMPD) spectroscopy study of complexes of the general form $[Na_nCp_{n-1}]^+$.[38] The largest complex that they characterized experimentally was the $[Na_4Cp_3]^+$ cluster, which may be visualized as Beauchamp's triple-decker sandwich but capped with sodium ions on either end. The authors referred to these clusters as "inverse sandwich complexes", but noted that this term had been previously coined for compounds containing a central dianion and two cationic aromatic rings as ligands.[179,180] Featherstone concluded that the gas-phase $[Na_nCp_{n-1}]^+$ complexes were bound primarily by ion-ion and ion-induced dipole interactions, based on relatively minor IR spectral shifts of the bound versus free Cp^- ligands and negligible computed orbital overlap between the Na^+ and Cp^- moieties. They also highlighted the fact that several vibrational bands, which were observed experimentally but not computed via DFT modelling, were consistent with overtone or combination bands associated with C–H out-of-plane bending and Na–Cp–Na bending.

An interesting open question with respect to the structures and properties of gas-phase aromatic organometallic complexes is the importance of ring symmetry. For example, how does lowering the symmetry of the Cp^- moiety (D_{5h}) by substituting heteroatoms (*e.g.*, N) in place of the carbon centres impact cluster geometry and stability? Such a substitution would introduce ion-dipole interactions and the possibility of charge-transfer of lone pair electron density to the metal cation, but Kebarle's work on $K^+[C_6H_6]$ and $K^+[H_2O]$ suggested that cation-π interactions might still be the dominant influence on cluster geometry.[37] Here, we investigate sodium and potassium clusters of 1,2,3-triazolide and 1,2,4-triazolide (see **Figure 4.1**), which have dipole moments of approximately 3.3 D and 1.4 D, respectively, thus bracketing the dipole moment of H_2O (*ca*. 1.84 D). Mass spectrometry, infrared multiple photon dissociation (IRMPD) action spectroscopy, and quantum chemical calculations are employed to study the structures and properties of these species.

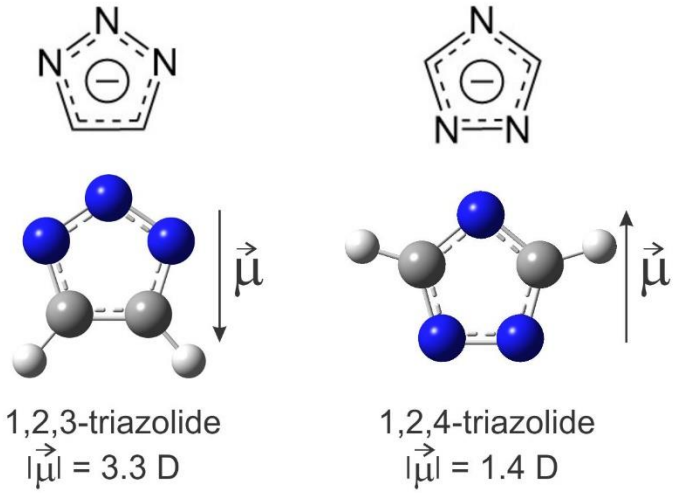


Figure 4.1. (**left**) deprotonated 1H-1,2,3-triazole and (**right**) deprotonated 1H-1,2,4-triazole. Molecular dipoles were computed at the ωB97X-D/def2-tzvpp level of theory.

4.2 – Methods

IRMPD spectra were recorded at the FELIX free electron laser laboratory.[78] 1H-1,2,3-triazole and 1H-1,2,4-triazole were sourced from Sigma Aldrich at 97% and 98% purity, respectively. Solutions for electrospray ionization were prepared in a 50:50 methanol:water mixture at a concentration of 10 μM with 1 μM of sodium hydroxide or potassium hydroxide added to deprotonate the triazole molecules and to provide the alkali metal cation to form the gas-phase ionic clusters of interest. Following electrospray ionization, complexes of interest were mass selected using a modified quadrupole ion trap mass spectrometer (Bruker Amazon) interfaced with the output of the FELIX IR beam. Parent clusters were irradiated, and fragment ions were produced via IRMPD across the 600 – 1850 cm^{-1} region. Vibrational spectra were then generated by recording the precursor fragmentation efficiency (**eq. 2.1**) as a function of the tunable free electron laser output.

Computational investigations were carried out using the ORCA computational suite and the CREST conformation sampling algorithm. Several different input structures were manually generated for conformer search via the CREST algorithm using the "nci" keyword.[106,110] Geometry optimizations were conducted at the ωB97 level of theory and employing the D3 dispersion corrections with the def2-tzvpp basis set for the lowest energy conformers identified by CREST.[117,181] This level of theory was selected due to its documented accuracy and efficiency.[182,183] Frequency calculations were then carried out at the same level of theory and basis set for comparison with the experimental IRMPD spectrum and to obtain thermal corrections for binding energy calculations. Electronic energy calculations were completed with the DLPNO-CCSD(T)/def2-tzvpp level of theory with the tightPNO parameter.[184,185] Natural bonding order (NBO) calculations are completed on the Gaussian computational suite, using the ωB97X-D/def2-tzvpp level of theory to analyze the bonding character between the cation and anion.[107]

4.3 – Results and Discussion

Under the conditions employed for experiments, the deprotonated 1H-1,2,3-triazole (hereafter 123T) and 1H-1,2,4-triazole (hereafter 124T) species were observed to cluster with Na^+ and K^+ to form complexes with stoichiometries of $[M_3(123T)_2]^+$, $[M_4(123T)_3]^+$, $[M_3(124T)_2]^+$ and $[M_4(124T)_3]^+$ where M = Na or K. In the case of $[Na_3(124T)_2]^+$, the parent ion signal was too low to record a reliable IRMPD spectrum. We also attempted to explore the analogous M = Cs species (using CsOH in the ESI mixture) but these were challenging to produce; the signal for $[Cs_3(124T)_2]^+$ was insufficient for analysis. However, we were able to record the spectrum for $[Cs_2(124T)]^+$ and $[K_5(124T)_4]^+$ (see **Figure 4.2** and **Figure 4.7** respectively). The lowest energy geometry of the $[M_2(124T)]^+$ are found to have to the metal cation located along the symmetry axis of the 124T. Geometry discussion for the larger 124T clusters is in **section 4.3.2**.

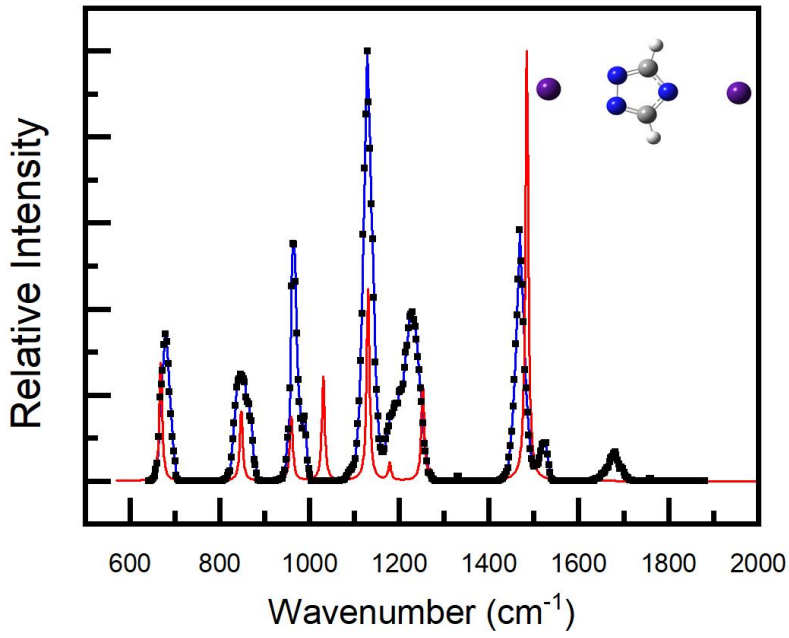


Figure 4.2. (**Blue**) IRMPD spectrum (**red**) computed spectrum for the $[Cs_2(124T)]^+$ cluster, with its lowest energy geometry located on the top left corner of the graph.

4.3.1 – 1,2,3-triazolide complexes

The major product channels accessed via IRMPD for the $[Na_3(123T)_2]^+$ (*m/z* 205) and $[K_3(123T)_2]^+$ (*m/z* 253) species are formation of $[Na_2(123T)]^+$ (*m/z* 114) and $[K_2(123T)]^+$ (*m/z* 146) via loss of a neutral Na(123T) or K(123T) fragment, respectively. Upon dissociation, the larger $[Na_4(123T)_3]^+$ (*m/z* 296) cluster yields $[Na_3(123T)_2]^+$ (*m/z* 205) and $[Na_2(123T)]^+$ (*m/z* 114) in a branching ratio of approximately 7:93, presumably by loss of neutral Na(123T) or $Na_2(123T)_2$ fragments. The analogous $[K_4(123T)_3]^+$ cluster exhibits analogous dissociation product channels with the similar branching ratios.

Figure 4.3 shows the IRMPD spectra recorded for $[Na_3(123T)_2]^+$, $[Na_4(123T)_3]^+$, $[K_3(123T)_2]^+$, and $[K_4(123T)_3]^+$; immediately apparent upon inspection are the similarities between their spectra. Although there are some differences in relative band intensities, the band positions are the same (within measurement error) from one cluster to another. In their study of $[Na_nCp_{n-1}]^-$,[38] Featherstone *et al*. reported similar invariance of band position with degree of clustering. This invariance suggests that clustering with Na^+ or K^+ negligibly perturbs the vibrational structure (*viz*. bonding) of the associated anions in these systems. The red traces overlayed on **Figure 4.3** are the computed harmonic vibrational spectra for the lowest energy conformers of the various clusters. The agreement between the computed and measured spectra is good. Based on these calculations and a FT-IR/Raman study of the bare 123T anion by Törnkvist *et al.,*[186] we can assign the most intense features in the IRMPD spectra (see **Table 4.1**). Interestingly, we also observe three weak spectral features in the 1600 – 1800 cm^{-1} region which are not reported by Törnkvist or computed via DFT modelling; these bands are most prominent in the $[K_4(123T)_3]^+$ spectrum and are completely absent in the $[Na_3(123T)_2]^+$ spectrum. Featherstone *et al*. reported similar observations for $[Na_nCp_{n-1}]^-$ and suggested that such features might be associated with vibrational overtones or combination bands. In this case, only the C-H out-of-plane bending mode (fundamental at *ca*. 805 cm^{-1}) could generate an overtone in this region. An alternative possibility is that these vibrational bands are combination bands involving those observed in the 950–1150 cm^{-1} region and the ring torsion mode (fundamental band at 628 cm^{-1}).[186] A future spectroscopic

study of isotopically labelled 123T might provide a more concrete assignment of these features.

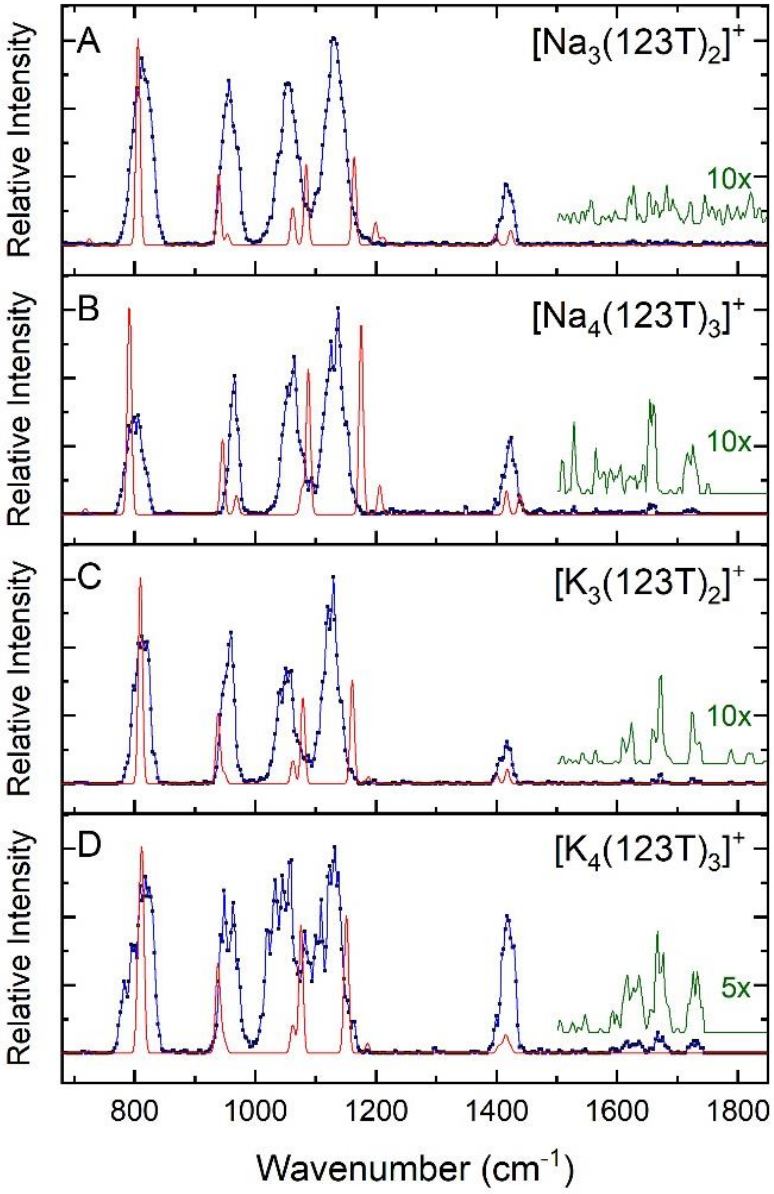


Figure 4.3. IRMPD spectra for (**A**) $[Na_3(123T)_2]^+$, (**B**) $[Na_4(123T)_3]^+$, (**C**) $[K_3(123T)_2]^+$, and (**D**) $[K_3(123T)_3]^+$. Computed IR spectra for the lowest energy conformation, which are overlayed in red, are scaled by 0.95 in accordance with literature convention.[187,188] The inset green traces show a zoom of the 1500 – 1900 cm^{-1} region.

Table 4.1. Assignments for the average observed IRMPD bands for the $[Na_x(123T)_y]^+$ and $[K_x(123T)_y]^+$ species (intensities; w = weak, m = medium, s = strong, vs = very strong). FT-IR band positions and symmetry assignments are those reported in reference 186 under a 0.5M NaOH environment.[186]

IRMPD $\bar{\nu}$ / cm^{-1}	FT-IR $\bar{\nu}$ / cm^{-1}	Description
1729 w	/	Combination band
1667 w	/	Combination band
1628 w	/	Combination band
1418 m	1439 m (A_1), 1412 m (B_1)	C-C str, C-N str
1130 s	1146 s (A_1)	C-C str + C-H def
1054 s	1097 m (A_1), 1068 vs (B_1)	N-N str + ring def + C-H def
957 s	963 s (A_1)	Ring def
805 s	800 m (B_2)	C-H out-of-plane bending

Figure 4.5 shows the computed global minima and the first excited isomers for the $[M_3(123T)_2]^+$ (M = Na, K) clusters. Computational analysis indicates that these species do not form inverse sandwich complexes like their Cp^- analogues. Instead, cluster geometries seem to be more strongly influenced by charge-dipole and charge-transfer (C-T) interactions than cation-π interactions. For example, the global minima exhibit compact 3D geometries that maximize overlap of the N lone pair density with the M^+ valence *s* orbitals. These interactions are somewhat reduced in the higher energy planar isomers, but there is still some directionality associated with the inter-moiety binding. An additional "drawbridge" like structure is found for $[K_3(123T)_2]^+$, where the triazolides are bridged by two potassium cations by the side and a potassium cation extended away from the bridge structure (See **Figure 4.4**).

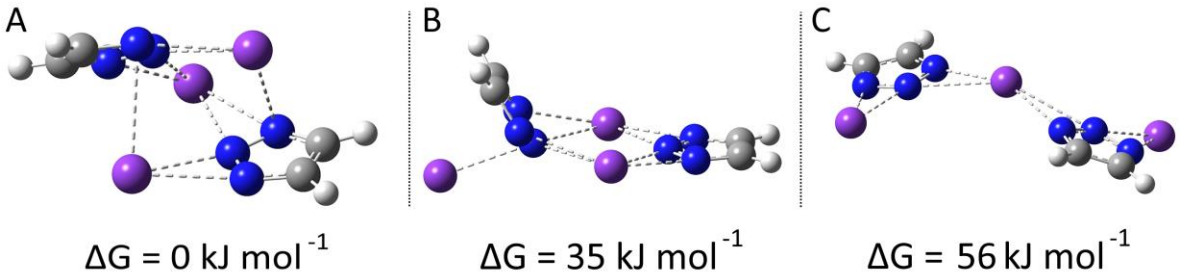


Figure 4.4. The different isomeric forms of $[K_3(123T)_2]^+$ and their relative Gibbs energies. (**A**) is the lowest energy geometry, (**B**) is "drawbridge" like structure, and (**C**) is the extended structure that has the highest energy.

The relative Gibbs energy of the "drawbridge" like structure **(Fig. 4.4B)** is 35 kJ mol^{-1} higher than the compact structure **(Fig. 4.4A)**. This "drawbridge" structure is not found for the sodiated analogue which is presumed to be caused by the size of the cations as the larger potassium cation can accept lone-pair donations at a further distance. The isomer 2 geometry for the sodiated species shown in **Figure 4.5** is about 20 kJ mol^{-1} in relative Gibbs energy higher than the compact 3D geometry. In contrast, the same isomer structure for the potassiated analogue is 56 kJ mol^{-1} higher in energy compared to the 3D compact form. **Figure 4.6** shows the computed global minima for the $[M_4(123T)_3]^+$ (M = Na, K) clusters. For $[Na_4(123T)_3]^+$, we find a nearly planar geometry that appears to be a flattened version of the more the compact 3D geometry computed for $[K_4(123T)_3]^+$. These clusters also exhibit directional bonding seemingly associated with M^+•••N interactions, suggesting that C-T interactions also strongly influence the structures of the larger clusters. Across the series of clusters that we investigated computationally, the average minimum distance between triazolide moieties is *ca*. 2.9 Å for the sodiated clusters and *ca*. 3.8 Å for the analogous potassiated clusters, a difference that is attributable to the larger ion radius for K^+ (1.33 Å) compared to Na^+ (0.99 Å).[189] The larger size and relative softness of the K^+ cation compared to the Na^+ cation likely also gives rise to the relative flexibility/fluxionality of potassiated clusters. With respect to the possible C-T interactions, sodiated clusters exhibit Na^+•••N distances of *ca*. 2.3 Å and potassiated clusters exhibit K^+•••N distances of *ca*. 2.9 Å, which compares favorably to the K^+•••N bond distance of 2.9 Å measured for potassium nitrite crystals.[190]

To further investigate the interactions giving rise to the computed cluster geometries, we undertook natural bonding orbital (NBO) analysis,[191,192] which on the basis of previous work we expect should be a valid approach here.[45,193–195] **Table 4.2** provides the computed C-T stabilization energies associated with electron density donation from the triazolide moieties to the alkali metal cations in the clusters studied. In all cases, the dominant contribution to C-T stabilization (*ca*. 80%) was donation of N lone pair electron density into the valence 3*s* orbital of Na^+ or 4*s* orbital of K^+. In general, we find that sodiated clusters exhibit slightly higher degrees of C-T than do the analogous potassiated clusters, possibly owing to better orbital overlap and closer approach of the nuclei. A similar trend is calculated for the Gibbs' energies of binding (also given in **Table 4.2**), which are slightly larger in magnitude for the sodiated species than the analogous potassiated species.

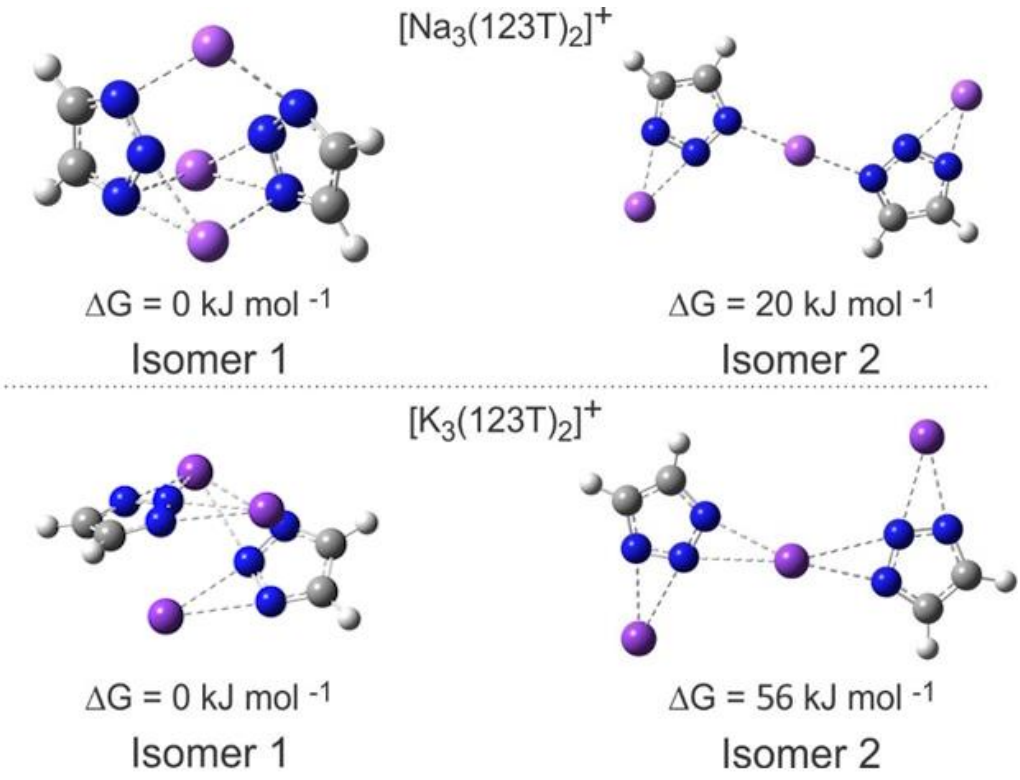


Figure 4.5. The global minima and the first higher energy isomers of $[M_3(123T)_2]^+$ (M = Na, K). Calculations were conducted at the ωB97X-D3/def2-tzvpp level of theory. NBO interaction energies are summarized in **Table 4.2**.

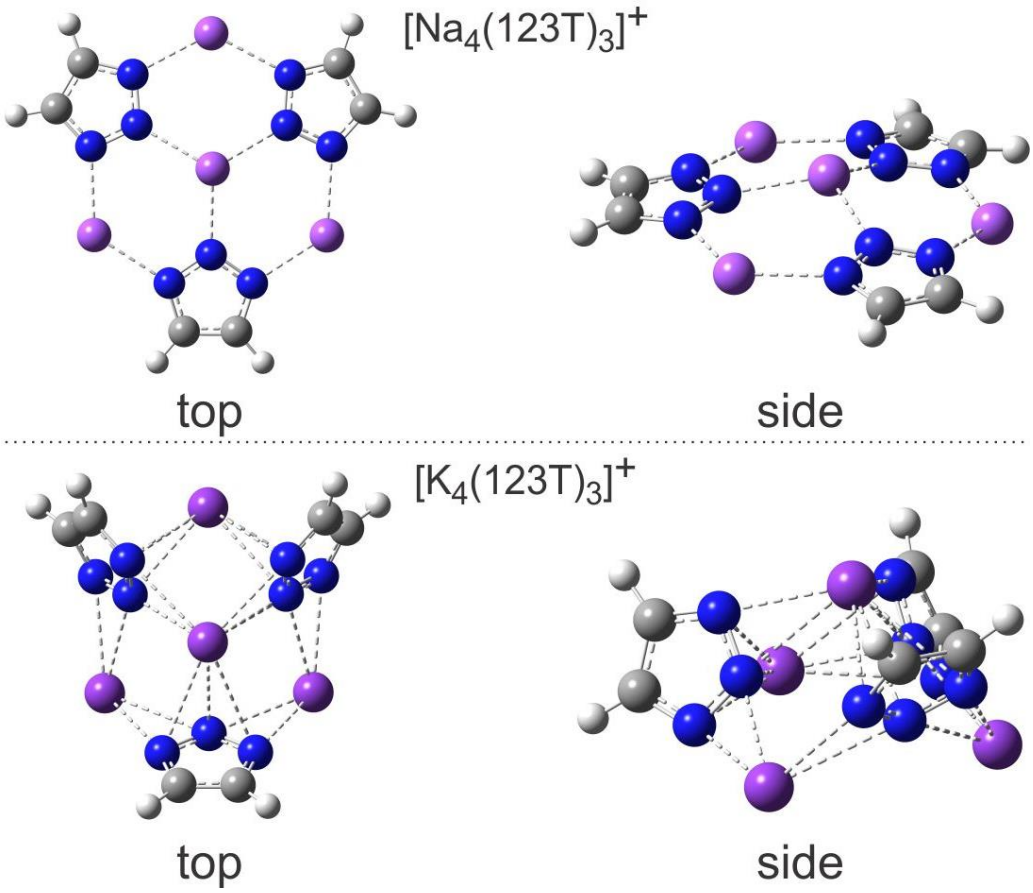


Figure 4.6. Computed global minima for the $[M_4(123T)_3]^+$ (M = Na, K) clusters. Calculations were conducted at the ωB97X-D3/def2-tzvpp level of theory.

Table 4.2. Computed cluster binding energies and stabilization energies associated with charge-transfer (C-T) interactions between the 123T anions and alkali metal cations. NBO calculations were undertaken at the ωB97X-D3/def2-tzvpp level of theory. Gibbs binding energies, ΔG°, are calculated using standard temperature and pressure.

Cluster	C-T Stabilization Energy / kJ mol^{-1}	Energy per C-T Interaction / kJ mol^{-1}	Fragmentation pathway	ΔG° Binding Energy / kJ mol^{-1}
$[Na_2(123T)]^+$	89	44	$Na^+ + Na(123T)$	141.8
$[Na_3(123T)_2]^+$	292	73	$[Na_2(123T)]^+ + Na(123T)$	81.3
$[Na_4(123T)_3]^+$	480	53	$[Na_3(123T)_2]^+ + Na(123T)$ $[Na_2(123T)_1]^+ + Na_2(123T)_2$	132.5 94.3
$[K_2(123T)]^+$	73	37	$K^+ + K(123T)$	114.1
$[K_3(123T)_2]^+$	237	59	$[K_2(123T)]^+ + K(123T)$	84.9
$[K_4(123T)_3]^+$	368	41	$[K_3(123T)_2]^+ + K(123T)$ $[K_2(123T)_1]^+ + K_2(123T)_2$	70.2 56.1

4.3.2 – 1,2,4-triazolide complexes

The 124T clusters exhibit similar IRMPD fragmentation products to the 123T clusters. The major product channel for $[K_3(124T)_2]^+$ (*m/z* 253) is loss of K(124T) to form $[K_2(124T)]^+$ (*m/z* 146). We were unable to reliably measure $[Na_3(124T)_2]^+$. The major product channels of $[Na_4(124T)_3]^+$ (*m/z* 296) are the loss of the neutral $Na_2(124T)_2$ to form $[Na_2(124T)]^+$ (*m/z* 114) and the loss of the neutral Na(124T) to form $[Na_3(124T)_2]^+$ (*m/z* 205), which occur with a branching ratio of approximately 71:29, respectively. Analogous behavior is observed for $[K_4(124T)_3]^+$, for which the product branching ratio was 89:11.

Figure 4.7 plots the IRMPD spectra recorded for $[Na_4(124T)_3]^+$, $[K_3(124T)_2]^+$, and $[K_4(124T)_3]^+$, $[K_5(124T)_4]^+$. As was observed for the 123T clusters, substitution of Na^+ with K^+ has only a minor impact on the observed spectra. The red traces in **Figure 4.7** show the computed harmonic vibrational spectra, which are in good agreement with those measured experimentally. Minor differences between the observed and calculated spectra occur near 1,000 cm^{-1}, where a resolved feature that is predicted by calculation is slightly shifted and

blended with another peak in the experimental spectrum, and at wavenumbers above *ca*. 1,500 cm^{-1}. The most intense spectral features are assigned in **Table 4.3** based on our DFT calculations and the bare 124T anion FT-IR/Raman study by El-Azhary *et al.*[196] The bands observed at *ca*. 1,550 cm^{-1} and *ca*. 1,700 cm^{-1} are not predicted by DFT calculations, nor are they reported by El-Azhary. Should the feature at 1,700 cm^{-1} be an overtone band, it would most likely correspond to the $v = 0 \rightarrow 2$ excitation of the C–H wag, the fundamental of which is measured at 865 cm^{-1} (corresponding to a first overtone of *ca*. 1,730 cm^{-1}). Alternatively, this band could be a combination of the ring deformation mode (962 cm^{-1}) and the ring torsion mode (680 cm^{-1}). Similarly, the band at *ca*. 1,550 cm^{-1} could be a combination of the C–H wag (865 cm^{-1}) and the ring torsion mode (680 cm^{-1}). Future measurements of isotopically substituted species would shed additional light on these bands.

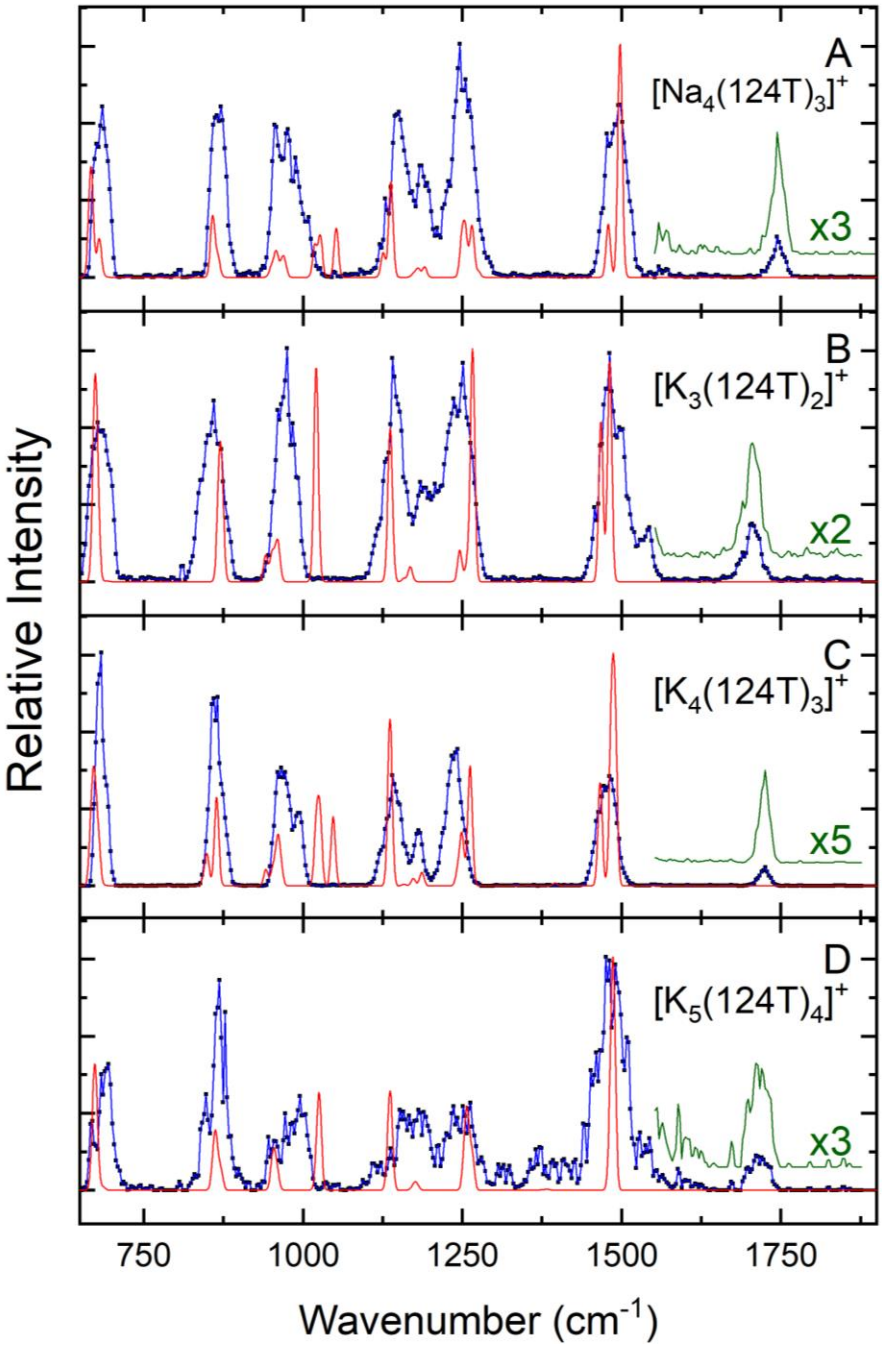


Figure 4.7. IRMPD spectra for (**A**) $[Na_4(124T)_3]^+$, (**B**) $[K_3(124T)_2]^+$, and (**C**) $[K_3(124T)_3]^+$. Computed IR spectra for the lowest energy conformation, which are overlayed in red, are scaled by 0.95 in accordance with literature convention.[187,188] The inset green traces show a zoom of the 1525 – 1825 cm^{-1} region.

Table 4.3. Assignments for the observed IRMPD bands for the $[Na_x(124T)_y]^+$ and $[K_x(124T)_y]^+$ species (intensities; w = weak, m = medium, s = strong, vs = very strong). FT-IR band positions and symmetry assignments are those reported in reference 196.[196]

IRMPD $\bar{\nu}$ / cm^{-1}	FT-IR $\bar{\nu}$ / cm^{-1}	Description
1703 – 1739 w	/	Combination band
1481 s	1439 (A_1), 1412 (B_2)	C-C str, C-N str
1240 s	1230 (B_2)	C-N str + C-H def
1181 w	1207 (A_1)	C-N str + C-H def
1143 m	1146 (A_1)	N-N str + ring def + C-H def
962 m	963 (A_1)	Ring def + C-H def
865 s	800 (B_1)*	C-H wag
680 s	668 (A_2)	Ring torsion

*Tentatively assigned in reference 196.

The computed global minima for the $[M_3(124T)_2]^+$, $[M_4(124T)_3]^+$, and $[M_5(124T)_4]^+$ (M = Na, K) clusters are shown in **Figure 4.8**. Akin to the 123T clusters, the sodiated and potassiated 124T clusters do not form inverse sandwich complexes like their Cp^- analogues. Instead, cluster geometries are strongly influenced by charge-dipole and C–T interactions; the C–T interaction energies reported in **Table 4.4** are of similar magnitudes to those reported in **Table 4.2** for the analogous 123T clusters. The lowest energy $[Na_3(124T)_2]^+$ cluster adopts a relatively planar/linear conformation. The first higher energy isomer is a more condensed structure at $\Delta G° = 31$ kJ mol^{-1}. Interestingly, substituting K^+ for Na^+ results in an energetic reordering of these structures, with the linear structure shifting $\Delta G° = 4$ kJ mol^{-1} to higher energy of the compact geometry. The larger $[M_4(124T)_3]^+$ (M = Na, K) clusters both adopt pseudo-planar global minimum geometries. For the 124T clusters, Na^+•••N distances of *ca*. 2.3 Å and K^+•••N distances of *ca*. 2.8 Å are computed, again comparing favorably to the K^+•••N bond distance of 2.9 Å measured for potassium nitrite crystals.[190]

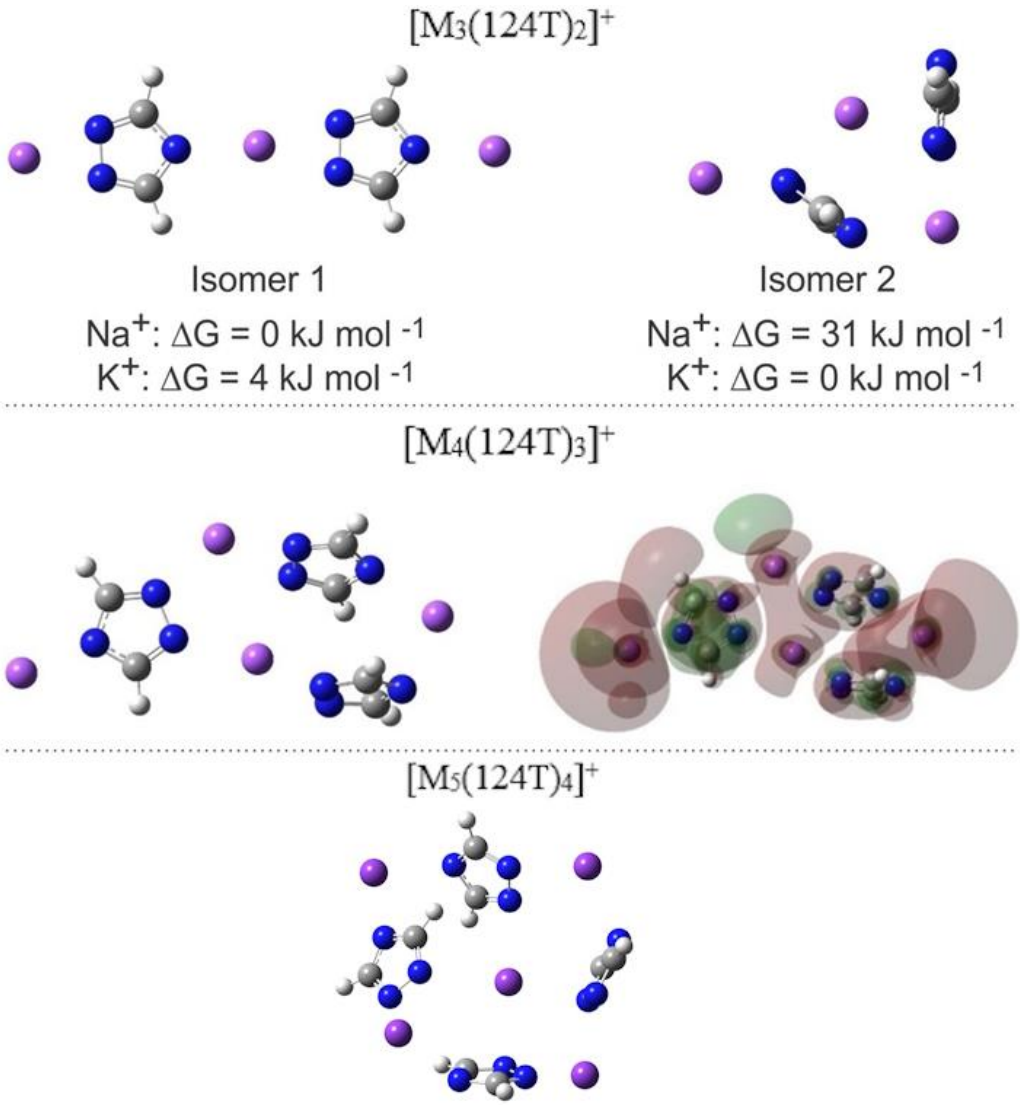


Figure 4.8. The lowest energy geometries of $[M_3(124T)_2]^+$, $[M_4(124T)_3]^+$, and $[M_5(124T)_4]^+$ (M = Na, K). Calculations were conducted at the ωB97X-D3/def2-tzvpp level of theory. The overlapping N lone pair and M^+ *s* orbitals, which give rise to C-T interactions, are plotted for the $[Na_4(124T)_3]^+$ cluster. NBO interaction energies are summarized in **Table 4.4**.

Table 4.4. Computed cluster binding energies and stabilization energies associated with charge-transfer (C-T) interactions between triazolide anions and alkali metal cations. NBO calculations were undertaken at the ωB97X-D3/def2-tzvpp level of theory. ΔG° are calculated using standard room temperature and pressure.

Cluster	C-T Stabilization Energy / kJ mol^{-1}	Energy per C-T Interaction / kJ mol^{-1}	Fragmentation pathway	ΔG° Binding Energy / kJ mol^{-1}
$[Na_2(124T)]^+$	89	45	$Na^+ + Na(124T)$	150.1
$[Na_3(124T)_2]^+$	234	58	$[Na_2(124T)]^+ + Na(124T)$	47.9
$[Na_4(124T)_3]^+$	451	50	$[Na_3(124T)_2]^+ + Na(124T)$	58.3
			$[Na_2(124T)_1]^+ + Na_2(124T)_2$	39.4
$[K_2(124T)]^+$	77	39	$K^+ + K(124T)$	114.9
$[K_3(124T)_2]^+$	199	50	$[K_2(124T)]^+ + K(124T)$	20.5
$[K_4(124T)_3]^+$	302	34	$[K_3(124T)_2]^+ + K(124T)$	41.3
			$[K_2(124T)_1]^+ + K_2(124T)_2$	27.6

4.4 – Conclusions

In this work, we explored the structures and properties of $[M_n(123T)_{n-1}]^+$ and $[M_n(124T)_{n-1}]^+$ (M = Na, K) clusters. In contrast with the analogous Cp^- species,[38] for which geometries are defined by cation–π interactions, the triazolide-containing clusters exhibited directional bonding associated with $N \rightarrow M^+$ electron density donation. For the 123T-containing clusters, ring symmetry resulted in compact clusters whereas 124T-containing clusters could adopt more open geometries with more distance between M^+ moieties. By lowering the symmetry of the anion, the cation–π interactions are less dominant, whereas ion-dipole and charge transfer interactions have the dominant influence on the structure geometry. In general, clusters that contain Na^+ are more strongly bound than those that contain K^+.

IRMPD action spectra, which were well modelled by DFT harmonic IR absorption spectra (at ωB97x-D3/def2-TZVPP), exhibited interesting additional band features in the 1,500 – 1,800 cm^{-1} region. These band features are believed to be an overtone band of the C-H wagging vibrational mode or combination band of the C-H wagging mode and the ring-torsion mode. Further spectroscopic study involved with labelled isotope of the 123T and 124T cluster may help to elucidate the potential source of these additional band features. In addition, transition metal cations such as silver can be used to examine the influence of the neutral triazolide or other neutral cyclic species towards the structure and properties of the cluster formed.

Computational geometries are available in the following link:

https://iochem-bd.bsc.es/browse/handle/100/330732

– Chapter 5 –

Gas-phase $B_{12}F_{12}^{2-}$ Diaminoalkane Clusters

5.1 – Introduction

Recent developments of small boron clusters demonstrate potentially significant applications in therapeutic use and boron-based nanomaterials.[197–200] Specifically, the *closo*-dodecaborate ($B_{12}X_{12}^{-}$, X = H, F, Cl, Br, I) cages are of interest due to their extraordinary structural and electronic stability allowing for various fundamental and applied research field such as energy storage, catalysis, and neutron capture cancer therapy.[39,40,201,202] These applications of the dodecaborate cages stem from their physicochemical properties and symmetry. The $B_{12}X_{12}^{2-}$ dianion has a quadruply degenerate g_u symmetry cage-centred HOMOs mainly localised on the boron cage and separated from complexing counterions by the fluorine atoms located on the surface.[41] In the case of $B_{12}F_{12}^{2-}$, the negative charges are delocalized around the surface fluorine atoms, whereas larger halogenated analogues such as $B_{12}I_{12}^{2-}$ have the negative charge delocalization within the boron core.[41] As a consequence, the delocalized excess electrons on the surface of the $B_{12}F_{12}^{2-}$ results in a weaker electrostatic interaction with its coordinating cation compared to common dianionic species in aqueous phase such as SO_4^{2-} and HPO_4^{2-}, thus the $B_{12}X_{12}^{2-}$ dianions are often referred to as 'weakly coordinating' anions.[41,42] However, dianions such as SO_4^{2-} and HPO_4^{2-} are often unstable in the gas phase, while $B_{12}X_{12}^{2-}$ are stable in the gas phase.[40,203] This allows for the study of clusters that involve multiple $B_{12}X_{12}^{2-}$ with dications, such as doubly protonated diaminoalkanes, to elucidate the structure and properties of larger multiply charged clusters.

Previous gas-phase study of $B_{12}X_{12}^{2-}$ (X=H, F, Cl, Br, I) cages indicated that the dodecaborate cages are prone to charge-transfer reaction during dissociation by collision or IR excitation due to their low oxidation potential.[45] $B_{12}F_{12}^{2-}$ has the lowest oxidation potential compared to the other halogenated dodecaborate clusters.[204] It is of interested to examine further the possibility of charge-transfer interactions when clustering with primary amines

through hydrogen bonding as previous studies have shown that $B_{12}F_{12}^{2-}$ can cluster with various molecules in the gas phase.[40,43,44,193,205] In the clustering study of the trimethyl- and triethylamine, and all-*cis* hexafluorocyclohexane, it is shown that the $B_{12}F_{12}^{2-}$ dianion binds with the counter ions or neutral molecule by dominantly electrostatic interactions in the gas phase.[40,43,44] Specifically, in the study by Carr *et al.* using the triethylammonium as a counter cation demonstrated that both proton transfer reaction and charge transfer reaction occur under activation.[44] The proton transfer reaction causes the formation of $[HB_{12}F_{12}]^-$ and the charge transfer reaction yields a singly charged $B_{12}F_{12}^-$. In addition, a higher energy dissociation channel of HF elimination can be observed to yield a highly nucleophilic $[B_{12}F_{11}]^-$ and other cage fragments involving loss of multiple BF or BF_3.[206] If trace water vapours are in the ion trap, hydroxide groups can replace the fluorine forming $[B_{12}F_{x-y-1}(OH)_y]^-$.[45] In addition, $B_{12}F_{11}^-$ were shown to bind with noble gases *via* the nucleophilic site remaining following fluorine abstraction.[207,208]

This work explores the potential structures and properties of clusters that contains very rigid and highly symmetric $B_{12}F_{12}^{2-}$ and very flexible diaminoalkanes, $(HN_2(CH_2)_n(NH_2)$ (n = 2–12). The focus is to study how electrostatic interactions, charge-transfer reactions and incipient chemical bonding influencing the properties and the geometry of each cluster. Furthermore, we want to examine if entropic effect dominates the cluster geometry, resulting in an extended geometry, or if it will fold into itself and adopt a bidentate biding motif owing to the strength of the hydrogen bonds between the amine moiety and $B_{12}F_{12}^{2-}$. It is also interesting to explore the dissociation pathway accessible to the diaminoalkane-$B_{12}F_{12}^{2-}$ cluster and if the dissociation pathways observed are consistent with the results reported for the protonated triethylamine-$B_{12}F_{12}^{2-}$ clusters, as the various length diaminoalkane chosen brackets the proton affinity and gas phase basicity of the triethylamine. Both singly and doubly charged clusters were elucidated, using the ion-mobility techniques, such as travelling wave ion mobility spectrometry (TWIMS) and differential ion mobility spectrometry (DMS). Spectroscopy methods such as infrared multiple photon dissociation (IRMPD) coupled with DFT calculations were used to aid in the interpretation of the experimental outcomes.

5.2 – Experimental Methods

$K_2B_{12}F_{12}$ (>97%) salt and linear diaminoalkanes of the form $[H_2N(CH_2)_nNH_2]$ (n = 2-10, 12) (>95%) were sourced from Sigma Aldrich, except for 1,11-diaminoundecane which was sourced from LGC Standards, Canada. To produce clusters of the form $[B_{12}F_{12} + H_2N(CH_2)_nNH_2 + H]^-$ and $[2B_{12}F_{12} + H_2N(CH_2)_nNH_2 + 2H]^{2-}$, electrospray ionization (ESI) solutions of 200 µM containing the appropriate analytes were prepared separately in a 50:50 methanol and water mixture with 6 % formic acid. This relatively high concentration of formic acid was employed to drive complete protonation of the diaminoalkanes.

High resolution mass spectrometry and collision cross-section (CCS) data was collected using a Waters Synapt G2-Si equipped with a TWIMS cell. A CCS calibration curve was created using the Waters Major Mix (Waters Canada, Major Mix IMS/Tof Calibration Kit) employing wave height settings of 36V, 38V, and 40V while maintaining the 500 m/s wave velocity as recommended by Gabelica *et al*.[90] The calibration curve (located in **Appendix B Figure B1**) is then used to obtain the CCS for each targeted analyte. As drift tube studies of $B_{12}X_{12}^{2-}$ CCS related clusters/compounds are not available, the CCS reported in this study is not perfectly representative because the geometry and composition of the calibrants are different from the target analyte. Samples CCSs were measured with the same wave height settings as used for calibration. The TWIMS data showed single features.

To further investigate the possibility of isomeric species being present in the ion ensemble, DMS was employed. To conduct these experiments, a SCIEX SelexION DMS cell (1 mm gap-height) was mounted between a Turbospray ion source and the sampling orifice of the SCIEX QTRAP 5500 hybrid triple quadrupole linear ion trap mass spectrometer. DMS measurements were recorded at separation voltages (SV) ranging from SV = 0 – 3000 V in steps of 500 V and from SV = 3000 – 4000 V in 200 V steps, while scanning the range of compensation voltage (CV) in a step size of 0.25 V of the range of (20 V, expanded to 25 V at SV > 3600 V). Enhanced product ion (EPI) mode was used for resolution with a collision

energy of –10 V to ensure signal intensity for taking DMS measurements. The DMS cell employed pure N_2 gas. Ionograms were measured at each SV value to identify the corresponding CV peak(s), which represent optimal ion transmission at the given SV. Dispersion curves for the ions of interest were produced by plotting their optimal CVs across the entire SV range. Cases where multiple features were observed in the ionograms were indicative of either the presence of multiple cluster isomers or the fragmentation of larger clusters (*e.g.*, dimers, ion-solvent clusters) to yield the analyte of interest.[209]

Spectroscopic fingerprints utilizing IRMPD were used to elucidate the potential isomeric conformations found in the ion mobility study. IRMPD spectra were recorded at the FELIX free electron laser laboratory (Radboud University, Nijmegen, Netherlands) over a wavenumber range of $1300 - 3500$ cm^{-1} without attenuation. Clusters of interest were produced and isolated within a modified Bruker Amazon quadrupole ion trap mass spectrometer that was interfaced with the FELIX IR beam.[14,78] Vibrational spectra were generated by recording the precursor fragmentation efficiency as a function of the tunable free electron laser frequency.

5.3 – Computational methods

Monomer input geometries were created manually and optimized using the ORCA computational suite.[106] The geometry optimized protonated diaminoalkane and $B_{12}F_{12}^{2-}$ species were then combined to create the appropriate clusters and the CREST algorithm was used to sample the possible conformations.[110] Following conformation sampling, candidate cluster structures were optimized using the ωb97x-D3 method with the def2-TZVPP basis set and refined with the ωb97x-D3BJ method with the def2-TZVPPD basis set.[117,181] The level of theory and the basis set were chosen to balance computational resources and accuracy. Frequency calculations were conducted on the optimized geometry at the same level of theory and basis set as optimization for the thermochemical data and for the comparison with the experimental IR spectra.

5.4 – Results and Discussion

5.4.1 – Mass Spectrometry Results

High resolution mass spectrometry (HRMS) was used to confirm the identities of the $B_{12}F_{12}^{2-}$ and diaminoalkane clusters. **Figure 5.1** shows the HRMS spectrum recorded for the singly charged $[B_{12}F_{12} + H_2N(CH_2)_6NH_2 + H]^-$ cluster (*m/z* ~ 475) along with its theoretical isotopic distribution, which arises predominantly from the 1:4 ratio of ^{10}B:^{11}B. Analogous plots for the other singly charged $[B_{12}F_{12} + H_2N(CH_2)_nNH_2 + H]^-$ (n = 2 – 5, 7 – 12) clusters, as well as for the doubly charged $[2B_{12}F_{12} + H_2N(CH_2)_nNH_2 + 2H]^{2-}$ (n = 2 – 12) clusters are available in Appendix B(**Figures B3–B23**). In some cases, the presence of other species with more intense MS signals introduced ambiguity to our analyses. For example, the isotopic distribution for the doubly charged $[2B_{12}F_{12} + H_2N(CH_2)_3NH_2 + 2H]^{2-}$ cluster (*m/z* ~ 396) overlapped with that of the $KB_{12}F_{12}^-$ cluster (*m/z* ~ 397), a challenge that was further confounded by the relatively low signal intensity of the n = 3 doubly charged cluster. In instances like this, we conducted additional experiments that used the TWIMS cell to separate the interfering species from those of interest prior to recording isotopic distributions. TWIMS experiments are discussed in more detail below. The TWIMS-isolated HRMS spectrum for the doubly charged n = 3 cluster is shown in **Figure B14**. A possible explanation for the relatively low intensity of this cluster (compared to the n = 2 and n = 4 analogues) is that singly-protonated 1,3-diaminopropane adopts a stable six-membered ring via intramolecular hydrogen bonding, which disfavours the second protonation and subsequent formation of the doubly charged n = 3 cluster. This is supported by calculations, which indicate that the linear isomer of protonated 1,3-dimainopropane is $\Delta G° = 63$ kJ mol^{-1} higher in energy than the 6-membered ring ground state.

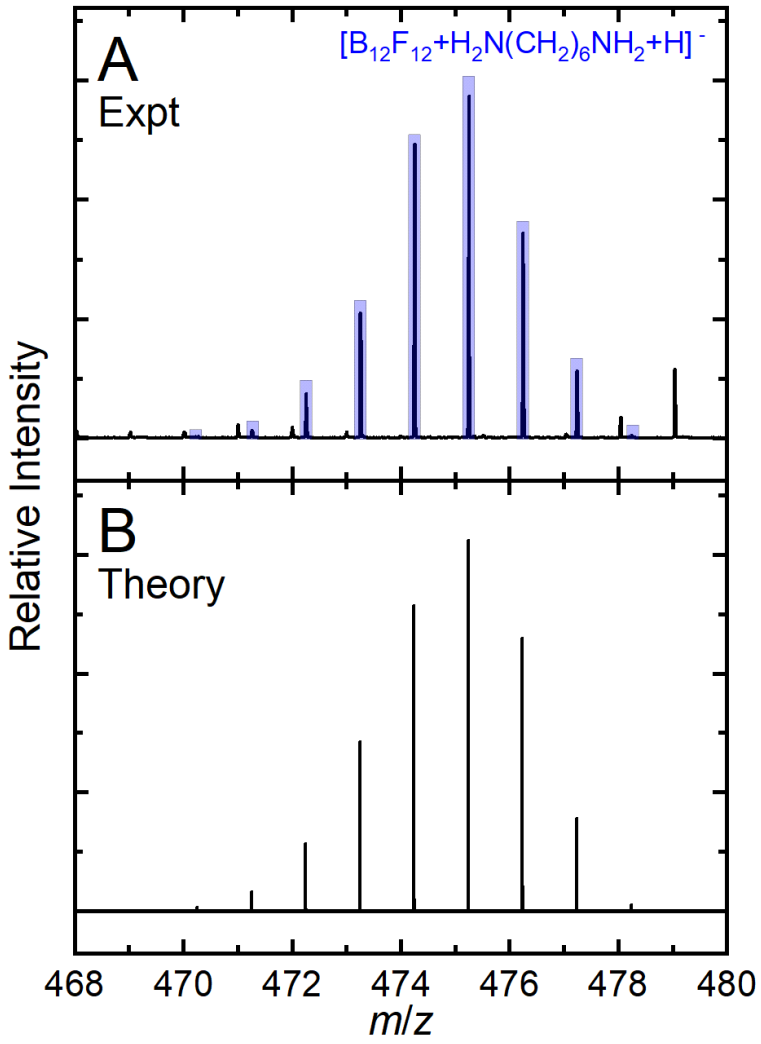


Figure 5.1. (**A**) The experimental mass spectrum recorded for the $[B_{12}F_{12} + H_2N(CH_2)_6NH_2 + H]^-$ cluster and (**B**) its theoretical isotopic distribution. Experimental *m/z* features associated with the various isotopologues of $[B_{12}F_{12} + H_2N(CH_2)_6NH_2 + H]^-$ are highlighted in blue.

Figure 5.2 shows the fragmentation mass spectrum of the $[B_{12}F_{12} + H_2N(CH_2)_6NH_2 + H]^-$ cluster as observed following IRMPD and CID. For the most part, both fragmentation techniques generated the same product ions, but with different relative intensities. Two minor features at *m/z* ~394 and *m/z* ~399, for which we do not have a definitive assignment, were observed in CID but not in IRMPD. Based on their masses, we

have tentatively provided molecular formulae for these ions (see **Figure 5.2**). The remaining product ions were assigned to a variety of boron and fluorine containing species, many of which had been identified previously in the $[B_{12}F_{12} + N(CH_2CH_3)_3 + H]^-$ study by Carr *et al*.[210] The most prominent product ion observed is $B_{12}F_{11}^-$ (*m*/*z* ~339), which is produced via HF elimination from $HB_{12}F_{12}^-$ (*m*/*z* ~359), which itself is a product of the parent $[B_{12}F_{12} + H_2N(CH_2)_6NH_2 + H]^-$ cluster. We note that very little $B_{12}F_{12}^{2-}$ (*m*/*z* ~179) is produced via CID or IRMPD, indicating that the proton transfer dissociation pathway is the dominant product channel. Loss of HF from $HB_{12}F_{12}^-$ to generate the (very reactive) $B_{12}F_{11}^-$ cluster results in further fragmentation of the boron cage cluster (*e.g.*, successive F losses) as well as reactions with the background N_2 gas to form the $[B_{12}F_{11} + N_2]^-$ cluster (*m*/*z* ~367). We also see formation of $[B_{12}F_{11} + Ar]^-$ (*m*/*z* ~379), which arises due to reaction with the $Ar_{(g)}$ that is used for CID. Reaction of $B_{12}X_{11}^-$ (X = halogens, CN) anions with inert gases was first reported by Rohdenburg *et al*.,[211] who demonstrated binding of Kr and Xe to the supernucleophilic site of $B_{12}Cl_{11}^-$ (produced via CID of $B_{12}Cl_{12}^{2-}$). With regard to the singly charged $[B_{12}F_{12} + H_2N(CH_2)_nNH_2 + H]^-$ ($n = 2 – 12$) and the doubly charged $[2B_{12}F_{12} + H_2N(CH_2)_nNH_2 + 2H]^{2-}$ ($n = 2 – 12$) clusters studied here, the fragmentation behaviour shown in **Figure 5.2** is relatively consistent across the entire series (see Appendix B **Figures B35 – B55**). To further confirm the identity of the $[B_{12}F_{11} + N_2]^-$ cluster, we conducted CID experiments for a few test cases with the source of N_2 (*i.e.*, the TWIMS cell) turned off. Doing so resulted in the disappearance of the $[B_{12}F_{11} + N_2]^-$ peak from the mass spectrum.

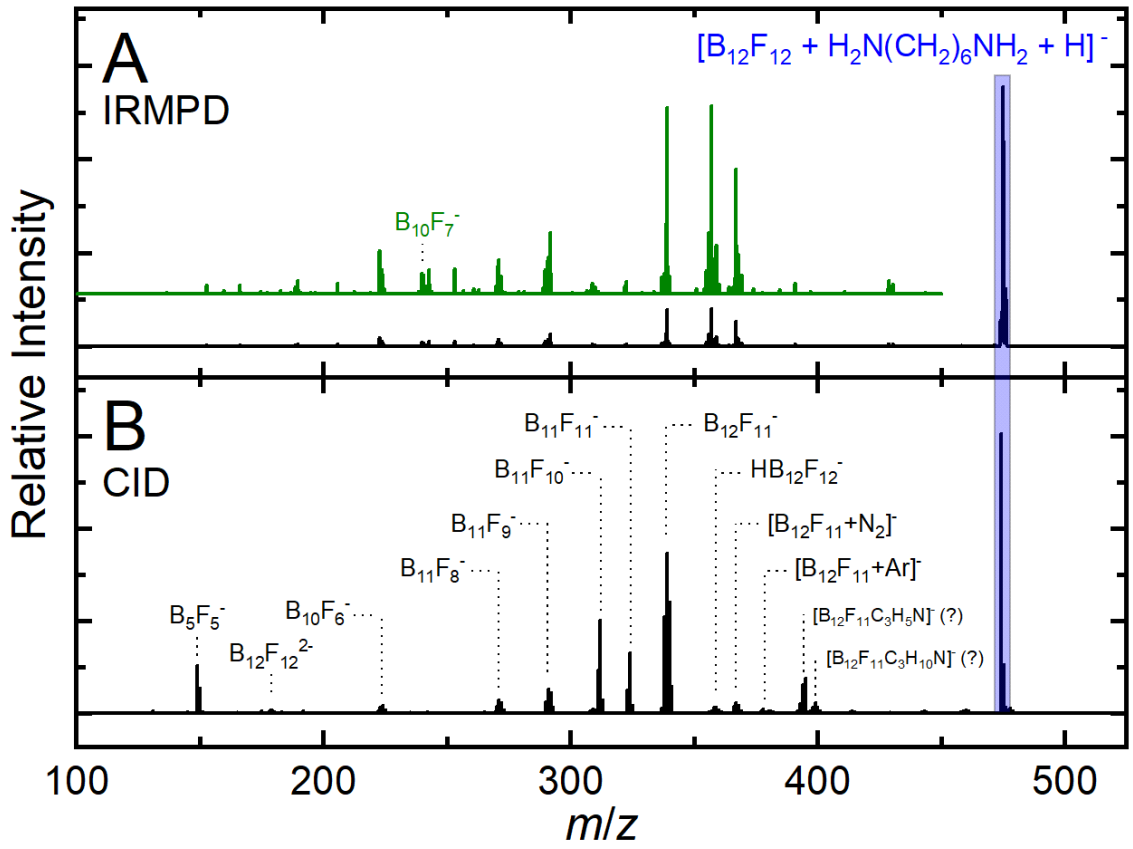


Figure 5.2. Fragment mass spectra observed for $[B_{12}F_{12} + H_2N(CH_2)_6NH_2 + H]^-$ ($m/z \sim 475$) following (**A**) IRMPD and (**B**) CID. The parent ion is highlighted in blue at 3200 cm^{-1}. Tentative assignments are provided for the features at $m/z \sim 394$ and $m/z \sim 399$. The remaining mass features are assigned based on the reference 210.

5.4.2 – Computational Results

To explore the structures and properties of the $[B_{12}F_{12} + H_2N(CH_2)_nNH_2 + H]^-$ ($n = 2 – 12$) and $[2B_{12}F_{12} + H_2N(CH_2)_nNH_2 + 2H]^{2-}$ ($n = 2 – 12$) clusters, we first conducted a detailed computational study. CREST sampling followed by DFT optimization yields three structural motifs for the singly-charged species, $[B_{12}F_{12} + H_2N(CH_2)_nNH_2 + H]^-$ ($n = 2 – 12$), based on the geometry of the diaminoalkane: (*i*) monodentate binding, (*ii*) bidentate binding, and (*iii*) proton-bound ring structures. **Figure 5.4A – C** shows examples of these structural motifs for the $[B_{12}F_{12} + H_2N(CH_2)_6NH_2 + H]^-$ cluster along with relative Gibbs energies. In

this case, the lowest energy structural motif is that of the proton-bound ring structure, which lies *ca.* 30 kJ mol^{-1} below the monodentate and bidentate structures. Calculations indicate that for the singly-charged species with $n \leq 8$, the proton-bound ring structural motif is the preferred geometry. However, for $n \geq 9$ the isomeric forms re-order energetically and the bidentate motif becomes the favoured geometry. **Figure 5.3** plots the relative energies of the structural motifs of the $[B_{12}F_{12} + H_2N(CH_2)_nNH_2 + H]^-$ clusters as a function of n.

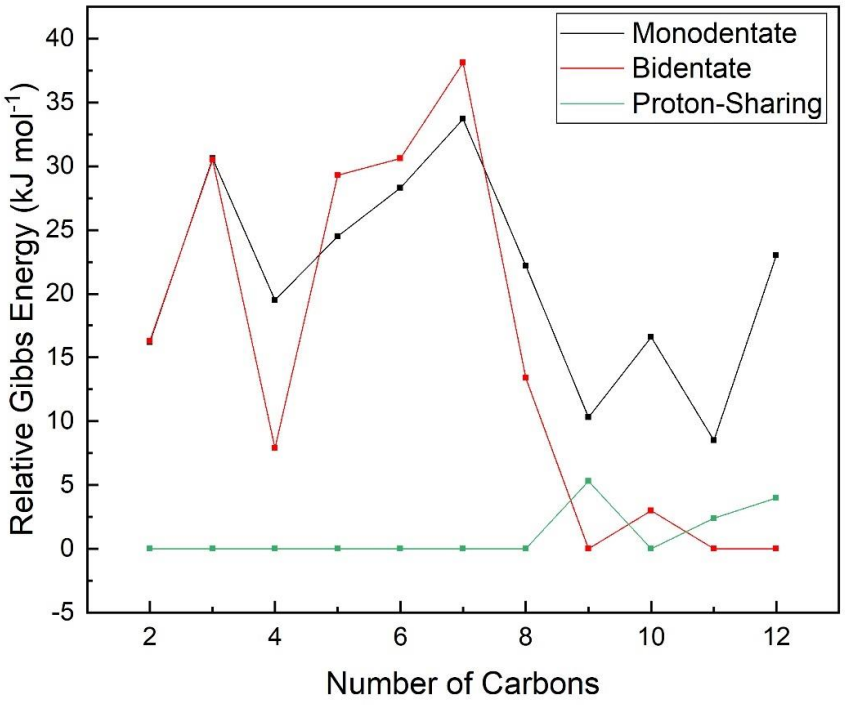


Figure 5.3. Relative energy differences between the three singly charged conformations. (black) monodentate geometry, (red) bidentate geometry, and (green) proton-bound geometry.

Figures 5.4D – F show the computed global minima for the $[2B_{12}F_{12} + H_2N(CH_2)_nNH_2 + 2H]^{2-}$ ($n = 3 – 5$) clusters. Calculations indicate compact geometries for clusters with $n \leq 3$ and extended structures for clusters with $n \geq 4$. Interestingly, for clusters with $n \leq 3$, the extended geometries were not stable minima and collapsed into the compact form upon geometry optimization. This behaviour is likely driven by four factors: (*i*) the Coulombic repulsion of the $B_{12}F_{12}^{2-}$ cages, (*ii*) the Coulombic repulsion of the ammonium groups of the doubly-protonated diaminoalkane, (*iii*) the entropy of the doubly-protonated diaminoalkane chain, and (*iv*) the attractive forces (*i.e.*, Coulombic and hydrogen-bonding) between the $B_{12}F_{12}^{2-}$ cages and the ammonium groups. For the short-chain diaminoalkanes ($n = 2, 3$), the distance between the $B_{12}F_{12}^{2-}$ cages in the compact and (hypothetical) extended forms is not significantly different so factors (*i*) and (*ii*) will be relatively similar in both cases by virtue of the $1/r$ dependence of Coulombic interactions. Moreover, the conformational space for these short-chain diaminoalkanes is relatively small and restricting their geometry in the compact cluster form has a relatively minor impact on the system entropy. However, as shown in **Figure 5.4** for the case of the $n = 3$ cluster, the proximity of the $B_{12}F_{12}^{2-}$ cages to both ammonium groups of the short-chain species enables the formation of additional stabilizing attractive interactions. The balance of these driving forces leads to the adoption of compact structures for the short chain species. In contrast, the stabilization afforded by introducing additional hydrogen bonding does not overcome the entropic penalty of restricted geometry in the clusters that contain longer chain diaminoalkanes. This behaviour is reflected in the computed gas phase basicity and proton affinity for the diaminoalkanes (see **Table B4** for singly charged and **Table B5** for doubly charged); gas phase basicities, for example, increase from 507 kJ mol^{-1} to 828 kJ mol^{-1} across the range $n = 2 – 12$.

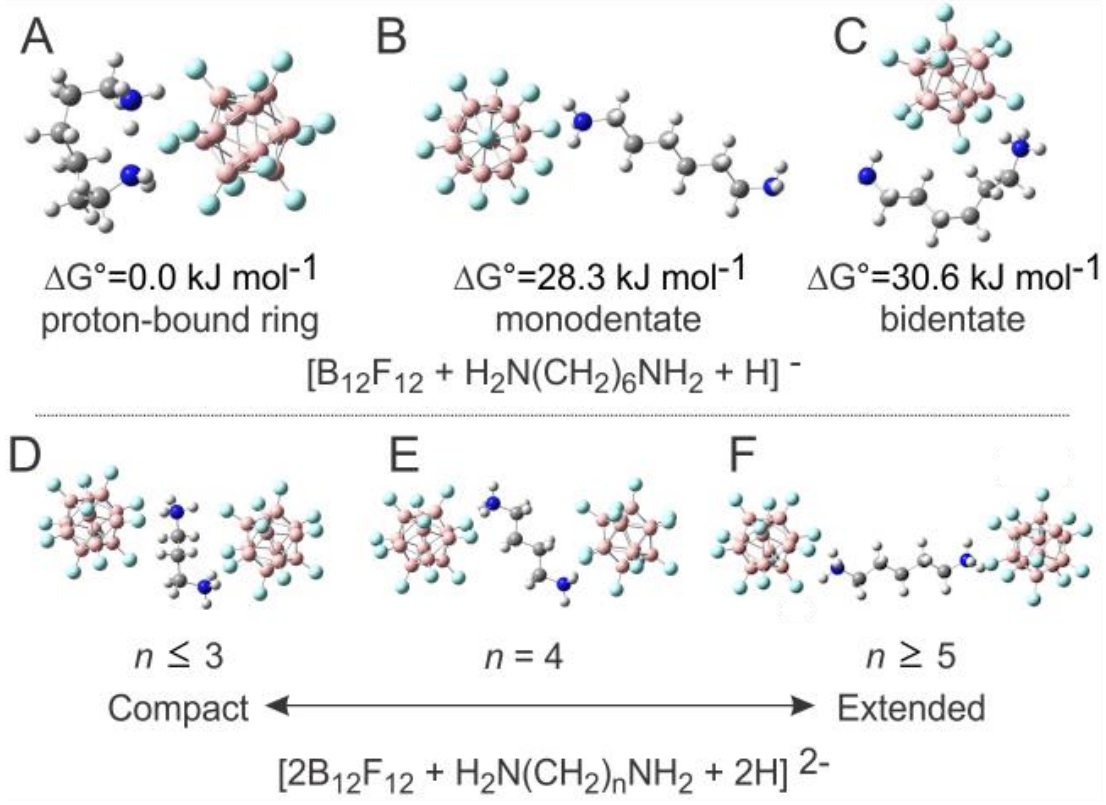


Figure 5.4. (**Top**) Computed geometries of the $[B_{12}F_{12} + H_2N(CH_2)_6NH_2 + H]^-$ cluster: (**A**) proton-bound ring structure, (**B**) monodentate-bound structure, and (**C**) bidentate-bound structure. Calculated relative Gibbs energies for the three isomers are given in kJ mol^{-1}. (**Bottom**) Computed geometries of the $[2B_{12}F_{12} + H_2N(CH_2)_nNH_2 + 2H]^{2-}$ (n = 3, 4, 5) clusters. (**D**) The structure of the n = 3 doubly-charged cluster is representative of the ground state of those containing diaminopropane and diaminoethane species. (**E**) The structure of the n = 4 doubly-charged cluster. (**F**) The structure of the n = 5 doubly-charged cluster is representative of the ground state of those containing diaminopentane and longer chain species.

The computed binding energies for the dissociation process $[B_{12}F_{12} + H_2N(CH_2)_nNH_2 + H]^- \rightarrow HB_{12}F_{12}^- + H_2N(CH_2)_nNH_2$ (n = 2, 6, 12) are provided in **Table 5.1** and energies for the remaining analogous $[B_{12}F_{12} + H_2N(CH_2)_nNH_2 + H]^-$ clusters are provided in Appendix B **Table B8–B10**. Standard Gibbs binding energies for the lowest energy conformations range from *ca*. 160 – 210 kJ mol^{-1}. As expected, the trend in binding energy as a function of n mirrors that of the relative conformer energies. In comparison, dissociation energies of the

singly-charged clusters to yield $B_{12}F_{12}^{2-}$ (*i.e.*, direct dissociation without proton transfer) are significantly higher in energy (see **Table B11–B13**), ranging from 491 – 576 kJ mol^{-1}. This result accords with experiment, where the formation of $B_{12}F_{12}^{2-}$ was observed to be a (very) minor product channel via CID and IRMPD for all clusters.

The computed binding energies for the doubly-charged $[2B_{12}F_{12} + H_2N(CH_2)_nNH_2 + 2H]^{2-}$ (n = 2 – 12) clusters are provided in **Table 5.2**. As was the case with the singly-charged species, the proton-transfer product channel (leading to formation of $HB_{12}F_{12}^-$) is thermodynamically favoured over the $B_{12}F_{12}^{2-}$ product channel. However, we find that the gap between these thresholds diminishes substantially with increasing length of the diaminoalkane chain; for the n = 2 cluster, the energy gap between thresholds is ΔE = 164 kJ mol^{-1}, whereas for n = 12 the gap is ΔE = 8 kJ mol^{-1}. This stabilization of the $B_{12}F_{12}^{2-}$ product channel relative to the $HB_{12}F_{12}^-$ product channel is reflected in the CID fragmentation spectra, which show significantly more intensity in the $B_{12}F_{12}^{2-}$ mass channel for clusters containing longer diaminoalkanes (0.3% of total ion signal for n = 2 versus 4.7% of total ion signal for n = 12). In comparison, a similar analysis of the singly-charged $[B_{12}F_{12} + H_2N(CH_2)_nNH_2 + H]^-$ clusters reveals that the energy gap between product thresholds diminishes from ΔE = 66 kJ mol^{-1} to ΔE = 28 kJ mol^{-1} across the n = 2 – 12 series, and the $B_{12}F_{12}^{2-}$ ion signal observed in CID increases from 0.2% to 2.0% of total ion signal, accordingly.

Table 5.1. Computed binding energies for $[B_{12}F_{12} + H_2N(CH_2)_nNH_2 + H]^-$ dissociating to $H_2N(CH_2)_nNH_2 + HB_{12}F_{12}^-$ products for $n = 2$, 6, 12. Electronic energies (ΔE_{elec}), zero-point corrected energies (ΔE_{zpe}), enthalpies (ΔH), and standard Gibbs energies ($\Delta G°$) are reported in kJ mol^{-1}, and entropy (ΔS) is reported in units of kJ mol^{-1} K^{-1}.

Cluster	ΔE_{elec}	ΔE_{zpe}	ΔH	ΔS	$\Delta G°$
Monodentate conformation					
$n = 2$	244.2	223.6	223.1	53.7	169.3
$n = 6$	243.9	224.0	223.4	56.9	166.5
$n = 12$	243.0	223.4	222.5	58.6	163.9
Bidentate conformation					
$n = 2$	244.2	223.5	223.0	53.8	169.2
$n = 6$	248.0	226.0	226.2	61.9	164.3
$n = 12$	278.6	255.2	256.1	69.2	186.9
Proton-bound ring conformation					
$n = 2$	256.4	236.6	236.4	55.0	181.4
$n = 6$	295.0	272.3	273.0	63.8	209.2
$n = 12$	278.3	251.5	182.8	254.1	182.8

Table 5.2. Computed binding energies for $[2B_{12}F_{12} + H_2N(CH_2)_nNH_2 + 2H]^{2-}$ dissociating to: (I.) $[B_{12}F_{12} + H_2N(CH_2)_nNH_2 + H]^- + HB_{12}F_{12}^-$ and (II.) $[B_{12}F_{12} + H_2N(CH_2)_nNH_2 + 2H]^0 + B_{12}F_{12}^{2-}$ products for n = 2, 6, 12. Electronic energies (ΔE_{elec}), zero-point corrected energies (ΔE_{zpe}), enthalpies (ΔH), and standard Gibbs energies ($\Delta G°$) are reported in kJ mol^{-1} , and entropy (ΔS) is reported in units of kJ mol^{-1} K^{-1}.

Cluster	ΔE_{elec}	ΔE_{zpe}	ΔH	ΔS	$\Delta G°$
		I.	$HB_{12}F_{12}^-$ Formation		
n = 2	199.0	180.5	188.4	85.2	103.2
n = 6	192.1	172.5	171.6	62.5	109.1
n = 12	229.8	211.7	217.6	81.4	136.2
		II.	$B_{12}F_{12}^{2-}$ Formation		
n = 2	345.4	341.2	346.8	79.6	267.2
n = 6	219.8	220.9	216.5	49.9	166.6
n = 12	202.8	207.2	209.2	65.2	144.0

5.4.3 – Ion Mobility Results

To investigate the possibility of multiple isomeric sub-populations in the gas phase ensemble, we conducted TWIMS experiments for the $[B_{12}F_{12} + H_2N(CH_2)_nNH_2 + H]^-$ and $[2B_{12}F_{12} + H_2N(CH_2)_nNH_2 + 2H]^{2-}$ clusters for $n = 2 – 12$. Collision cross-sections (CCSs) for all ions measured are tabulated in Appendix B (**Table B2**). The $[B_{12}F_{12} + H_2N(CH_2)_nNH_2 + H]^-$ clusters are found to have CCSs that range from 180 $Å^2$ (n = 2) to 218 $Å^2$ (n = 12), with a relatively linear increase in CCS values as a function of the length of the diaminoalkane chain (see **Figure 5.5**). We do not resolve multiple features in our TWIMS experiments. However, we note that the linear trend of increasing CCS with increasing size of diaminoalkane chain length deviates slightly at n = 10, which also exhibits a significantly broader arrival time distribution than the other clusters. This is approximately the same region that calculations predict there to be an energetic reordering of the low-energy structural motifs; the proton-bound ring structure being favoured for $n \leq 8$ and the bidentate structure favoured for $n \geq 9$. Overlayed on Figure 4 are CCSs for the various cluster isomers, which we computed using MobCal-MPI.[212] Because MobCal-MPI is not parameterized to include boron, we employed the force field parameters for sp^3 hybridized carbon to approximate the boron parameters while maintaining the DFT-calculated cluster geometries and partial charges. Since this treatment will introduce minor systematic errors to the calculations, one is cautioned against over-interpreting the resulting CCS values. However, we anticipate qualitative agreement for the relative CCS trends of the cluster structural motifs owing to the internal consistency of our computational approach. When comparing the computed CCSs to those measured experimentally, we find relatively good agreement with the trends for the proton-bound ring and bidentate motifs. Considered collectively, our TWIMS measurements and supporting CCS calculations suggest that there may be multiple isomers present for the longer chain species, which accords with expectations based on DFT calculations.

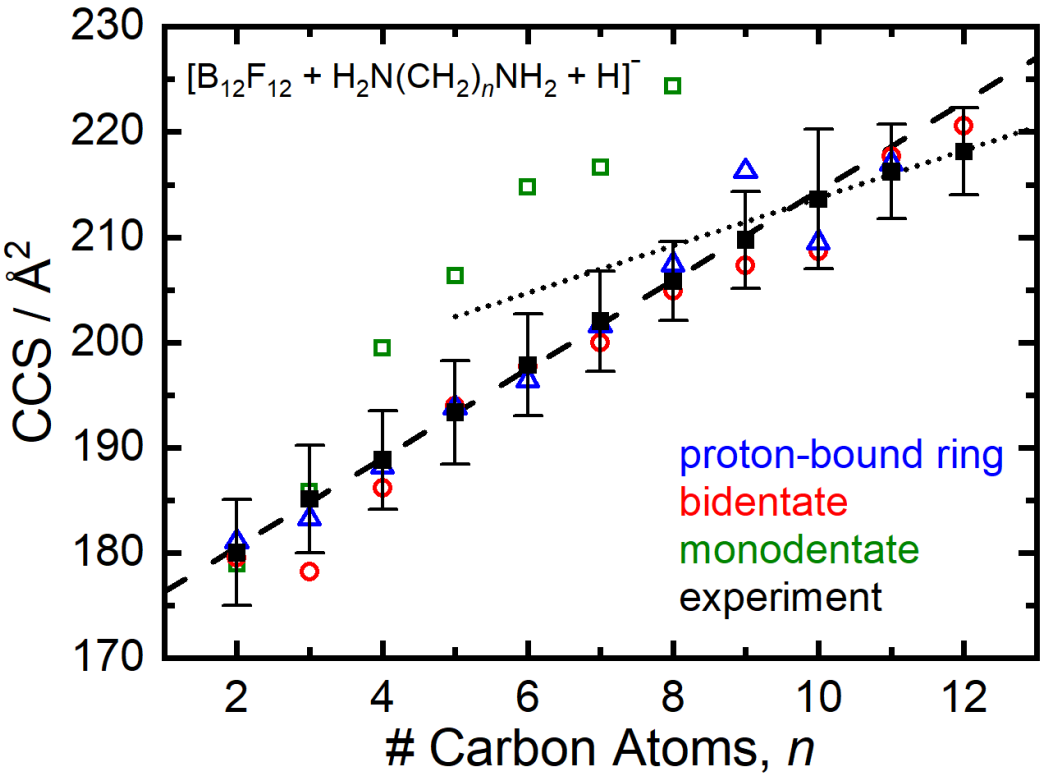


Figure 5.5. (**Black**) Measured CCSs for the $[B_{12}F_{12} + H_2N(CH_2)_nNH_2 + H]^-$ ($n = 2 – 12$) clusters. Error bars indicate the full width at half maximum for the arrival time distributions. The dashed line shows a linear trend that was fit to the $n = 2 – 9$ clusters. The dotted line shows a linear trend that was fit to the $n = 10 – 12$ clusters. Computed CCS values for the (**green**) monodentate, (**red**) bidentate, and (**blue**) proton-bound ring structures.

To explore further the isomeric composition of the gas phase cluster ensembles, we measured the differential ion mobility behaviour of each cluster. DMS has been shown to resolve isomeric features that cannot be resolved via TWIMS, although care must be taken to account for artefacts associated with fragmentation of larger cluster species.[94,213,214] **Figure 5.6** shows the DMS ionograms measured for the $[B_{12}F_{12} + H_2N(CH_2)_nNH_2 + H]^-$ ($n = 4$, 10) clusters. Overlayed in red are the ionograms measured for the $[2B_{12}F_{12} + H_2N(CH_2)_nNH_2 + 2H]^{2-}$ ($n = 4$, 10) clusters, which fragment in the post-DMS transfer ion optics to generate the singly-charged analogues (observed at CV ≈ 13 V). Analogous plots for the other clusters studied are provided in the supplementation information (**Figure B24-34**). The remaining feature observed in the ionogram of

$[B_{12}F_{12} + H_2N(CH_2)_4NH_2 + H]^-$ suggests that this cluster exhibits a single structural motif in its gas phase ensemble under these experimental conditions (see **Figure 5.6A**). In contrast, the ionogram of $[B_{12}F_{12} + H_2N(CH_2)_{10}NH_2 + H]^-$ exhibits two features after accounting for fragmentation of the $[2B_{12}F_{12} + H_2N(CH_2)_4NH_2 + 2H]^{2-}$ cluster to generate the singly-charged analogue and $HB_{12}F_{12}^-$ (see **Figure 5.6B**). In fact, the second, lower intensity feature is visible in all $[B_{12}F_{12} + H_2N(CH_2)_nNH_2 + H]^-$ (n = 6 – 12) ionograms (see **Figures B28-34**), suggesting that two isomeric forms are present for the larger clusters. Unfortunately, both features exhibited the same fragmentation behaviour and precursor ion scans, so we cannot conclusively assign the observed peaks to specific cluster geometries. Nevertheless, given our computational results, we favour the larger peak at CV ≈ 7 V to be the proton-bound ring structure.

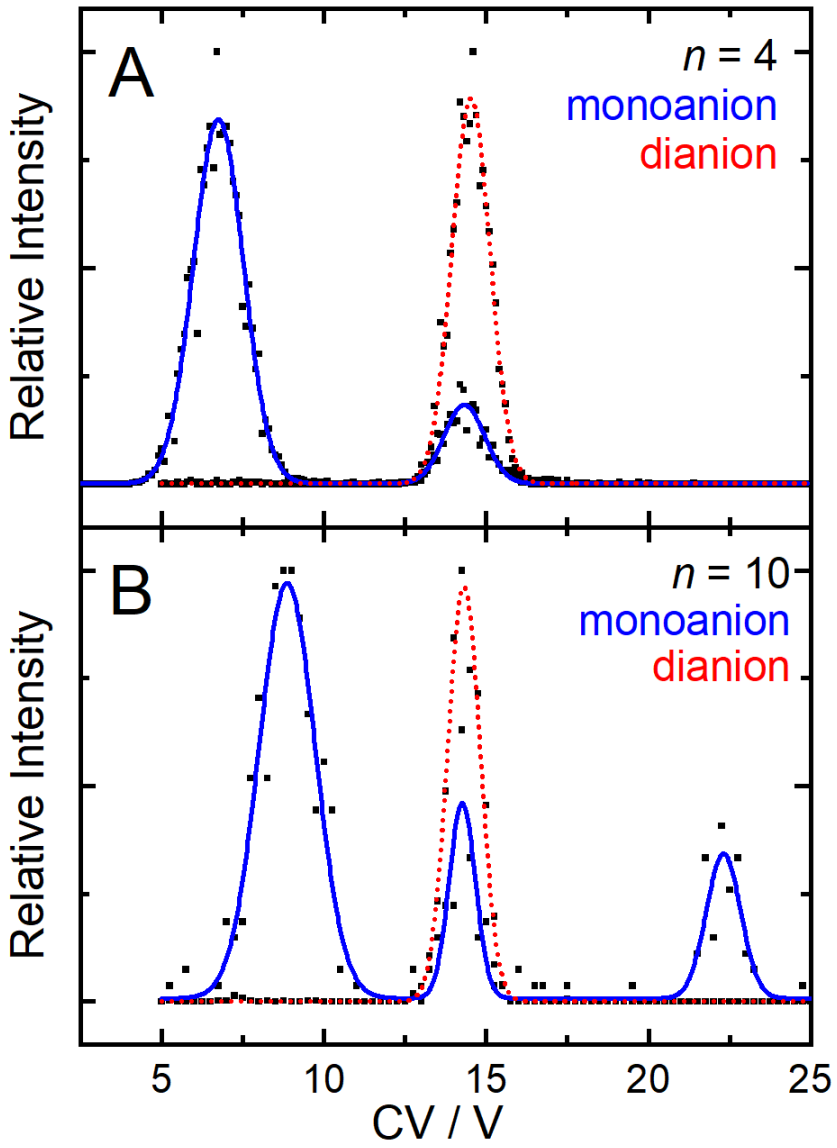


Figure 5.6. Ionograms of (**A, blue**) $[B_{12}F_{12} + H_2N(CH_2)_4NH_2 + H]^-$ and (**A, red**) $[2B_{12}F_{12} + H_2N(CH_2)_4NH_2 + 2H]^{2-}$ measured at SV = 3800 V in a pure N_2 environment. (**B, blue**) Ionograms of $[B_{12}F_{12} + H_2N(CH_2)_{10}NH_2 + H]^-$ and (**B, red**) $[2B_{12}F_{12} + H_2N(CH_2)_{10}NH_2 + 2H]^{2-}$ measured at SV = 3800 V in a pure N_2 environment. Ionograms for the other clusters measured at the same SV are provided in Appendix B(**Figure B24-34**).

5.4.4 – Infrared Ion Spectroscopy (IRIS) Results

As a final exploration of cluster structure, IRIS experiments were performed on the mass-selected singly-charged $[B_{12}F_{12} + H_2N(CH_2)_nNH_2 + H]^-$ and the doubly-charged $[2B_{12}F_{12} + H_2N(CH_2)_nNH_2 + 2H]^{2-}$ (n = 2 – 12) clusters. **Figure 5.7** provides a comparison of the experimental spectrum recorded for the $[B_{12}F_{12} + H_2N(CH_2)_{12}NH_2 + H]^-$ cluster along with the computed spectra for the monodentate, bidentate, and proton-bound ring isomers. **Table B14** in Appendix Boutlines the assignments for the fundamental vibrational band systems observed in the doubly-charged and the singly-charged clusters. The spectral intensity near 3,300 cm^{-1} demonstrates the presence of the bidentate and/or the proton-bound ring structure since the monodentate isomer does not absorb in this region. Similarly, the intensity observed near 2,700 cm^{-1} demonstrates the presence of the proton-bound ring structure since only this isomer absorbs at wavenumbers in the 2,500 – 2,900 cm^{-1} region. That this band is not as sharp and intense as predicted by theory stems from the fact that it is associated with the shared proton vibration of the protonated 1,12-diaminododecane moiety; shared protons are notoriously anharmonic and often exhibit broad bands of relatively low intensity.[215,216] By monitoring this region as a function of diaminoalkane chain length indicates that the proton-bound ring structure is present for all clusters sizes. Unfortunately, owing to spectral congestion there are no isolated diagnostic vibrational bands for either of the other two motifs. As a note for completeness, the doubly-charged $[2B_{12}F_{12} + H_2N(CH_2)_nNH_2 + 2H]^{2-}$ (n = 2 – 12) clusters, for which there was only a single low-energy isomer for each cluster size, exhibited relatively sparse spectra that aligned very well with computed harmonic absorption spectra (see **Appendix B Figures B67-70**).

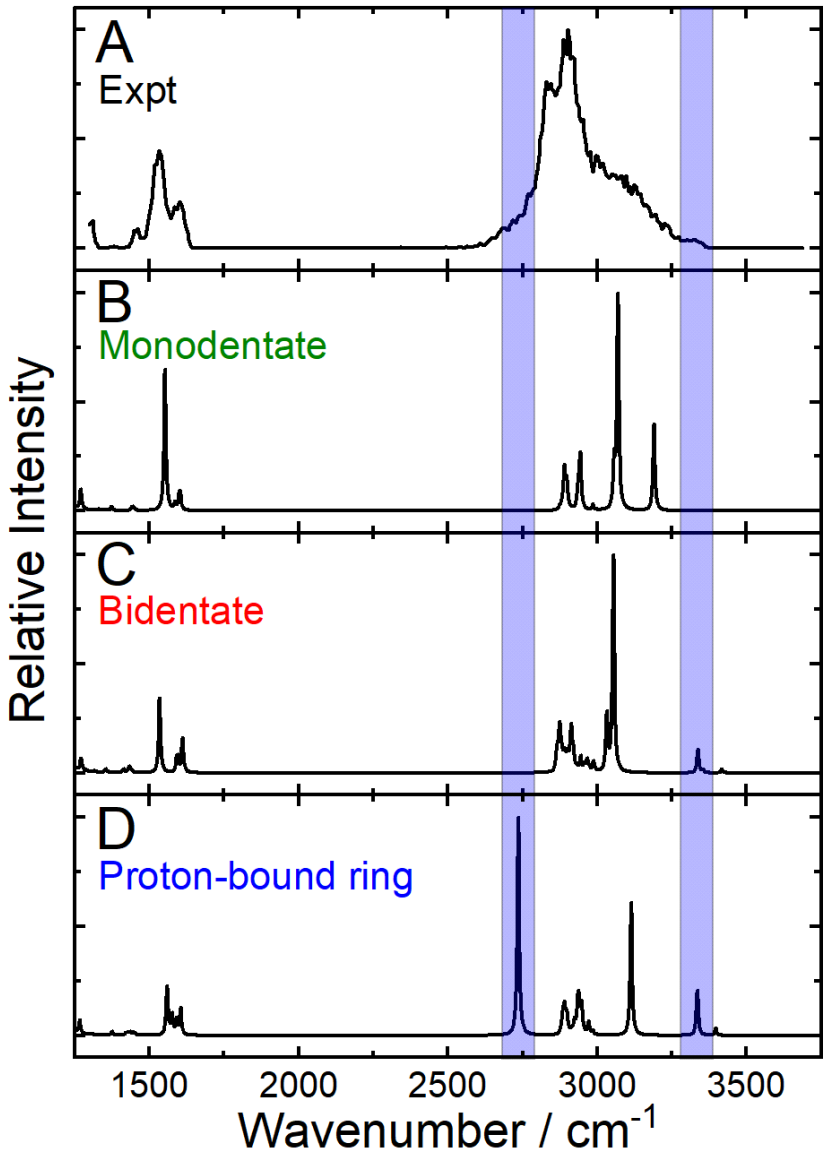


Figure 5.7. (**A**) The experimental IRIS spectrum for the $[B_{12}F_{12} + H_2N(CH_2)NH_2 + H]^-$ cluster and the computed spectra of the (**B**) monodentate, (**C**) bidentate, and (**D**) proton-bound ring isomers. The intensity observed near 2,700 cm^{-1} demonstrates that the proton-bound-ring structure is present in the probed ensemble.

A final interesting observation was that different band intensities were observed in spectra from different IRMPD product channels of the same parent molecule. For example, the spectra observed in the *m*/*z* ~ 358 ($HB_{12}F_{12}^-$) and *m*/*z* ~ 339 ($B_{12}F_{11}^-$) product channels of the $[B_{12}F_{12} + H_2N(CH_2)_{12}NH_2 + H]^-$ cluster are marked different as seen in. For example, the *m*/*z* 339 channel exhibits relatively narrow bands with substantially more intensity in the >2,900 cm^{-1} region than in the *ca*. 1,500 cm^{-1} region, whereas the *m*/*z* 358 channel exhibits relatively broad bands with substantially higher intensity in the *ca*. 1,500 cm^{-1} region than at >2,900 cm^{-1} (see **Figure 5.8**). This behaviour can likely be attributed to the power dependence of the processes to produce $HB_{12}F_{12}^-$ and *m*/*z* ~ 339 $B_{12}F_{11}^-$. Because $B_{12}F_{11}^-$ is produced via HF loss from $HB_{12}F_{12}^-$, excitation via the high absorption cross-section bands in the 2,900 – 3,200 cm^{-1} region leads to a reaction cascade from the parent to $HB_{12}F_{12}^-$ to $B_{12}F_{11}^-$, thus artificially diminishing the band intensity in the *m*/*z* ~ 358 channel and inflating that observed in the *m*/*z* ~ 339 ($B_{12}F_{11}^-$) product channel. We attempted to confirm this with a power study at the FELIX facility, but results were inconclusive because there is a significant reduction in the fragmentation signal when any attenuations are applied.

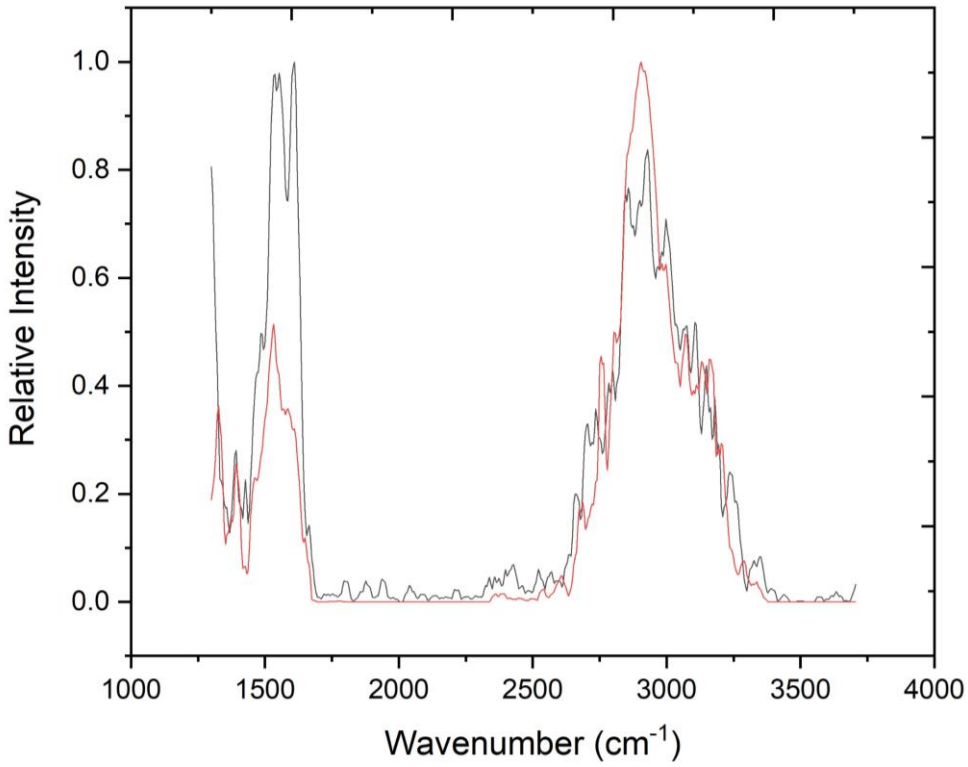


Figure 5.8. Comparisons of the IRMPD spectra for the (black) *m/z* 358 fragment and (red) *m/z* 339 fragment from the singly charged diaminoheptane cluster $[(B_{12}F_{12})\bullet H_3N\text{-}(CH_2)_7\text{-}NH_2]^-$.

5.5 – Conclusions

Multiple $B_{12}F_{12}^{2-}$ cages can be observed to form a doubly charged cluster in the form, $[2(B_{12}F_{12})+ H_2N\text{-}(CH_2)_n\text{-}NH_2+2H]^{2-}$. Fragmentations of the dianion complex proceeds *via* two dissociation pathways: (*i*) proton-transfer to yield $[HB_{12}F_{12}]^-$ and (*ii*) a direct dissociation of the protonated diaminoalkane and $B_{12}F_{12}^{2-}$. In the proton-transfer product channel, further gas phase reaction by HF elimination yields the highly electrophilic $[B_{12}F_{11}]^-$ species that subsequently reacts with inert gases in the ion trap to form species such as $[B_{12}F_{11} + N_2]^-$ and $[B_{12}F_{11}+Ar]^-$. The doubly charged species are found to adopt an extended geometry where the negative charges can be maximally separated, until $n \leq 4$, where a more compact structure is adopted to maximize the Coulombic attraction between the $B_{12}F_{12}^{2-}$ cages and the ammonium groups. Three unique geometries are found for the singly charged species, a monodentate, a bidentate, and a proton-bound ring structure. Two major fragmentation pathways are observed, the formation of $HB_{12}F_{12}^-$ and the loss of $B_{12}F_{12}^-$. The computed standard Gibbs binding energies for the formation of $HB_{12}F_{12}^-$ from the doubly charged species is found to be a 103.2 kJ mol^{-1} at $n = 2$ and increases to 136.2 kJ mol^{-1} at $n = 12$. In contrast, the standard Gibbs binding energies for the loss of $B_{12}F_{12}^{2-}$ is found to be 267 kJ mol^{-1} at $n = 2$ and decreases to 144 kJ mol^{-1} at $n = 12$. For the singly charged species, similar trend to the doubly charged species can be observed, with the formation of $HB_{12}F_{12}^-$ to be the more favourable fragmentation pathway than the loss of $B_{12}F_{12}^{2-}$.

To investigate further the possibility of multiple isomers presenting in the gas-phase ensemble, TWIMS and DMS experiments were conducted. The singly charged species are found to have a CCS of 180 Å^2 ($n = 2$) to 218 Å^2 ($n = 12$), with a relatively linear increase in CCS value as a function of the diaminoalkane chain length. Linear trend of increasing CCS with increasing size begins to deviate at $n = 10$, this leads to the believe that there are potential conformations change as the chain length increases. Following the TWIMS experiments, DMS experiments were undertaken to attempt to resolve the potential isomers within the gas-phase ensemble. For diaminoalkane chain length with $n \leq 4$, two features can

be observed in the ionogram for the singly charged species, with a peak-feature that perfectly coincides with the doubly charged analogue. This means that the doubly charged analogue has fragmented in the post-DMS transfer to generate the singly charged species. For the longer diaminoalkanes ($n \geq 5$), three features can be observed in the ionogram. While one feature is similar to the cases of the shorter chain length, two features remain to be observed and are believed to be potentially the different isomers within the gas-phase ensemble. We assign the larger peak to be the proton-sharing geometry, with the smaller peak to be the monodentate geometry based on the relative energy differences.

Finally, IRIS experiments were completed to elucidate the potential isomeric candidates in the gas-phase ensemble. The unique peak feature around 2700 cm^{-1} demonstrates the presence of the proton-sharing structure for all diaminoalkane chain length. However, due to spectral congestion, no diagnostic vibrational bands can be determined for the other motifs. The doubly charged species with a single low-energy isomer for all chain length, exhibited a relatively sparse spectra that aligned well with the computed harmonic absorption spectra. An interesting observation is also found for the $HB_{12}F_{12}^-$ product channel and the $B_{12}F_{11}^-$ product channel for the diaminododecane cluster, where the $B_{12}F_{11}^-$ fragmentation channel is more intense in the region > 2900 cm^{-1} compared to the *ca.* 1500 cm^{-1} region. This behaviour is found to be different for the $HB_{12}F_{12}^-$ product channel, where *ca.* 1500 cm^{-1} region is found to be more intense than the region of > 2900 cm^{-1}. This is believed to be caused by the power dependence to produce $HB_{12}F_{12}^-$ and $B_{12}F_{11}^-$. Future studies can couple DMS with IRMPD to potentially mobility select before IR interrogation to confirm the isomeric structure for different peaks shown in the ionogram. In addition, further studies can be done with other $B_{12}X_{12}^{2-}$ (X = H, Cl, Br, I) species to observe similar behaviour or if the structures found in this study can only be formed by $B_{12}F_{12}^{2-}$.

Computational geometries are available through the following link:

http://dx.doi.org/10.19061/iochem-bd-6-420

– Chapter 6 –
Conclusions

IRMPD and tandem mass spectrometry were used to study three different chemical systems to elucidate their physicochemical properties and dissociation behaviour. In the case of deprotonated fluorinated propionic acids, we observed that isomerization leads to different fragmentation behaviours and unique IR fingerprints. For the triazolide species, the substitution of the isomeric form of the triazolide moieties significantly impacted cluster geometry, owing to differences in the charge-dipole interactions and lone-pair donation interactions that stabilize the various clusters. The diaminoalkane–$B_{12}F_{12}^{2-}$ study demonstrated that successive addition of CH_2 groups results in changes to the cluster geometry, with one structural motif being favoured for small clusters and another for larger species. As a summary, the different chemical systems studied in this thesis have demonstrated interesting properties, interactions, and fragmentation patterns governed by structural changes within the gas phase clusters.

To summarize chapter 3, the family of the different fluorinated propionic acids were studied with IRMPD and CID. Under IRMPD, it was possible to separate isomeric forms of fluorinated propionic acids such as the 3,3,2,2-tetrafluoropropionic acid and the 3,3,3,2-tetrafluoropropionic acid. We discovered that formation of the fluoroformate, FCO_2^-, anion and HF elimination were accessible fragmentation pathways, in addition to the commonly seen CO_2 loss fragmentation pathway. The FCO_2^- formation pathway was the only accessible for fluorinated propionic acids with a fluorine bonded to the β-carbon, whereas the HF elimination pathway is only accessible if a hydrogen is bonded to the β-carbon and a fluorine bonded to an α-carbon. At high energies, it was possible to observe further fragmentation by HF elimination after the loss of CO_2. The discovery of the new fragmentation pathways leads to the investigation of the product ratio between the loss of CO_2 and the formation of FCO_2^- or HF elimination. Under IRMPD, the FCO_2^- pathway was more favourable for species such

as the 3,3,3-trifluoropropionic acids and the 3,3,3,2-tetrafluoropropionic acid. In comparison, the CO_2 loss pathway was more favourable under CID for the 3,3,3-trifluoro and the 3,3,3,2-tetrafluoropropionic acid. Curiously, similar fragmentation behaviour can be observed from 2,2-difluoropropionic acid, where CID demonstrated that the dominant fragmentation to be the loss of CO_2 but IRMPD favours HF elimination. This result is interesting as it is rare to observe a significant difference in fragmentation for IRMPD and CID for small covalent bonded molecules. The transition states structure for the FCO_2^- formation and the HF elimination pathway was found to be a pseudo-four-membered ring structure. It is of interest to investigate further the fragmentation behaviour of other PFAS compounds such as fluorotelomers and fluoroethers that are commonly used as substitutes for legacy PFASs, as more interesting fragments can form with different substituents. In addition, more studies are required to elucidate the reasoning behind the differences in the fragmentation ratio between IRMPD and CID, to verify if IVR can be non-ergodic for a covalently bonded ion. This study showed that extra cares are needed when examining complex PFAS compounds during analytical studies to account for unexpected product channels.

In chapter 4, I discussed the cluster geometry and the forces influencing the geometry of different triazolide and alkali metal cations complexes in the form of $[M_n(123T)_{n-1}]^+$ and $[M_n(124T)_{n-1}]^+$ (M = Na, K). Comparing the cluster geometry of the 1,2,3-triazolide (123T) and the 1,2,4-triazolide (124T) structures to the analogous cyclopentadienyl (Cp^-) cluster, it was found that the triazolide clusters no longer form an "inverse-sandwich" like complex and instead formed unique compacted structures strongly influenced by ion-dipole interactions and lone pair charge donation interaction. The largest clusters observed for the 123T was $[M_4(123T)_3]^+$ with a compact 3D structure for the potassiated analogue and a flatter and more planar for the sodiated analogue. In contrast, the analogous cluster observed for both K-124T and Na-124T adopts a more open structure with longer distances between the 124T and the metal cation. The binding energy of the sodiated 123T and 124T clusters were found to be higher than the potassiated analogues. Overtone bands of C-H out-of-plane bending mode or combination bands of C-H out-of-plane bending and ring torsion modes can be observed in

the region of 1500 cm^{-1} to 1850 cm^{-1} for both 124T and 123T clusters regardless of the ion partner. More studies utilizing isotope labelled 124T and 123T are needed to elucidate the origin of these bands that were not predicted by harmonic oscillator DFT methods. Hence, the reduction in symmetry by substituting C with N can have a major effect on the geometry of the cluster and the interactions between the cation-anion pair.

In Chapter 5, we found that the $B_{12}F_{12}^{2-}$ cages complexing with diaminoalkanes of the form $H_2N\text{-}CH_n\text{-}NH_2$ (n = 2 – 12) results in unique geometry based on the alkyl chain length through IRMPD and ion mobility methods. Doubly charged clusters containing two $B_{12}F_{12}^{2-}$ at different diaminoalkane lengths, $[2(B_{12}F_{12})+H_2N\text{-}CH_n\text{-}H_2N+2H]^{2-}$ (n = 2 – 12) were observed. The two major fragmentation pathways, the formation of $HB_{12}F_{12}^-$ was found to be more favourable compared to the loss of $B_{12}F_{12}^{2-}$. Nucleophilic sites arose from fluoride abstraction can be observed to interact with inert gas such as N_2 and Ar to form $[B_{12}F_{11} + N_2]^-$ and $[B_{12}F_{11} + Ar]^-$. CID and IRMPD yielded smaller $B_xF_y^-$ fragments that were from consecutive loss of BF_3 or loss of BF. The shorter alkane length (n = 2 and 3) doubly charged clusters had a compact geometry owing to maximize the Coulombic attraction between the $B_{12}F_{12}^{2-}$ cages and both protonated terminus amine groups. In contrast, the longer alkane length doubly charged clusters had a charge separated geometry, where each $B_{12}F_{12}^{2-}$ only interacts with one protonated amine group. The lowest energy singly charged cluster of the form $[B_{12}F_{12}+H_2N\text{-}CH_2\text{-}H_2N+H]^-$ were found to have three unique geometries: monodentate, bidentate, and a proton-sharing geometry. The monodentate geometry had the highest relative Gibbs energy compared to both proton-sharing and bidentate geometry. The singly charged clusters were found to have a CCS of 180 $Å^2$ (n = 2) to 218 $Å^2$ (n = 12). Isomeric geometries were not separable in TWIMS but are separable on the DMS for longer chain length species ($n \geq 5$). In fact, two distinct peaks could be observed on the ionogram for n = 2 – 5, whereas three distinct peaks can be seen for n = 6 – 12. One of the distinct peak features was determined to be the doubly charged analogue dissociating into the singly charged species during transmission post DMS cell. IRMPD results of the doubly charged species indicated a single conformation. For the singly charged clusters, the unique vibrational band of the

proton-sharing at 2700 cm^{-1} could be observed across the different chain length. However, it was not possible to confidently determine if the monodentate and the bidentate motifs were present in the gas-phase ensemble due to spectral congestion. Future studies could couple ion mobility method to mobility select the isomers before IR interrogation to determine the potential isomeric structure in the gas-phase. In addition, it is of interest to see if similar fragmentation behaviour and cluster geometry can be observed for the other dodecaborate cages, $B_{12}X_{12}^{2-}$ (X = H, Cl, Br, I). In general, this study demonstrated the novel potential of clustering the $B_{12}F_{12}^{2-}$ cages with other molecules or ions to generate clusters with interesting geometries.

The studies presented in this thesis demonstrates that small changes in cluster structure, whether it is isomerisation or sequential addition to alkyl chain length, can significantly impact the system's physicochemical properties. Moreover, these variations in cluster properties were often non-intuitive (*e.g.*, FCO_2^- production depending on fluorine position), signalling the need for further studies to probe analogous systems (*e.g.*, FSO_3^- production from sulphonate analogues). However, limitations with IRMPD and tandem mass spectrometry leaves some open questions regarding the structure and fragmentation behaviour. For example, in the case of fluorinated propionic acids, questions were raised regarding whether IRMPD is always an ergodic process for covalently bonded molecules or if exceptions may occur. Future work could also be envisioned which employs labelled isotopologues of the triazolides to probe the identity of the overtone band/combination bands. Furthermore, in the case of the diaminoalkane-$B_{12}F_{12}^{2-}$ clusters, differentiating the cluster geometries via IRMPD spectroscopy is challenging due to spectral congestion of similar vibration absorption bands; ion mobility separation prior to IR interrogation could assist in decongesting IRMPD spectra and enabling unambiguous structural elucidation. Research like this will provide a deeper description of how small changes in cluster structure can influence their physicochemical properties.

References

(1) Cox, A. J.; Louderback, J. G.; Apsel, S. E.; Bloomfield, L. A. Magnetism in 4 *d* - Transition Metal Clusters. *Phys. Rev. B* **1994**, *49* (17), 12295–12298. https://doi.org/10.1103/PhysRevB.49.12295.

(2) Plattner, D. A. Electrospray Mass Spectrometry beyond Analytical Chemistry: Studies of Organometallic Catalysis in the Gas Phase. *Int. J. Mass Spectrom.* **2001**, *207* (3), 125–144. https://doi.org/10.1016/S1387-3806(01)00371-2.

(3) *Organometallic Bonding and Reactivity: Fundamental Studies*; Brown, J. M., Hofmann, P., Eds.; Topics in organometallic chemistry; Springer: Berlin ; New York, 1999.

(4) Moore, D. T.; Oomens, J.; Eyler, J. R.; Meijer, G.; Von Helden, G.; Ridge, D. P. Gas-Phase IR Spectroscopy of Anionic Iron Carbonyl Clusters. *J. Am. Chem. Soc.* **2004**, *126* (45), 14726–14727. https://doi.org/10.1021/ja0449527.

(5) Armentrout, P. B.; Baer, T. Gas-Phase Ion Dynamics and Chemistry. *J. Phys. Chem.* **1996**, *100* (31), 12866–12877. https://doi.org/10.1021/jp953329t.

(6) Ieritano, C.; Rickert, D.; Featherstone, J.; Honek, J. F.; Campbell, J. L.; Blanc, J. C. Y. L.; Schneider, B. B.; Hopkins, W. S. The Charge-State and Structural Stability of Peptides Conferred by Microsolvating Environments in Differential Mobility Spectrometry. *J. Am. Soc. Mass Spectrom.* **2021**, *32* (4), 956–968. https://doi.org/10.1021/jasms.0c00469.

(7) Mizoguchi, A.; Ohshima, Y.; Endo, Y. The Study for the Incipient Solvation Process of NaCl in Water: The Observation of the NaCl–(H2O) *n* (*n* = 1, 2, and 3) Complexes Using Fourier-Transform Microwave Spectroscopy. *J. Chem. Phys.* **2011**, *135* (6), 064307. https://doi.org/10.1063/1.3616047.

(8) Atkins, C. G.; Banu, L.; Rowsell, M.; Blagojevic, V.; Bohme, D. K.; Fridgen, T. D. Structure of $[Pb(Gly-H)]^+$ and the Monosolvated Water and Methanol Solvated Species by Infrared Multiple-Photon Dissociation Spectroscopy, Energy-Resolved Collision-Induced Dissociation, and Electronic Structure Calculations. *J. Phys. Chem. B* **2009**, *113* (43), 14457–14464. https://doi.org/10.1021/jp905654v.

(9) Okumura, M.; Yeh, L. I.; Lee, Y. T. Vibrational Predissociation Spectroscopy of Hydrogen Cluster Ions. In *Laser Spectroscopy VII*; Hänsch, T. W., Shen, Y. R., Eds.; Springer Berlin Heidelberg: Berlin, Heidelberg, 1985; pp 122–125.

(10) Okumura, M.; Yeh, L. I.; Myers, J. D.; Lee, Y. T. Infrared Spectra of the Cluster Ions H7O+3 · H2 and H9O+4 · H2. *J. Chem. Phys.* **1986**, *85* (4), 2328–2329. https://doi.org/10.1063/1.451079.

(11) Yeh, L. I.; Okumura, M.; Myers, J. D.; Price, J. M.; Lee, Y. T. Vibrational Spectroscopy of the Hydrated Hydronium Cluster Ions H3O+ · (H2O) *n* (*n* =1, 2, 3). *J. Chem. Phys.* **1989**, *91* (12), 7319–7330. https://doi.org/10.1063/1.457305.

(12) Petrov, A. K.; Chesnokov, E. N.; Gorelik, S. R.; Straub, K. D.; Szarmes, E. B.; Madey, J. M. J. Multiphoton Isotope-Selective Dissociation of Formic Acid Molecules under

Action of a Free Electron Laser. *J. Phys. Chem. A* **1997**, *101* (39), 7200–7207. https://doi.org/10.1021/jp971010y.

(13) Kuribayashi, S.; Tomimasu, T.; Kawanishi, S.; Arai, S. Infrared Multiple Photon Decomposition of CHBrF 2 Induced by a Free-Electron Laser. *Appl. Phys. B Lasers Opt.* **1997**, *65* (3), 393–398. https://doi.org/10.1007/s003400050286.

(14) Oomens, J.; Sartakov, B. G.; Meijer, G.; Von Helden, G. Gas-Phase Infrared Multiple Photon Dissociation Spectroscopy of Mass-Selected Molecular Ions. *Int. J. Mass Spectrom.* **2006**, *254* (1–2), 1–19. https://doi.org/10.1016/j.ijms.2006.05.009.

(15) Biemann, K.; Scoble, H. A. Characterization by Tandem Mass Spectrometry of Structural Modifications in Proteins. *Science* **1987**, *237* (4818), 992–998. https://doi.org/10.1126/science.3303336.

(16) Shukla, A. K.; Futrell, J. H. Tandem Mass Spectrometry: Dissociation of Ions by Collisional Activation. *J. Mass Spectrom.* **2000**, *35* (9), 1069–1090. https://doi.org/10.1002/1096-9888(200009)35:9<1069::AID-JMS54>3.0.CO;2-C.

(17) *Protein sequencing by tandem mass spectrometry.* https://doi.org/10.1073/pnas.83.17.6233.

(18) Crotti, S.; Menicatti, M.; Pallecchi, M.; Bartolucci, G. Tandem Mass Spectrometry Approaches for Recognition of Isomeric Compounds Mixtures. *Mass Spectrom. Rev.* **2023**, *42* (4), 1244–1260. https://doi.org/10.1002/mas.21757.

(19) Oomens, J.; Tielens, A. G. G. M.; Sartakov, B. G.; Von Helden, G.; Meijer, G. Laboratory Infrared Spectroscopy of Cationic Polycyclic Aromatic Hydrocarbon Molecules. *Astrophys. J.* **2003**, *591* (2), 968–985. https://doi.org/10.1086/375515.

(20) Depraz Depland, A.; Renois-Predelus, G.; Schindler, B.; Compagnon, I. Identification of Sialic Acid Linkage Isomers in Glycans Using Coupled InfraRed Multiple Photon Dissociation (IRMPD) Spectroscopy and Mass Spectrometry. *Int. J. Mass Spectrom.* **2018**, *434*, 65–69. https://doi.org/10.1016/j.ijms.2018.09.005.

(21) Becher, S.; Berden, G.; Martens, J.; Oomens, J.; Heiles, S. IRMPD Spectroscopy of [PC (4:0/4:0) + M]+ (M = H, Na, K) and Corresponding CID Fragment Ions. *J. Am. Soc. Mass Spectrom.* **2021**, *32* (12), 2874–2884. https://doi.org/10.1021/jasms.1c00277.

(22) Wu, Q.; Wang, J.-Y.; Han, D.-Q.; Yao, Z.-P. Recent Advances in Differentiation of Isomers by Ion Mobility Mass Spectrometry. *TrAC Trends Anal. Chem.* **2020**, *124*, 115801. https://doi.org/10.1016/j.trac.2019.115801.

(23) Bowman, A. P.; Abzalimov, R. R.; Shvartsburg, A. A. Broad Separation of Isomeric Lipids by High-Resolution Differential Ion Mobility Spectrometry with Tandem Mass Spectrometry. *J. Am. Soc. Mass Spectrom.* **2017**, *28* (8), 1552–1561. https://doi.org/10.1007/s13361-017-1675-2.

(24) Buck, R. C.; Franklin, J.; Berger, U.; Conder, J. M.; Cousins, I. T.; de Voogt, P.; Jensen, A. A.; Kannan, K.; Mabury, S. A.; van Leeuwen, S. P. Perfluoroalkyl and Polyfluoroalkyl Substances in the Environment: Terminology, Classification, and Origins. *Integr. Environ. Assess. Manag.* **2011**, *7* (4), 513–541. https://doi.org/10.1002/ieam.258.

(25) Peshoria, S.; Nandini, D.; Tanwar, R. K.; Narang, R. Short-Chain and Long-Chain Fluorosurfactants in Firefighting Foam: A Review. *Environ. Chem. Lett.* **2020**, *18* (4), 1277–1300. https://doi.org/10.1007/s10311-020-01015-8.
(26) Braun, J. M.; Chen, A.; Romano, M. E.; Calafat, A. M.; Webster, G. M.; Yolton, K.; Lanphear, B. P. Prenatal Perfluoroalkyl Substance Exposure and Child Adiposity at 8 Years of Age: The HOME Study. *Obesity* **2016**, *24* (1), 231–237. https://doi.org/10.1002/oby.21258.
(27) Timshina, A.; Aristizabal-Henao, J. J.; Da Silva, B. F.; Bowden, J. A. The Last Straw: Characterization of per- and Polyfluoroalkyl Substances in Commercially-Available Plant-Based Drinking Straws. *Chemosphere* **2021**, *277*, 130238. https://doi.org/10.1016/j.chemosphere.2021.130238.
(28) Gordon, S. C. Toxicological Evaluation of Ammonium 4,8-Dioxa-3H-Perfluorononanoate, a New Emulsifier to Replace Ammonium Perfluorooctanoate in Fluoropolymer Manufacturing. *Regul. Toxicol. Pharmacol.* **2011**, *59* (1), 64–80. https://doi.org/10.1016/j.yrtph.2010.09.008.
(29) Xiao, F. Emerging Poly- and Perfluoroalkyl Substances in the Aquatic Environment: A Review of Current Literature. *Water Res.* **2017**, *124*, 482–495. https://doi.org/10.1016/j.watres.2017.07.024.
(30) Foster, M.; Rainey, M.; Watson, C.; Dodds, J. N.; Kirkwood, K. I.; Fernández, F. M.; Baker, E. S. Uncovering PFAS and Other Xenobiotics in the Dark Metabolome Using Ion Mobility Spectrometry, Mass Defect Analysis, and Machine Learning. *Environ. Sci. Technol.* **2022**, *56* (12), 9133–9143. https://doi.org/10.1021/acs.est.2c00201.
(31) K. Longendyke, G.; Katel, S.; Wang, Y. PFAS Fate and Destruction Mechanisms during Thermal Treatment: A Comprehensive Review. *Environ. Sci. Process. Impacts* **2022**, *24* (2), 196–208. https://doi.org/10.1039/D1EM00465D.
(32) Mulabagal, V.; Liu, L.; Qi, J.; Wilson, C.; Hayworth, J. S. A Rapid UHPLC-MS/MS Method for Simultaneous Quantitation of 23 Perfluoroalkyl Substances (PFAS) in Estuarine Water. *Talanta* **2018**, *190*, 95–102. https://doi.org/10.1016/j.talanta.2018.07.053.
(33) Kealy, T. J.; Pauson, P. L. A New Type of Organo-Iron Compound. *Nature* **1951**, *168* (4285), 1039–1040. https://doi.org/10.1038/1681039b0.
(34) Harder, S.; Prosenc, M. H. The Simplest Metallocene Sandwich: The Lithocene Anion. *Angew. Chem. Int. Ed. Engl.* **1994**, *33* (17), 1744–1746. https://doi.org/10.1002/anie.199417441.
(35) Zhu, J. Open Questions on Aromaticity in Organometallics. *Commun. Chem.* **2020**, *3* (1), 1–3. https://doi.org/10.1038/s42004-020-00419-5.
(36) Jutzi, P.; Burford, N. Structurally Diverse π-Cyclopentadienyl Complexes of the Main Group Elements. *Chem. Rev.* **1999**, *99* (4), 969–990. https://doi.org/10.1021/cr941099t.
(37) Sunner, J.; Nishizawa, K.; Kebarle, P. Ion-Solvent Molecule Interactions in the Gas Phase. The Potassium Ion and Benzene. *J. Phys. Chem.* **1981**, *85* (13), 1814–1820. https://doi.org/10.1021/j150613a011.

(38) Featherstone, J.; Chong, T.; Martens, J. K.; Oomens, J.; McMahon, T. B. Inverse Sandwich Cyclopentadienyl Complexes of Sodium in the Gas Phase. *J. Phys. Chem. A* **2018**, *122* (43), 8659–8664. https://doi.org/10.1021/acs.jpca.8b09366.

(39) Udovic, T. J.; Matsuo, M.; Unemoto, A.; Verdal, N.; Stavila, V.; Skripov, A. V.; Rush, J. J.; Takamura, H.; Orimo, S. Sodium Superionic Conduction in $Na_2B_{12}H_{12}$. *Chem Commun* **2014**, *50* (28), 3750–3752. https://doi.org/10.1039/C3CC49805K.

(40) Jenne, C.; Keßler, M.; Warneke, J. Protic Anions [H(B12X12)]− (X=F, Cl, Br, I) That Act as Brønsted Acids in the Gas Phase. *Chem. – Eur. J.* **2015**, *21* (15), 5887–5891. https://doi.org/10.1002/chem.201500034.

(41) Warneke, J.; Hou, G.-L.; Aprà, E.; Jenne, C.; Yang, Z.; Qin, Z.; Kowalski, K.; Wang, X.-B.; Xantheas, S. S. Electronic Structure and Stability of $[B_{12}X_{12}]^{2-}$ (X = F–At): A Combined Photoelectron Spectroscopic and Theoretical Study. *J. Am. Chem. Soc.* **2017**, *139* (41), 14749–14756. https://doi.org/10.1021/jacs.7b08598.

(42) Strauss, S. H. The Search for Larger and More Weakly Coordinating Anions. *Chem. Rev.* **1993**, *93* (3), 927–942. https://doi.org/10.1021/cr00019a005.

(43) Lecours, M. J.; Marta, R. A.; Steinmetz, V.; Keddie, N.; Fillion, E.; O'Hagan, D.; McMahon, T. B.; Hopkins, W. S. Interaction of $B_{12}F_{12}^{2-}$ with All- *Cis* 1,2,3,4,5,6 Hexafluorocyclohexane in the Gas Phase. *J. Phys. Chem. Lett.* **2017**, *8* (1), 109–113. https://doi.org/10.1021/acs.jpclett.6b02629.

(44) Carr, P. J. J.; Warneke, J.; Featherstone, J.; Jenne, C.; Loire, E.; Hopkins, W. S. The Structure of Proton-Bound Triethylammonia (X = F, Cl) Clusters. *Mol. Phys.* **2019**, *117* (21), 2972–2979. https://doi.org/10.1080/00268976.2019.1595203.

(45) De Vlugt, I. J. S.; Lecours, M. J.; Carr, P. J. J.; Anwar, A.; Marta, R. A.; Fillion, E.; Steinmetz, V.; Hopkins, W. S. Infrared-Driven Charge-Transfer in Transition Metal-Containing $B_{12}X_{12}^{2-}$ (X = H, F) Clusters. *J. Phys. Chem. A* **2018**, *122* (35), 7051–7061. https://doi.org/10.1021/acs.jpca.8b05750.

(46) Bruins, A. P. Mechanistic Aspects of Electrospray Ionization. *J. Chromatogr. A* **1998**, *794* (1), 345–357. https://doi.org/10.1016/S0021-9673(97)01110-2.

(47) Awad, H.; Khamis, M. M.; El-Aneed, A. Mass Spectrometry, Review of the Basics: Ionization. *Appl. Spectrosc. Rev.* **2015**, *50* (2), 158–175. https://doi.org/10.1080/05704928.2014.954046.

(48) Konermann, L.; Ahadi, E.; Rodriguez, A. D.; Vahidi, S. Unraveling the Mechanism of Electrospray Ionization. *Anal. Chem.* **2013**, *85* (1), 2–9. https://doi.org/10.1021/ac302789c.

(49) Cech, N. B.; Enke, C. G. Practical Implications of Some Recent Studies in Electrospray Ionization Fundamentals. *Mass Spectrom. Rev.* **2001**, *20* (6), 362–387. https://doi.org/10.1002/mas.10008.

(50) Wu, Z.; Gao, W.; Phelps, M. A.; Wu, D.; Miller, D. D.; Dalton, J. T. Favorable Effects of Weak Acids on Negative-Ion Electrospray Ionization Mass Spectrometry. *Anal. Chem.* **2004**, *76* (3), 839–847. https://doi.org/10.1021/ac0351670.

(51) Prabhu, G. R. D.; Williams, E. R.; Wilm, M.; Urban, P. L. Mass Spectrometry Using Electrospray Ionization. *Nat. Rev. Methods Primer* **2023**, *3* (1), 1–22. https://doi.org/10.1038/s43586-023-00203-4.

(52) Awad, H.; Khamis, M. M.; El-Aneed, A. Mass Spectrometry, Review of the Basics: Ionization. *Appl. Spectrosc. Rev.* **2015**, *50* (2), 158–175. https://doi.org/10.1080/05704928.2014.954046.
(53) Kebarle, P.; Verkerk, U. H. Electrospray: From Ions in Solution to Ions in the Gas Phase, What We Know Now. *Mass Spectrom. Rev.* **2009**, *28* (6), 898–917. https://doi.org/10.1002/mas.20247.
(54) Ho, C.; Lam, C.; Chan, M.; Cheung, R.; Law, L.; Lit, L.; Ng, K.; Suen, M.; Tai, H. Electrospray Ionisation Mass Spectrometry: Principles and Clinical Applications. **2003**, *24*.
(55) Wilm, M. Principles of Electrospray Ionization. *Mol. Cell. Proteomics* **2011**, *10* (7), M111.009407. https://doi.org/10.1074/mcp.M111.009407.
(56) Iavarone, A. T.; Williams, E. R. Mechanism of Charging and Supercharging Molecules in Electrospray Ionization. *J. Am. Chem. Soc.* **2003**, *125* (8), 2319–2327. https://doi.org/10.1021/ja021202t.
(57) Iribarne, J. V.; Thomson, B. A. On the Evaporation of Small Ions from Charged Droplets. *J. Chem. Phys.* **1976**, *64* (6), 2287–2294. https://doi.org/10.1063/1.432536.
(58) Fenn, J. B.; Mann, M.; Meng, C. K.; Wong, S. F.; Whitehouse, C. M. Electrospray Ionization–Principles and Practice. *Mass Spectrom. Rev.* **1990**, *9* (1), 37–70. https://doi.org/10.1002/mas.1280090103.
(59) Gross, J. H. Tandem Mass Spectrometry. In *Mass Spectrometry: A Textbook*; Gross, J. H., Ed.; Springer International Publishing: Cham, 2017; pp 539–612. https://doi.org/10.1007/978-3-319-54398-7_9.
(60) Macias, L. A.; Santos, I. C.; Brodbelt, J. S. Ion Activation Methods for Peptides and Proteins. *Anal. Chem.* **2020**, *92* (1), 227–251. https://doi.org/10.1021/acs.analchem.9b04859.
(61) Bayat, P.; Lesage, D.; Cole, R. B. Tutorial: Ion Activation in Tandem Mass Spectrometry Using Ultra-High Resolution Instrumentation. *Mass Spectrom. Rev.* **2020**, *39* (5–6), 680–702. https://doi.org/10.1002/mas.21623.
(62) Bayat, P.; Lesage, D.; Cole, R. B. Low-Energy Collision-Induced Dissociation (Low-Energy CID), Collision-Induced Dissociation (CID), and Higher Energy Collision Dissociation (HCD) Mass Spectrometry for Structural Elucidation of Saccharides and Clarification of Their Dissolution Mechanism in DMAc/LiCl. *J. Mass Spectrom.* **2018**, *53* (8), 705–716. https://doi.org/10.1002/jms.4205.
(63) Sleno, L.; Volmer, D. A. Ion Activation Methods for Tandem Mass Spectrometry. *J. Mass Spectrom.* **2004**, *39* (10), 1091–1112. https://doi.org/10.1002/jms.703.
(64) Schwartz, R. N.; Slawsky, Z. I.; Herzfeld, K. F. Calculation of Vibrational Relaxation Times in Gases. *J. Chem. Phys.* **1952**, *20* (10), 1591–1599. https://doi.org/10.1063/1.1700221.
(65) Hoffmann, E. de; Stroobant, V. *Mass Spectrometry: Principles and Applications*, 3rd ed.; J. Wiley: Chichester, West Sussex, England ; Hoboken, NJ, 2007.
(66) Bakker, J. M.; Aleese, L. M.; Meijer, G.; Von Helden, G. Fingerprint IR Spectroscopy to Probe Amino Acid Conformations in the Gas Phase. *Phys. Rev. Lett.* **2003**, *91* (20), 203003. https://doi.org/10.1103/PhysRevLett.91.203003.

(67) Aleese, L. M.; Simon, A.; McMahon, T. B.; Ortega, J.-M.; Scuderi, D.; Lemaire, J.; Maître, P. Mid-IR Spectroscopy of Protonated Leucine Methyl Ester Performed with an FTICR or a Paul Type Ion-Trap. *Int. J. Mass Spectrom.* **2006**, *249–250*, 14–20. https://doi.org/10.1016/j.ijms.2006.01.008.
(68) Houthuijs, K. J.; Van Tetering, L.; Schuurman, J. L.; Wootton, C. A.; Gebhardt, C. R.; Ridgeway, M. E.; Berden, G.; Martens, J.; Oomens, J. A Trapped Ion Mobility Enabled Fourier Transform Ion Cyclotron Resonance Mass Spectrometer for Infrared Ion Spectroscopy at FELIX. *Int. J. Mass Spectrom.* **2024**, *505*, 117323. https://doi.org/10.1016/j.ijms.2024.117323.
(69) Polfer, N. C.; Oomens, J.; Dunbar, R. C. IRMPD Spectroscopy of Metal-Ion/Tryptophan Complexes. *Phys. Chem. Chem. Phys.* **2006**, *8* (23), 2744. https://doi.org/10.1039/b603665a.
(70) Scott Hopkins, W.; Marta, R. A.; Steinmetz, V.; McMahon, T. B. Mode-Specific Fragmentation of Amino Acid-Containing Clusters. *Phys. Chem. Chem. Phys.* **2015**, *17* (43), 28548–28555. https://doi.org/10.1039/C5CP03517A.
(71) Carlo, M. J.; Patrick, A. L. Infrared Multiple Photon Dissociation (IRMPD) Spectroscopy and Its Potential for the Clinical Laboratory. *J. Mass Spectrom. Adv. Clin. Lab* **2022**, *23*, 14–25. https://doi.org/10.1016/j.jmsacl.2021.12.004.
(72) Stevenson, B. C.; Berden, G.; Martens, J.; Oomens, J.; Armentrout, P. B. Determining Gas-Phase Chelation of Zinc, Cadmium, and Copper Cations with HisHis Dipeptide Using Action Spectroscopy and Theoretical Calculations. *Int. J. Mass Spectrom.* **2024**, *495*, 117154. https://doi.org/10.1016/j.ijms.2023.117154.
(73) Ternov, I. M. Synchrotron Radiation. *Phys.-Uspekhi* **1995**, *38* (4), 409–434. https://doi.org/10.1070/PU1995v038n04ABEH000082.
(74) *Synchrotron Radiation: Basics, Methods and Applications*; Mobilio, S., Boscherini, F., Meneghini, C., Eds.; Springer Berlin Heidelberg: Berlin, Heidelberg, 2015. https://doi.org/10.1007/978-3-642-55315-8.
(75) Deacon, D. A. G.; Elias, L. R.; Madey, J. M. J.; Ramian, G. J.; Schwettman, H. A.; Smith, T. I. First Operation of a Free-Electron Laser. *Phys. Rev. Lett.* **1977**, *38* (16), 892–894. https://doi.org/10.1103/PhysRevLett.38.892.
(76) Freund, H. P.; Antonsen, T. M. *Principles of Free Electron Lasers*; Springer International Publishing: Cham, 2024. https://doi.org/10.1007/978-3-031-40945-5.
(77) Sprangle, P.; Smith, R. A. Theory of Free-Electron Lasers. *Phys. Rev. A* **1980**, *21* (1), 293–301. https://doi.org/10.1103/PhysRevA.21.293.
(78) Martens, J.; Berden, G.; Gebhardt, C. R.; Oomens, J. Infrared Ion Spectroscopy in a Modified Quadrupole Ion Trap Mass Spectrometer at the FELIX Free Electron Laser Laboratory. *Rev. Sci. Instrum.* **2016**, *87* (10), 103108. https://doi.org/10.1063/1.4964703.
(79) Lehmann, K. K.; Scoles, G.; Pate, B. H. Intramolecular Dynamics from Eigenstate-Resolved Infrared Spectra. *Annual Review of Physical Chemistry*, 1994, *45*, 241–274. https://doi.org/10.1146/annurev.pc.45.100194.001325.
(80) Hopkins, W. S. Determining the Properties of Gas-Phase Clusters. *Mol. Phys.* **2015**, *113* (21), 3151–3158. https://doi.org/10.1080/00268976.2015.1053545.

(81) Dodds, J. N.; Baker, E. S. Ion Mobility Spectrometry: Fundamental Concepts, Instrumentation, Applications, and the Road Ahead. *J. Am. Soc. Mass Spectrom.* **2019**, *30* (11), 2185–2195. https://doi.org/10.1007/s13361-019-02288-2.

(82) Smith, D. P.; Knapman, T. W.; Campuzano, I.; Malham, R. W.; Berryman, J. T.; Radford, S. E.; Ashcroft, A. E. Deciphering Drift Time Measurements from Travelling Wave Ion Mobility Spectrometry-Mass Spectrometry Studies. *Eur. J. Mass Spectrom.* **2009**, *15* (2), 113–130. https://doi.org/10.1255/ejms.947.

(83) Gabelica, V.; Marklund, E. Fundamentals of Ion Mobility Spectrometry. *Curr. Opin. Chem. Biol.* **2018**, *42*, 51–59. https://doi.org/10.1016/j.cbpa.2017.10.022.

(84) Giles, K.; Pringle, S. D.; Worthington, K. R.; Little, D.; Wildgoose, J. L.; Bateman, R. H. Applications of a Travelling Wave-Based Radio-Frequency-Only Stacked Ring Ion Guide. *Rapid Commun. Mass Spectrom.* **2004**, *18* (20), 2401–2414. https://doi.org/10.1002/rcm.1641.

(85) Richardson, K.; Langridge, D.; Giles, K. Fundamentals of Travelling Wave Ion Mobility Revisited: I. Smoothly Moving Waves. *Int. J. Mass Spectrom.* **2018**, *428*, 71–80. https://doi.org/10.1016/j.ijms.2018.03.007.

(86) Pringle, S. D.; Giles, K.; Wildgoose, J. L.; Williams, J. P.; Slade, S. E.; Thalassinos, K.; Bateman, R. H.; Bowers, M. T.; Scrivens, J. H. An Investigation of the Mobility Separation of Some Peptide and Protein Ions Using a New Hybrid Quadrupole/Travelling Wave IMS/Oa-ToF Instrument. *Int. J. Mass Spectrom.* **2007**, *261* (1), 1–12. https://doi.org/10.1016/j.ijms.2006.07.021.

(87) Shvartsburg, A. A.; Smith, R. D. Fundamentals of Traveling Wave Ion Mobility Spectrometry. *Anal. Chem.* **2008**, *80* (24), 9689–9699. https://doi.org/10.1021/ac8016295.

(88) Hinnenkamp, V.; Klein, J.; Meckelmann, S. W.; Balsaa, P.; Schmidt, T. C.; Schmitz, O. J. Comparison of CCS Values Determined by Traveling Wave Ion Mobility Mass Spectrometry and Drift Tube Ion Mobility Mass Spectrometry. *Anal. Chem.* **2018**, *90* (20), 12042–12050. https://doi.org/10.1021/acs.analchem.8b02711.

(89) Ruotolo, B. T.; Benesch, J. L. P.; Sandercock, A. M.; Hyung, S.-J.; Robinson, C. V. Ion Mobility–Mass Spectrometry Analysis of Large Protein Complexes. *Nat. Protoc.* **2008**, *3* (7), 1139–1152. https://doi.org/10.1038/nprot.2008.78.

(90) Gabelica, V.; Shvartsburg, A. A.; Afonso, C.; Barran, P.; Benesch, J. L. P.; Bleiholder, C.; Bowers, M. T.; Bilbao, A.; Bush, M. F.; Campbell, J. L.; Campuzano, I. D. G.; Causon, T.; Clowers, B. H.; Creaser, C. S.; De Pauw, E.; Far, J.; Fernandez-Lima, F.; Fjeldsted, J. C.; Giles, K.; Groessl, M.; Hogan Jr, C. J.; Hann, S.; Kim, H. I.; Kurulugama, R. T.; May, J. C.; McLean, J. A.; Pagel, K.; Richardson, K.; Ridgeway, M. E.; Rosu, F.; Sobott, F.; Thalassinos, K.; Valentine, S. J.; Wyttenbach, T. Recommendations for Reporting Ion Mobility Mass Spectrometry Measurements. *Mass Spectrom. Rev.* **2019**, *38* (3), 291–320. https://doi.org/10.1002/mas.21585.

(91) Jin, W.; Jarvis, M.; Star-Weinstock, M.; Altemus, M. A Sensitive and Selective LC-Differential Mobility-Mass Spectrometric Analysis of Allopregnanolone and Pregnanolone in Human Plasma. *Anal. Bioanal. Chem.* **2013**, *405* (29), 9497–9508. https://doi.org/10.1007/s00216-013-7391-2.

(92) Shvartsburg, A. A.; Creese, A. J.; Smith, R. D.; Cooper, H. J. Separation of Peptide Isomers with Variant Modified Sites by High-Resolution Differential Ion Mobility Spectrometry. *Anal. Chem.* **2010**, *82* (19), 8327–8334. https://doi.org/10.1021/ac101878a.
(93) Šala, M.; Lísa, M.; Campbell, J. L.; Holčapek, M. Determination of Triacylglycerol Regioisomers Using Differential Mobility Spectrometry. *Rapid Commun. Mass Spectrom.* **2016**, *30* (2), 256–264. https://doi.org/10.1002/rcm.7430.
(94) Anwar, A.; Psutka, J.; Walker, S. W. C.; Dieckmann, T.; Janizewski, J. S.; Larry Campbell, J.; Scott Hopkins, W. Separating and Probing Tautomers of Protonated Nucleobases Using Differential Mobility Spectrometry. *Int. J. Mass Spectrom.* **2018**, *429*, 174–181. https://doi.org/10.1016/j.ijms.2017.08.008.
(95) Liu, C.; Gómez-Ríos, G. A.; Schneider, B. B.; Le Blanc, J. C. Y.; Reyes-Garcés, N.; Arnold, D. W.; Covey, T. R.; Pawliszyn, J. Fast Quantitation of Opioid Isomers in Human Plasma by Differential Mobility Spectrometry/Mass Spectrometry via SPME/Open-Port Probe Sampling Interface. *Anal. Chim. Acta* **2017**, *991*, 89–94. https://doi.org/10.1016/j.aca.2017.08.023.
(96) Guevremont, R. High-Field Asymmetric Waveform Ion Mobility Spectrometry: A New Tool for Mass Spectrometry. *J. Chromatogr. A* **2004**, *1058* (1–2), 3–19. https://doi.org/10.1016/S0021-9673(04)01478-5.
(97) Schneider, B. B.; Nazarov, E. G.; Londry, F.; Vouros, P.; Covey, T. R. Differential Mobility Spectrometry/Mass Spectrometry History, Theory, Design Optimization, Simulations, and Applications. *Mass Spectrom. Rev.* **2016**, *35* (6), 687–737. https://doi.org/10.1002/mas.21453.
(98) Mashmoushi, N.; Larry Campbell, J.; Di Lorenzo, R.; Scott Hopkins, W. Rapid Separation of Cannabinoid Isomer Sets Using Differential Mobility Spectrometry and Mass Spectrometry. *The Analyst* **2022**, *147* (10), 2198–2206. https://doi.org/10.1039/D1AN02327F.
(99) Ruskic, D.; Hopfgartner, G. Modifier Selectivity Effect on Differential Ion Mobility Resolution of Isomeric Drugs and Multidimensional Liquid Chromatography Ion Mobility Analysis. *Anal. Chem.* **2019**, *91* (18), 11670–11677. https://doi.org/10.1021/acs.analchem.9b02212.
(100) Campbell, J. L.; Zhu, M.; Hopkins, W. S. Ion-Molecule Clustering in Differential Mobility Spectrometry: Lessons Learned from Tetraalkylammonium Cations and Their Isomers. *J. Am. Soc. Mass Spectrom.* **2014**, *25* (9), 1583–1591. https://doi.org/10.1007/s13361-014-0939-3.
(101) Hopkins, W. S. Dynamic Clustering and Ion Microsolvation. In *Comprehensive Analytical Chemistry*; Elsevier, 2019; Vol. 83, pp 83–122.
(102) Ieritano, C.; Hopkins, W. S. The Hitchhiker's Guide to Dynamic Ion–Solvent Clustering: Applications in Differential Ion Mobility Spectrometry. *Phys. Chem. Chem. Phys.* **2022**, *24* (35), 20594–20615. https://doi.org/10.1039/D2CP02540J.
(103) Price, W. D.; Jockusch, R. A.; Williams, E. R. Is Arginine a Zwitterion in the Gas Phase? *J. Am. Chem. Soc.* **1997**, *119* (49), 11988–11989. https://doi.org/10.1021/ja9711627.

(104) Wyttenbach, T.; von Helden, G.; Bowers, M. T. Gas-Phase Conformation of Biological Molecules: Bradykinin. *J. Am. Chem. Soc.* **1996**, *118* (35), 8355–8364. https://doi.org/10.1021/ja9535928.
(105) Pracht, P.; Grimme, S.; Bannwarth, C.; Bohle, F.; Ehlert, S.; Feldmann, G.; Gorges, J.; Müller, M.; Neudecker, T.; Plett, C.; Spicher, S.; Steinbach, P.; Wesołowski, P. A.; Zeller, F. CREST—A Program for the Exploration of Low-Energy Molecular Chemical Space. *J. Chem. Phys.* **2024**, *160* (11), 114110. https://doi.org/10.1063/5.0197592.
(106) Neese, F.; Wennmohs, F.; Becker, U.; Riplinger, C. The ORCA Quantum Chemistry Program Package. *J. Chem. Phys.* **2020**, *152* (22), 224108. https://doi.org/10.1063/5.0004608.
(107) Frisch, M. J.; Trucks, G. W.; Schlegel, H. B.; Scuseria, G. E.; Robb, M. A.; Cheeseman, J. R.; Scalmani, G.; Barone, V.; Petersson, G. A.; Nakatsuji, H.; Li, X.; Caricato, M.; Marenich, A. V.; Bloino, J.; Janesko, B. G.; Gomperts, R.; Mennucci, B.; Hratchian, H. P.; Ortiz, J. V.; Izmaylov, A. F.; Sonnenberg, J. L.; Williams; Ding, F.; Lipparini, F.; Egidi, F.; Goings, J.; Peng, B.; Petrone, A.; Henderson, T.; Ranasinghe, D.; Zakrzewski, V. G.; Gao, J.; Rega, N.; Zheng, G.; Liang, W.; Hada, M.; Ehara, M.; Toyota, K.; Fukuda, R.; Hasegawa, J.; Ishida, M.; Nakajima, T.; Honda, Y.; Kitao, O.; Nakai, H.; Vreven, T.; Throssell, K.; Montgomery Jr., J. A.; Peralta, J. E.; Ogliaro, F.; Bearpark, M. J.; Heyd, J. J.; Brothers, E. N.; Kudin, K. N.; Staroverov, V. N.; Keith, T. A.; Kobayashi, R.; Normand, J.; Raghavachari, K.; Rendell, A. P.; Burant, J. C.; Iyengar, S. S.; Tomasi, J.; Cossi, M.; Millam, J. M.; Klene, M.; Adamo, C.; Cammi, R.; Ochterski, J. W.; Martin, R. L.; Morokuma, K.; Farkas, O.; Foresman, J. B.; Fox, D. J. Gaussian 16 Rev. C.01, 2016.
(108) Liakos, D. G.; Sparta, M.; Kesharwani, M. K.; Martin, J. M. L.; Neese, F. Exploring the Accuracy Limits of Local Pair Natural Orbital Coupled-Cluster Theory. *J. Chem. Theory Comput.* **2015**, *11* (4), 1525–1539. https://doi.org/10.1021/ct501129s.
(109) Liakos, D. G.; Guo, Y.; Neese, F. Comprehensive Benchmark Results for the Domain Based Local Pair Natural Orbital Coupled Cluster Method (DLPNO-CCSD(T)) for Closed- and Open-Shell Systems. *J. Phys. Chem. A* **2020**, *124* (1), 90–100. https://doi.org/10.1021/acs.jpca.9b05734.
(110) Pracht, P.; Bohle, F.; Grimme, S. Automated Exploration of the Low-Energy Chemical Space with Fast Quantum Chemical Methods. *Phys. Chem. Chem. Phys.* **2020**, *22* (14), 7169–7192. https://doi.org/10.1039/C9CP06869D.
(111) Grimme, S. Exploration of Chemical Compound, Conformer, and Reaction Space with Meta-Dynamics Simulations Based on Tight-Binding Quantum Chemical Calculations. *J. Chem. Theory Comput.* **2019**, *15* (5), 2847–2862. https://doi.org/10.1021/acs.jctc.9b00143.
(112) Bannwarth, C.; Caldeweyher, E.; Ehlert, S.; Hansen, A.; Pracht, P.; Seibert, J.; Spicher, S.; Grimme, S. Extended Tight-Binding Quantum Chemistry Methods. *WIREs Comput. Mol. Sci.* **2021**, *11* (2), e1493. https://doi.org/10.1002/wcms.1493.
(113) Mardirossian, N.; Head-Gordon, M. Thirty Years of Density Functional Theory in Computational Chemistry: An Overview and Extensive Assessment of 200 Density

Functionals. *Mol. Phys.* **2017**, *115* (19), 2315–2372. https://doi.org/10.1080/00268976.2017.1333644.
(114) Kohn, W.; Sham, L. J. Self-Consistent Equations Including Exchange and Correlation Effects. *Phys. Rev.* **1965**, *140* (4A), A1133–A1138. https://doi.org/10.1103/PhysRev.140.A1133.
(115) Walker, M.; Harvey, A. J. A.; Sen, A.; Dessent, C. E. H. Performance of M06, M06-2X, and M06-HF Density Functionals for Conformationally Flexible Anionic Clusters: M06 Functionals Perform Better than B3LYP for a Model System with Dispersion and Ionic Hydrogen-Bonding Interactions. *J. Phys. Chem. A* **2013**, *117* (47), 12590–12600. https://doi.org/10.1021/jp408166m.
(116) M. Kreienborg, N.; Merten, C. How to Treat C–F Stretching Vibrations? A Vibrational CD Study on Chiral Fluorinated Molecules. *Phys. Chem. Chem. Phys.* **2019**, *21* (7), 3506–3511. https://doi.org/10.1039/C8CP02395F.
(117) Chai, J.-D.; Head-Gordon, M. Long-Range Corrected Hybrid Density Functionals with Damped Atom–Atom Dispersion Corrections. *Phys. Chem. Chem. Phys.* **2008**, *10* (44), 6615. https://doi.org/10.1039/b810189b.
(118) Lin, Y.-S.; Li, G.-D.; Mao, S.-P.; Chai, J.-D. Long-Range Corrected Hybrid Density Functionals with Improved Dispersion Corrections. *J. Chem. Theory Comput.* **2013**, *9* (1), 263–272. https://doi.org/10.1021/ct300715s.
(119) Grimme, S.; Ehrlich, S.; Goerigk, L. Effect of the Damping Function in Dispersion Corrected Density Functional Theory. *J. Comput. Chem.* **2011**, *32* (7), 1456–1465. https://doi.org/10.1002/jcc.21759.
(120) Najibi, A.; Goerigk, L. The Nonlocal Kernel in van Der Waals Density Functionals as an Additive Correction: An Extensive Analysis with Special Emphasis on the B97M-V and ωB97M-V Approaches. *J. Chem. Theory Comput.* **2018**, *14* (11), 5725–5738. https://doi.org/10.1021/acs.jctc.8b00842.
(121) Schuchardt, K. L.; Didier, B. T.; Elsethagen, T.; Sun, L.; Gurumoorthi, V.; Chase, J.; Li, J.; Windus, T. L. Basis Set Exchange: A Community Database for Computational Sciences. *J. Chem. Inf. Model.* **2007**, *47* (3), 1045–1052. https://doi.org/10.1021/ci600510j.
(122) Rappoport, D.; Furche, F. Property-Optimized Gaussian Basis Sets for Molecular Response Calculations. *J. Chem. Phys.* **2010**, *133* (13), 134105. https://doi.org/10.1063/1.3484283.
(123) Hellweg, A.; Rappoport, D. Development of New Auxiliary Basis Functions of the Karlsruhe Segmented Contracted Basis Sets Including Diffuse Basis Functions (Def2-SVPD, Def2-TZVPPD, and Def2-QVPPD) for RI-MP2 and RI-CC Calculations. *Phys. Chem. Chem. Phys.* **2015**, *17* (2), 1010–1017. https://doi.org/10.1039/C4CP04286G.
(124) Jensen, F. Atomic Orbital Basis Sets. *WIREs Comput. Mol. Sci.* **2013**, *3* (3), 273–295. https://doi.org/10.1002/wcms.1123.
(125) Henkelman, G.; Uberuaga, B. P.; Jónsson, H. A Climbing Image Nudged Elastic Band Method for Finding Saddle Points and Minimum Energy Paths. *J. Chem. Phys.* **2000**, *113* (22), 9901–9904. https://doi.org/10.1063/1.1329672.

(126) Ásgeirsson, V.; Birgisson, B. O.; Bjornsson, R.; Becker, U.; Neese, F.; Riplinger, C.; Jónsson, H. Nudged Elastic Band Method for Molecular Reactions Using Energy-Weighted Springs Combined with Eigenvector Following. *J. Chem. Theory Comput.* **2021**, *17* (8), 4929–4945. https://doi.org/10.1021/acs.jctc.1c00462.
(127) Blake, B. E.; Fenton, S. E. Early Life Exposure to Per- and Polyfluoroalkyl Substances (PFAS) and Latent Health Outcomes: A Review Including the Placenta as a Target Tissue and Possible Driver of Peri- and Postnatal Effects. *Toxicology* **2020**, *443*, 152565. https://doi.org/10.1016/j.tox.2020.152565.
(128) Bell, E. M.; De Guise, S.; McCutcheon, J. R.; Lei, Y.; Levin, M.; Li, B.; Rusling, J. F.; Lawrence, D. A.; Cavallari, J. M.; O'Connell, C.; Javidi, B.; Wang, X.; Ryu, H. Exposure, Health Effects, Sensing, and Remediation of the Emerging PFAS Contaminants – Scientific Challenges and Potential Research Directions. *Sci. Total Environ.* **2021**, *780*, 146399. https://doi.org/10.1016/j.scitotenv.2021.146399.
(129) Gordon, S. C. Toxicological Evaluation of Ammonium 4,8-Dioxa-3H-Perfluorononanoate, a New Emulsifier to Replace Ammonium Perfluorooctanoate in Fluoropolymer Manufacturing. *Regul. Toxicol. Pharmacol.* **2011**, *59* (1), 64–80. https://doi.org/10.1016/j.yrtph.2010.09.008.
(130) Xiao, F. Emerging Poly- and Perfluoroalkyl Substances in the Aquatic Environment: A Review of Current Literature. *Water Res.* **2017**, *124*, 482–495. https://doi.org/10.1016/j.watres.2017.07.024.
(131) Williams, A. J.; Grulke, C. M.; Edwards, J.; McEachran, A. D.; Mansouri, K.; Baker, N. C.; Patlewicz, G.; Shah, I.; Wambaugh, J. F.; Judson, R. S.; Richard, A. M. The CompTox Chemistry Dashboard: A Community Data Resource for Environmental Chemistry. *J. Cheminformatics* **2017**, *9* (1), 61. https://doi.org/10.1186/s13321-017-0247-6.
(132) Foster, M.; Rainey, M.; Watson, C.; Dodds, J. N.; Kirkwood, K. I.; Fernández, F. M.; Baker, E. S. Uncovering PFAS and Other Xenobiotics in the Dark Metabolome Using Ion Mobility Spectrometry, Mass Defect Analysis, and Machine Learning. *Environ. Sci. Technol.* **2022**, *56* (12), 9133–9143. https://doi.org/10.1021/acs.est.2c00201.
(133) Luo, Y.-S.; Aly, N. A.; McCord, J.; Strynar, M. J.; Chiu, W. A.; Dodds, J. N.; Baker, E. S.; Rusyn, I. Rapid Characterization of Emerging Per- and Polyfluoroalkyl Substances in Aqueous Film-Forming Foams Using Ion Mobility Spectrometry–Mass Spectrometry. *Environ. Sci. Technol.* **2020**, *54* (23), 15024–15034. https://doi.org/10.1021/acs.est.0c04798.
(134) Koelmel, J. P.; Stelben, P.; McDonough, C. A.; Dukes, D. A.; Aristizabal-Henao, J. J.; Nason, S. L.; Li, Y.; Sternberg, S.; Lin, E.; Beckmann, M.; Williams, A. J.; Draper, J.; Finch, J. P.; Munk, J. K.; Deigl, C.; Rennie, E. E.; Bowden, J. A.; Godri Pollitt, K. J. FluoroMatch 2.0—Making Automated and Comprehensive Non-Targeted PFAS Annotation a Reality. *Anal. Bioanal. Chem.* **2022**, *414* (3), 1201–1215. https://doi.org/10.1007/s00216-021-03392-7.
(135) Munoz, G.; Michaud, A. M.; Liu, M.; Vo Duy, S.; Montenach, D.; Resseguier, C.; Watteau, F.; Sappin-Didier, V.; Feder, F.; Morvan, T.; Houot, S.; Desrosiers, M.; Liu, J.; Sauvé, S. Target and Nontarget Screening of PFAS in Biosolids, Composts, and

Other Organic Waste Products for Land Application in France. *Environ. Sci. Technol.* **2022**, *56* (10), 6056–6068. https://doi.org/10.1021/acs.est.1c03697.
(136) K. Longendyke, G.; Katel, S.; Wang, Y. PFAS Fate and Destruction Mechanisms during Thermal Treatment: A Comprehensive Review. *Environ. Sci. Process. Impacts* **2022**, *24* (2), 196–208. https://doi.org/10.1039/D1EM00465D.
(137) Esfahani, E. B.; Zeidabadi, F. A.; Zhang, S.; Mohseni, M. Photo-Chemical/Catalytic Oxidative/Reductive Decomposition of per- and Poly-Fluoroalkyl Substances (PFAS), Decomposition Mechanisms and Effects of Key Factors: A Review. *Environ. Sci. Water Res. Technol.* **2022**, *8* (4), 698–728. https://doi.org/10.1039/D1EW00774B.
(138) Mulabagal, V.; Liu, L.; Qi, J.; Wilson, C.; Hayworth, J. S. A Rapid UHPLC-MS/MS Method for Simultaneous Quantitation of 23 Perfluoroalkyl Substances (PFAS) in Estuarine Water. *Talanta* **2018**, *190*, 95–102. https://doi.org/10.1016/j.talanta.2018.07.053.
(139) Zweigle, J.; Bugsel, B.; Zwiener, C. FindPFΔS: Non-Target Screening for PFAS─Comprehensive Data Mining for MS2 Fragment Mass Differences. *Anal. Chem.* **2022**, *94* (30), 10788–10796. https://doi.org/10.1021/acs.analchem.2c01521.
(140) Martens, J.; Berden, G.; Gebhardt, C. R.; Oomens, J. Infrared Ion Spectroscopy in a Modified Quadrupole Ion Trap Mass Spectrometer at the FELIX Free Electron Laser Laboratory. *Rev. Sci. Instrum.* **2016**, *87* (10), 103108. https://doi.org/10.1063/1.4964703.
(141) Thomas, D. A.; Mucha, E.; Gewinner, S.; Schöllkopf, W.; Meijer, G.; von Helden, G. Vibrational Spectroscopy of Fluoroformate, FCO_2^-, Trapped in Helium Nanodroplets. *J. Phys. Chem. Lett.* **2018**, *9* (9), 2305–2310. https://doi.org/10.1021/acs.jpclett.8b00664.
(142) McMahon, T. B.; Northcott, C. J. The Fluoroformate Ion, FCO_2^-. An Ion Cyclotron Resonance Study of the Gas Phase Lewis Acidity of Carbon Dioxide and Related Isoelectronic Species. *Can. J. Chem.* **1978**, *56* (8), 1069–1074. https://doi.org/10.1139/v78-181.
(143) Larson, J. W.; McMahon, T. B. Fluoride and Chloride Affinities of Main Group Oxides, Fluorides, Oxofluorides, and Alkyls. Quantitative Scales of Lewis Acidities from Ion Cyclotron Resonance Halide-Exchange Equilibria. *J. Am. Chem. Soc.* **1985**, *107* (4), 766–773. https://doi.org/10.1021/ja00290a005.
(144) Roy, M.; McMahon, T. B. The Anomalous Gas Phase Acidity of Ethyl Fluoride. An *Ab Initio* Investigation of the Importance of Hydrogen Bonding between F^- and Sp^2 and *Sp* C—H Bonds. *Can. J. Chem.* **1985**, *63* (3), 708–715. https://doi.org/10.1139/v85-117.
(145) Neese, F.; Wennmohs, F.; Becker, U.; Riplinger, C. The ORCA Quantum Chemistry Program Package. *J. Chem. Phys.* **2020**, *152* (22), 224108. https://doi.org/10.1063/5.0004608.
(146) Weigend, F.; Ahlrichs, R. Balanced Basis Sets of Split Valence, Triple Zeta Valence and Quadruple Zeta Valence Quality for H to Rn: Design and Assessment of Accuracy. *Phys. Chem. Chem. Phys.* **2005**, *7* (18), 3297. https://doi.org/10.1039/b508541a.

(147) Zhao, Y.; Truhlar, D. G. The M06 Suite of Density Functionals for Main Group Thermochemistry, Thermochemical Kinetics, Noncovalent Interactions, Excited States, and Transition Elements: Two New Functionals and Systematic Testing of Four M06-Class Functionals and 12 Other Functionals. *Theor. Chem. Acc.* **2008**, *120* (1), 215–241. https://doi.org/10.1007/s00214-007-0310-x.
(148) M. Kreienborg, N.; Merten, C. How to Treat C–F Stretching Vibrations? A Vibrational CD Study on Chiral Fluorinated Molecules. *Phys. Chem. Chem. Phys.* **2019**, *21* (7), 3506–3511. https://doi.org/10.1039/C8CP02395F.
(149) Sert, Y.; Miroslaw, B.; Çırak, Ç.; Doğan, H.; Szulczyk, D.; Struga, M. Vibrational Spectroscopy (FT-IR and Laser-Raman) Investigation, and Computational (M06-2X and B3LYP) Analysis on the Structure of 4-(3-Fluorophenyl)-1-(Propan-2-Ylidene)-Thiosemicarbazone. *Spectrochim. Acta. A. Mol. Biomol. Spectrosc.* **2014**, *128*, 91–99. https://doi.org/10.1016/j.saa.2014.02.134.
(150) Riplinger, C.; Neese, F. An Efficient and near Linear Scaling Pair Natural Orbital Based Local Coupled Cluster Method. *J. Chem. Phys.* **2013**, *138* (3), 034106. https://doi.org/10.1063/1.4773581.
(151) Riplinger, C.; Sandhoefer, B.; Hansen, A.; Neese, F. Natural Triple Excitations in Local Coupled Cluster Calculations with Pair Natural Orbitals. *J. Chem. Phys.* **2013**, *139* (13), 134101. https://doi.org/10.1063/1.4821834.
(152) Kendall, R. A.; Dunning, T. H.; Harrison, R. J. Electron Affinities of the First-Row Atoms Revisited. Systematic Basis Sets and Wave Functions. *J. Chem. Phys.* **1992**, *96* (9), 6796–6806. https://doi.org/10.1063/1.462569.
(153) Dunning, T. H. Gaussian Basis Sets for Use in Correlated Molecular Calculations. I. The Atoms Boron through Neon and Hydrogen. *J. Chem. Phys.* **1989**, *90* (2), 1007–1023. https://doi.org/10.1063/1.456153.
(154) Ásgeirsson, V.; Birgisson, B. O.; Bjornsson, R.; Becker, U.; Neese, F.; Riplinger, C.; Jónsson, H. Nudged Elastic Band Method for Molecular Reactions Using Energy-Weighted Springs Combined with Eigenvector Following. *J. Chem. Theory Comput.* **2021**, *17* (8), 4929–4945. https://doi.org/10.1021/acs.jctc.1c00462.
(155) Tantirungrotechai, Y.; Phanasant, K.; Roddecha, S.; Surawatanawong, P.; Sutthikhum, V.; Limtrakul, J. Scaling Factors for Vibrational Frequencies and Zero-Point Vibrational Energies of Some Recently Developed Exchange-Correlation Functionals. *J. Mol. Struct. THEOCHEM* **2006**, *760* (1), 189–192. https://doi.org/10.1016/j.theochem.2005.12.007.
(156) Zapata Trujillo, J. C.; McKemmish, L. K. Meta-Analysis of Uniform Scaling Factors for Harmonic Frequency Calculations. *WIREs Comput. Mol. Sci.* **2022**, *12* (3), e1584. https://doi.org/10.1002/wcms.1584.
(157) Harmony, M. D. The Equilibrium Carbon–Carbon Single-Bond Length in Ethane. *J. Chem. Phys.* **1990**, *93* (10), 7522–7523. https://doi.org/10.1063/1.459380.
(158) Singh, R. K.; Fernando, S.; Baygi, S. F.; Multari, N.; Thagard, S. M.; Holsen, T. M. Breakdown Products from Perfluorinated Alkyl Substances (PFAS) Degradation in a Plasma-Based Water Treatment Process. *Environ. Sci. Technol.* **2019**, *53* (5), 2731–2738. https://doi.org/10.1021/acs.est.8b07031.

(159) Wilkinson, G.; Rosenblum, M.; Whiting, M. C.; Woodward, R. B. THE STRUCTURE OF IRON BIS-CYCLOPENTADIENYL. *J. Am. Chem. Soc.* **1952**, *74* (8), 2125–2126. https://doi.org/10.1021/ja01128a527.
(160) Breslow, R. SYNTHESIS OF THE S-TRIPHENYLCYCLOPROPENYL CATION. *J. Am. Chem. Soc.* **1957**, *79* (19), 5318–5318. https://doi.org/10.1021/ja01576a067.
(161) Lee, V. Ya.; Sekiguchi, A. Aromaticity of Group 14 Organometallics: Experimental Aspects. *Angew. Chem. Int. Ed.* **2007**, *46* (35), 6596–6620. https://doi.org/10.1002/anie.200604869.
(162) Tokitoh, N. New Progress in the Chemistry of Stable Metallaaromatic Compounds of Heavier Group 14 Elements. *Acc. Chem. Res.* **2004**, *37* (2), 86–94. https://doi.org/10.1021/ar020093k.
(163) Tokitoh, N. Synthesis of Aromatic Species Containing a Heavier Group 14 Element by Taking Advantage of Kinetic Stabilization. *Bull. Chem. Soc. Jpn.* **2004**, *77* (3), 429–441. https://doi.org/10.1246/bcsj.77.429.
(164) Shen, T.; Chen, D.; Lin, L.; Zhu, J. Dual Aromaticity in Both the T0 and S1 States: Osmapyridinium with Phosphonium Substituents. *J. Am. Chem. Soc.* **2019**, *141* (14), 5720–5727. https://doi.org/10.1021/jacs.8b11564.
(165) Buil, M. L.; Esteruelas, M. A.; Oñate, E.; Picazo, N. R. Dissimilarity in the Chemical Behavior of Osmaoxazolium Salts and Osmaoxazoles: Two Different Aromatic Metalladiheterocycles. *Organometallics* **2021**, *40* (24), 4150–4162. https://doi.org/10.1021/acs.organomet.1c00621.
(166) Buil, M. L.; Esteruelas, M. A.; Oñate, E.; Picazo, N. R. Osmathiazole Ring: Extrapolation of an Aromatic Purely Organic System to Organometallic Chemistry. *Organometallics* **2023**, *42* (4), 327–338. https://doi.org/10.1021/acs.organomet.2c00631.
(167) Amicangelo, J. C.; Armentrout, P. B. Absolute Binding Energies of Alkali-Metal Cation Complexes with Benzene Determined by Threshold Collision-Induced Dissociation Experiments and Ab Initio Theory. *J. Phys. Chem. A* **2000**, *104* (48), 11420–11432. https://doi.org/10.1021/jp002652f.
(168) Dougherty, D. A. The Cation−π Interaction. *Acc. Chem. Res.* **2013**, *46* (4), 885–893. https://doi.org/10.1021/ar300265y.
(169) Kolakkandy, S.; Pratihar, S.; Aquino, A. J. A.; Wang, H.; Hase, W. L. Properties of Complexes Formed by Na+, Mg2+, and Fe2+ Binding with Benzene Molecules. *J. Phys. Chem. A* **2014**, *118* (40), 9500–9511. https://doi.org/10.1021/jp5029257.
(170) Davis, M. R.; Dougherty, D. A. Cation–π Interactions: Computational Analyses of the Aromatic Box Motif and the Fluorination Strategy for Experimental Evaluation. *Phys. Chem. Chem. Phys.* **2015**, *17* (43), 29262–29270. https://doi.org/10.1039/C5CP04668H.
(171) Dunbar, R. C. Complexation of Na+ and K+ to Aromatic Amino Acids: A Density Functional Computational Study of Cation-π Interactions. *J. Phys. Chem. A* **2000**, *104* (34), 8067–8074. https://doi.org/10.1021/jp000524l.
(172) Fu, W.; Carr, P. J. J.; Lecours, M. J.; Burt, M.; Marta, R. A.; Steinmetz, V.; Fillion, E.; McMahon, T. B.; Hopkins, W. S. Intramolecular Cation–π Interactions in Protonated

Phenylalanine Derivatives. *Phys. Chem. Chem. Phys.* **2017**, *19* (1), 729–734. https://doi.org/10.1039/C6CP07337A.
(173) Foster, M. S.; Beauchamp, J. L. Ion-Molecule Reactions and Gas-Phase Basicity of Ferrocene. *J. Am. Chem. Soc.* **1975**, *97* (17), 4814–4817. https://doi.org/10.1021/ja00850a005.
(174) Corderman, R. R.; Beauchamp, J. L. Ion Chemistry and Gas-Phase Basicity of Nickelocene by Ion Cyclotron Resonance Spectroscopy. *Inorg. Chem.* **1976**, *15* (3), 665–668. https://doi.org/10.1021/ic50157a034.
(175) Hunt, D. F.; Sethi, S. K. Gas-Phase Ion/Molecule Isotope-Exchange Reactions: Methodology for Counting Hydrogen Atoms in Specific Organic Structural Environments by Chemical Ionization Mass Spectrometry. *J. Am. Chem. Soc.* **1980**, *102* (23), 6953–6963. https://doi.org/10.1021/ja00543a009.
(176) Ikonomou, M. G.; Sunner, J.; Kebarle, P. Kinetics and Thermodynamics of Protonation of Ferrocene in the Gas Phase. *J. Phys. Chem.* **1988**, *92* (22), 6308–6312. https://doi.org/10.1021/j100333a027.
(177) Meot-Ner, M. Ion Chemistry of Ferrocene. Thermochemistry of Ionization and Protonation and Solvent Clustering. Slow and Entropy-Driven Proton-Transfer Kinetics. *J. Am. Chem. Soc.* **1989**, *111* (8), 2830–2834. https://doi.org/10.1021/ja00190a014.
(178) Hop, C. E. C. A.; McMahon, T. B. Protonation of Ferrocene in the Gas Phase. *J. Am. Soc. Mass Spectrom.* **1994**, *5* (4), 274–281. https://doi.org/10.1016/1044-0305(94)85017-8.
(179) Streitwieser, A.; Smith, K. A. Inverse Sandwich Compounds. *J. Mol. Struct. THEOCHEM* **1988**, *163*, 259–265. https://doi.org/10.1016/0166-1280(88)80394-4.
(180) Wessel, J.; Lork, E.; Mews, R. Alkali Metallocene Anions: Syntheses and Structures. *Angew. Chem. Int. Ed. Engl.* **1995**, *34* (21), 2376–2378. https://doi.org/10.1002/anie.199523761.
(181) Weigend, F.; Ahlrichs, R. Balanced Basis Sets of Split Valence, Triple Zeta Valence and Quadruple Zeta Valence Quality for H to Rn: Design and Assessment of Accuracy. *Phys. Chem. Chem. Phys.* **2005**, *7* (18), 3297. https://doi.org/10.1039/b508541a.
(182) Sundaramoorthy, R.; Vadivelu, M.; Karthikeyan, K.; Praveen, C. Mechanosynthesis of Triazolyl-Bis(Indolyl)Methane Pharmacophores via Gold Catalysis: A Prelude to Their Molecular Electronic Properties and Biological Potency. *ChemMedChem* **2023**, *18* (4), e202200529. https://doi.org/10.1002/cmdc.202200529.
(183) Spiekermann, K.; Pattanaik, L.; Green, W. H. High Accuracy Barrier Heights, Enthalpies, and Rate Coefficients for Chemical Reactions. *Sci. Data* **2022**, *9* (1), 417. https://doi.org/10.1038/s41597-022-01529-6.
(184) Riplinger, C.; Sandhoefer, B.; Hansen, A.; Neese, F. Natural Triple Excitations in Local Coupled Cluster Calculations with Pair Natural Orbitals. *J. Chem. Phys.* **2013**, *139* (13), 134101. https://doi.org/10.1063/1.4821834.
(185) Riplinger, C.; Neese, F. An Efficient and near Linear Scaling Pair Natural Orbital Based Local Coupled Cluster Method. *J. Chem. Phys.* **2013**, *138* (3), 034106. https://doi.org/10.1063/1.4773581.

(186) Toernkvist, C.; Bergman, J.; Liedberg, B. Geometry and Vibrations of the 1,2,3-Triazole Anion. A Theoretical and Experimental Study. *J. Phys. Chem.* **1991**, *95* (8), 3119–3123. https://doi.org/10.1021/j100161a030.
(187) Johnson, R. D. I.; Irikura, K. K.; Kacker, R. N.; Kessel, R. Scaling Factors and Uncertainties for Ab Initio Anharmonic Vibrational Frequencies. *J. Chem. Theory Comput.* **2010**, *6* (9), 2822–2828. https://doi.org/10.1021/ct100244d.
(188) Alecu, I. M.; Zheng, J.; Zhao, Y.; Truhlar, D. G. Computational Thermochemistry: Scale Factor Databases and Scale Factors for Vibrational Frequencies Obtained from Electronic Model Chemistries. *J. Chem. Theory Comput.* **2010**, *6* (9), 2872–2887. https://doi.org/10.1021/ct100326h.
(189) Shannon, R. D. Revised Effective Ionic Radii and Systematic Studies of Interatomic Distances in Halides and Chalcogenides. *Acta Crystallogr. Sect. A* **1976**, *32* (5), 751–767. https://doi.org/10.1107/S0567739476001551.
(190) Iwadate, Y.; Harada, T.; Ohkubo, T.; Fukushima, K.; Misawa, M.; Fukunaga, T.; Itoh, K. Pulsed Neutron Diffraction Study of NaNO2 and KNO2 Pure Melts. *Electrochemistry* **2009**, *77* (8), 741–744. https://doi.org/10.5796/electrochemistry.77.741.
(191) Foster, J. P.; Weinhold, F. Natural Hybrid Orbitals. *J. Am. Chem. Soc.* **1980**, *102* (24), 7211–7218. https://doi.org/10.1021/ja00544a007.
(192) Reed, A. E.; Weinhold, F. Natural Bond Orbital Analysis of Near-Hartree–Fock Water Dimer. *J. Chem. Phys.* **1983**, *78* (6), 4066–4073. https://doi.org/10.1063/1.445134.
(193) Hopkins, W. S.; Carr, P. J. J.; Huang, D.; Bishop, K. P.; Burt, M.; McMahon, T. B.; Steinmetz, V.; Fillion, E. Infrared-Driven Charge Transfer in Transition Metal B_{12} F_{12} Clusters. *J. Phys. Chem. A* **2015**, *119* (31), 8469–8475. https://doi.org/10.1021/acs.jpca.5b03932.
(194) Zhang, G.; Li, X.; Li, Y.; Chen, D. Electron Density Characteristics and Charge Transfer Effect of Hydrogen Bond O–H···Pt(II): Atoms in Molecules Study and Natural Bond Orbital Analysis. *Mol. Phys.* **2013**, *111* (21), 3276–3282. https://doi.org/10.1080/00268976.2013.780665.
(195) Cappelletti, D.; Ronca, E.; Belpassi, L.; Tarantelli, F.; Pirani, F. Revealing Charge-Transfer Effects in Gas-Phase Water Chemistry. *Acc. Chem. Res.* **2012**, *45* (9), 1571–1580. https://doi.org/10.1021/ar3000635.
(196) El-Azhary, A. A.; Suter, H. U.; Kubelka, J. Experimental and Theoretical Investigation of the Geometry and Vibrational Frequencies of 1,2,3-Triazole, 1,2,4-Triazole, and Tetrazole Anions. *J. Phys. Chem. A* **1998**, *102* (3), 620–629. https://doi.org/10.1021/jp9719568.
(197) Barba-Bon, A.; Salluce, G.; Lostalé-Seijo, I.; Assaf, K. I.; Hennig, A.; Montenegro, J.; Nau, W. M. Boron Clusters as Broadband Membrane Carriers. *Nature* **2022**, *603* (7902), 637–642. https://doi.org/10.1038/s41586-022-04413-w.
(198) Murphy, N.; McCarthy, E.; Dwyer, R.; Farràs, P. Boron Clusters as Breast Cancer Therapeutics. *J. Inorg. Biochem.* **2021**, *218*, 111412. https://doi.org/10.1016/j.jinorgbio.2021.111412.

(199) An, L.; Yu, Y.; Cai, Q.; Mateti, S.; Li, L. H.; Chen, Y. I. Hexagonal Boron Nitride Nanosheets: Preparation, Heat Transport Property and Application as Thermally Conductive Fillers. *Prog. Mater. Sci.* **2023**, *138*, 101154. https://doi.org/10.1016/j.pmatsci.2023.101154.
(200) Rasul, M. G.; Kiziltas, A.; Arfaei, B.; Shahbazian-Yassar, R. 2D Boron Nitride Nanosheets for Polymer Composite Materials. *Npj 2D Mater. Appl.* **2021**, *5* (1), 1–18. https://doi.org/10.1038/s41699-021-00231-2.
(201) Shmalko, A. V.; Anufriev, S. A.; Timofeev, S. V.; Sivaev, I. B.; Bregadze, V. I. Synthesis of New Fluoro Derivatives of O-Carborane [3-F-7,8-C2B9H11]−, 3,6-F2-1,2-C2B10H10, and [6,6′-F2-3,3′-Co(1,2-C2B9H10)2]−. *Russ. Chem. Bull.* **2024**, *73* (1), 146–152. https://doi.org/10.1007/s11172-024-4126-9.
(202) Soloway, A. H.; Tjarks, W.; Barnum, B. A.; Rong, F.-G.; Barth, R. F.; Codogni, I. M.; Wilson, J. G. The Chemistry of Neutron Capture Therapy. *Chem. Rev.* **1998**, *98* (4), 1515–1562. https://doi.org/10.1021/cr941195u.
(203) Sabzyan, H.; Keshavarz, E.; Noorisafa, Z. Diatomic Dications and Dianions. *J. Iran. Chem. Soc.* **2014**, *11* (3), 871–945. https://doi.org/10.1007/s13738-013-0359-5.
(204) Boeré, R. T.; Derendorf, J.; Jenne, C.; Kacprzak, S.; Keßler, M.; Riebau, R.; Riedel, S.; Roemmele, T. L.; Rühle, M.; Scherer, H.; Vent-Schmidt, T.; Warneke, J.; Weber, S. On the Oxidation of the Three-Dimensional Aromatics [B12X12]2− (X=F, Cl, Br, I). *Chem. – Eur. J.* **2014**, *20* (15), 4447–4459. https://doi.org/10.1002/chem.201304405.
(205) Warneke, J.; Jenne, C.; Bernarding, J.; Azov, V. A.; Plaumann, M. Evidence for an Intrinsic Binding Force between Dodecaborate Dianions and Receptors with Hydrophobic Binding Pockets. *Chem. Commun.* **2016**, *52* (37), 6300–6303. https://doi.org/10.1039/C6CC01233G.
(206) Warneke, J.; Dülcks, T.; Knapp, C.; Gabel, D. Collision-Induced Gas-Phase Reactions of Perhalogenated Closo-Dodecaborate Clusters – a Comparative Study. *Phys. Chem. Chem. Phys.* **2011**, *13* (13), 5712. https://doi.org/10.1039/c0cp02386h.
(207) Warneke, J.; Wang, X.-B. Measuring Electronic Structure of Multiply Charged Anions to Understand Their Chemistry: A Case Study on Gaseous Polyhedral Closo-Borate Dianions. *J. Phys. Chem. A* **2021**, *125* (31), 6653–6661. https://doi.org/10.1021/acs.jpca.1c04618.
(208) Wöhner, K.; Wulf, T.; Vankova, N.; Heine, T. Strong Binding of Noble Gases to $[B_{12}X_{11}]^-$: A Theoretical Study. *J. Phys. Chem. A* **2021**, *125* (22), 4760–4765. https://doi.org/10.1021/acs.jpca.1c01909.
(209) Ieritano, C.; Hopkins, W. S. The Hitchhiker's Guide to Dynamic Ion–Solvent Clustering: Applications in Differential Ion Mobility Spectrometry. *Phys. Chem. Chem. Phys.* **2022**, *24* (35), 20594–20615. https://doi.org/10.1039/D2CP02540J.
(210) Carr, P. J. J. Computational and Spectroscopic Investigations of Intermolecular Interactions in Clusters.
(211) Rohdenburg, M.; Mayer, M.; Grellmann, M.; Jenne, C.; Borrmann, T.; Kleemiss, F.; Azov, V. A.; Asmis, K. R.; Grabowsky, S.; Warneke, J. Superelectrophilic Behavior of an Anion Demonstrated by the Spontaneous Binding of Noble Gases to [B12Cl11]−.

Angew. Chem. Int. Ed. **2017**, *56* (27), 7980–7985. https://doi.org/10.1002/anie.201702237.
(212) Haack, A.; Ieritano, C.; Hopkins, W. S. MobCal-MPI 2.0: An Accurate and Parallelized Package for Calculating Field-Dependent Collision Cross Sections and Ion Mobilities. *The Analyst* **2023**, *148* (14), 3257–3273. https://doi.org/10.1039/D3AN00545C.
(213) Ieritano, C.; Yves Le Blanc, J. C.; Schneider, B. B.; Bissonnette, J. R.; Haack, A.; Hopkins, W. S. Protonation-Induced Chirality Drives Separation by Differential Ion Mobility Spectrometry. *Angew. Chem. Int. Ed.* **2022**, *n/a* (n/a), e202116794. https://doi.org/10.1002/anie.202116794.
(214) Campbell, M. T.; Glish, G. L. Fragmentation in the Ion Transfer Optics after Differential Ion Mobility Spectrometry Produces Multiple Artifact Monomer Peaks. *Int. J. Mass Spectrom.* **2018**, *425*, 47–54. https://doi.org/10.1016/j.ijms.2018.01.007.
(215) Atkins, C. G.; Rajabi, K.; Gillis, E. A. L.; Fridgen, T. D. Infrared Multiple Photon Dissociation Spectra of Proton- and Sodium Ion-Bound Glycine Dimers in the N−H and O−H Stretching Region. *J. Phys. Chem. A* **2008**, *112* (41), 10220–10225. https://doi.org/10.1021/jp805514b.
(216) Ung, H. U.; Moehlig, A. R.; Khodagholian, S.; Berden, G.; Oomens, J.; Morton, T. H. Proton-Bridge Motions in Amine Conjugate Acid Ions Having Intramolecular Hydrogen Bonds to Hydroxyl and Amine Groups. *J. Phys. Chem. A* **2013**, *117* (6), 1360–1369. https://doi.org/10.1021/jp311506y.
(217) Thomas, D. A.; Mucha, E.; Gewinner, S.; Schöllkopf, W.; Meijer, G.; von Helden, G. Vibrational Spectroscopy of Fluoroformate, FCO_2^-, Trapped in Helium Nanodroplets. *J. Phys. Chem. Lett.* **2018**, *9* (9), 2305–2310. https://doi.org/10.1021/acs.jpclett.8b00664.

Appendix A

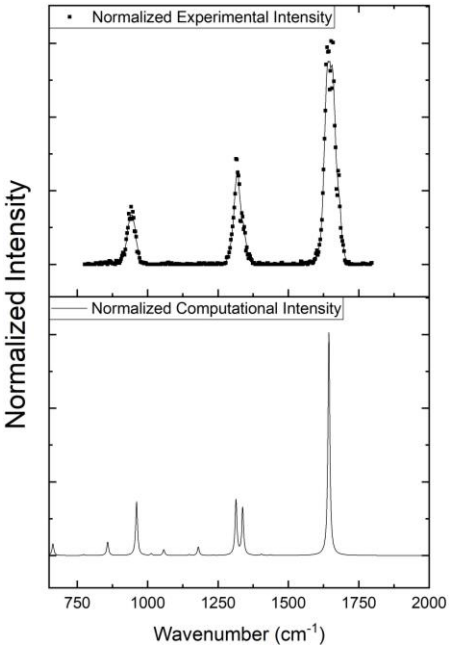


Figure A1. IRMPD and computed harmonic vibrational spectra for deprotonated 3-monofluoropropionic acid.

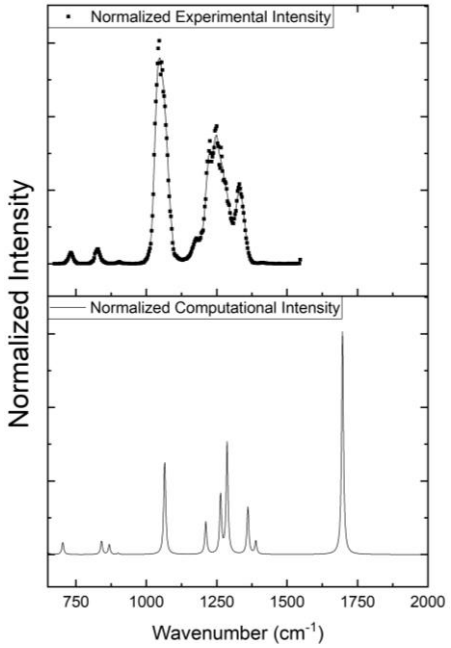


Figure A2. IRMPD and computed harmonic vibrational spectra for deprotonated 3,3,3-trifluoropropionic acid.

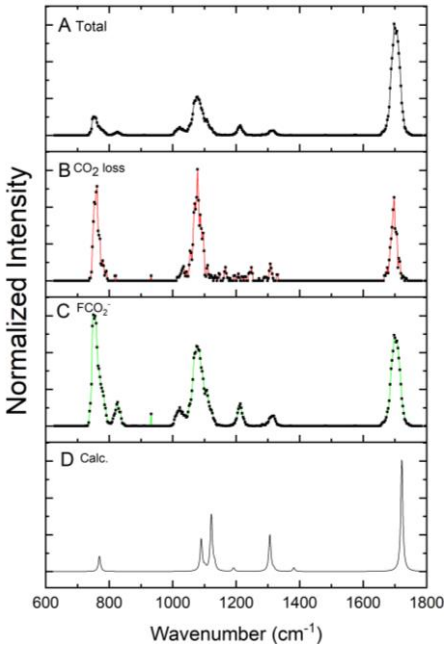


Figure A3. IRMPD and computed harmonic vibrational spectra for deprotonated 3,3,2,2-tetrafluoropropionic acid.

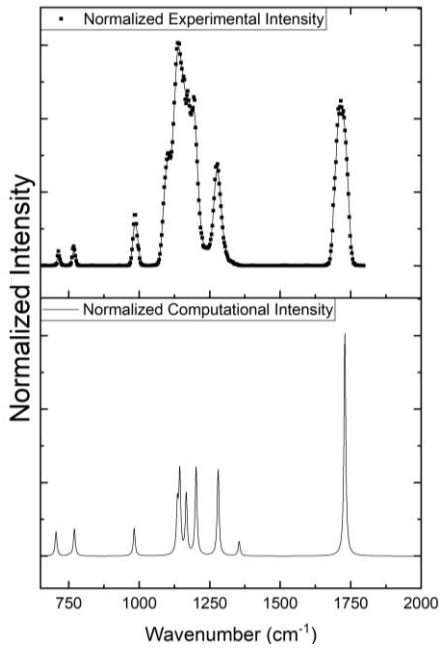


Figure A4. IRMPD and computed harmonic vibrational spectra for deprotonated pentafluoropropionic acid.

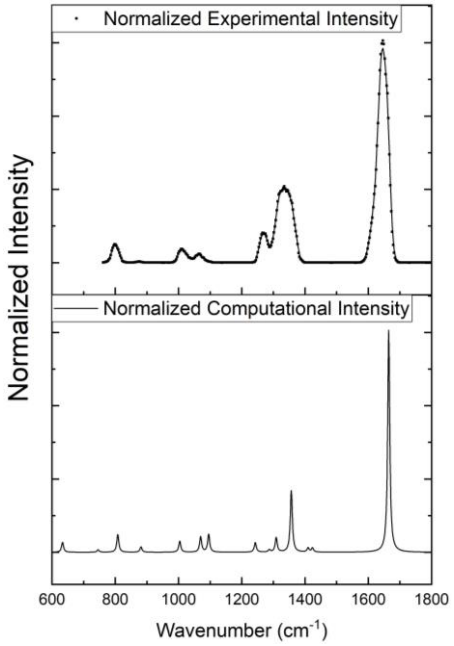


Figure A5. IRMPD and computed harmonic vibrational spectra for deprotonated 2-monofluoropropionic acid.

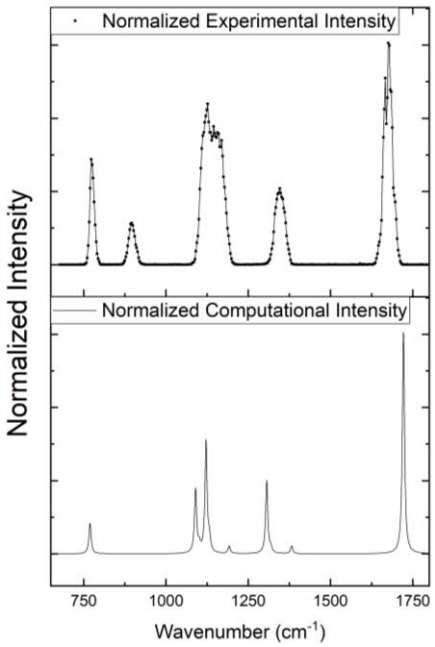


Figure A6. IRMPD and computed harmonic vibrational spectra for deprotonated 2,2-difluoropropionic acid.

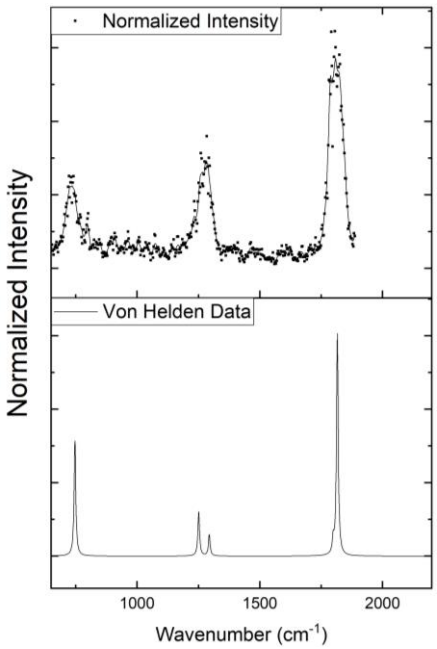


Figure A7. Comparison between the FCO_2^- helium droplet experiment from Von Helden and the FCO_2^- IRMPD spectrum.[217]

Table A1. Calculated and observed vibrational modes for the deprotonated 2-monofluoropropionic acid. Computational Frequency is scaled by a factor of 0.95. Frequencies are reported in cm^{-1}.

Experimental Frequency	Computational Frequency	Vibrational Mode
804	808	CO_2 Wagging
894	881	CF Stretch/CO_2 Scissoring
1014	1004	CHF Twisting
1071	1070	β-CH_2 twisting
1275	1287	CH_3 Umbrella
1338	1357	CH_3 Umbrella
1646	1664	CO_2 Asymmetric Stretch

Table A2. Calculated and observed vibrational modes for the deprotonated 3-monofluoropropionic acid. Computational Frequency is scaled by a factor of 0.95. Peaks that do not have a distinct feature or under a gaussian distribution are marked as N/A. Frequencies are reported in cm^{-1}.

Experimental Frequency	Computational Frequency	Vibrational Mode
N/A	837	CH_2 Twisting
942	942	CH_2 Rocking
N/A	1031	CF Stretch
N/A	1308	β-CH_2 Wagging/α-CH_2 Twisting
1338	1351	CH_2 Wagging
1659	1649	CO_2 Asymmetric Stretch

Table A3. Calculated and observed vibrational modes for the deprotonated 2, 2-difluoropropionic acid. Frequencies are reported in cm^{-1}.

Experimental Frequency	Computational Frequency	Vibrational Mode
773	771	CO_2 Wagging
899	909	CH_2 Twisting
1127	1119	CF_2 Asym Stretch
1160	1159	CF_2 Wagging
1169	1177	CF_2 Sym Stretch
1349	1357	CH_3 Umbrella
1679	1688	CO_2 Asymmetric Stretch

Table A4. Calculated and observed for the deprotonated 3, 3, 3-trifluoropropionic acid. The experimental frequency for the asymmetric stretch were not recorded due to error.

Experimental Frequency	Computational Frequency	Vibrational Mode
737	753	CO_2 Wagging
833	853	CO_2 Scissoring/CH_2 Wagging
1058	1061	CF Stretch/ CH_2 Wagging
1184	1202	CF_2 Asymmetric Stretch/CH_2 Twisting
1250	1239	CF_3 Umbrella/ CH_2 Twisting
1265	1249	CF_3 Umbrella/ CH_2 Wagging
1334	1336	CF_3 Umbrella/ CH_2 Scissoring
N/A	1680	CO_2 Asymmetric Stretch

Table A5. Calculated and observed vibrational motion for the deprotonated 3, 3, 2, 2-tetrafluoropropionic acid.

Experimental Frequency (cm^{-1})	Computational Frequency (cm^{-1})	Vibrational Mode
759	769	CO_2 Scissoring
835	808	CO_2 Wagging
1023	1090	CF_2H Umbrella
1081	1101	A-CF_2 Asymmetric Stretch
1110	1132	A-CF_2 Sym Stretch
1216	1192	CF_2H Wagging
1323	1319	CH rocking
1697	1722	CO_2 Asymmetric Stretch

Table A6. Calculated and observed vibrational motion for the deprotonated 3, 3, 3, 2-tetrafluoropropionic acid.

Experimental Frequency (cm^{-1})	Computational Frequency (cm^{-1})	Vibrational Mode
693	672	CHF Twisting
767	759	CF_3 Sym Stretch/CO_2 Scissoring
1068	1083	α-CF Stretch
1089	1095	CF_2 Asymmetric Stretch
1162	1162	β-CF_2 Wagging
1251	1242	CF_3 Umbrella
1319	1305	CF_2 Asymmetric Stretch
1695	1710	CO_2 Asymmetric Stretch

Table A7. Calculated and observed vibrational motion for the deprotonated pentafluoropropionic acid.

Experimental Frequency (cm^{-1})	Computational Frequency (cm^{-1})	Vibrational Mode
714	705	CO_2 Wagging
768	770	CO_2 Scissoring
987	982	CF_3 Umbrella/α-CF_2 Wagging
1142	1135	α-CF Asymmetric Stretch
1158	1144	α-CF Symmetric Stretch
1197	1202	β-CF Asymmetric Stretch
1281	1280	CF_3 Umbrella/ CO_2 Symmetric Stretch
1716	1730	CO_2 Asymmetric Stretch

For the Thermal LTQ mass spectrometer the collision energy is calculated with the following formula:

$$CE\ (eV) = \frac{NCE\ \cdot m/z\ of\ precursor\ mass \cdot f}{500}\ ;\ f = 1$$

Where f is a correction factor according to the charge state, for all the breakdown curve presented in this appendix, f is always equal to one.

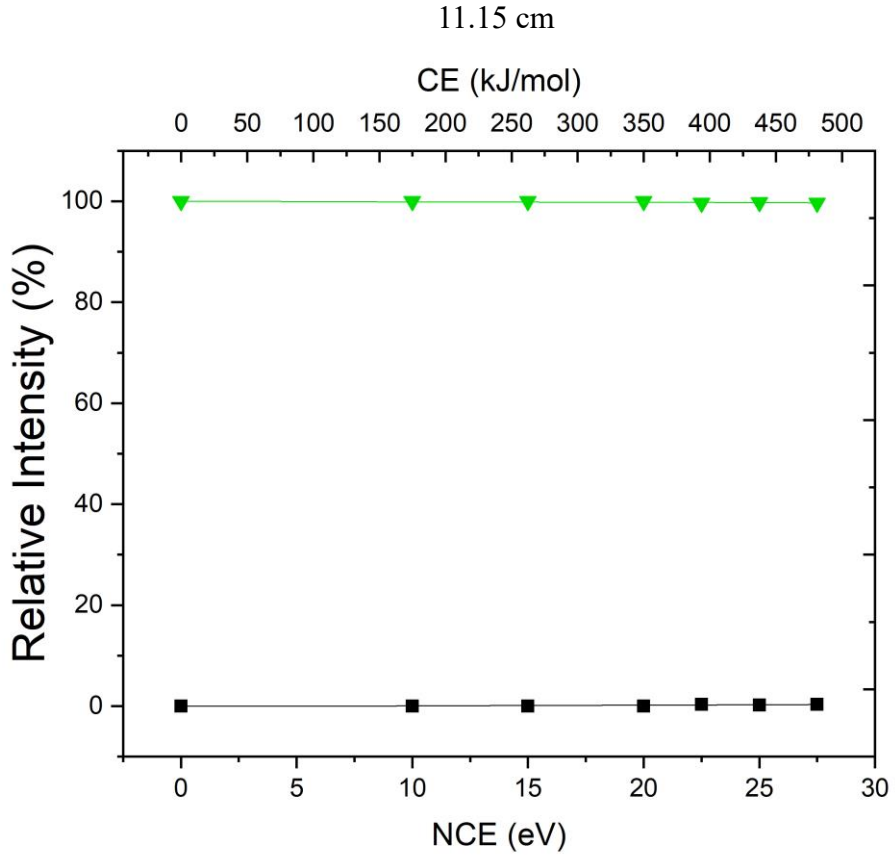


Figure A8. Breakdown curve for the deprotonated 3-monofluoropropionic acid (*m/z* 91) between 10 – 30 eV. Precursor intensity shown in green, and fluoroformate (*m/z* 63) intensity shown in black.

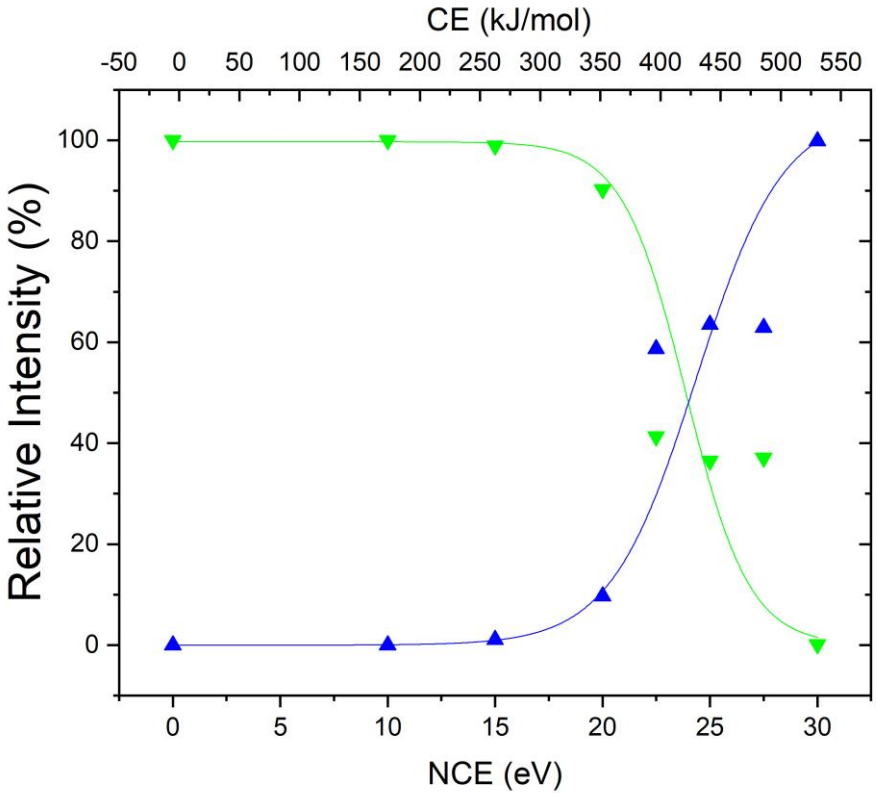


Figure A9. Breakdown curve for the deprotonated 2-monofluoropropionic acid between the NCE of 0-30 eV. Precursor intensity is in green and the loss of HF in blue (*m/z* 89).

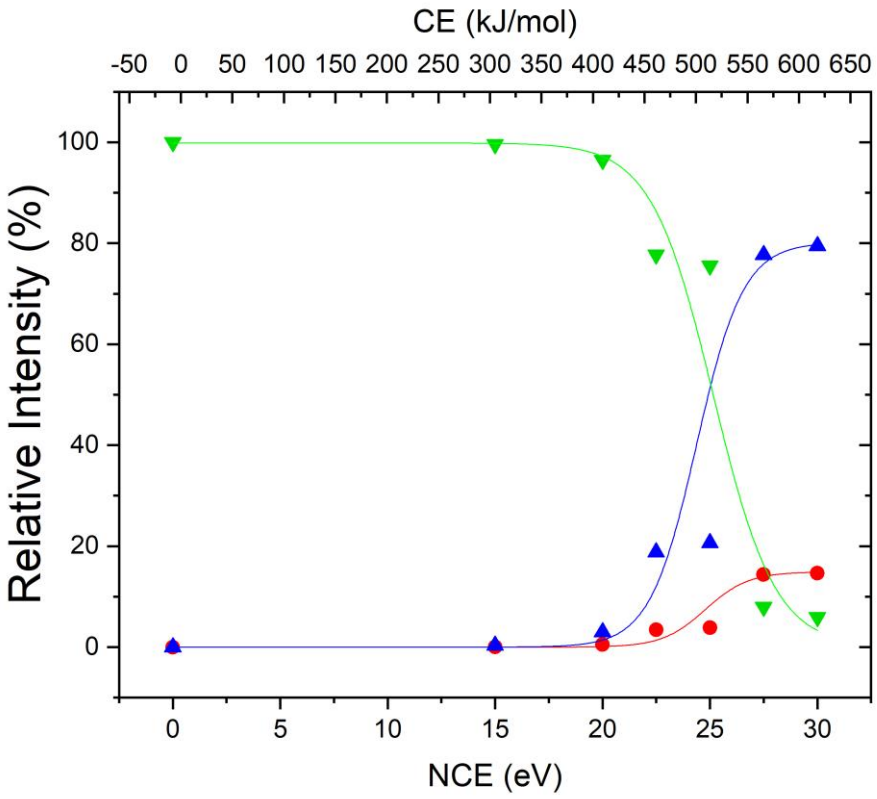


Figure A10. Breakdown curve for the deprotonated 2,2-difluoropropionic acid between the NCE of 0-30 eV. Precursor intensity is in green, loss of CO_2 in red (*m/z* 65), and the loss of HF in blue (*m/z* 89).

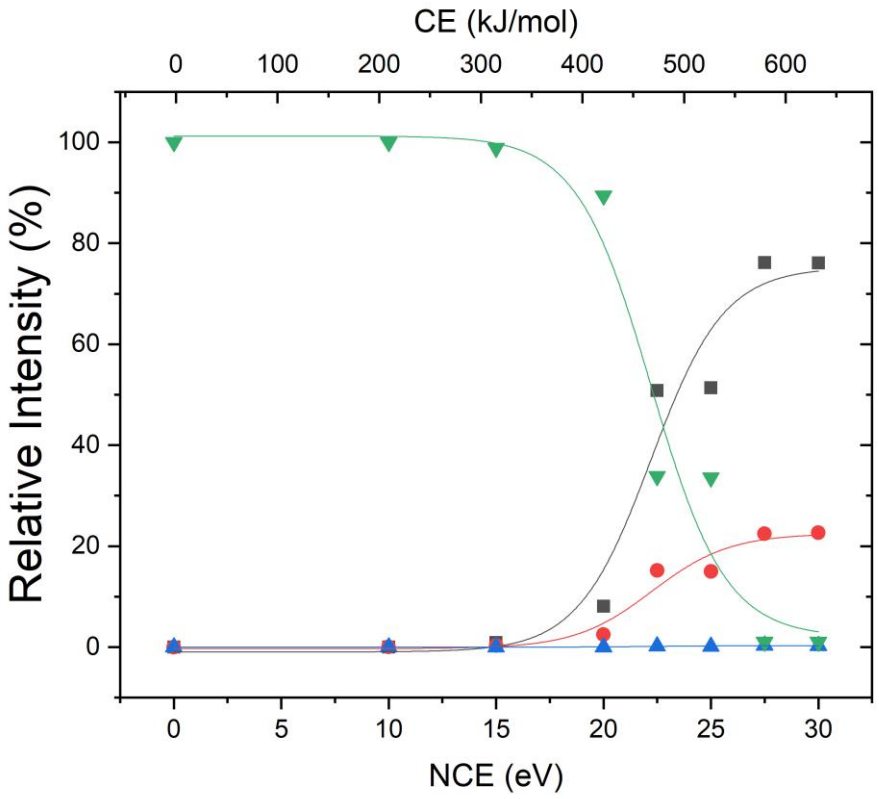


Figure A11. Breakdown curve of deprotonated 3,3-difluoropropionic acid between 10 – 30 eV. Precursor intensity shown in green, fluoroformate (*m/z* 63) intensity shown in black, loss of CO_2 (*m/z* 65) shown in red, and HF loss shown in blue (*m/z* 89).

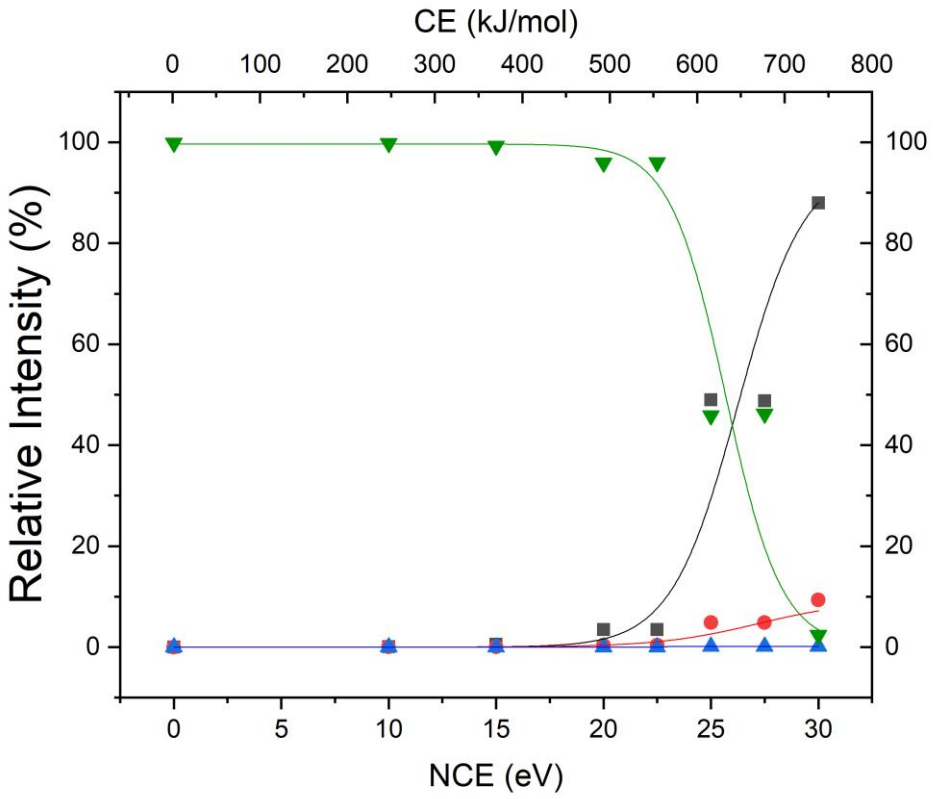


Figure A12. Breakdown curve of the deprotonated 3,2,2-trifluoropropionic acid between 10 – 30 eV. Precursor intensity shown in green, fluoroformate (*m/z* 63) intensity shown in black, loss of CO_2 (*m/z* 83) shown in red, and HF loss shown in blue (*m/z* 107).

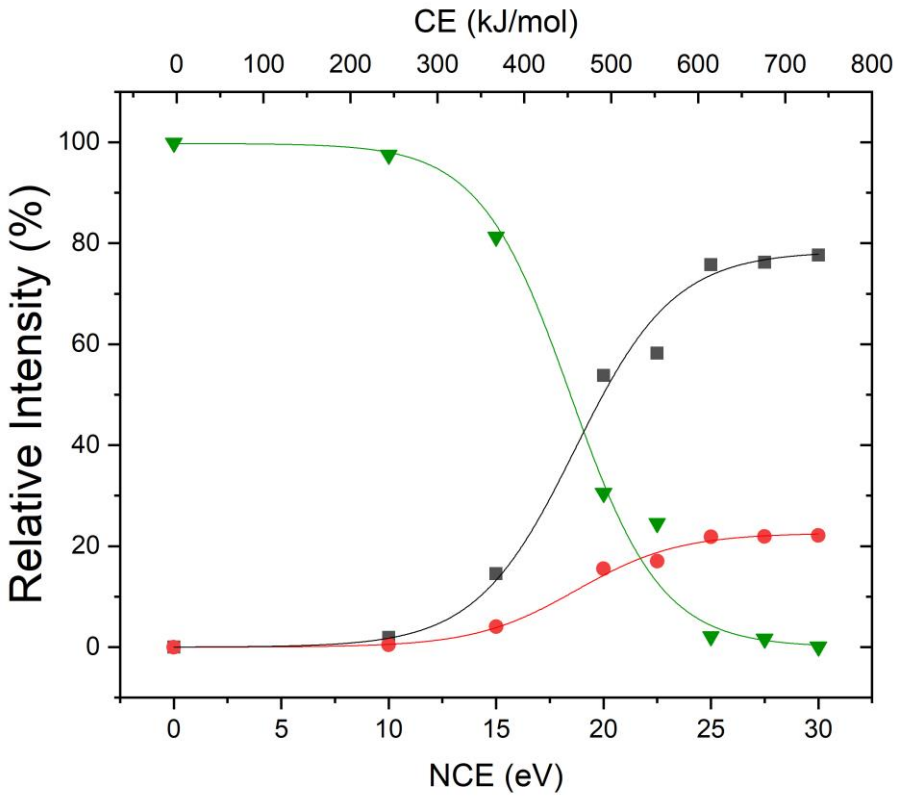


Figure A13. Breakdown curve of the deprotonated 3,3,3-trifluoropropionic acid between 10 – 30 eV. Precursor intensity shown in green, fluoroformate (m/z 63) intensity shown in black, loss of CO2 (m/z 83) shown in red.

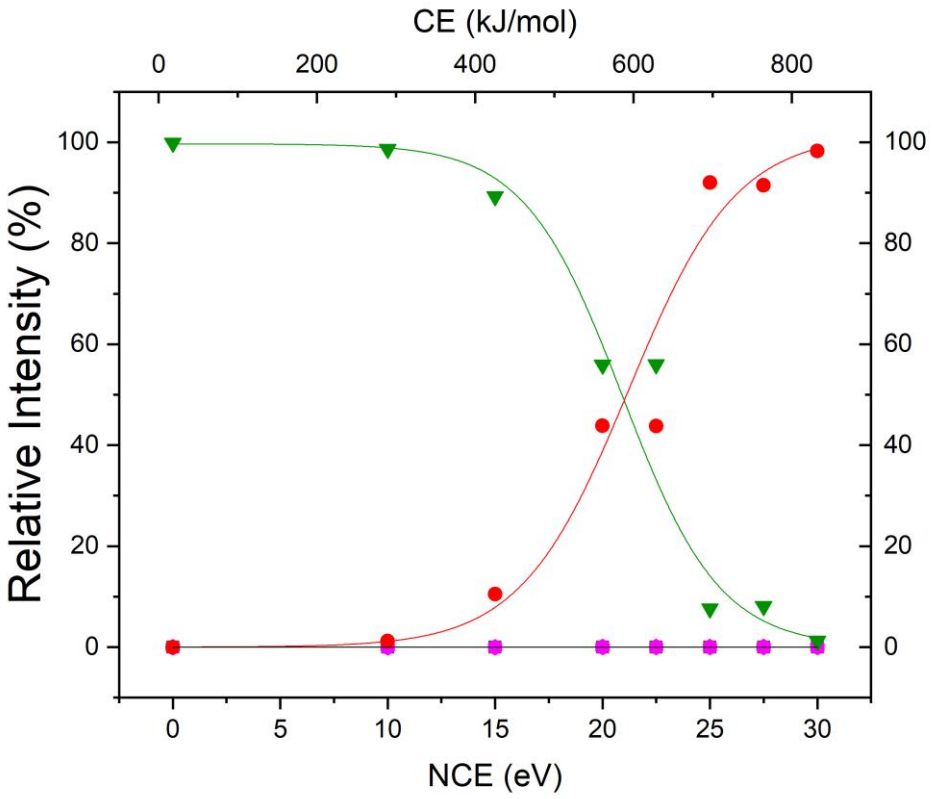


Figure A14. Breakdown curve of deprotonated 3,3,2,2-tetrafluoropropionic acid between for NCE of 10 – 30 eV. Precursor intensity shown in green, fluoroformate (*m/z* 63) intensity shown in black, loss of CO_2 (*m/z* 83) shown in red, and HF loss after the loss of CO_2 shown in magenta (*m/z* 81). The black trace and the pink trace are overlapped over each other.

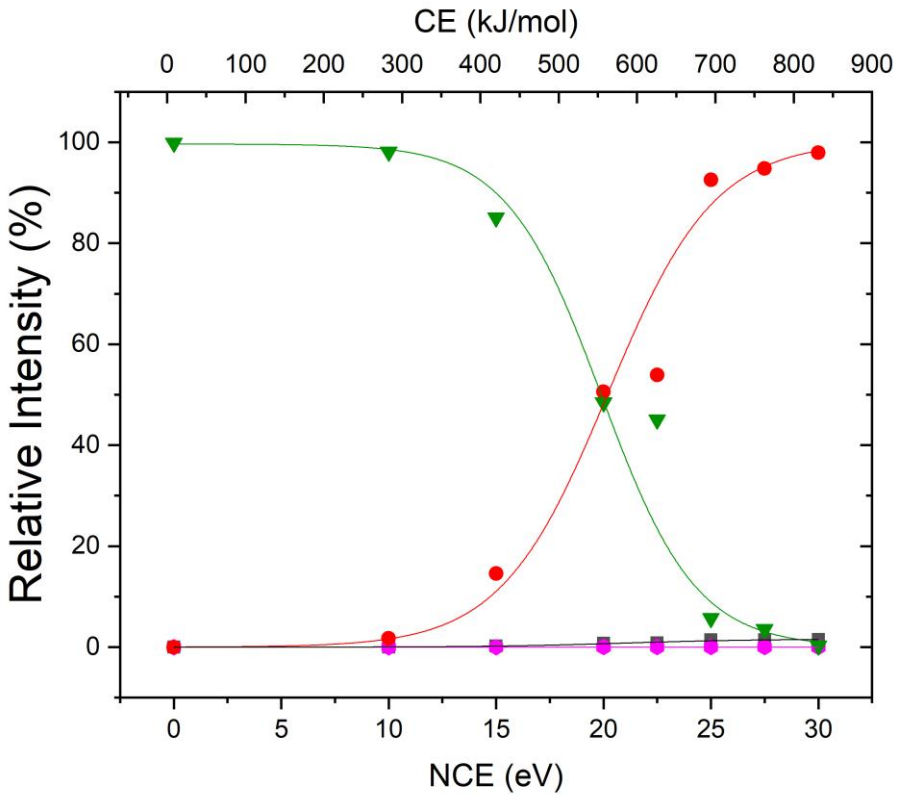


Figure A15. Breakdown curve of the deprotonated 3,3,3,2-tetrafluoropropionic acid between the NCE of 10 – 30 eV. Precursor intensity shown in green, fluoroformate (*m/z* 63) intensity shown in black, loss of CO_2 (*m/z* 83) shown in red, and HF loss after the loss of CO_2 shown in magenta (*m/z* 81).

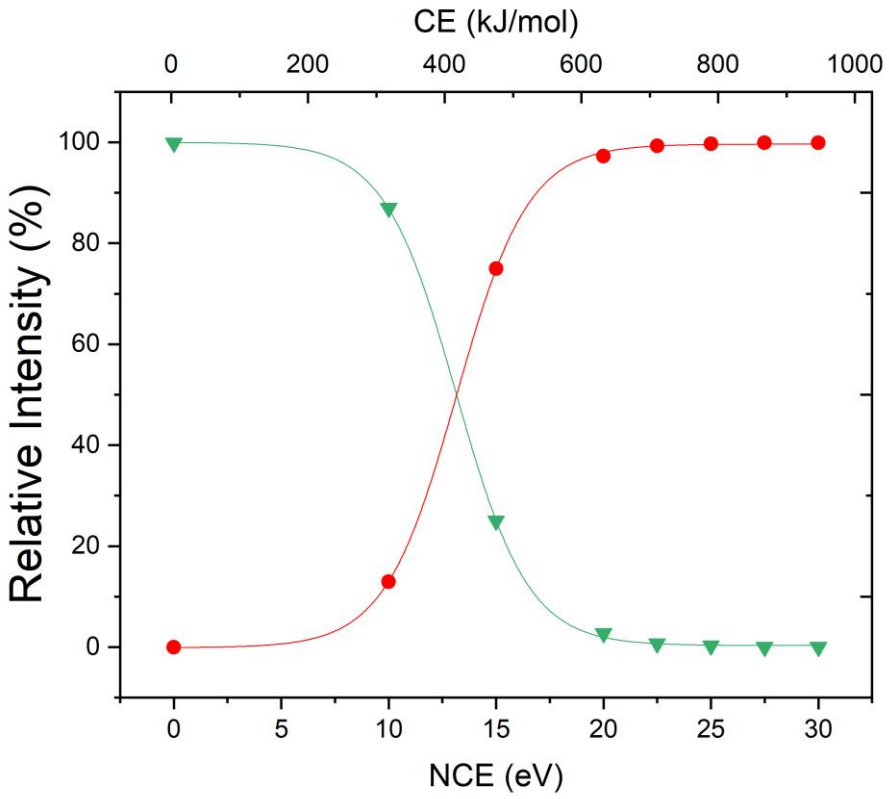


Figure A16: Breakdown curve of deprotonated pentafluoropropionic acid between the NCE of 10 – 30 eV. Precursor intensity shown in green, loss of CO_2 (*m/z* 119) shown in red.

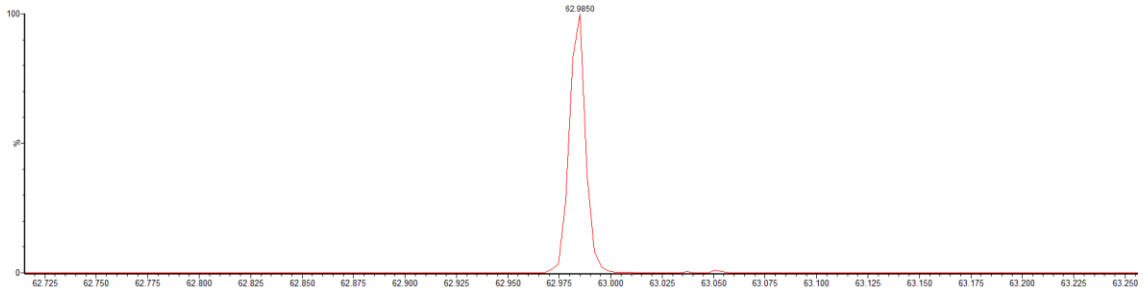


Figure A17. The fragmentation result of the *m/z* 63 for the deprotonated 3,3,3-trifluoropropionic acid using the Waters Synapt G2-Si

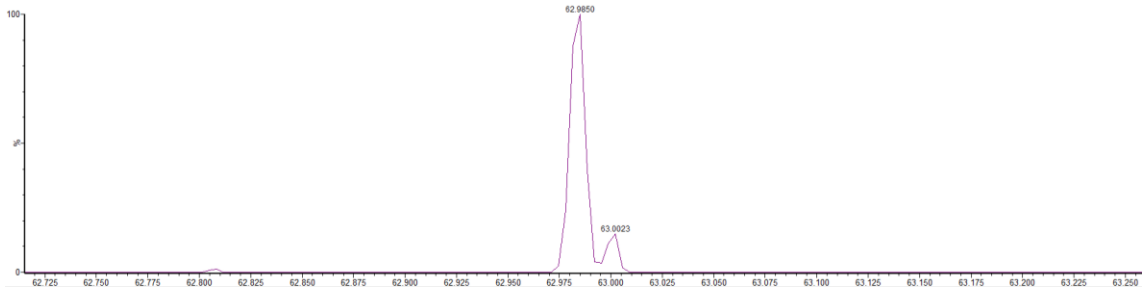


Figure A18. The fragmentation results of the *m/z* 63 for the deprotonated 3,2,2-trifluoropropionic acid using the Waters Synapt G2-Si

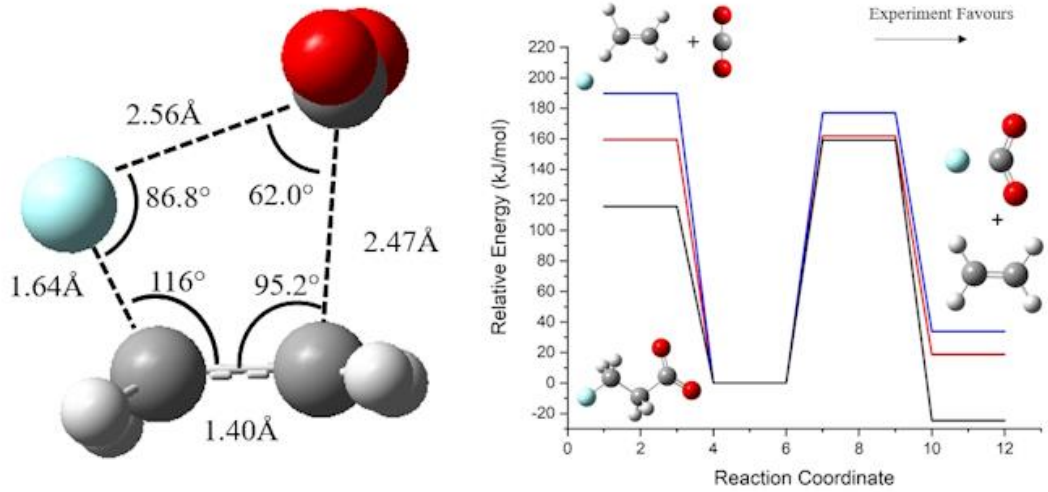


Figure A19. Transition state and potential minimum pathway leading to FCO_2^- or loss of CO_2 for the deprotonated 3-monofluoropropionic acid using thermal corrections at M06-2X/def2-tzvp level of theory and energetics from DLPNO-CCSD(T)/def2-tzvp. (Black trace) relative standard Gibbs energy, (red trace) relative zero-point corrected energy, and (blue trace) relative electronic energy.

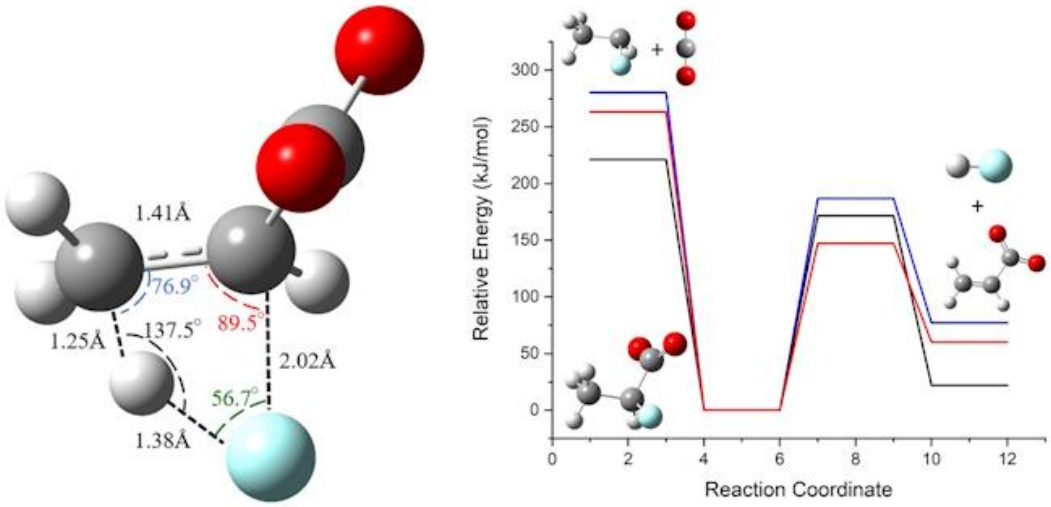


Figure A20. Transition state and potential minimum energy pathway leading to HF loss for the deprotonated 2-monofluoropropionic acid at M06-2X/def2-tzvp level of theory and energetics from DLPNO-CCSD(T)/def2-tzvp. (Black trace) relative standard Gibbs energy, (red trace) relative zero-point corrected energy, and (blue trace) relative electronic energy.

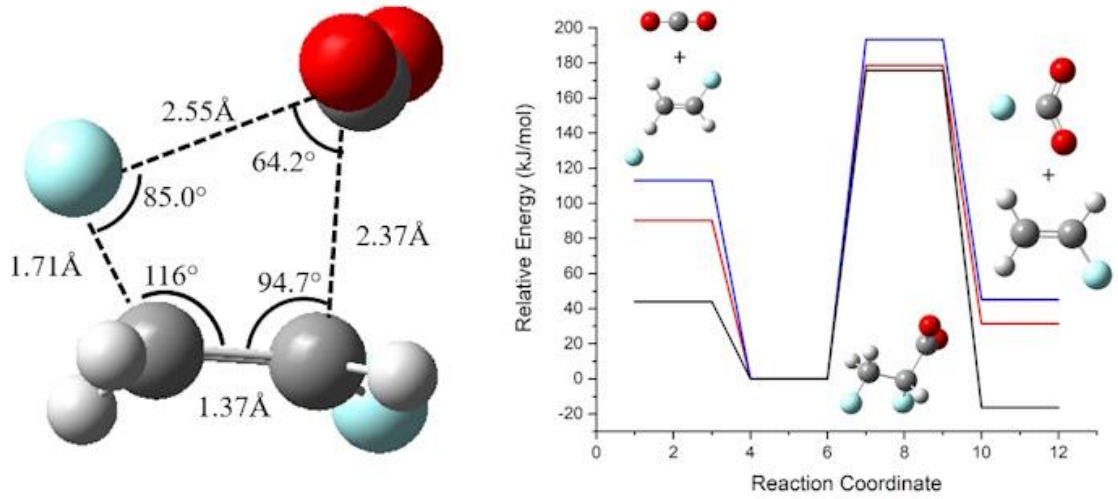


Figure A21. Transition state and potential minimum pathway leading to FCO_2^- or loss of CO_2 for the deprotonated 3,2-difluoropropionic acid using thermal corrections at M06-2X/def2-tzvp level of theory and energetics from DLPNO-CCSD(T)/def2-tzvp. (Black trace) relative standard Gibbs energy, (red trace) relative zero-point corrected energy, and (blue trace) relative electronic energy.

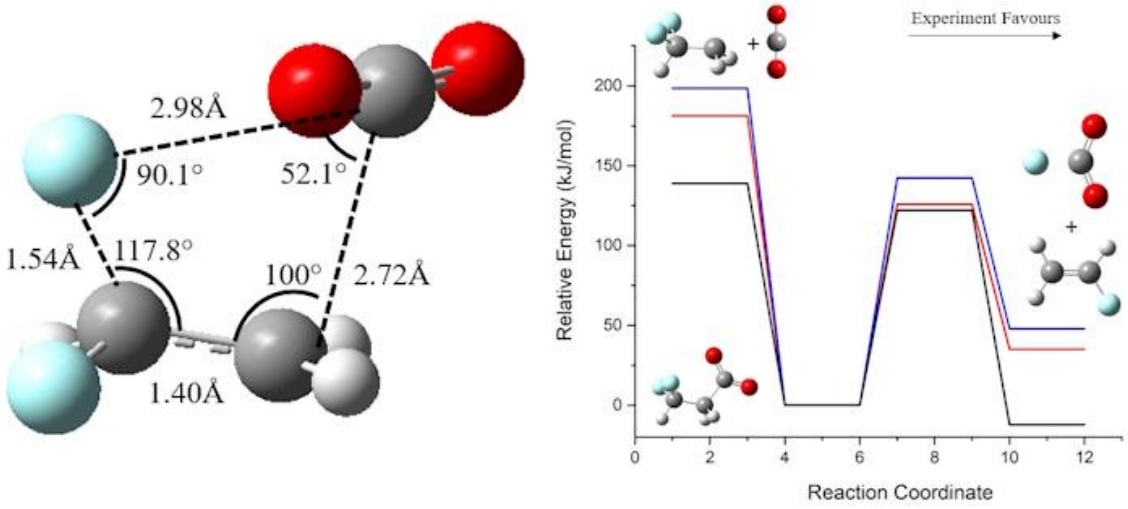


Figure A22. Transition state and potential minimum pathway leading to FCO_2^- or loss of CO_2 for the deprotonated 3,3-difluoropropionic acid using thermal corrections from M06-2X/def2-tzvp level of theory and energetics from DLPNO-CCSD(T)/def2-tzvp. (Black trace) relative standard Gibbs energy, (red trace) relative zero-point corrected energy, and (blue trace) relative electronic energy.

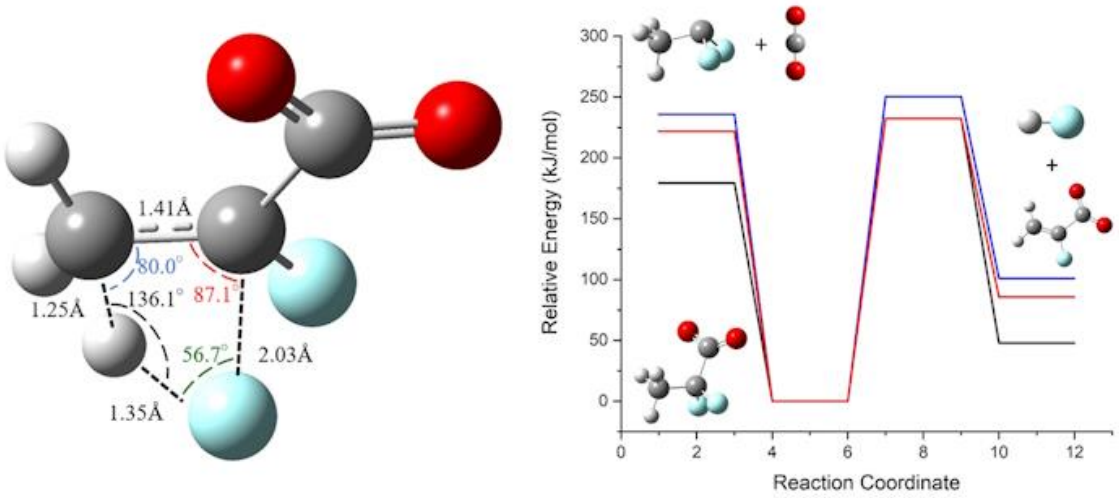


Figure A23. Transition state and potential minimum energy pathway leading to HF loss for the deprotonated 2,2-difluoropropionic acid at M06-2X/def2-tzvp level of theory and energetics from DLPNO-CCSD(T)/def2-tzvp. (Black trace) relative standard Gibbs energy, (red trace) relative zero-point corrected energy, and (blue trace) relative electronic energy.

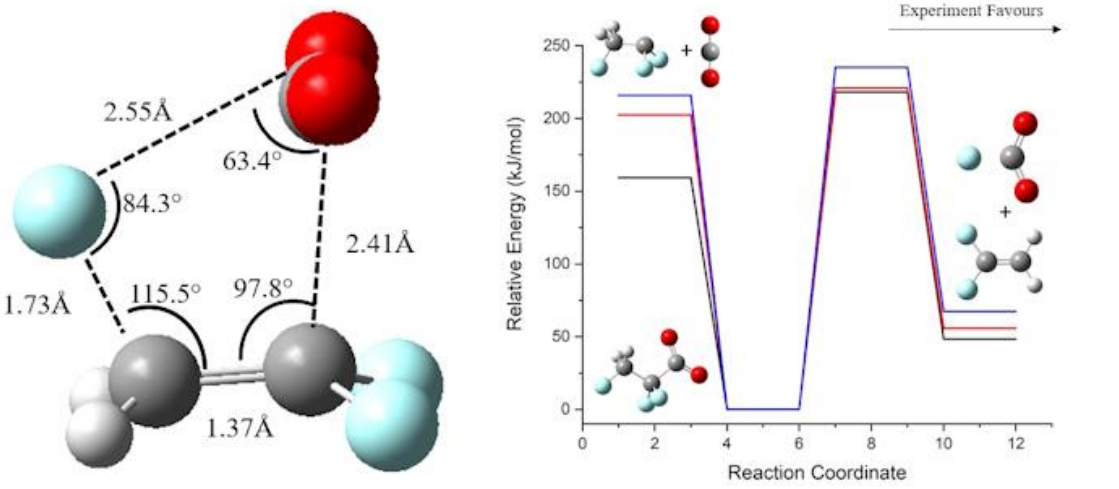


Figure A24. Transition state and potential minimum energy pathway leading to FCO_2^- or loss of CO_2 for the deprotonated 3,2,2-trifluoropropionic acid using thermal corrections at M06-2X/def2-tzvp level of theory and energetics from DLPNO-CCSD(T)/def2-tzvp. (Black trace) relative standard Gibbs energy, (red trace) relative zero-point corrected energy, and (blue trace) relative electronic energy.

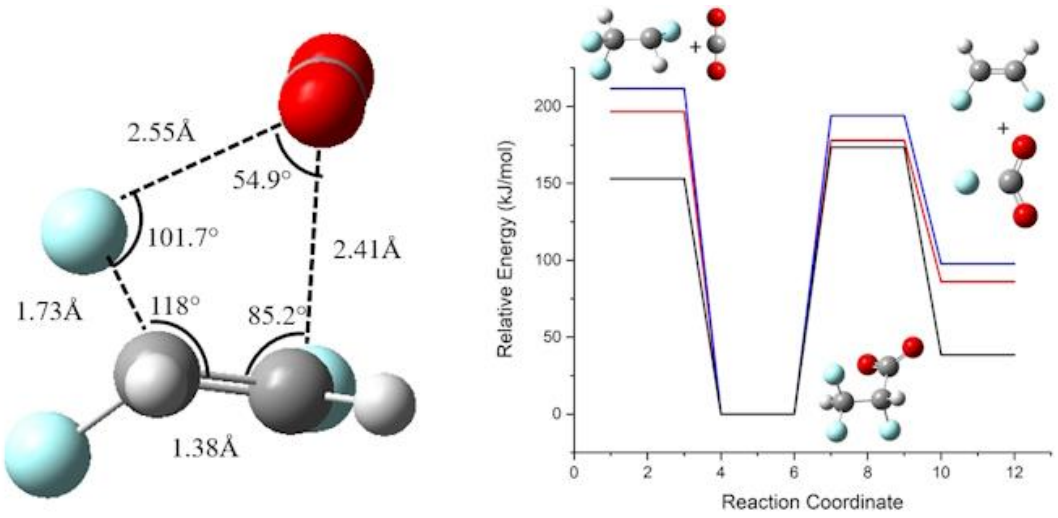


Figure A25. Transition state and potential minimum energy pathway leading to FCO_2^- or loss of CO_2 for the deprotonated 3,3,2-trifluoropropionic acid leading to the cis conformation for the neutral fluoroethene using thermal corrections at M06-2X/def2-tzvp level of theory and energetics from DLPNO-CCSD(T)/def2-tzvp. (Black trace) relative standard Gibbs energy, (red trace) relative zero-point corrected energy, and (blue trace) relative electronic energy.

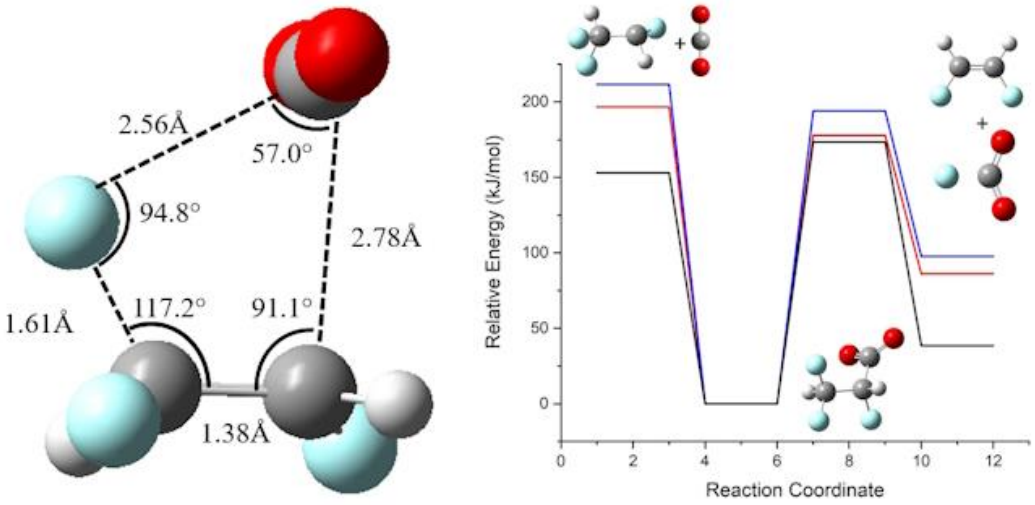


Figure A26. Transition state and potential minimum energy pathway leading to FCO_2^- or loss of CO_2 for the deprotonated 3,3,2-trifluoropropionic acid leading to the trans conformation for the neutral fluoroethene using thermal corrections at M06-2X/def2-tzvp

level of theory and energetics from DLPNO-CCSD(T)/def2-tzvp. (Black trace) relative standard Gibbs energy, (red trace) relative zero-point corrected energy, and (blue trace) relative electronic energy.

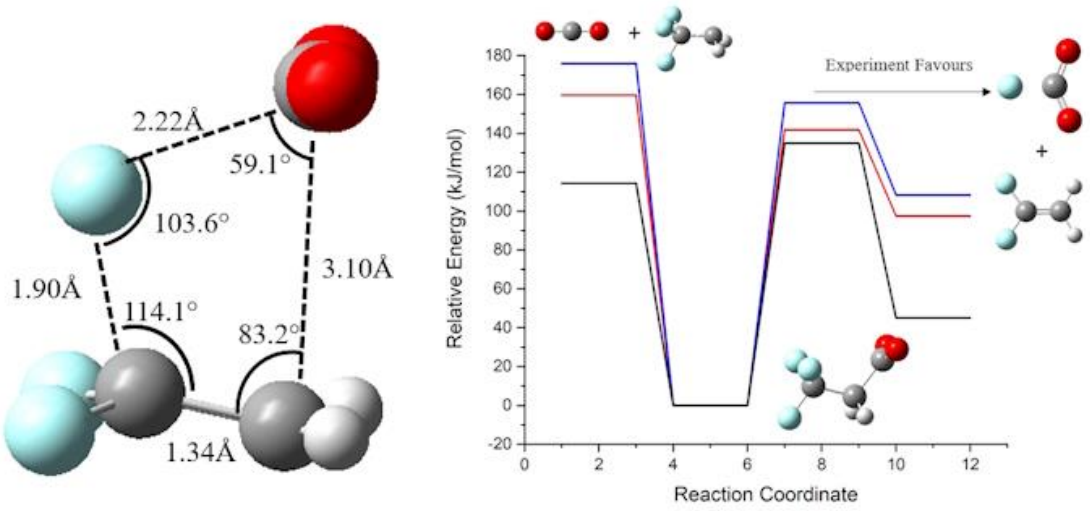


Figure A27. Transition state and potential minimum energy pathway leading to FCO_2^- or loss of CO_2 for the deprotonated 3,3,3-trifluoropropionic acid using thermal corrections at M06-2X/def2-tzvp level of theory and energetics from DLPNO-CCSD(T)/def2-tzvp. (Black trace) relative standard Gibbs energy, (red trace) relative zero-point corrected energy, and (blue trace) relative electronic energy.

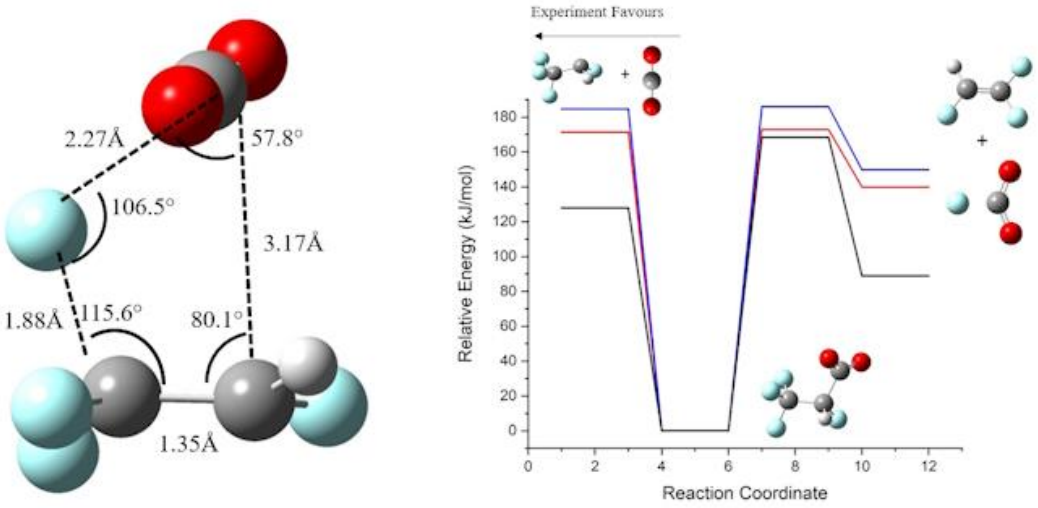


Figure A28. Transition state and potential minimum energy pathway leading to FCO_2^- or loss of CO_2 for the deprotonated 3,3,3,2-tetrafluoropropionic acid at M06-2X/def2-tzvp level of theory and energetics from DLPNO-CCSD(T)/def2-tzvp. (Black trace) relative standard

Gibbs energy, (red trace) relative zero-point corrected energy, and (blue trace) relative electronic energy.

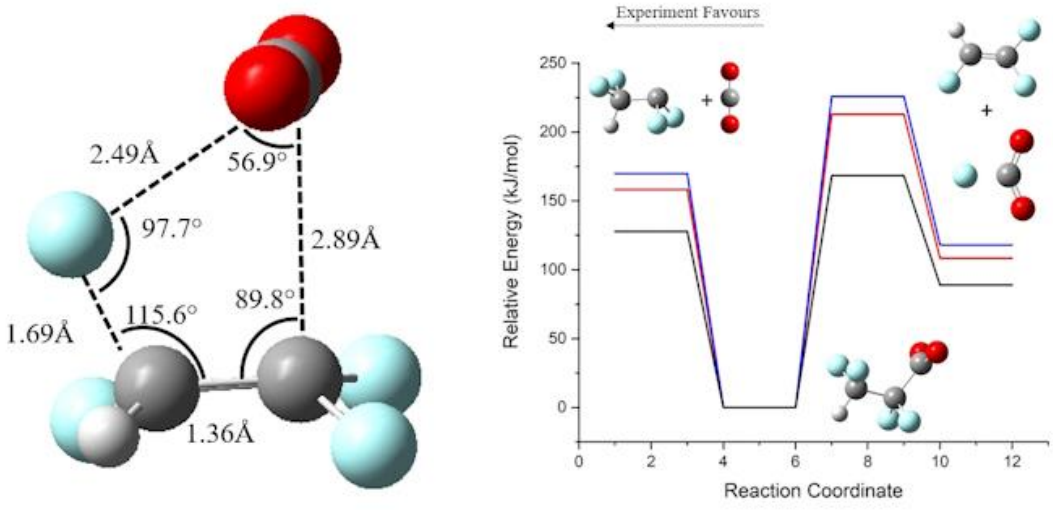


Figure A29. Transition state and potential minimum energy pathway leading to FCO_2^- or loss of CO_2 for the deprotonated 3,3,2,2-tetrafluoropropionic acid using thermal corrections at M06-2X/def2-tzvp level of theory and energetics from DLPNO-CCSD(T)/def2-tzvp. (Black trace) relative standard Gibbs energy, (red trace) relative zero-point corrected energy, and (blue trace) relative electronic energy.

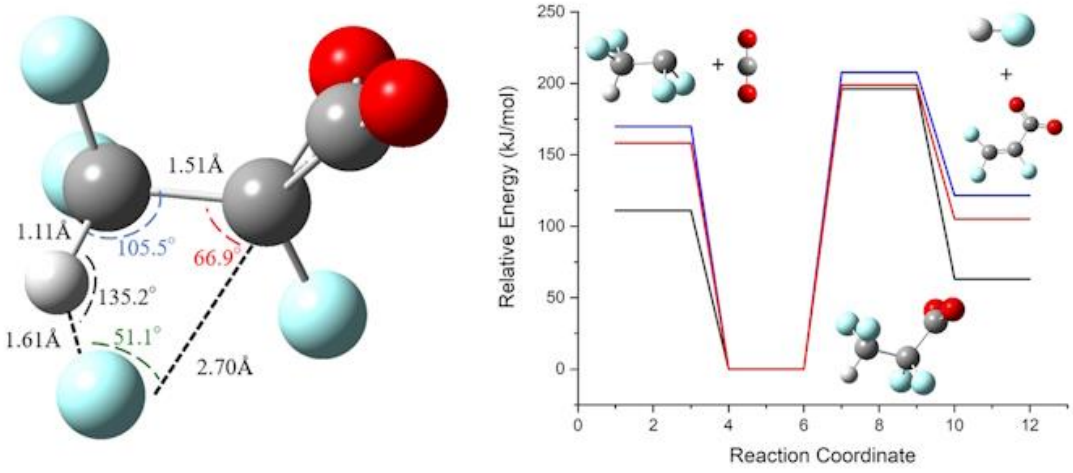


Figure A30. Transition state and potential minimum energy pathway leading to HF loss for the deprotonated 3,3,2,2-tetrafluoropropionic acid at M06-2X/def2-tzvp level of theory and energetics from DLPNO-CCSD(T)/def2-tzvp. (Black trace) relative standard Gibbs energy, (red trace) relative zero-point corrected energy, and (blue trace) relative electronic energy.

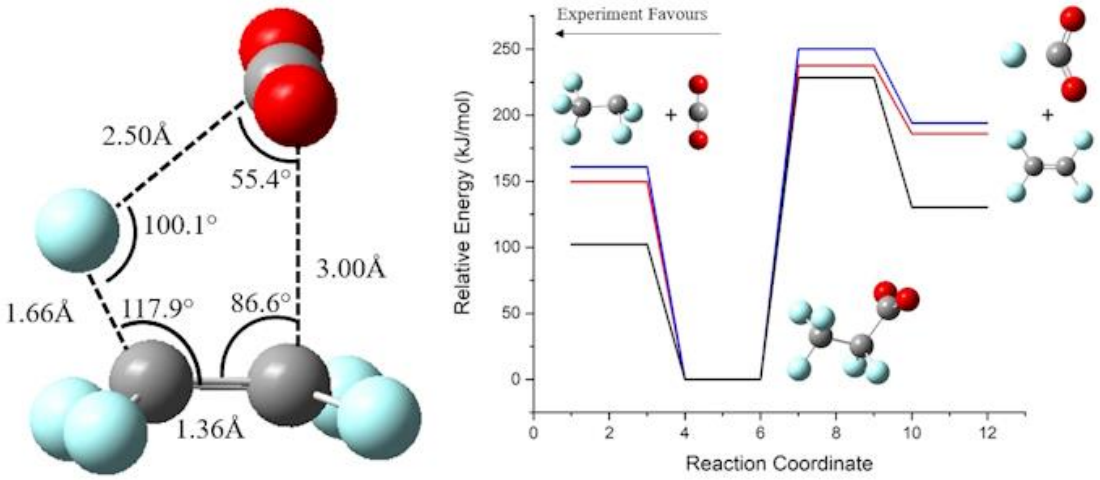


Figure A31. Transition state and potential minimum energy pathway leading to FCO_2^- or loss of CO_2 for the deprotonated pentafluoropropionic acid at M06-2X/def2-tzvp level of theory and energetics from DLPNO-CCSD(T)/def2-tzvp. (Black trace) relative standard Gibbs energy, (red trace) relative zero-point corrected energy, and (blue trace) relative electronic energy.

Table A8. Calculated thresholds for production of CO_2 and FCO_2^- for 3-monofluoropropionic acid (3-F), 3,2-difluoropropionic acid, 3,3-difluoropropionic acid (3,3-F_2), 3,2,2-trifluoropropionic acid (3,2,2-F_3), 3,3,2-trifluoropropionic acid (3,3,2-F_3), 3,3,3-trifluoropropionic acid (3,3,3-F_3), 3,3,2,2-tetrafluoropropionic acid (3,3,2,2-F_4), 3,3,3,2-tetrafluoropropionic acid (3,3,3,2-F_4), and pentafluoropropionic acid (F_5). Calculations were conducted at the M06-2X/aug-cc-pVTZ level of theory with single point energy calculated with DLPNO-CCSD(T)/aug-cc-pVTZ.

Precursor Ion	CO_2 loss			FCO_2^- TS			FCO_2^- Production		
	ΔE_{elec}	ΔE_{zpe}	$\Delta G°$	$\Delta E_{elec‡}$	$\Delta E_{zpe‡}$	$\Delta G‡°$	ΔE_{elec}	ΔE_{zpe}	$\Delta G°$
3-F	190	159	116	177	162	159	33.8	18.7	-24.6
3,2-F_2	113	90.1	44.0	193	179	176	45.1	31.4	-16.4
3,3-F_2	198	181	139	142	126	122	47.8	35.1	-12.2
3,2,2-F_3	216	203	159	235	221	218	67.5	55.7	48.4
3,3,2-F_3	212	197	153	200(trans) 194(cis)	184(trans) 178(cis)	179(trans) 174(cis)	102(trans) 97.7(cis)	89.5(trans) 86.1(cis)	42.3(trans) 38.5(cis)
3,3,3-F_3	176	160	114	156	142	135	108	97.6	45.1
3,3,2,2-F_4	170	158	111	226	213	205	118	108	54.5
3,3,3,2-F_4	185	171	128	186	173	168	150	140	89.0
F_5	161	150	102	250	238	228	194	186	122

Table A11. Fragmentation efficiency of different vibrational modes for the deprotonated 3,3,3,2-tetrafluoropropionic acid.

Peak location (cm^{-1})	[$-CO_2$] Fragmentation	[FCO_2^-] Fragmentation	Total Fragmentation	Ratio of [$-CO_2$]	Ratio of [FCO_2^-]
677	215914.1	344464.3	560378.3	0.385	0.615
757	532861.3	1052638.6	1585499.9	0.336	0.664
859	69946.7	79069.2	149015.8	0.469	0.531
1088	1582371.5	3687565.7	5269937.1	0.300	0.700
1154	1821569.1	3695129.0	5516698.1	0.330	0.670
1250	1642505.0	3588213.5	5230718.5	0.314	0.686
1319	855477.8	1834271.6	2689749.4	0.318	0.682
1701	1752358.1	3162341.6	4914699.7	0.357	0.643

Table A10. Fragmentation efficiency of different vibrational modes for the deprotonated 3,3,2,2-tetrafluoropropionic acid.

Peak location (cm^{-1})	[$-CO_2$] Fragmentation	[FCO_2^-] Fragmentation	Total Fragmentation	Ratio of [$-CO_2$]	Ratio of [FCO_2^-]
777	4170807.9	111027.4	4281835.3	0.974	0.026
819	1793842.2	5797.6	1799639.9	0.997	0.003
927	121092.1	2873.2	123965.2	0.977	0.023
1023	1770206.8	41542.0	1811748.8	0.977	0.023
1107	6185785.4	232565.1	6418350.5	0.964	0.036
1215	1970389.3	72695.7	2043085.1	0.964	0.036
1326	1229711.7	60813.4	1290525.0	0.953	0.047
1719	6970919.3	195711.4	7166630.8	0.973	0.027

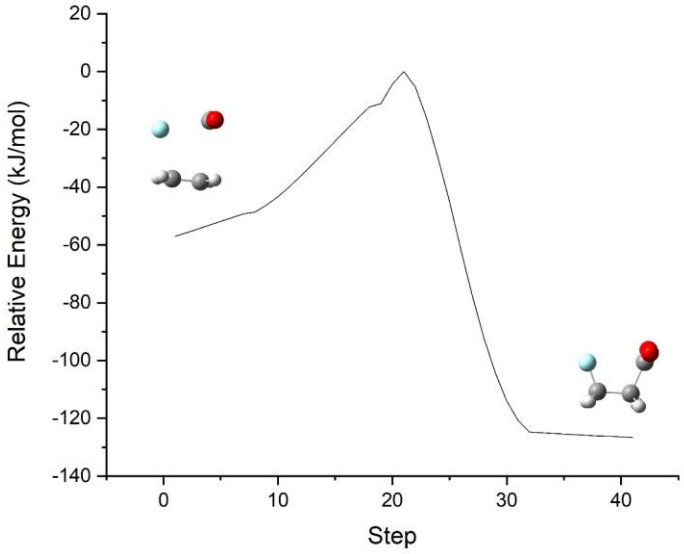


Figure A32. IRC profile for the deprotonated 3-monofluoropropionic acid. Step 20 is the transition state.

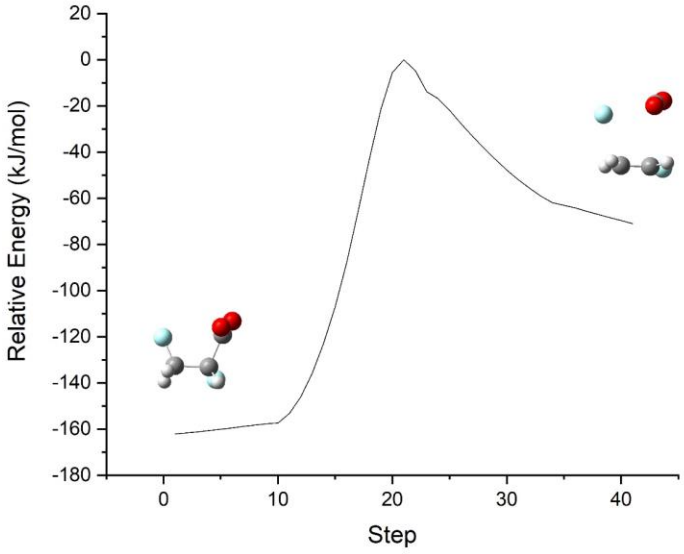


Figure A33. IRC profile for the deprotonated 3,2-difluoropropionic acid. Step 20 is the transition state.

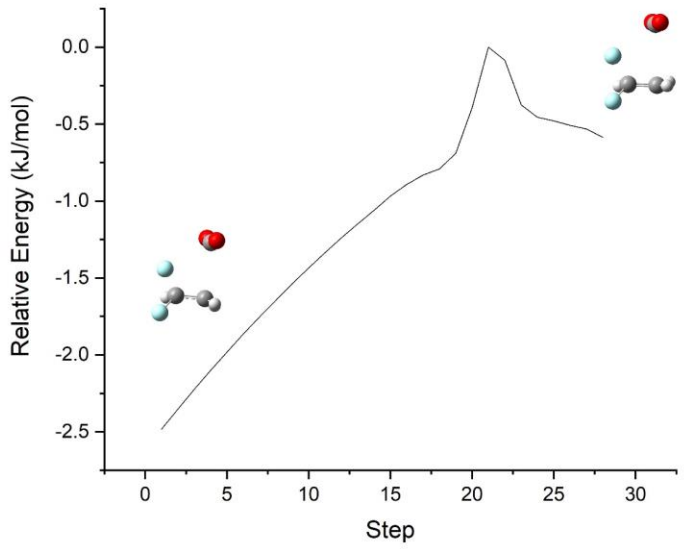


Figure A34. IRC profile for the deprotonated 3,3-difluoropropionic acid. Step 20 is the transition state.

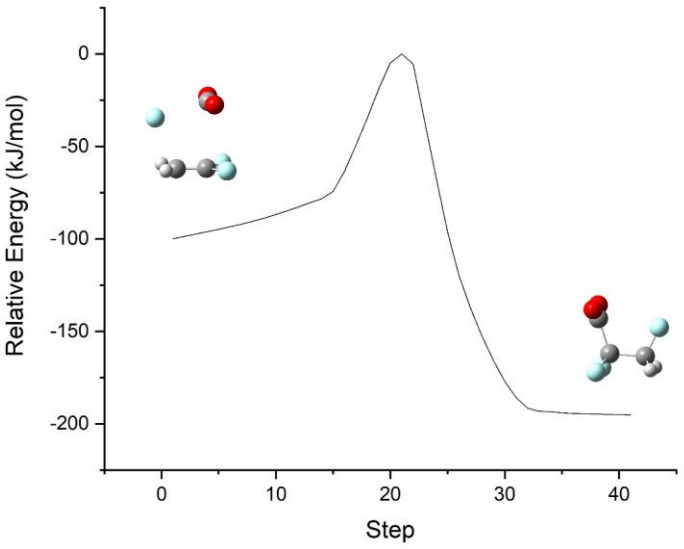


Figure A35. IRC profile for the deprotonated 3,2,2-trifluoropropionic acid. Step 20 is the transition state.

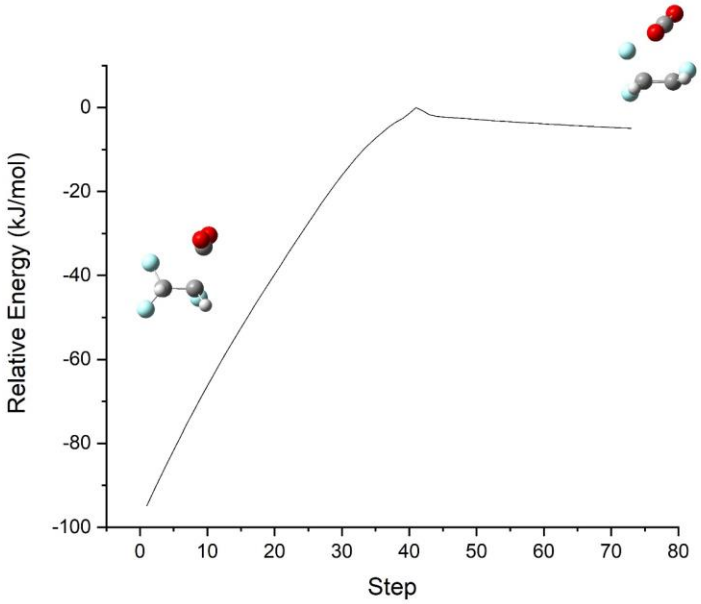


Figure A36. IRC profile for the deprotonated 3,3,2-trifluoropropionic acid leading to the cis conformation for the ethene. Step 20 is the transition state.

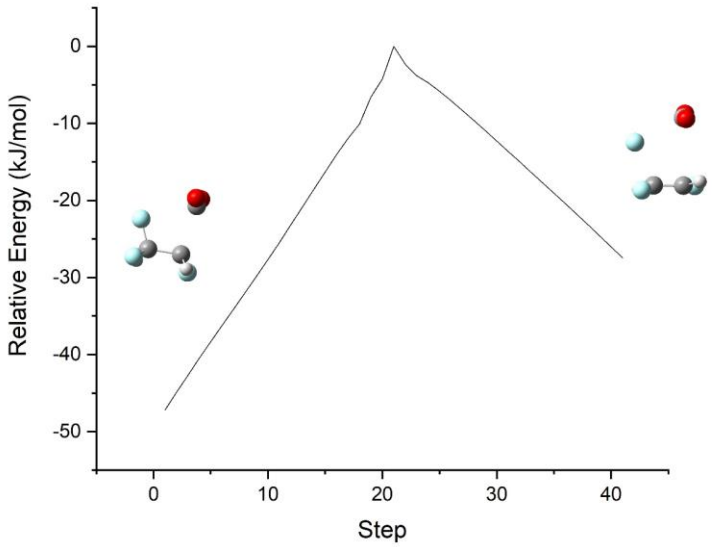


Figure A37. IRC profile for the deprotonated 3,3,2-trifluoropropionic acid leading to the trans conformation for the ethene. Step 20 is the transition state.

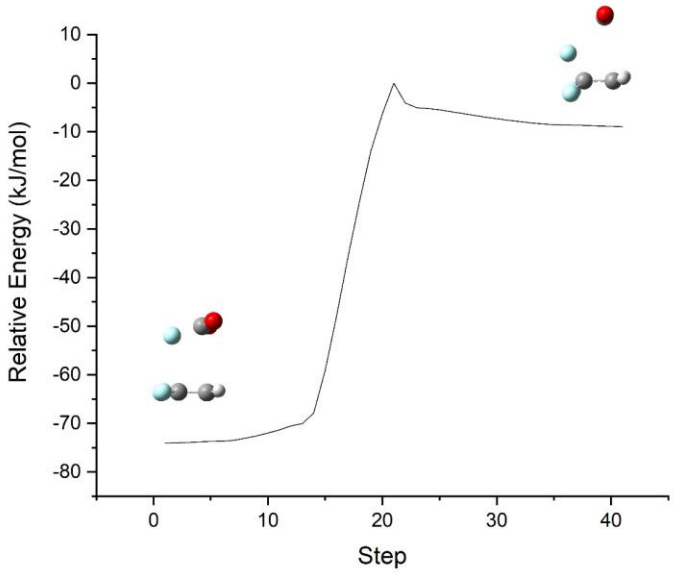


Figure A38. IRC profile for the deprotonated 3,3,3-trifluoropropionic acid. Step 20 is the transition state.

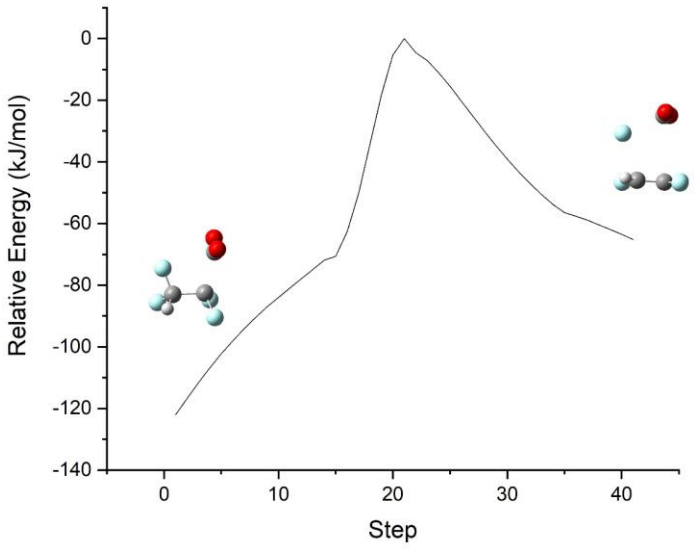


Figure A39. IRC profile for the deprotonated 3,3,2,2-tetrafluoropropionic acid leading to FCO_2^-. Step 20 is the transition state.

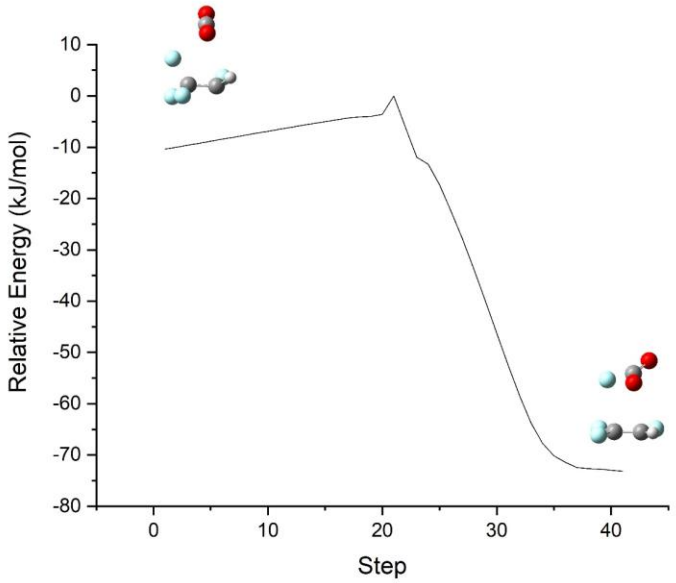


Figure A40. IRC profile for the deprotonated 3,3,3,2-tetrafluoropropionic acid. Step 20 is the transition state.

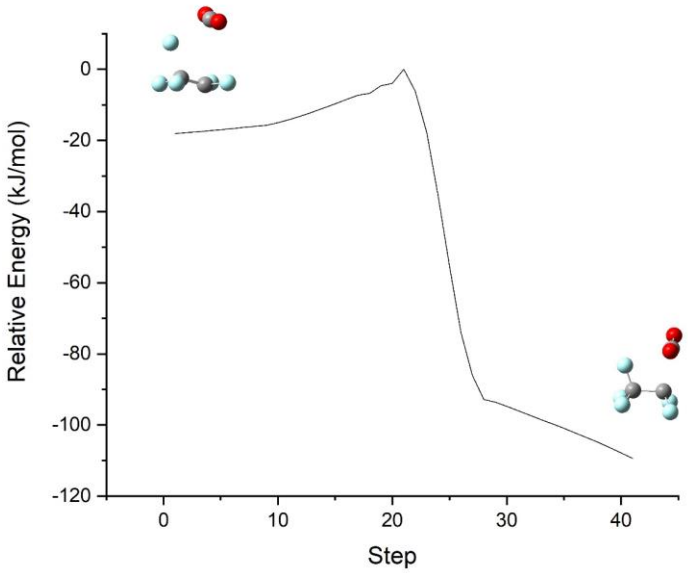


Figure A41. IRC profile for the deprotonated pentafluoropropionic acid. Step 20 is the transition state.

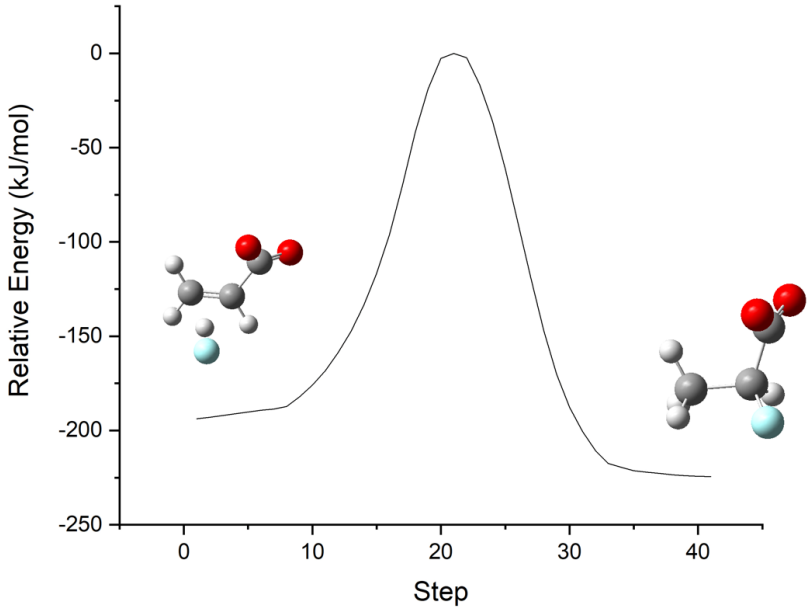


Figure A42. IRC profile for the deprotonated 2-monofluoropropionic acid leading to HF loss. Step 20 is the transition state.

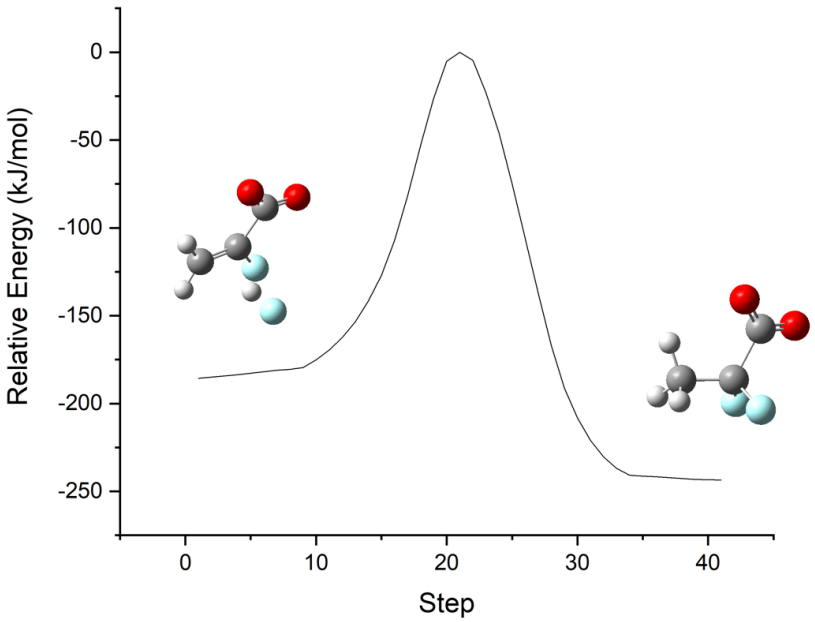


Figure A43. IRC profile for the deprotonated 2,2-difluoropropionic acid leading to HF loss. Step 20 is the transition state.

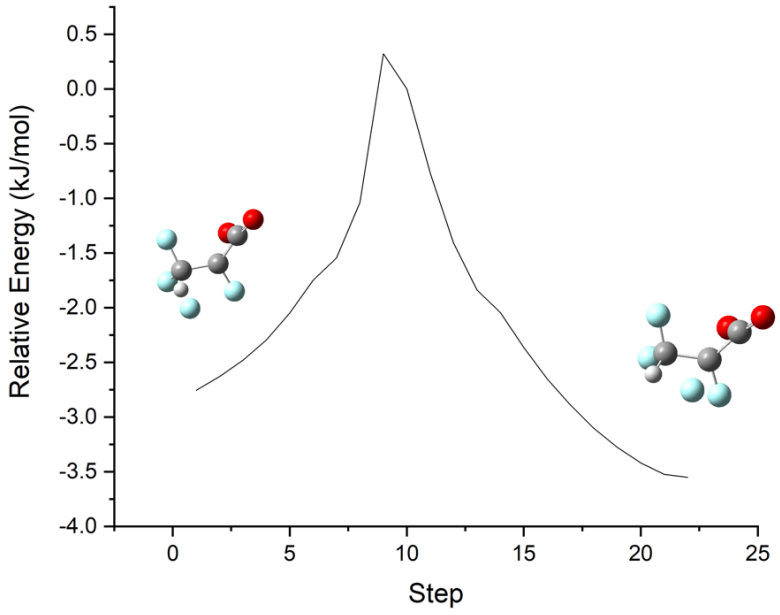


Figure A44. IRC profile for the deprotonated 3,3,2,2-tetrafluoropropionic acid leading to HF loss. Step 10 is the transition state.

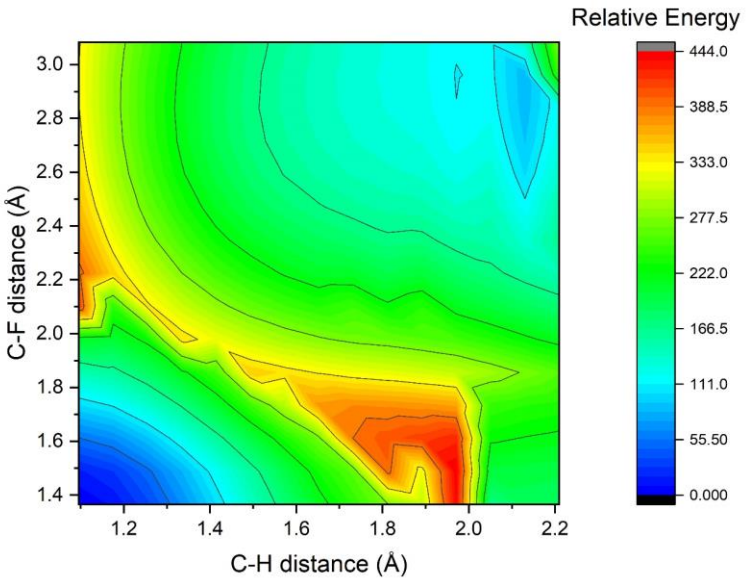


Figure A45. Heatmap of a scan for the potential energy surface of the deprotonated 3,3,2,2-tetrafluoropropionic acid leading to HF loss at M06-2X/def2-tzvp level of theory. A total of 100 points are sampled with ten points along each axis.

Geometries for chapter 3 can be found through the following link:

https://iochem-bd.bsc.es/browse/handle/100/337081

Geometries for chapter 3 can be found through the following link:

https://iochem-bd.bsc.es/browse/handle/100/337081

Appendix B

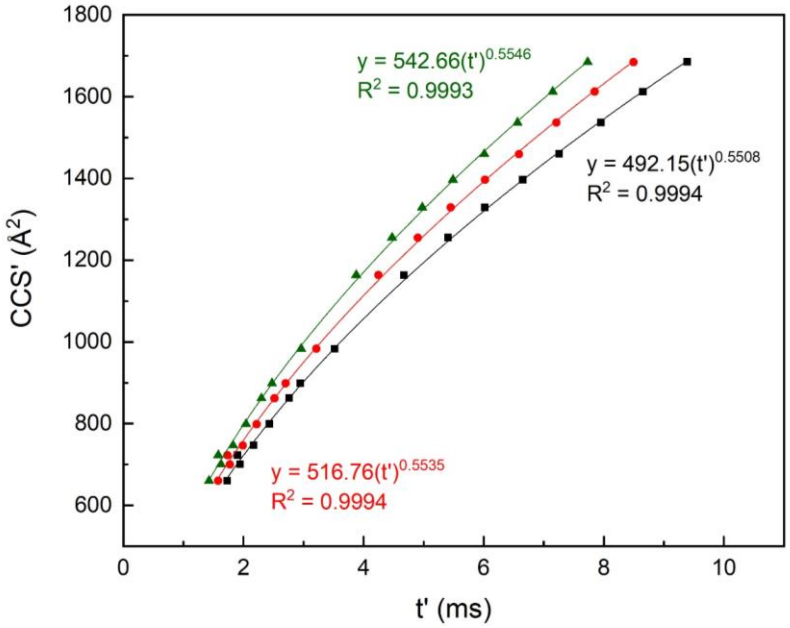


Figure B1. CCS_{TWIMS} calibration curves using the Waters Major Mix IMS/Tof calibration kit. A power function is used to fit to the data. *a* and *n* are fit parameters. The data was acquired at travelling wave velocities of 500 m s^{-1} at wave height of 40V (green), 38V (red), and 36V (black).

Table B1. Calibrant ion's m/z, CCS, and CCS′ values are listed. Arrival times for the calibrant ions were determined at velocities of 500 m s^{-1} at the WH of 36V (green), 38V (red), and 40V (black), respectively. Arrival times (t_A) are corrected for their mass dependent drift times (t').

m/z	CCS/Å^2	WH/V	CCS′/Å^2	t_A/ms	t′/ms
213.05	145.2	40	722.39	1.60	1.58
		38	722.39	1.75	1.73
		36	722.39	1.92	1.90
309.07	170.1	40	861.98	2.32	2.30
		38	861.98	2.54	2.51
		36	861.98	2.79	2.76
318.98	130.1	40	660.13	1.45	1.43
		38	660.13	1.60	1.58
		36	660.13	1.76	1.73
368.98	137.2	40	699.99	1.65	1.62
		38	699.99	1.80	1.77
		36	699.99	1.98	1.95
378.21	192.5	40	982.98	2.99	2.96
		38	982.98	3.24	3.21
		36	982.98	3.55	3.52
418.98	145.7	40	746.51	1.86	1.83
		38	746.51	2.02	1.99
		36	746.51	2.20	2.17
468.98	155.4	40	798.88	2.07	2.04
		38	798.88	2.25	2.22
		36	798.88	2.47	2.44
554.26	225.3	40	1163.28	3.91	3.88
		38	1163.28	4.28	4.25
		36	1163.28	4.71	4.68
568.96	173.9	40	898.45	2.51	2.48
		38	898.45	2.74	2.70
		36	898.45	2.98	2.95
656.3368	242.1	40	1254.72	4.51	4.47
		38	1254.72	4.94	4.91
		36	1254.72	5.44	5.41
727.3739	255.9	40	1328.90	5.01	4.98
		38	1328.90	5.49	5.45
		36	1328.90	6.06	6.02
798.411	268.5	40	1396.64	5.53	5.49
		38	1396.64	6.06	6.02
		36	1396.64	6.69	6.65
869.4481	280.2	40	1459.52	6.05	6.01

		38	1459.52	6.63	6.59
		36	1459.52	7.30	7.26
940.4852	294.6	40	1536.34	6.61	6.56
		38	1536.34	7.25	7.21
		36	1536.34	8.00	7.96
1011.522	308.8	40	1612.03	7.19	7.15
		38	1612.03	7.89	7.85
		36	1612.03	8.70	8.65
1082.559	322.4	40	1684.52	7.78	7.73
		38	1684.52	8.54	8.49
		36	1684.52	9.43	9.39

Table B2. $[B_{12}F_{12}{+}NH_2(CH_2)_nNH_2{+}H]^+$ (n = 2 – 12) and $HB_{12}F_{12}^-$, CCS, and CCS' values are listed. Arrival times for the calibrant ions were determined at velocities of 500 m s^{-1} at the wave height (WH) of 36V (c1), 38V (c2), and 40V (c3), respectively. Arrival times (t_A) are corrected for their mass dependent drift times (t').

Compound	WH/V	CCS/Å^2	CCS′/Å^2	t_A/ms	t′/ms
$HB_{12}F_{12}$	40	145.43	741.19	1.78	1.75
	38	145.67	742.43	1.95	1.92
	36	145.86	743.39	2.14	2.11
n = 2	40	181.54	930.17	2.67	2.64
	38	181.21	928.45	2.91	2.88
	36	180.15	923.05	3.16	3.13
n = 3	40	186.61	957.11	2.81	2.78
	38	186.16	954.81	3.06	3.03
	36	185.58	951.82	3.34	3.31
n = 4	40	190.47	977.83	2.92	2.89
	38	189.68	973.76	3.17	3.14
	36	189.36	972.15	3.47	3.44
n = 5	40	194.98	1001.89	3.05	3.02
	38	194.12	997.47	3.31	3.28
	36	193.98	996.73	3.63	3.60
n = 6	40	199.06	1023.69	3.17	3.14
	38	198.48	1020.73	3.45	3.42
	36	198.79	1022.31	3.80	3.77
n = 7	40	203.06	1045.13	3.29	3.26
	38	202.76	1043.58	3.59	3.56
	36	202.93	1044.45	3.95	3.92
n = 8	40	206.66	1064.46	3.40	3.37
	38	206.66	1064.44	3.72	3.69
	36	207.00	1066.22	4.10	4.07
n = 9	40	210.88	1086.97	3.53	3.50
	38	210.80	1086.54	3.86	3.83
	36	210.73	1086.21	4.24	4.21
n = 10	40	214.70	1107.42	3.65	3.62
	38	214.87	1108.29	4.00	3.97
	36	214.68	1107.30	4.39	4.36
n = 11	40	217.17	1120.86	3.73	3.70
	38	217.11	1120.53	4.08	4.05
	36	217.23	1121.16	4.49	4.46
n = 12	40	219.29	1132.51	3.80	3.77
	38	219.03	1131.15	4.15	4.12
	36	218.96	1130.77	4.56	4.53

Table B3. Relative energy between the different conformations of the singly charged species. Energies are reported in kJ/mol.

Length, Conformation	ΔE_{elec}	ΔE_{zpe}	ΔH	ΔS	$\Delta G°$
2, monodentate	18.0	17.9	18.8	2.6	16.2
2, bidentate	18.1	18.0	18.9	2.5	16.3
2, proton-sharing	0.0	0.1	0.0	0.1	0.0
3, monodentate	36.2	34.9	37.0	6.3	30.6
3, bidentate	34.0	33.3	34.8	4.3	30.5
3, proton-sharing	0.0	0.0	0.0	0.0	0.0
4, monodentate	29.4	25.3	27.7	8.2	19.5
4, bidentate	12.1	10.1	11.7	3.8	7.9
4, proton-sharing	0.0	0.0	0.0	0.0	0.0
5, monodentate	35.3	30.9	33.5	9.0	24.5
5, bidentate	34.3	32.2	34.4	5.1	29.3
5, proton-sharing	0.0	0.0	0.0	0.0	0.0
6, monodentate	43.8	37.2	40.8	12.5	28.3
6, bidentate	39.7	35.2	38.0	7.5	30.6
6, proton-sharing	0.0	0.0	0.0	0.0	0.0
7, monodentate	46.5	40.8	43.9	10.2	33.7
7, bidentate	43.5	40.3	42.2	4.1	38.1
7, proton-sharing	0.0	0.0	0.0	0.0	0.0
8, monodentate	37.9	32.8	38.4	16.3	22.2
8, bidentate	22.9	19.4	23.9	10.6	13.4
8, proton-sharing	0.0	0.0	0.0	0.0	0.0
9, monodentate	20.0	16.7	17.9	11.6	10.3
9, bidentate	1.0	0.0	0.0	3.9	0.0
9, proton-sharing	0.0	4.0	1.3	0.0	5.3
10, monodentate	36.4	28.2	32.2	15.5	16.6
10, bidentate	8.5	5.0	6.8	3.8	3.0
10, proton-sharing	0.0	0.0	0.0	0.0	0.0
11, monodentate	25.1	15.5	17.9	11.8	8.5
11, bidentate	6.7	1.7	4.9	7.3	0.0
11, proton-sharing	0.0	0.0	0.0	0.0	2.4
12, monodentate	35.6	31.8	33.6	12.7	23.0
12, bidentate	0.0	0.0	0.0	2.1	0.0
12, proton-sharing	0.3	3.7	1.9	0.0	4.0

Table B4. Proton affinity and gas-phase basicity of the neutral diamino alkane, $N_2H(CH_2)_nNH_2$ (n = 2-12). Energies are reported in kJ mol^{-1}.

n	Proton Affinity	Gas-phase basicity
2	-923.43	-915.85
3	-929.23	-921.15
4	-931.29	-922.95
5	-932.92	-924.51
6	-933.65	-925.22
7	-931.53	-923.13
8	-932.46	-924.05
9	-933.02	-924.63
10	-933.54	-925.16
11	-935.35	-926.88
12	-934.20	-925.82

Table B5. Proton affinity and gas-phase basicity of the doubly charged species, $[N_2H(CH_2)_nNH_2+H]^+$ (n = 2-12). Energies are reported in kJ mol^{-1}.

n	Proton Affinity	Gas-phase basicity
2	-516.08	-506.55
3	-600.75	-591.62
4	-661.52	-652.56
5	-705.24	-696.32
6	-739.02	-730.11
7	-766.97	-758.13
8	-787.09	-778.22
9	-803.25	-794.38
10	-816.54	-807.63
11	-826.75	-817.79
12	-836.83	-827.92

Table B6. Binding energy for the doubly charged clusters yielding $HB_{12}F_{12}^-$, denoted by the length of the diaminoalkane.

Cluster	ΔE_{elec}	ΔE_{zpe}	ΔH	ΔS	$\Delta G°$
$[2(B_{12}F_{12}) + N_2H(CH_2)_nNH_2 + 2H]^{2-} \rightarrow [(B_{12}F_{12}) + N_2H(CH_2)_nNH_2 + H]^- + HB_{12}F_{12}^-$					
$n = 2$	199.0	180.5	188.4	85.2	103.2
$n = 3$	202.8	180.7	180.0	66.1	113.9
$n = 4$	189.7	168.4	167.0	62.3	104.7
$n = 5$	176.8	157.9	156.6	60.5	96.0
$n = 6$	192.1	172.5	171.6	62.5	109.1
$n = 7$	186.7	168.1	167.1	61.4	105.6
$n = 8$	197.2	178.1	177.2	62.1	115.1
$n = 9$	194.0	175.1	174.1	62.3	111.8
$n = 10$	201.8	182.2	181.3	62.9	118.3
$n = 11$	202.3	182.0	177.1	54.8	122.2
$n = 12$	229.8	211.7	217.6	81.4	136.2

Table B7. Binding energy for the doubly charged clusters yielding $B_{12}F_{12}^{2-}$, denoted by the length of the diaminoalkane.

Cluster	ΔE_{elec}	ΔE_{zpe}	ΔH	ΔS	$\Delta G°$
$[2(B_{12}F_{12}) + N_2H(CH_2)_nNH_2 + 2H]^{2-} \rightarrow [(B_{12}F_{12}) + N_2H(CH_2)_nNH_2 + 2H] + B_{12}F_{12}^{2-}$					
$n = 2$	345.4	341.2	346.8	79.6	267.2
$n = 3$	322.0	316.4	312.9	58.2	254.6
$n = 4$	258.7	257.0	252.6	52.4	200.3
$n = 5$	233.6	234.4	230.6	50.9	179.7
$n = 6$	219.8	220.9	216.5	49.9	166.6
$n = 7$	204.1	205.9	201.6	49.6	152.0

n = 8	213.1	215.2	211.2	49.9	161.2
n = 9	187.3	190.4	185.7	47.9	137.7
n = 10	193.2	195.3	190.8	49.0	141.8
n = 11	195.9	198.5	194.2	48.9	145.3
n = 12	202.8	207.2	209.2	65.2	144.0

Table B8. Computed binding energies for the monodentate conformation, $[B_{12}F_{12} + H_2N(CH_2)_nNH_2 + H]^-$, dissociating to $H_2N(CH_2)_nNH_2 + HB_{12}F_{12}^-$, denoted by the length of the diaminoalkane.

Cluster	ΔE_{elec}	ΔE_{zpe}	ΔH	ΔS	$\Delta G°$
n = 2	244.2	223.6	223.1	53.7	169.3
n = 3	246.5	225.8	225.3	55.8	169.5
n = 4	243.2	223.3	222.9	56.2	166.7
n = 5	244.9	224.9	224.4	56.3	168.0
n = 6	243.9	224.0	223.4	56.9	166.5
n = 7	245.4	224.9	224.1	57.9	166.3
n = 8	243.9	223.6	222.8	58.0	164.8
n = 9	244.7	224.4	223.5	58.0	165.5
n = 10	243.3	223.6	222.7	57.8	164.9
n = 11	241.7	222.8	225.9	66.3	159.6
n = 12	243.0	223.4	222.5	58.6	163.9

Table B9. Computed binding energies for the bidentate conformation, $[B_{12}F_{12} + H_2N(CH_2)_nNH_2 + H]^-$, dissociating to $H_2N(CH_2)_nNH_2 + HB_{12}F_{12}^-$, denoted by the length of the diaminoalkane.

Cluster	ΔE_{elec}	ΔE_{zpe}	ΔH	ΔS	$\Delta G°$
n = 2	244.2	223.5	223.0	53.8	169.2
n = 3	248.8	227.3	227.5	57.8	169.6
n = 4	260.5	238.5	238.9	60.6	178.4
n = 5	245.9	223.6	223.5	60.3	163.2
n = 6	248.0	226.0	226.2	61.9	164.3
n = 7	248.4	225.3	225.8	64.0	161.8
n = 8	258.9	237.0	237.3	63.7	173.6
n = 9	263.7	241.1	241.4	65.6	175.8
n = 10	271.1	246.8	248.1	69.5	178.6
n = 11	260.1	236.6	238.9	70.8	168.1
n = 12	278.6	255.2	256.1	69.2	186.9

Table B10. Computed binding energies for the proton-sharing conformation, $[B_{12}F_{12} + H_2N(CH_2)_nNH_2 + H]^-$, dissociating to $H_2N(CH_2)_nNH_2 + HB_{12}F_{12}^-$, denoted by the length of the diaminoalkane.

Cluster	ΔE_{elec}	ΔE_{zpe}	ΔH	ΔS	$\Delta G°$
n = 2	262.2	241.5	241.9	56.4	185.5
n = 3	282.8	260.7	262.3	62.1	200.2
n = 4	272.6	248.6	250.6	64.4	186.2
n = 5	280.2	255.8	257.9	65.3	192.5
n = 6	287.7	261.2	264.2	69.4	194.8
n = 7	291.9	265.6	268.0	68.1	199.9

n = 8	281.9	256.4	261.2	74.2	187.0
n = 9	264.7	237.1	240.1	69.6	170.5
n = 10	279.7	251.8	254.9	73.3	181.6
n = 11	266.7	238.3	243.8	78.1	165.7
n = 12	278.3	251.5	254.1	71.3	182.8

Table B11. Computed binding energies for the monodentate conformation, $[B_{12}F_{12} + H_2N(CH_2)_nNH_2 + H]^-$ dissociating to $(H_2N(CH_2)_nNH_2+H)^+ + B_{12}F_{12}^{2-}$, denoted by the length of the diaminoalkane.

Cluster	ΔE_{elec}	ΔE_{zpe}	ΔH	ΔS	$\Delta G°$
n = 2	621.3	615.0	614.7	54.9	559.8
n = 3	617.4	611.6	611.2	56.5	554.7
n = 4	612.0	607.2	606.7	56.6	550.1
n = 5	611.9	607.1	606.5	56.7	549.8
n = 6	610.1	605.5	604.8	57.2	547.6
n = 7	613.8	608.5	607.7	58.2	549.5
n = 8	611.3	606.3	605.4	58.3	547.1
n = 9	611.5	606.5	605.6	58.4	547.2
n = 10	609.5	605.1	604.3	58.2	546.1
n = 11	606.0	602.6	605.6	66.6	539.1
n = 12	608.5	604.3	603.4	59.0	544.4

Table B12. Computed binding energies for the bidentate conformation, $[B_{12}F_{12} + H_2N(CH_2)_nNH_2 + H]^-$ dissociating to $(H_2N(CH_2)_nNH_2+H)^+ + B_{12}F_{12}^{2-}$, denoted by the length of the diaminoalkane.

Cluster	ΔE_{elec}	ΔE_{zpe}	ΔH	ΔS	$\Delta G°$
$n = 2$	621.3	615.0	614.6	55.0	559.6
$n = 3$	619.7	613.2	613.3	58.5	554.8
$n = 4$	629.3	622.4	622.7	61.0	561.7
$n = 5$	612.8	605.8	605.7	60.6	545.0
$n = 6$	614.2	607.5	607.6	62.2	545.4
$n = 7$	616.8	608.9	609.4	64.4	545.0
$n = 8$	626.3	619.7	619.9	64.0	555.9
$n = 9$	630.5	623.2	623.5	66.0	557.5
$n = 10$	637.4	628.3	629.7	69.9	559.8
$n = 11$	624.4	616.4	618.6	71.0	547.6
$n = 12$	644.1	636.1	636.9	69.6	567.4

Table B13. Computed binding energies for the proton-sharing conformation, $[B_{12}F_{12} + H_2N(CH_2)_nNH_2 + H]^-$ dissociating to $(H_2N(CH_2)_nNH_2+H)^+ + B_{12}F_{12}^{2-}$, denoted by the length of the diaminoalkane.

Cluster	ΔE_{elec}	ΔE_{zpe}	ΔH	ΔS	$\Delta G°$
$n = 2$	639.3	632.9	633.5	57.5	576.0
$n = 3$	653.7	646.5	648.1	62.8	585.3
$n = 4$	641.3	632.5	634.4	64.8	569.6
$n = 5$	647.1	638.0	640.1	65.7	574.4
$n = 6$	653.9	642.7	645.7	69.7	576.0
$n = 7$	660.3	649.2	651.6	68.4	583.1
$n = 8$	649.3	639.1	643.8	74.6	569.3

n = 9	566.4	559.8	558.0	57.9	500.1
n = 10	572.4	566.2	563.6	58.8	504.8
n = 11	562.5	554.7	554.6	63.8	490.8
n = 12	555.3	550.5	547.3	56.4	490.9

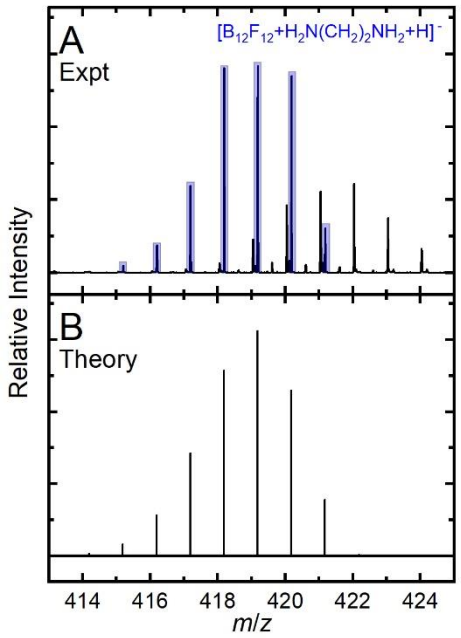


Figure B3. (A) experimental mass spectrum of $[B_{12}F_{12} + H_2N(CH_2)_nNH_2 + H]^-$, ($n$ = 2), (B) theoretical isotopic distribution of the same cluster.

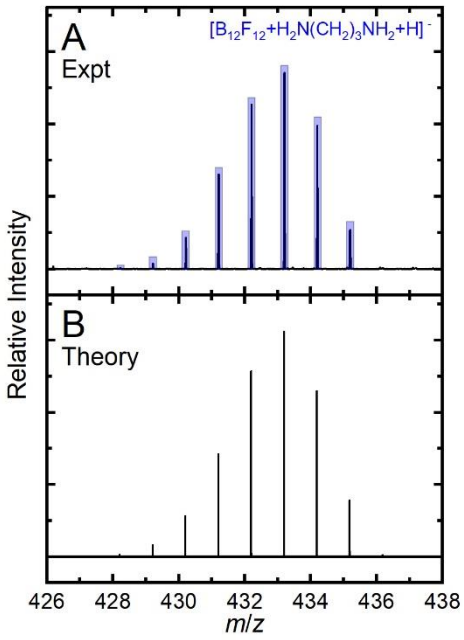


Figure B4. (A) experimental mass spectrum of $[B_{12}F_{12} + H_2N(CH_2)_nNH_2 + H]^-$, ($n$ = 3), (B) theoretical isotopic distribution of the same cluster.

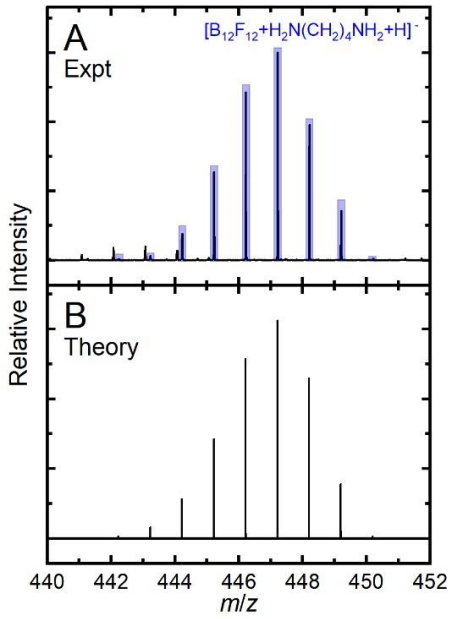


Figure B5. (A) experimental mass spectrum of $[B_{12}F_{12} + H_2N(CH_2)_nNH_2 + H]^-$, ($n$ = 4), (B) theoretical isotopic distribution of the same cluster.

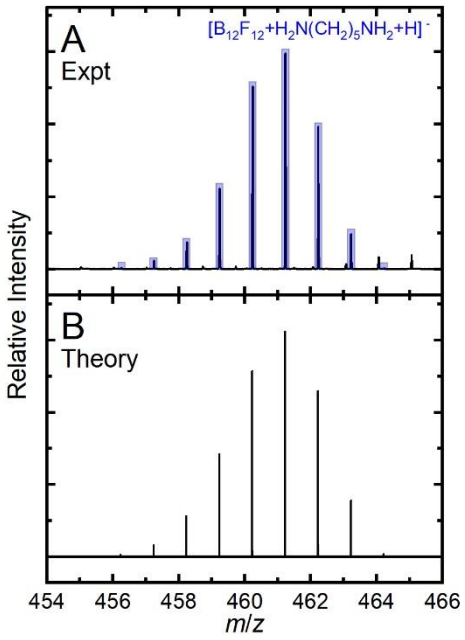


Figure B6. (A) experimental mass spectrum of $[B_{12}F_{12} + H_2N(CH_2)_nNH_2 + H]^-$, ($n$ = 5), (B) theoretical isotopic distribution of the same cluster.

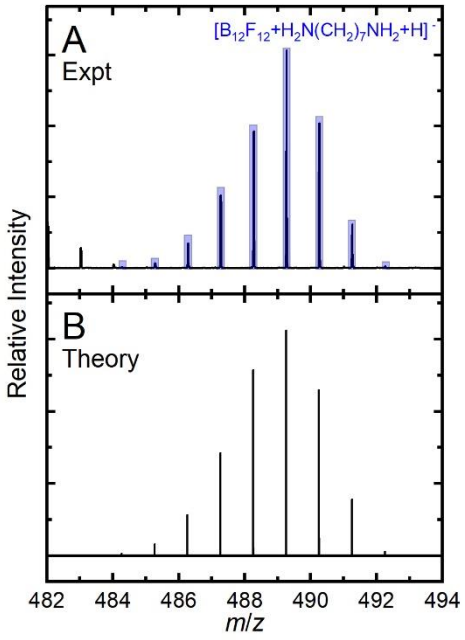


Figure B7. (A) experimental mass spectrum of $[B_{12}F_{12} + H_2N(CH_2)_nNH_2 + H]^-$, ($n$ = 7), (B) theoretical isotopic distribution of the same cluster.

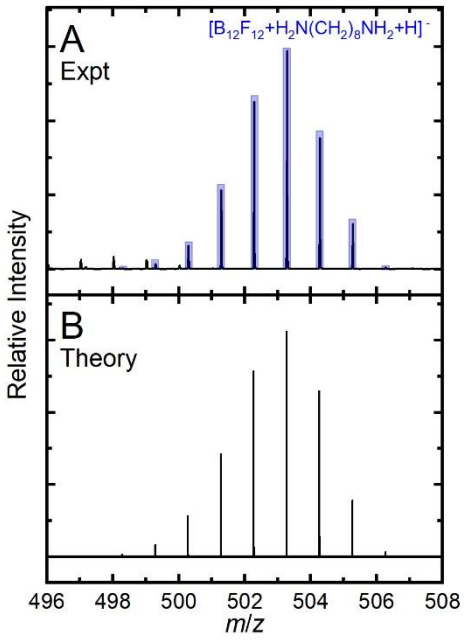


Figure B8. (A) experimental mass spectrum of $[B_{12}F_{12} + H_2N(CH_2)_nNH_2 + H]^-$, ($n$ = 8), (B) theoretical isotopic distribution of the same cluster.

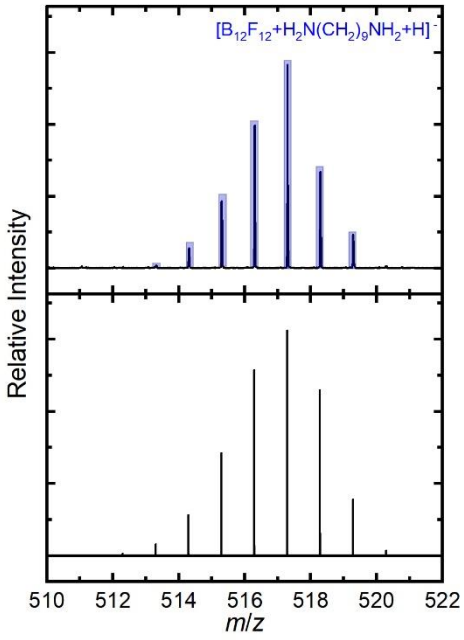


Figure B9. (A) experimental mass spectrum of $[B_{12}F_{12} + H_2N(CH_2)_nNH_2 + H]^-$, ($n$ = 9), (B) theoretical isotopic distribution of the same cluster.

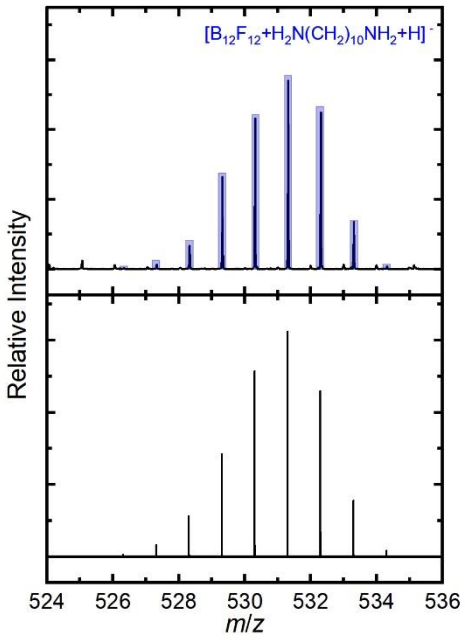


Figure B10. (A) experimental mass spectrum of $[B_{12}F_{12} + H_2N(CH_2)_nNH_2 + H]^-$, ($n$ = 10), (B) theoretical isotopic distribution of the same cluster.

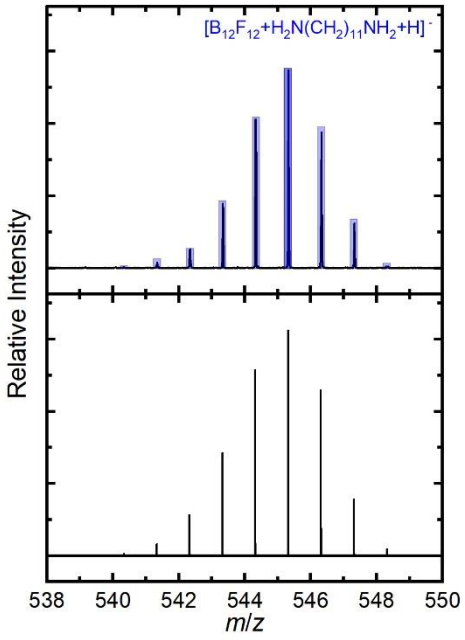


Figure B11. (A) experimental mass spectrum of $[B_{12}F_{12} + H_2N(CH_2)_nNH_2 + H]^-$, ($n$ = 11), (B) theoretical isotopic distribution of the same cluster.

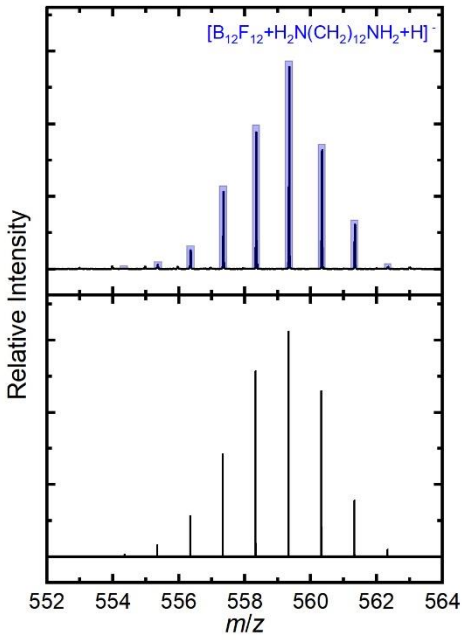


Figure B12. (A) experimental mass spectrum of $[B_{12}F_{12} + H_2N(CH_2)_nNH_2 + H]^-$, ($n$ = 12), (B) theoretical isotopic distribution of the same cluster.

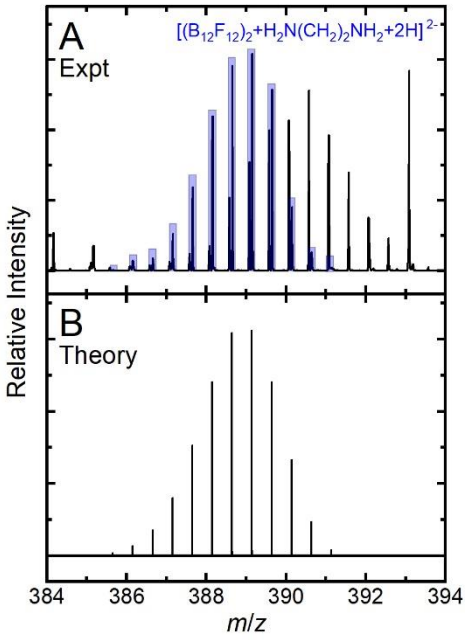


Figure B13. (A) experimental mass spectrum of $[2(B_{12}F_{12}) + H_2N(CH_2)_nNH_2 + 2H]^{2-}$, ($n$ = 2), (B) theoretical isotopic distribution of the same cluster.

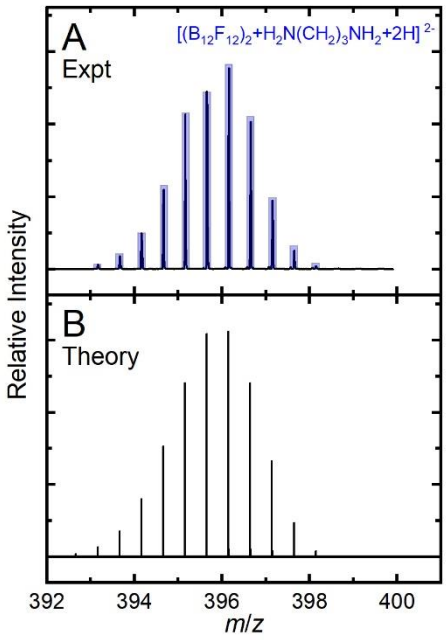


Figure B14. (A) experimental mass spectrum of $[2(B_{12}F_{12}) + H_2N(CH_2)_nNH_2 + 2H]^{2-}$ obtained by mobility selection ($n = 3$), (B) theoretical isotopic distribution of the same cluster.

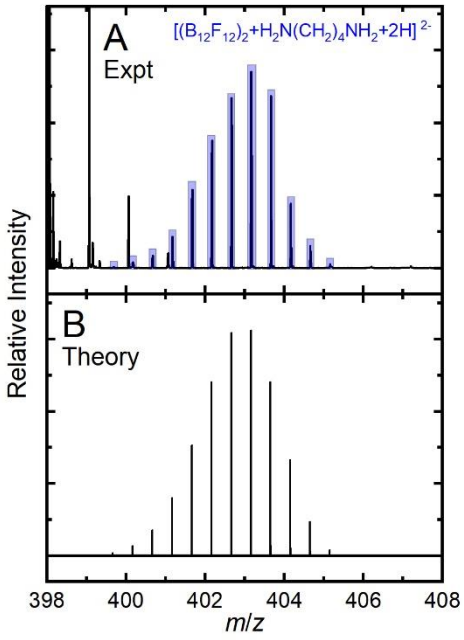


Figure B15. (A) experimental mass spectrum of $[2(B_{12}F_{12}) + H_2N(CH_2)_nNH_2 + 2H]^{2-}$, ($n$ = 4), (B) theoretical isotopic distribution of the same cluster.

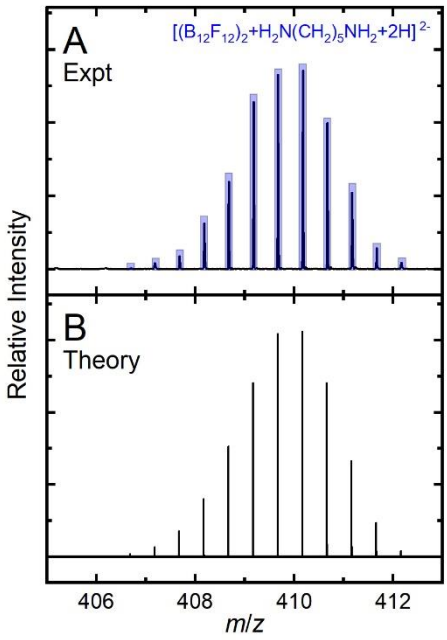


Figure B16. (A) experimental mass spectrum of $[2(B_{12}F_{12}) + H_2N(CH_2)_nNH_2 + 2H]^{2-}$, ($n$ = 5), (B) theoretical isotopic distribution of the same cluster.

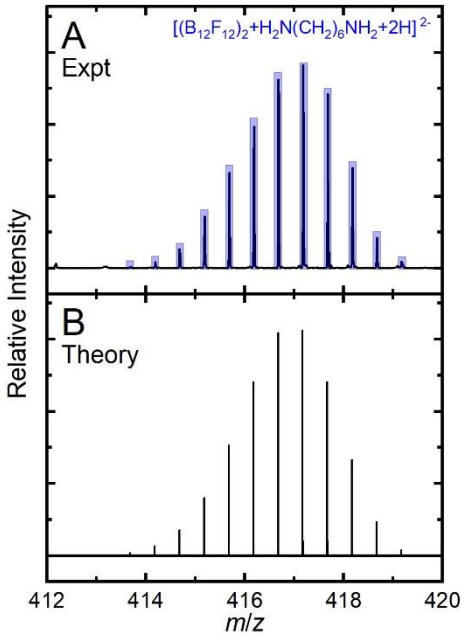


Figure B17. (A) experimental mass spectrum of $[2(B_{12}F_{12}) + H_2N(CH_2)_nNH_2 + 2H]^{2-}$, ($n$ = 6), (B) theoretical isotopic distribution of the same cluster.

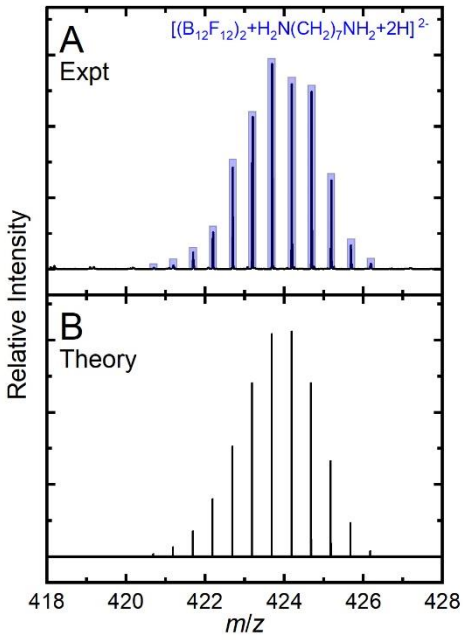


Figure B18. (A) experimental mass spectrum of $[2(B_{12}F_{12}) + H_2N(CH_2)_nNH_2 + 2H]^{2-}$, ($n$ = 7), (B) theoretical isotopic distribution of the same cluster.

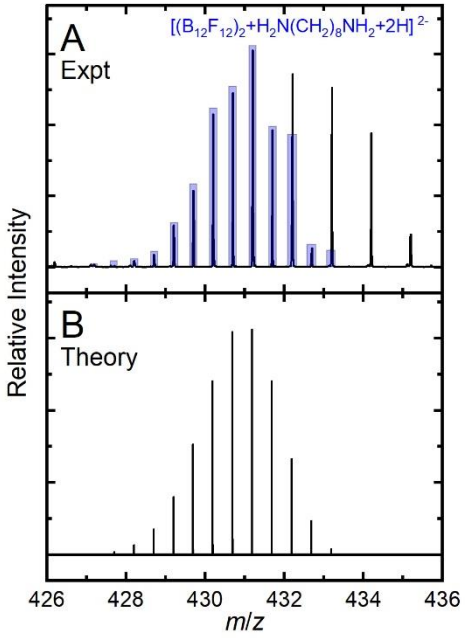


Figure B19. (A) experimental mass spectrum of $[2(B_{12}F_{12}) + H_2N(CH_2)_nNH_2 + 2H]^{2-}$, ($n$ = 8), (B) theoretical isotopic distribution of the same cluster.

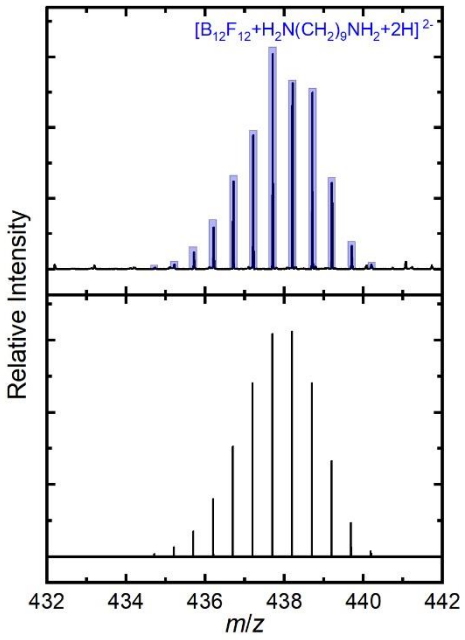


Figure B20. (A) experimental mass spectrum of $[2(B_{12}F_{12}) + H_2N(CH_2)_nNH_2 + 2H]^{2-}$, ($n$ = 9), (B) theoretical isotopic distribution of the same cluster.

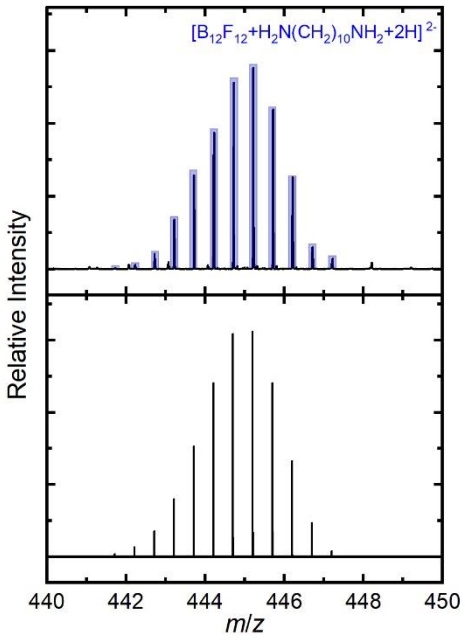


Figure B21. (A) experimental mass spectrum of $[2(B_{12}F_{12}) + H_2N(CH_2)_nNH_2 + 2H]^{2-}$, ($n$ = 10), (B) theoretical isotopic distribution of the same cluster.

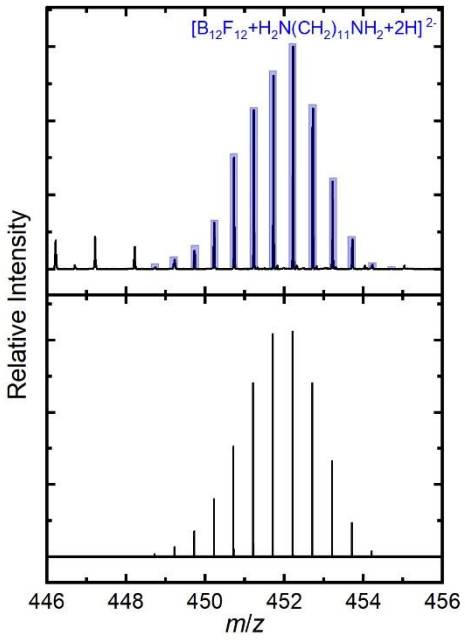


Figure B22. (A) experimental mass spectrum of $[2(B_{12}F_{12}) + H_2N(CH_2)_nNH_2 + 2H]^{2-}$, ($n$ = 11), (B) theoretical isotopic distribution of the same cluster.

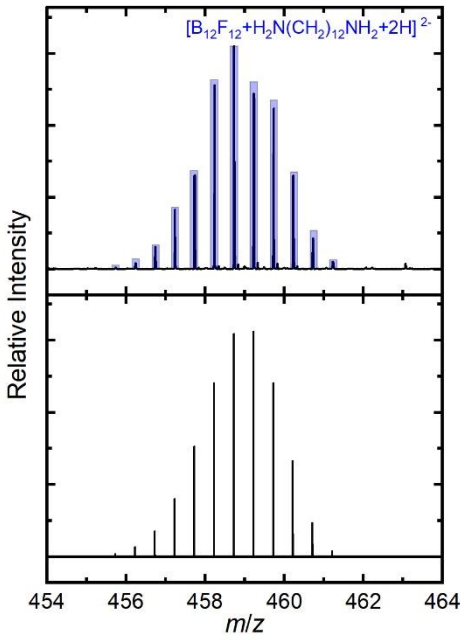


Figure B23. (A) experimental mass spectrum of $[2(B_{12}F_{12}) + H_2N(CH_2)_nNH_2 + 2H]^{2-}$, ($n$ = 12), (B) theoretical isotopic distribution of the same cluster.

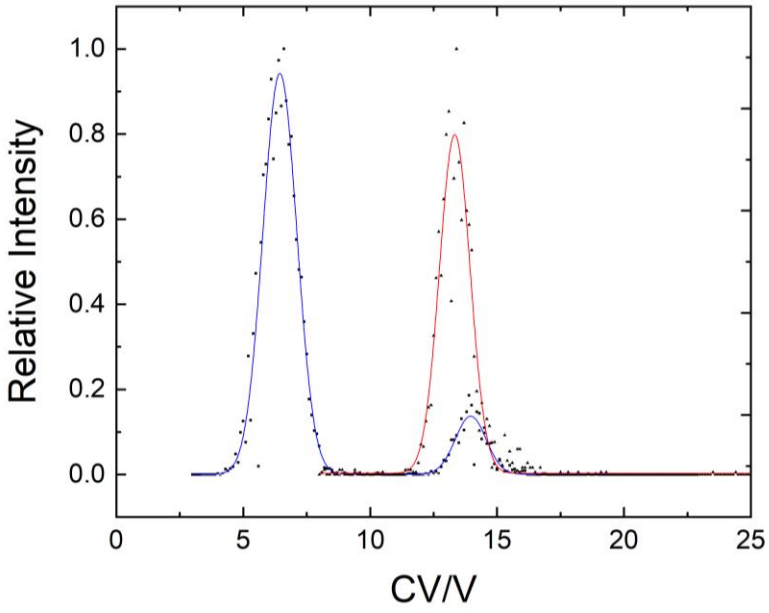


Figure B24. Ionogram of (blue) $[(B_{12}F_{12}) + H_2N(CH_2)_nNH_2 + H]^-$ and (red) $[2(B_{12}F_{12}) + H_2N(CH_2)_nNH_2 + 2H]^{2-}$ (n = 2) at SV=3800V.

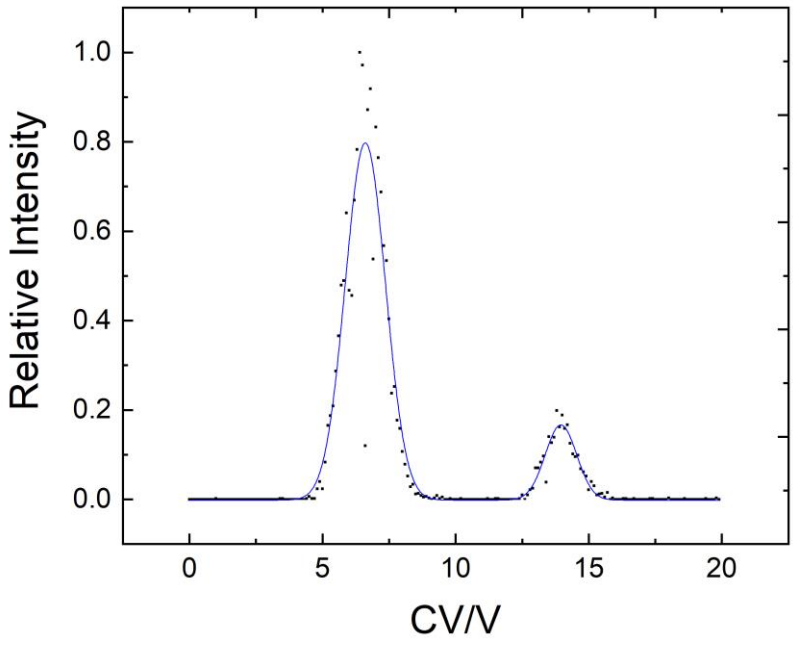


Figure B25. Ionogram of (blue) $[(B_{12}F_{12}) + H_2N(CH_2)_nNH_2 + H]^-$ (n = 3) at SV=3800V.

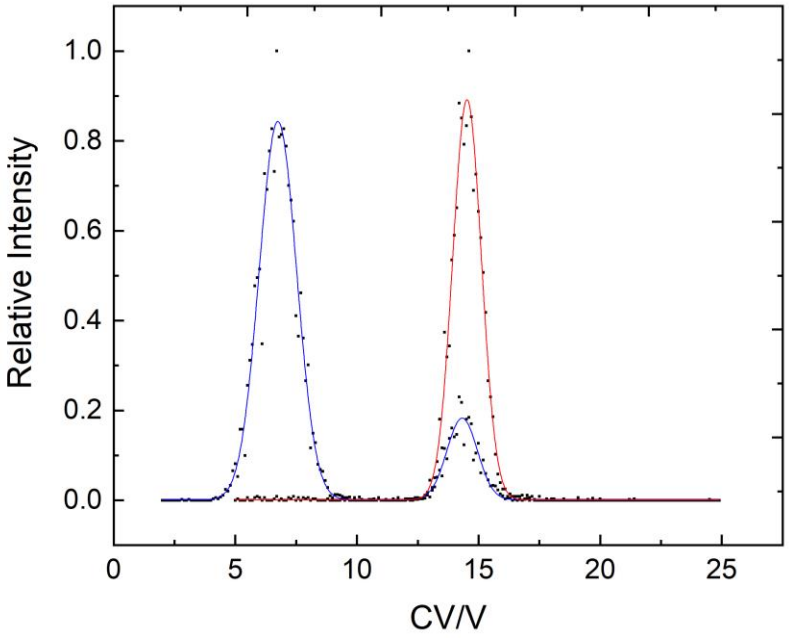


Figure B26. Ionogram of (blue) $[(B_{12}F_{12}) + H_2N(CH_2)_nNH_2 + H]^-$ and (red) $[2(B_{12}F_{12}) + H_2N(CH_2)_nNH_2 + 2H]^{2-}$ (n = 4) at SV=3800V.

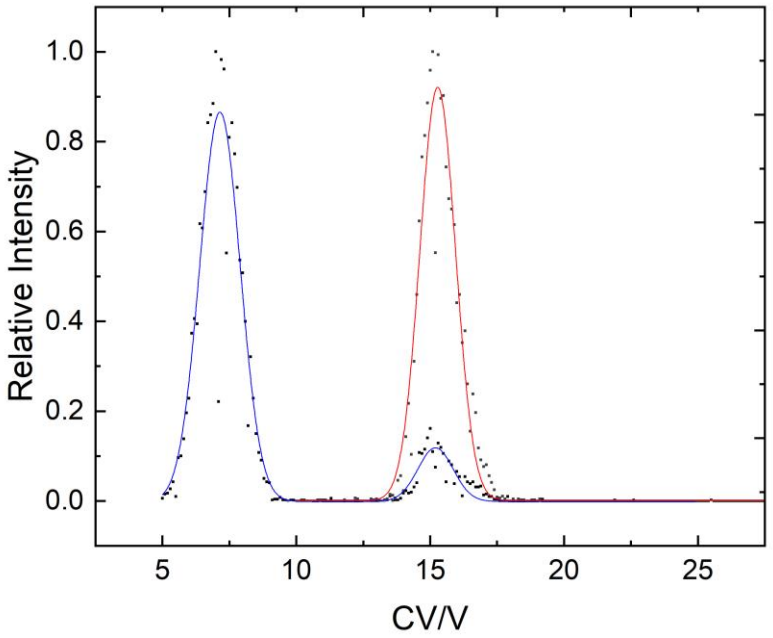


Figure B27. Ionogram of (blue) $[(B_{12}F_{12}) + H_2N(CH_2)_nNH_2 + H]^-$ and (red) $[2(B_{12}F_{12}) + H_2N(CH_2)_nNH_2 + 2H]^{2-}$ (n = 5) at SV=3800V.

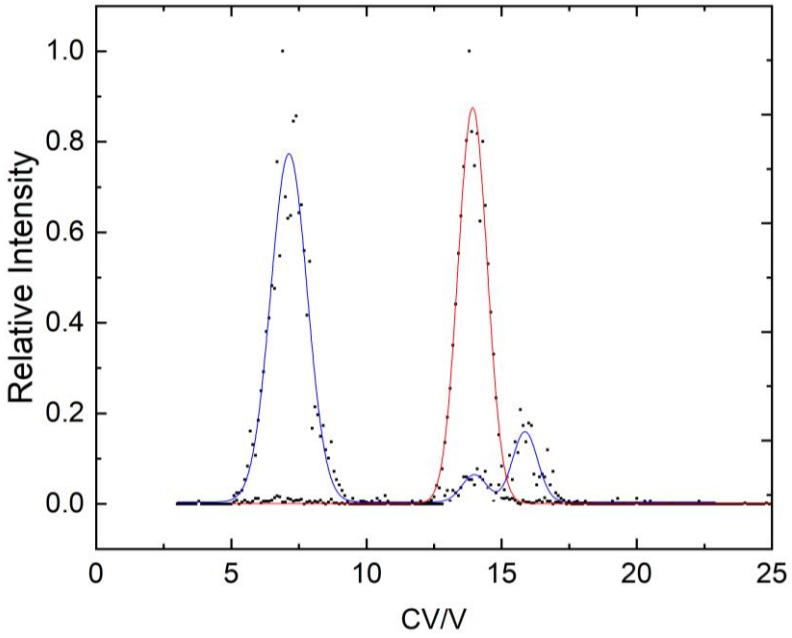


Figure B28. Ionogram of (blue) $[(B_{12}F_{12}) + H_2N(CH_2)_nNH_2 + H]^-$ and (red) $[2(B_{12}F_{12}) + H_2N(CH_2)_nNH_2 + 2H]^{2-}$ (n = 6) at SV=3800V.

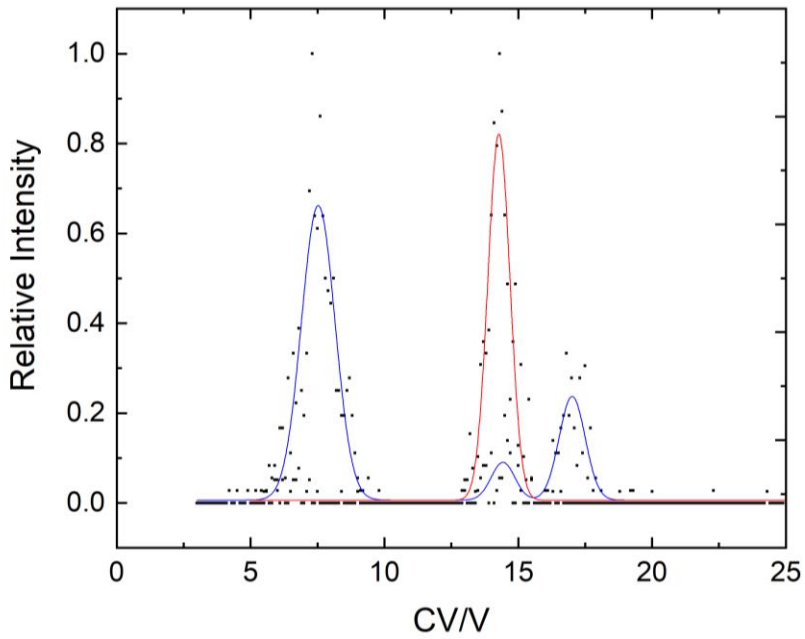


Figure B29. Ionogram of (blue) $[(B_{12}F_{12}) + H_2N(CH_2)_nNH_2 + H]^-$ and (red) $[2(B_{12}F_{12}) + H_2N(CH_2)_nNH_2 + 2H]^{2-}$ (n = 7) at SV=3800V.

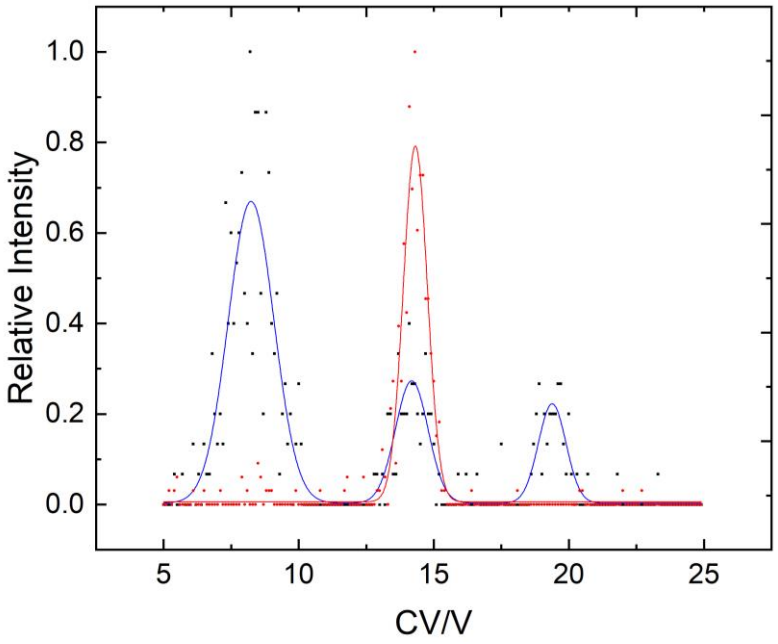


Figure B30. Ionogram of (blue) $[(B_{12}F_{12}) + H_2N(CH_2)_nNH_2 + H]^-$ and (red) $[2(B_{12}F_{12}) + H_2N(CH_2)_nNH_2 + 2H]^{2-}$ (n = 8) at SV=3800V.

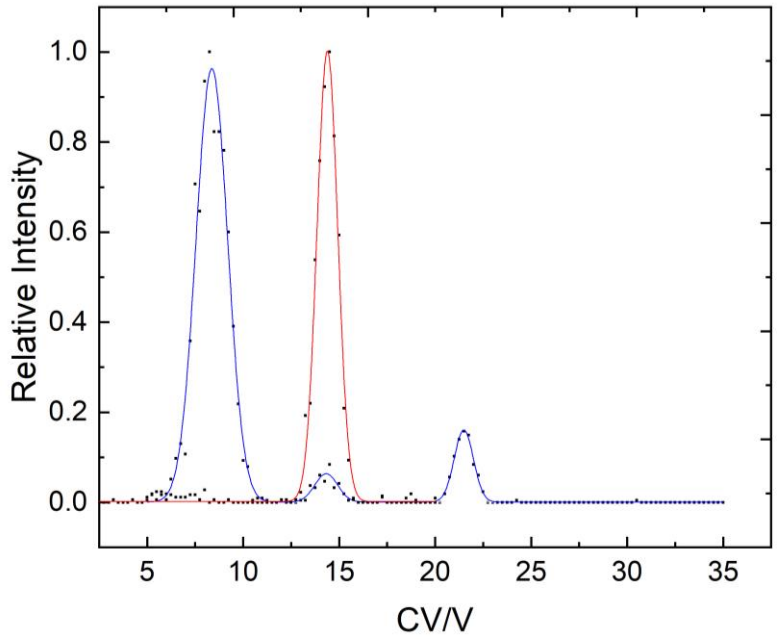


Figure B31. Ionogram of (blue) $[(B_{12}F_{12}) + H_2N(CH_2)_nNH_2 + H]^-$ and (red) $[2(B_{12}F_{12}) + H_2N(CH_2)_nNH_2 + 2H]^{2-}$ (n = 9) at SV=3800V.

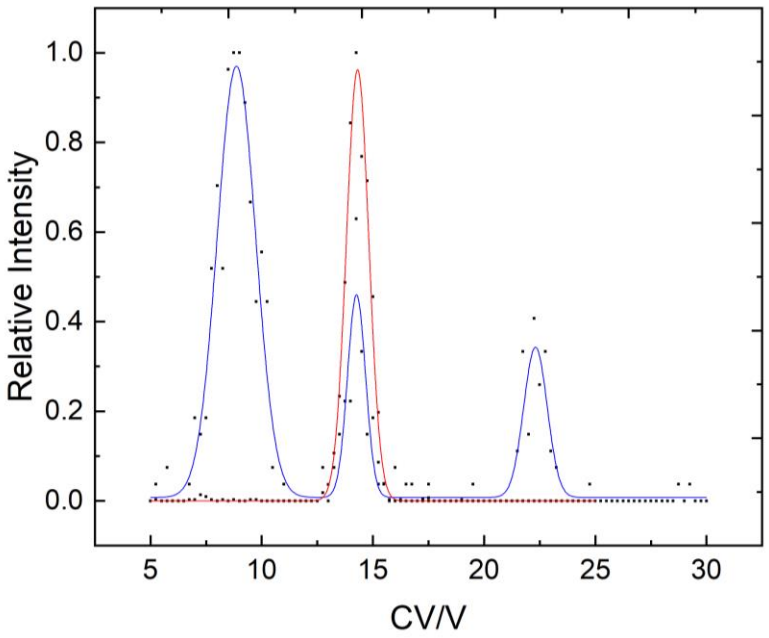


Figure B32. Ionogram of (blue) $[(B_{12}F_{12}) + H_2N(CH_2)_nNH_2 + H]^-$ and (red) $[2(B_{12}F_{12}) + H_2N(CH_2)_nNH_2 + 2H]^{2-}$ (n = 10) at SV=3800V.

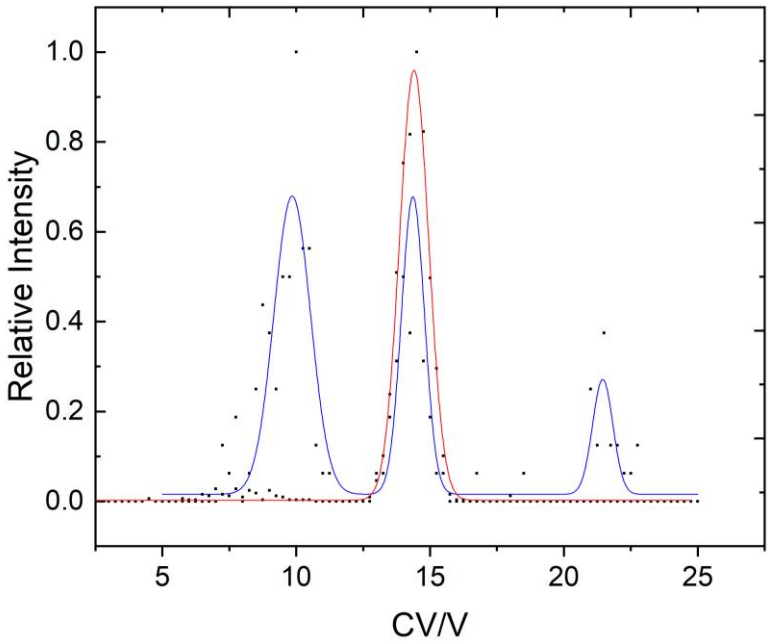


Figure B33. Ionogram of (blue) $[(B_{12}F_{12}) + H_2N(CH_2)_nNH_2 + H]^-$ and (red) $[2(B_{12}F_{12}) + H_2N(CH_2)_nNH_2 + 2H]^{2-}$ (n = 11) at SV=3800V.

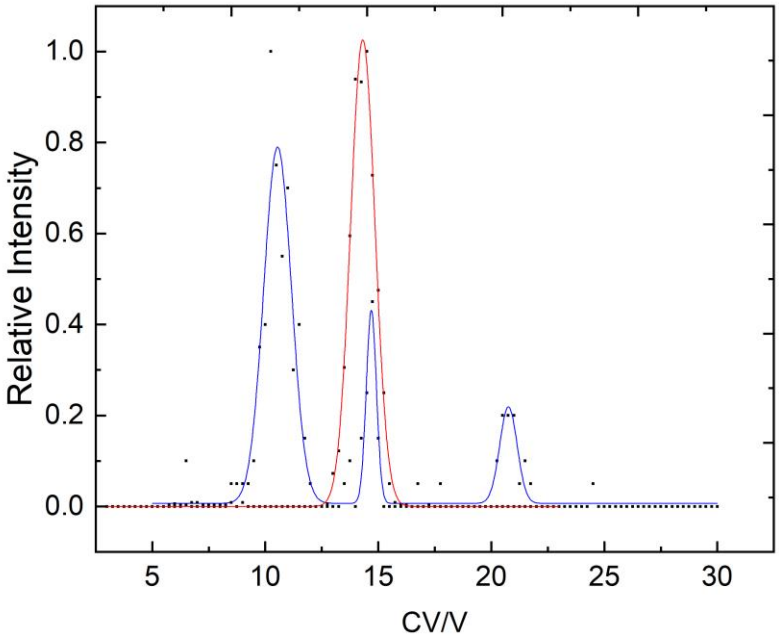


Figure B34. Ionogram of (blue) $[(B_{12}F_{12}) + H_2N(CH_2)_nNH_2 + H]^-$ and (red) $[2(B_{12}F_{12}) + H_2N(CH_2)_nNH_2 + 2H]^{2-}$ (n = 12) at SV=3800V.

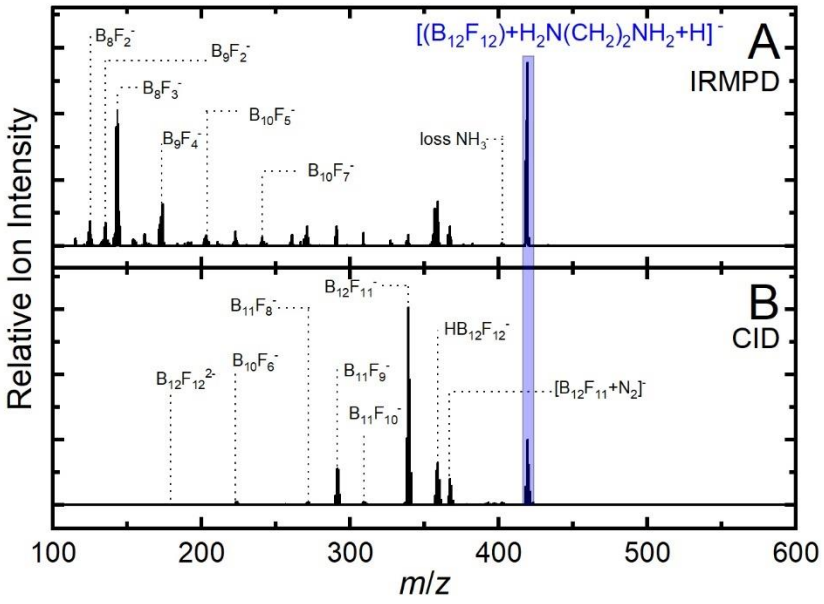


Figure B35. (A) IRMPD fragmentation at the 2900 cm^{-1} – 3000 cm^{-1} region for the singly charged $[(B_{12}F_{12}) + H_2N(CH_2)_nNH_2 + H]^-$ (n = 2) cluster. (B) CID at CE = 30V setting.

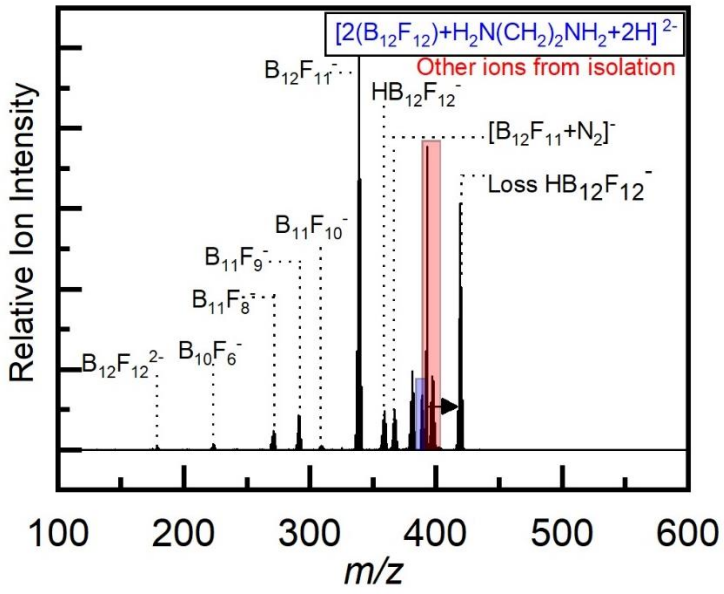


Figure B36. CID at CE = 30V setting for the doubly charged $[2(B_{12}F_{12}) + H_2N(CH_2)_nNH_2 + 2H]^{2-}$ ($n = 2$) cluster.

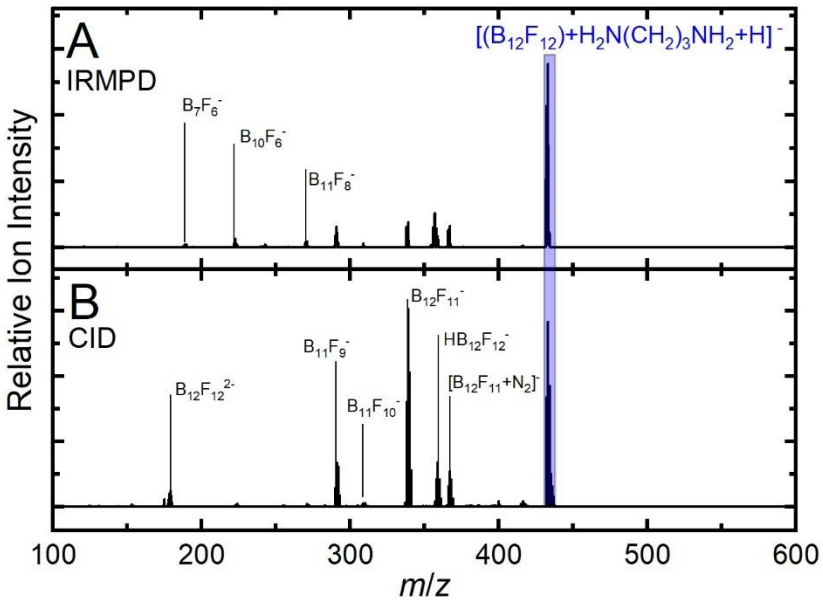


Figure B37. (A) IRMPD fragmentation at the 2900 cm^{-1} – 3000 cm^{-1} region for the singly charged $[(B_{12}F_{12}) + H_2N(CH_2)_nNH_2 + H]^-$ ($n = 3$) cluster. (B) CID at CE = 30V setting.

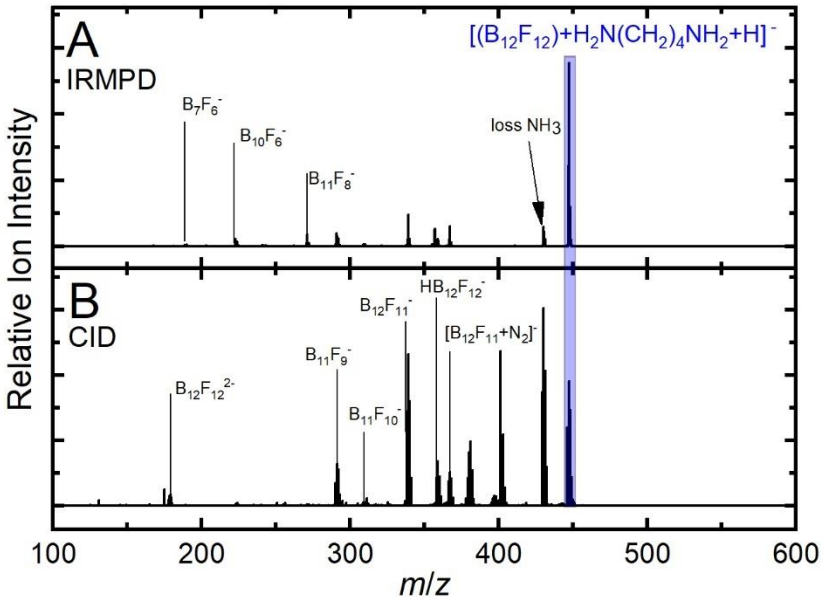


Figure B38. (A) IRMPD fragmentation at the 2900 cm^{-1} – 3000 cm^{-1} region for the singly charged $[(B_{12}F_{12}) + H_2N(CH_2)_nNH_2 + H]^-$ ($n = 4$) cluster. (B) CID at CE = 30V setting.

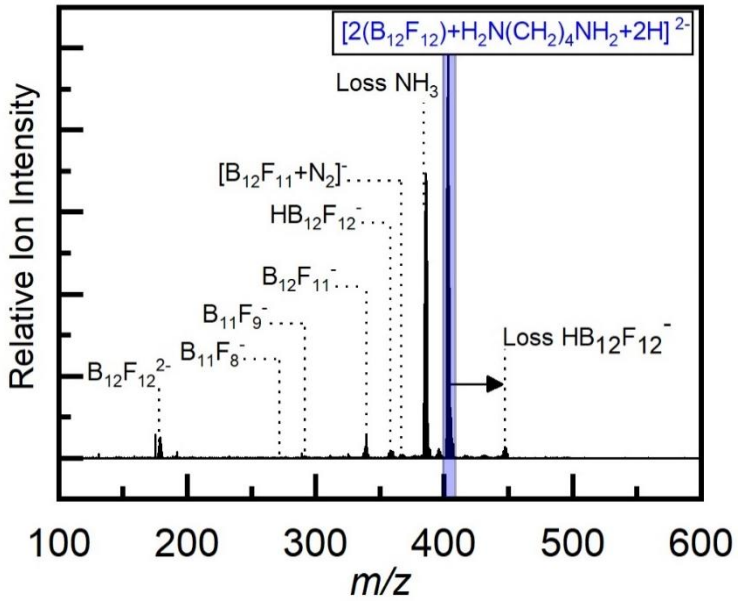


Figure B39. CID at CE = 30V setting for the doubly charged $[2(B_{12}F_{12}) + H_2N(CH_2)_nNH_2 + 2H]^{2-}$ ($n = 4$) cluster.

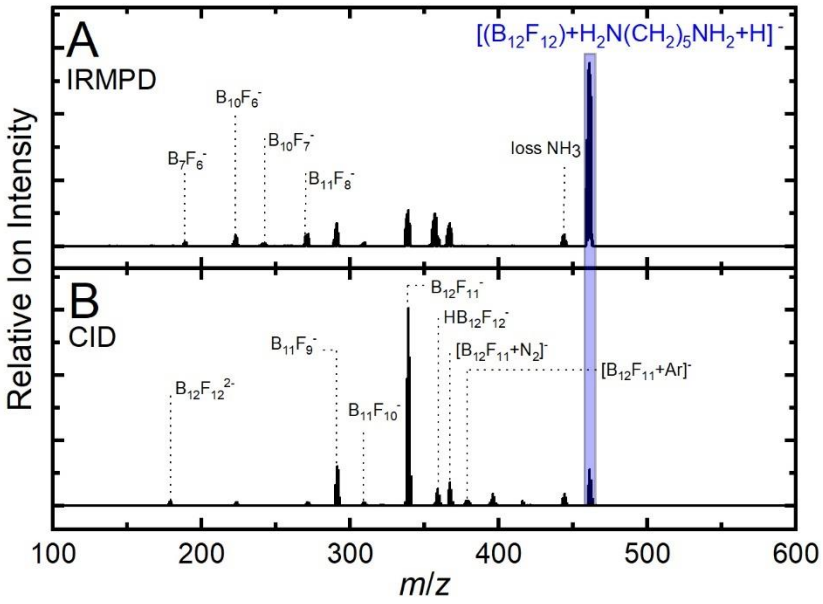


Figure B40. (A) IRMPD fragmentation at the 2900 cm^{-1} – 3000 cm^{-1} region for the singly charged $[(B_{12}F_{12}) + H_2N(CH_2)_nNH_2 + H]^-$ (n = 5) cluster. (B) CID at CE = 30V setting.

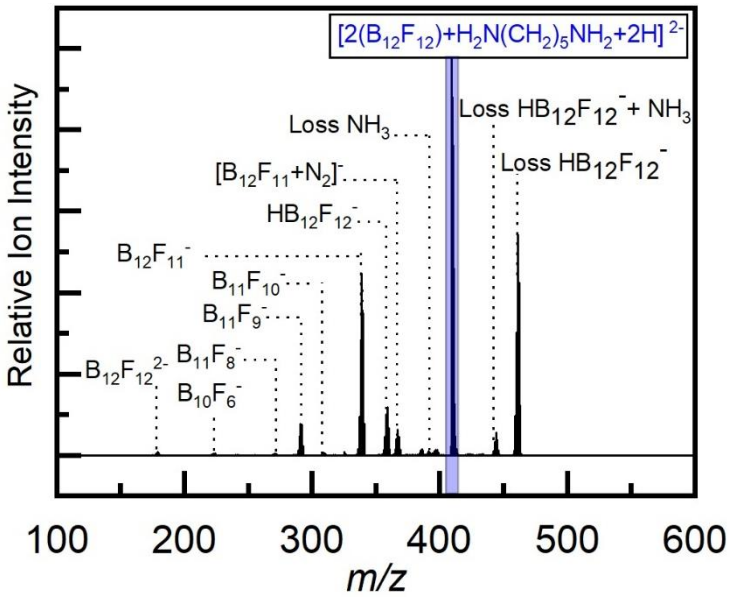


Figure B41. CID at CE = 25V setting for the doubly charged $[2(B_{12}F_{12}) + H_2N(CH_2)_nNH_2 + 2H]^{2-}$ (n = 5) cluster.

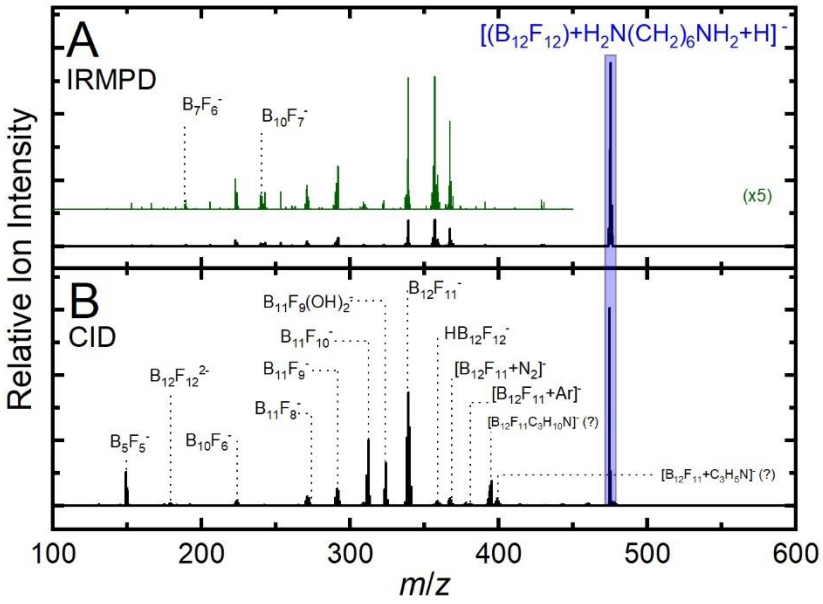


Figure B42. (A) IRMPD fragmentation at the 2900 cm^{-1} – 3000 cm^{-1} region for the singly charged $[(B_{12}F_{12}) + H_2N(CH_2)_nNH_2 + H]^-$ (n = 6) cluster. (B) CID at CE = 30V setting.

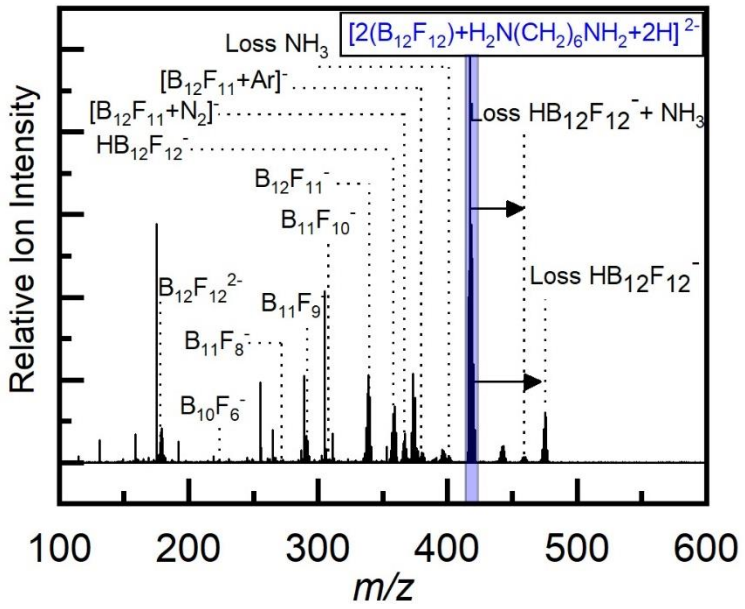


Figure B43. CID at CE = 30V setting for the doubly charged $[2(B_{12}F_{12}) + H_2N(CH_2)_nNH_2 + 2H]^{2-}$ (n = 6) cluster.

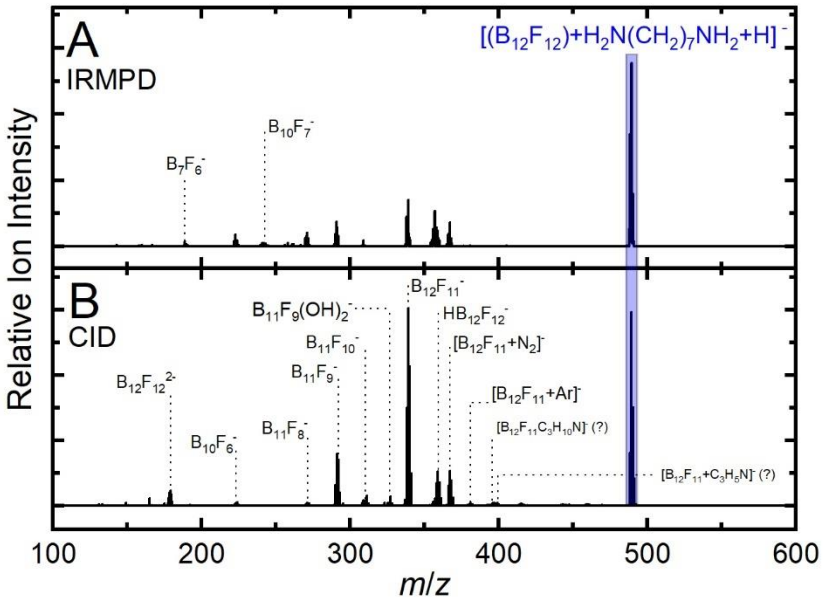


Figure B44. (A) IRMPD fragmentation at the 2900 cm^{-1} – 3000 cm^{-1} region for the singly charged $[(B_{12}F_{12}) + H_2N(CH_2)_nNH_2 + H]^-$ (n = 7) cluster. (B) CID at CE = 30V setting.

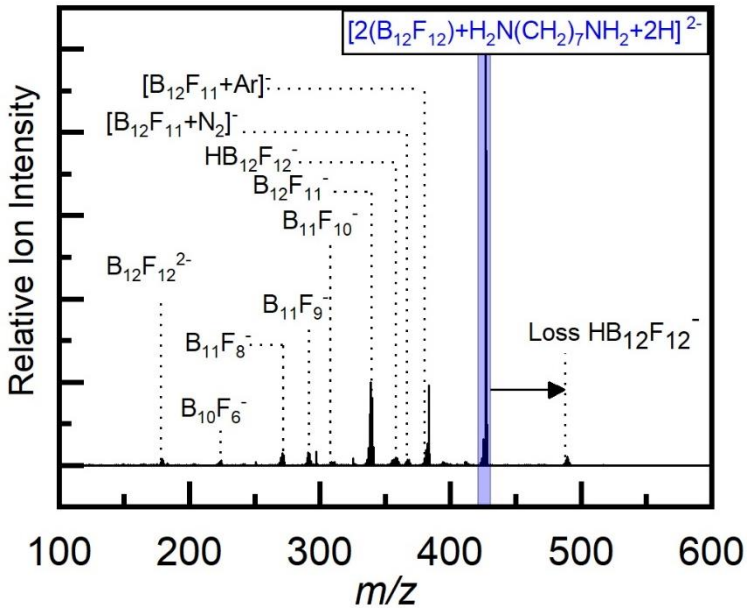


Figure B45. CID at CE = 35V setting for the doubly charged $[2(B_{12}F_{12}) + H_2N(CH_2)_nNH_2 + 2H]^{2-}$ (n = 7) cluster.

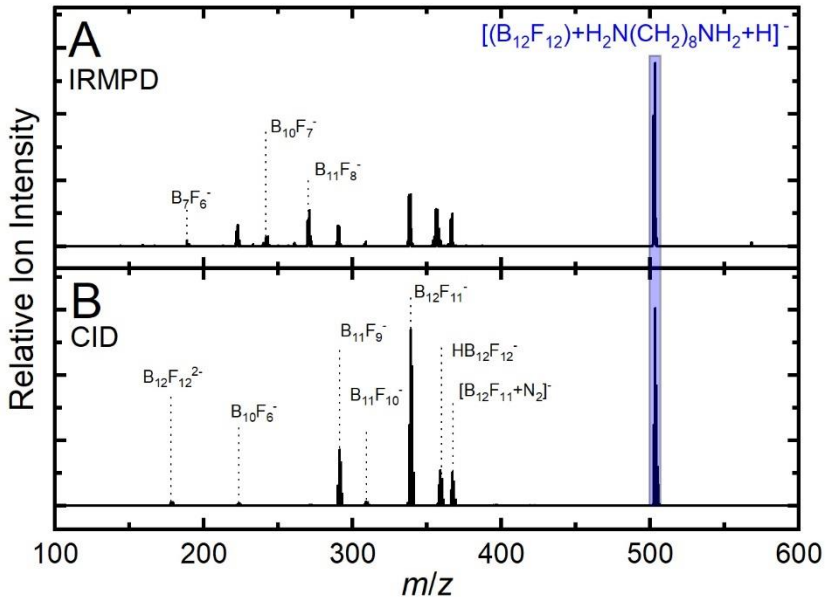


Figure B46. (A) IRMPD fragmentation at the 2900 cm^{-1} – 3000 cm^{-1} region for the singly charged $[(B_{12}F_{12}) + H_2N(CH_2)_nNH_2 + H]^-$ (n = 8) cluster. (B) CID at CE = 30V setting.

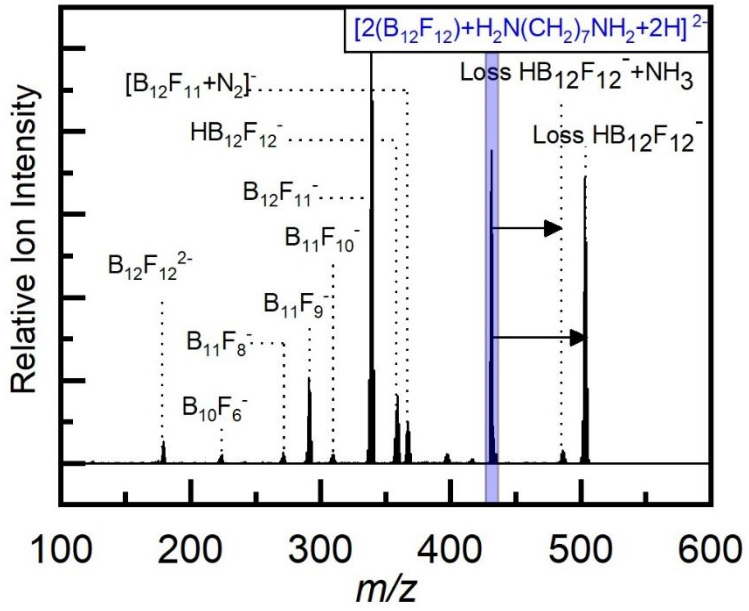


Figure B47. CID at CE = 30V setting for the doubly charged $[2(B_{12}F_{12}) + H_2N(CH_2)_nNH_2 + 2H]^{2-}$ (n = 8) cluster.

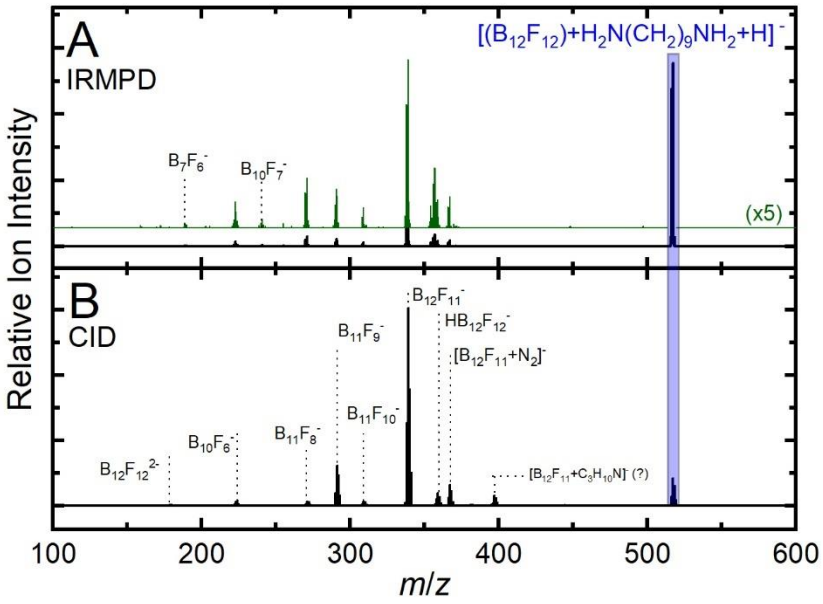


Figure B48. (A) IRMPD fragmentation at the 2900 cm^{-1} – 3000 cm^{-1} region for the singly charged $[(B_{12}F_{12}) + H_2N(CH_2)_nNH_2 + H]^-$ (n = 9) cluster. (B) CID at CE = 30V setting.

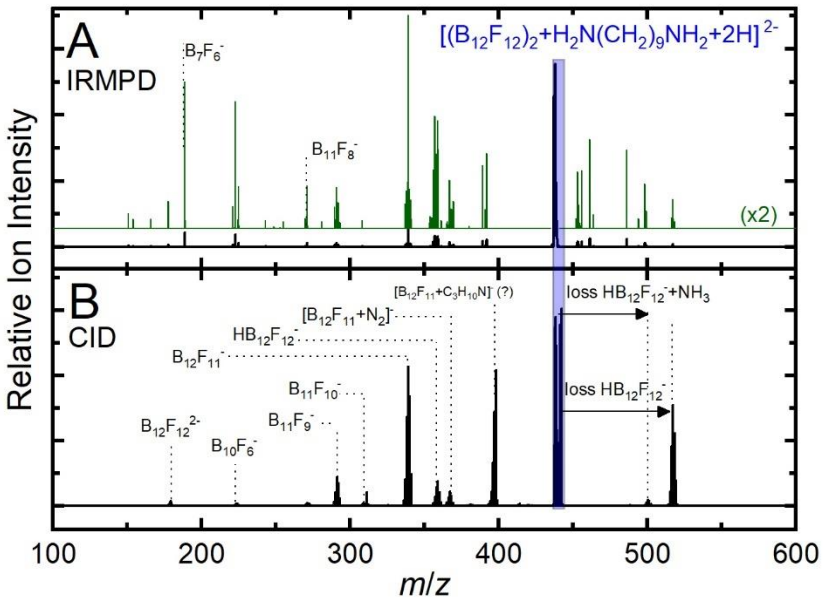


Figure B49. (A) IRMPD fragmentation at the 2900 cm^{-1} – 3000 cm^{-1} region for the doubly charged $[2(B_{12}F_{12}) + H_2N(CH_2)_nNH_2 + H]^{2-}$ (n = 9) cluster. (B) CID at CE = 40V setting.

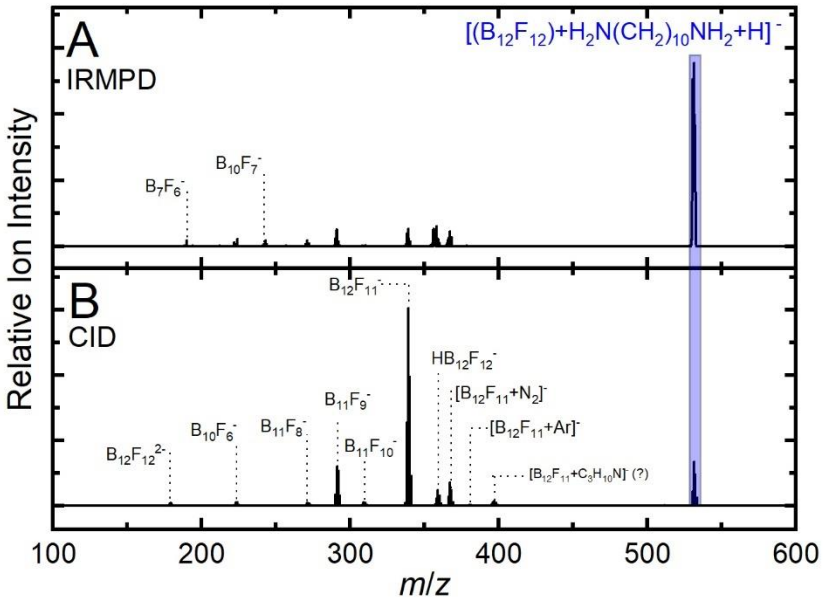


Figure B50. (A) IRMPD fragmentation at the 2900 cm^{-1} – 3000 cm^{-1} region for the singly charged $[(B_{12}F_{12}) + H_2N(CH_2)_nNH_2 + H]^-$ (n = 10) cluster. (B) CID at CE = 30V setting.

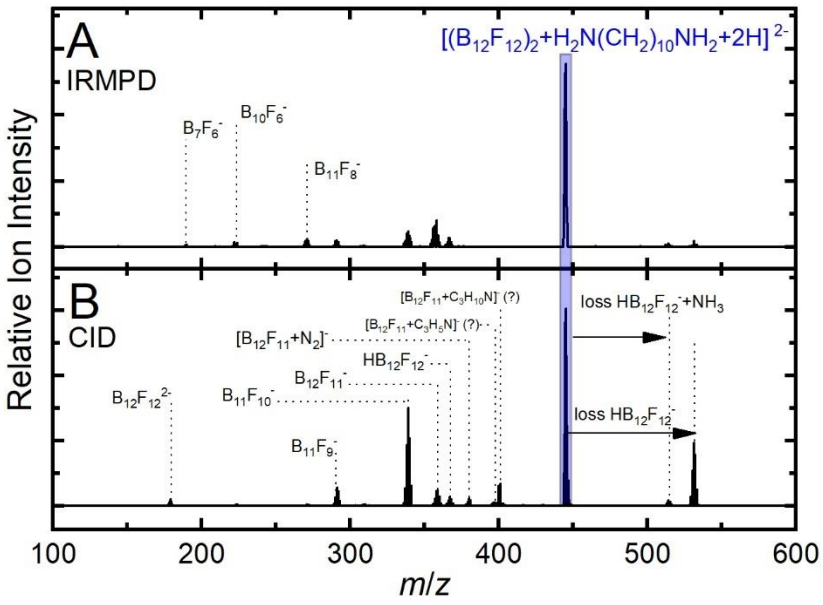


Figure B51. (A) IRMPD fragmentation at the 2900 cm^{-1} – 3000 cm^{-1} region for the doubly charged $[2(B_{12}F_{12}) + H_2N(CH_2)_nNH_2 + H]^{2-}$ (n = 10) cluster. (B) CID at CE = 40V setting.

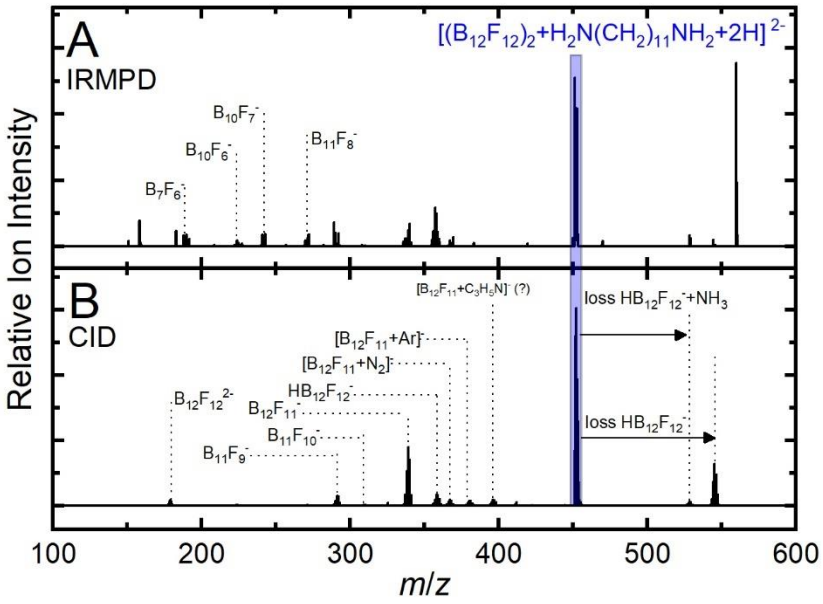


Figure B52. (A) IRMPD fragmentation at the 2900 cm^{-1} – 3000 cm^{-1} region for the singly charged $[(B_{12}F_{12}) + H_2N(CH_2)_nNH_2 + H]^-$ (n = 11) cluster. (B) CID at CE = 30V setting.

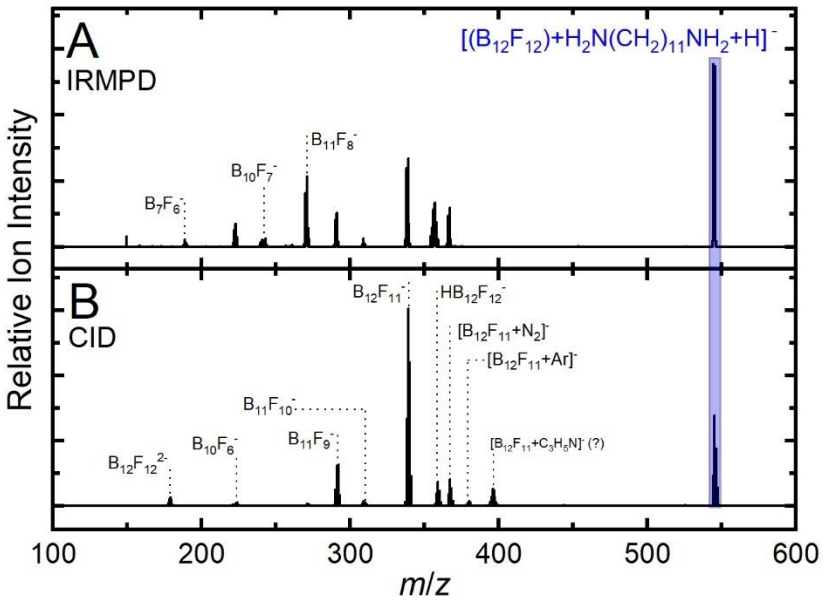


Figure B53. (A) IRMPD fragmentation at the 2900 cm^{-1} – 3000 cm^{-1} region for the doubly charged $[2(B_{12}F_{12}) + H_2N(CH_2)_nNH_2 + H]^{2-}$ (n = 11) cluster. (B) CID at CE = 40V setting.

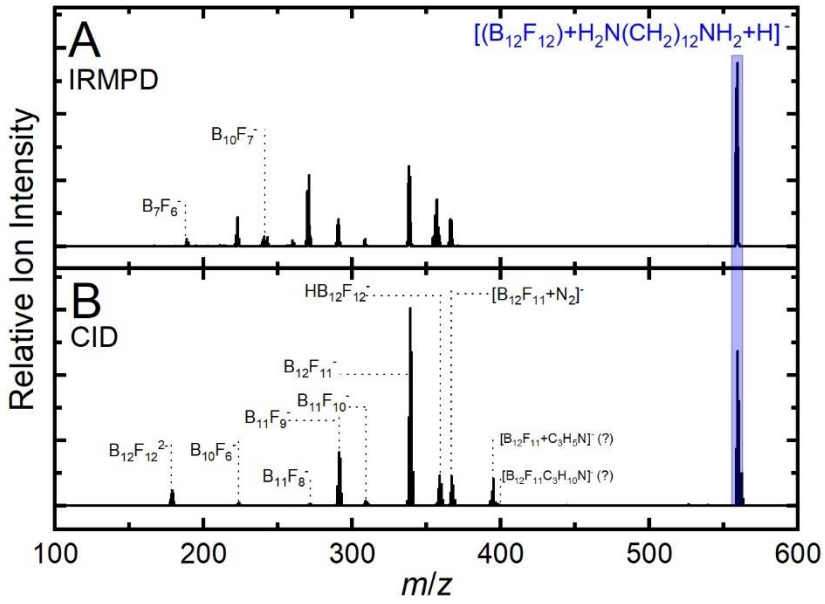


Figure B54. (A) IRMPD fragmentation at the 2900 cm^{-1} – 3000 cm^{-1} region for the singly charged $[(B_{12}F_{12}) + H_2N(CH_2)_nNH_2 + H]^-$ (n = 12) cluster. (B) CID at CE = 30V setting.

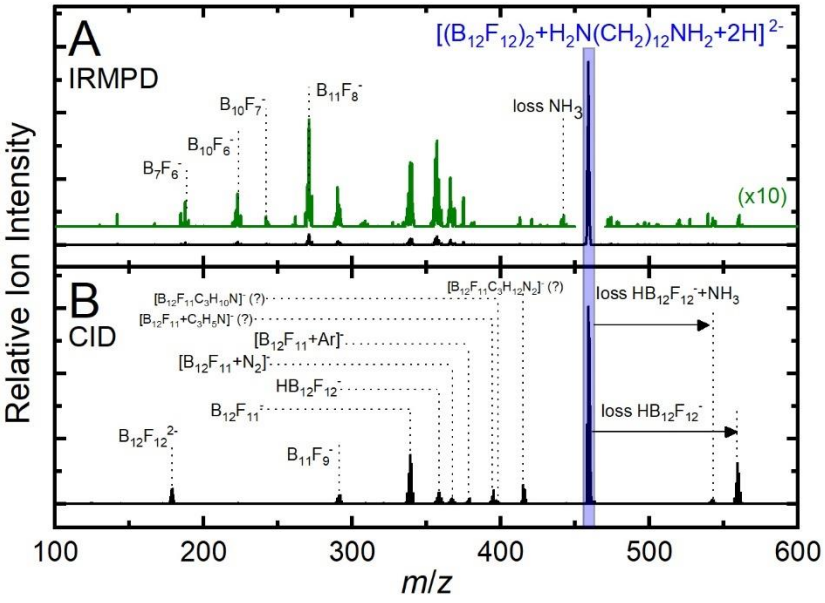


Figure B55. (A) IRMPD fragmentation at the 2900 cm^{-1} – 3000 cm^{-1} region for the doubly charged $[2(B_{12}F_{12}) + H_2N(CH_2)_nNH_2 + H]^{2-}$ (n = 12) cluster. (B) CID at CE = 40V setting.

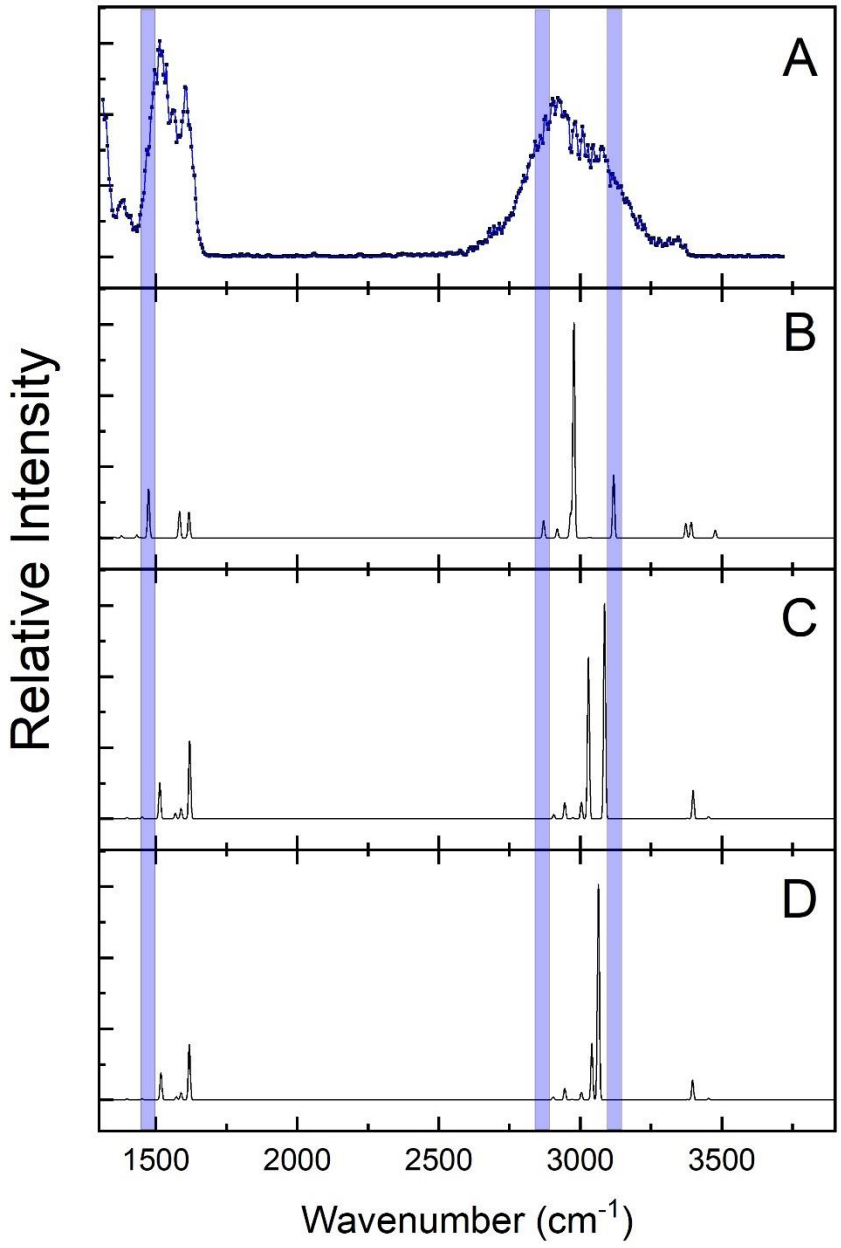


Figure B56. Comparison of the (A) experimental IRMPD spectrum of the singly charged diaminoethane cluster, $[(B_{12}F_{12}) + H_2N(CH_2)_nNH_2 + H]^-$ (n = 2), and the computed IR spectrum of the (B) proton-sharing conformation, (C) bidentate conformation, and (D) monodentate conformation. Highlighted in (blue) are the diagnostic peaks belonging to the proton-sharing conformation.

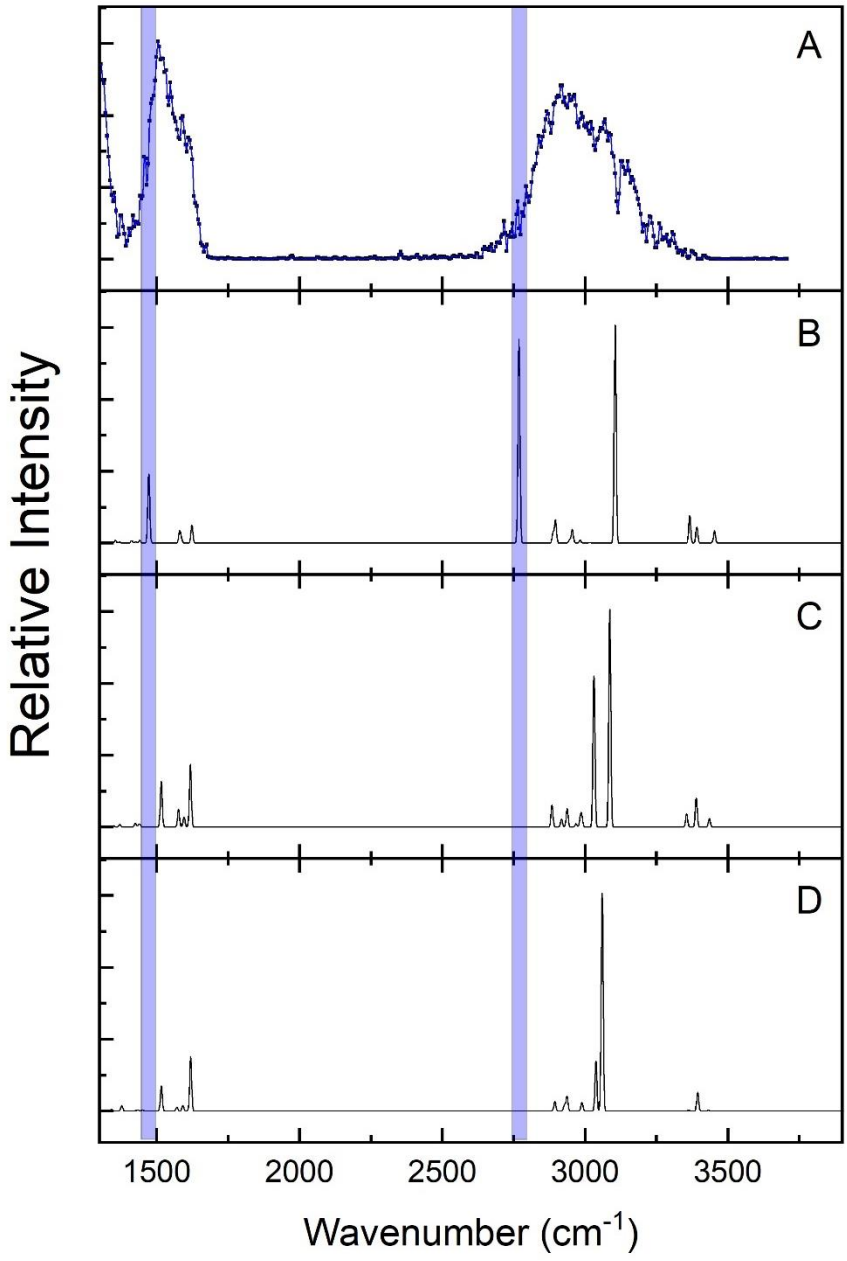


Figure B57. Comparison of the (A) experimental IRMPD spectrum of the singly charged diaminopropane cluster, $[(B_{12}F_{12}) + H_2N(CH_2)_nNH_2 + H]^-$ (n = 3), and the computed IR spectrum of the (B) proton-sharing conformation, (C) bidentate conformation, and (D) monodentate conformation. Highlighted in (blue) are the diagnostic peaks belonging to the proton-sharing conformation.

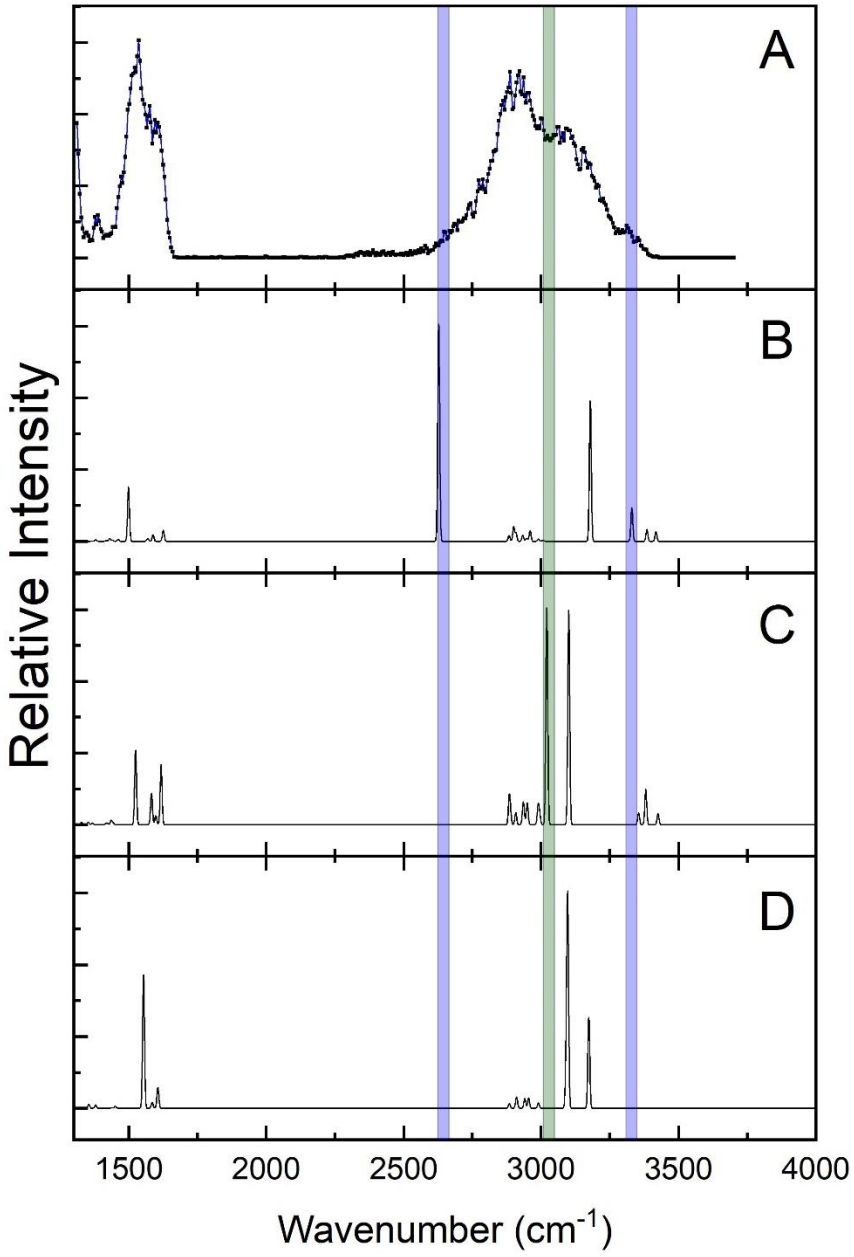


Figure B58. Comparison of the (A) experimental IRMPD spectrum of the singly charged diaminobutane cluster, $[(B_{12}F_{12}) + H_2N(CH_2)_nNH_2 + H]^-$ (n = 4), and the computed IR spectrum of the (B) proton-sharing conformation, (C) bidentate conformation, and (D) monodentate conformation. Highlighted in (blue) are the diagnostic peaks belonging to the proton-sharing conformation and (green) belongs to the bidentate conformation.

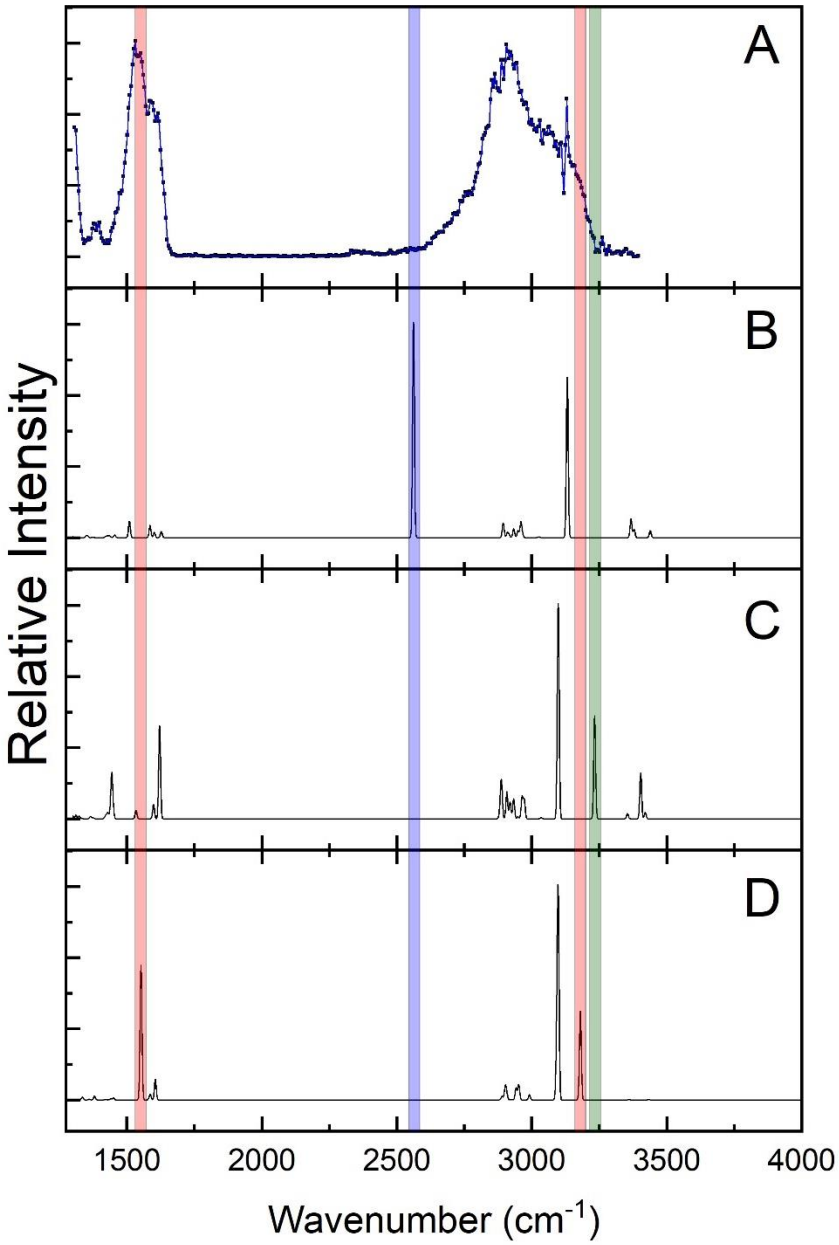


Figure B59. Comparison of the (A) experimental IRMPD spectrum of the singly charged diaminopentane cluster, $[(B_{12}F_{12}) + H_2N(CH_2)_nNH_2 + H]^-$ (n = 5), and the computed IR spectrum of the (B) proton-sharing conformation, (C) bidentate conformation, and (D) monodentate conformation. Highlighted in (blue) is the diagnostic peak belonging to the proton-sharing conformation, (green) is the diagnostic peak belonging to the bidentate conformation, and (red) are the diagnostic peaks belonging to the monodentate conformation.

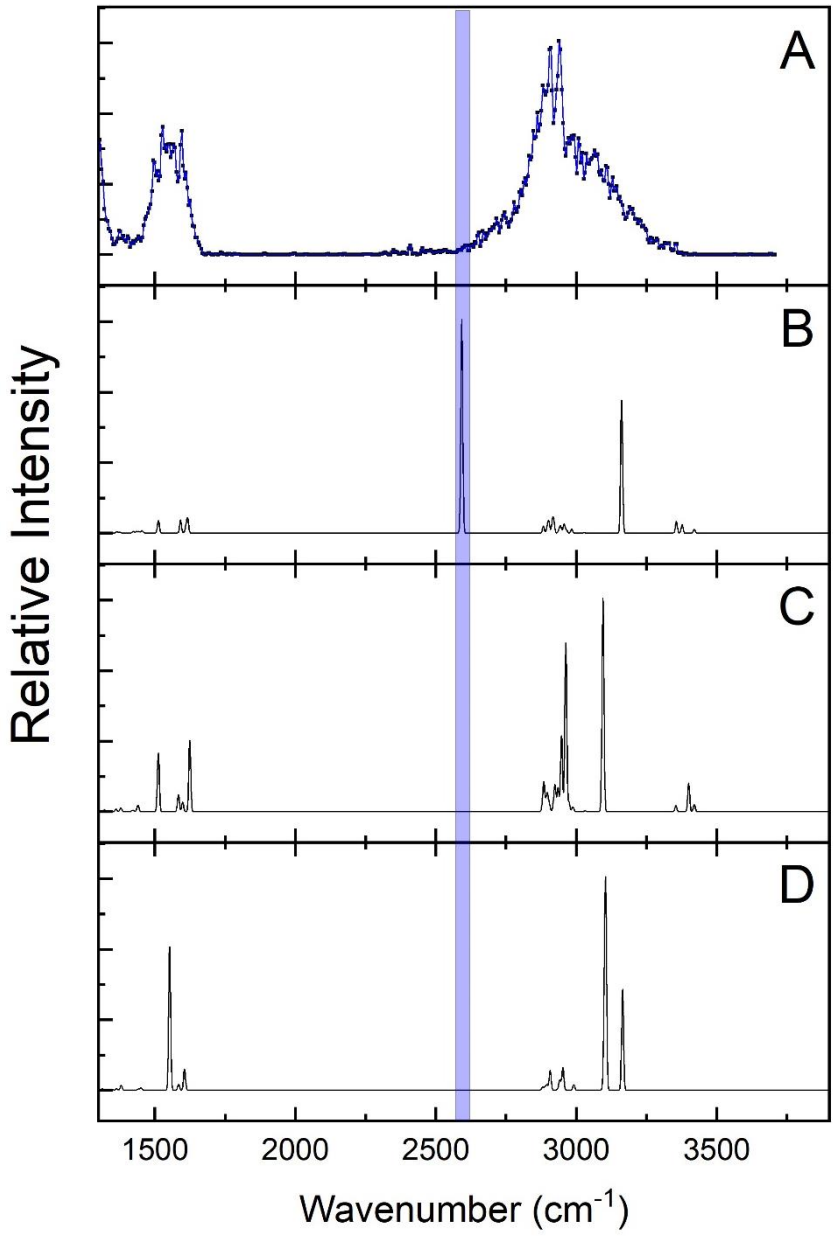


Figure B60. Comparison of the (A) experimental IRMPD spectrum of the singly charged diaminohexane cluster, $[(B_{12}F_{12}) + H_2N(CH_2)_nNH_2 + H]^-$ (n = 6), and the computed IR spectrum of the (B) proton-sharing conformation, (C) bidentate conformation, and (D) monodentate conformation. Highlighted in (blue) are the diagnostic peaks belonging to the proton-sharing conformation.

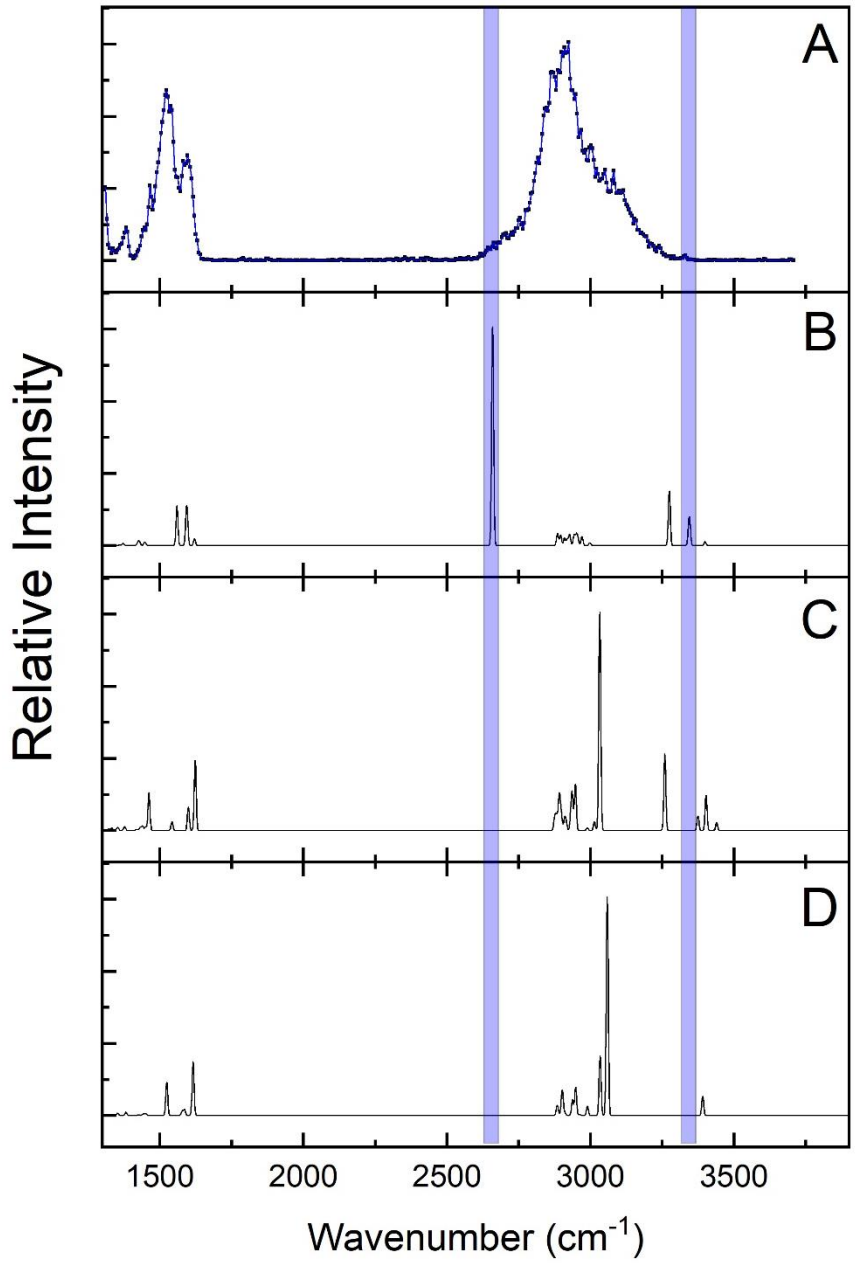


Figure B61. Comparison of the (A) experimental IRMPD spectrum of the singly charged diaminoheptane cluster, $[(B_{12}F_{12}) + H_2N(CH_2)_nNH_2 + H]^-$ (n = 7), and the computed IR spectrum of the (B) proton-sharing conformation, (C) bidentate conformation, and (D) monodentate conformation. Highlighted in (blue) are the diagnostic peaks belonging to the proton-sharing conformation.

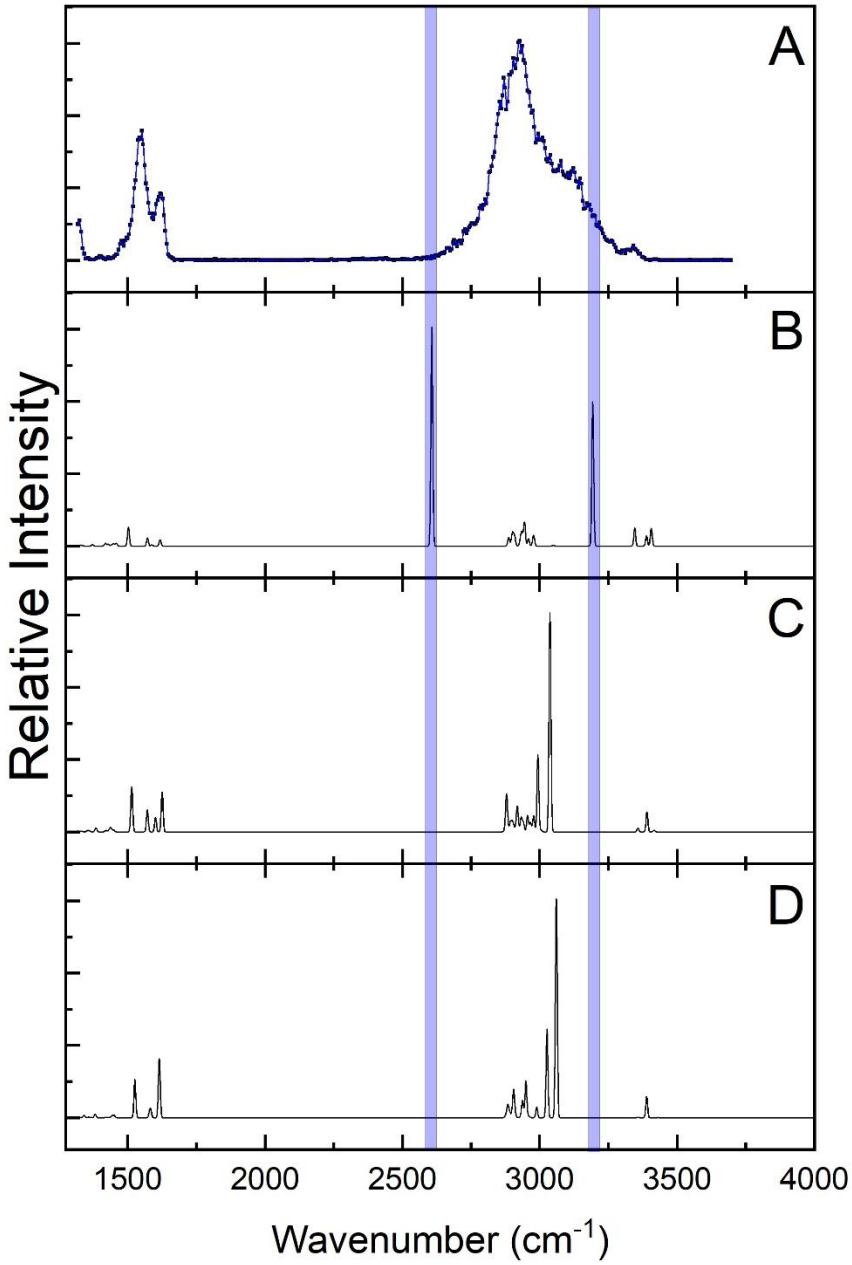


Figure B62. Comparison of the (A) experimental IRMPD spectrum of the singly charged diaminooctane cluster, $[(B_{12}F_{12}) + H_2N(CH_2)_nNH_2 + H]^-$ (n = 8), and the computed IR spectrum of the (B) proton-sharing conformation, (C) bidentate conformation, and (D) monodentate conformation. Highlighted in (blue) are the diagnostic peaks belonging to the proton-sharing conformation.

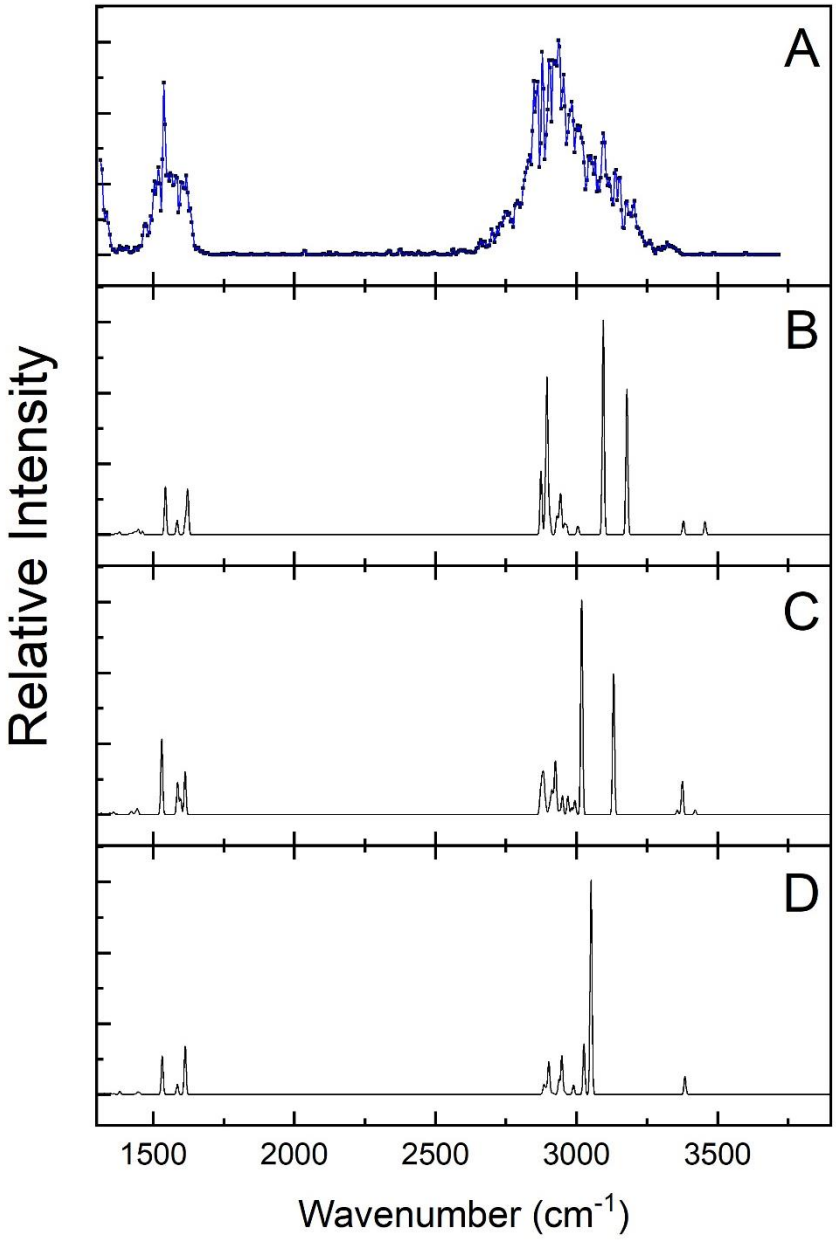


Figure B63. Comparison of the (A) experimental IRMPD spectrum of the singly charged diaminononane cluster, $[(B_{12}F_{12}) + H_2N(CH_2)_nNH_2 + H]^-$ (n = 9), and the computed IR spectrum of the (B) proton-sharing conformation, (C) bidentate conformation, and (D) monodentate conformation.

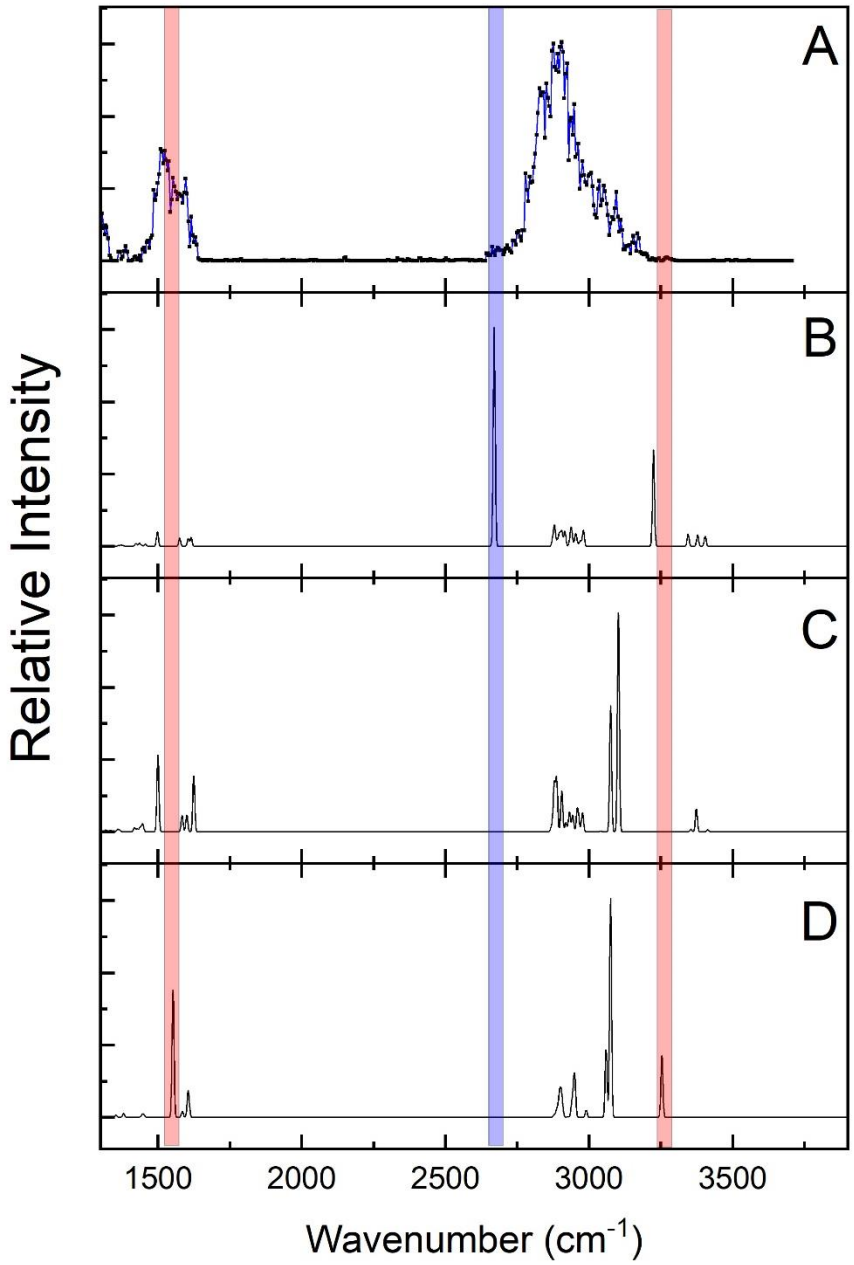


Figure B64. Comparison of the (A) experimental IRMPD spectrum of the singly charged diaminodecane cluster, $[(B_{12}F_{12}) + H_2N(CH_2)_nNH_2 + H]^-$ (n = 10), and the computed IR spectrum of the (B) proton-sharing conformation, (C) bidentate conformation, and (D) monodentate conformation. Highlighted in (blue) are the diagnostic peaks belonging to the proton-sharing conformation and (red) belongs to the monodentate conformation.

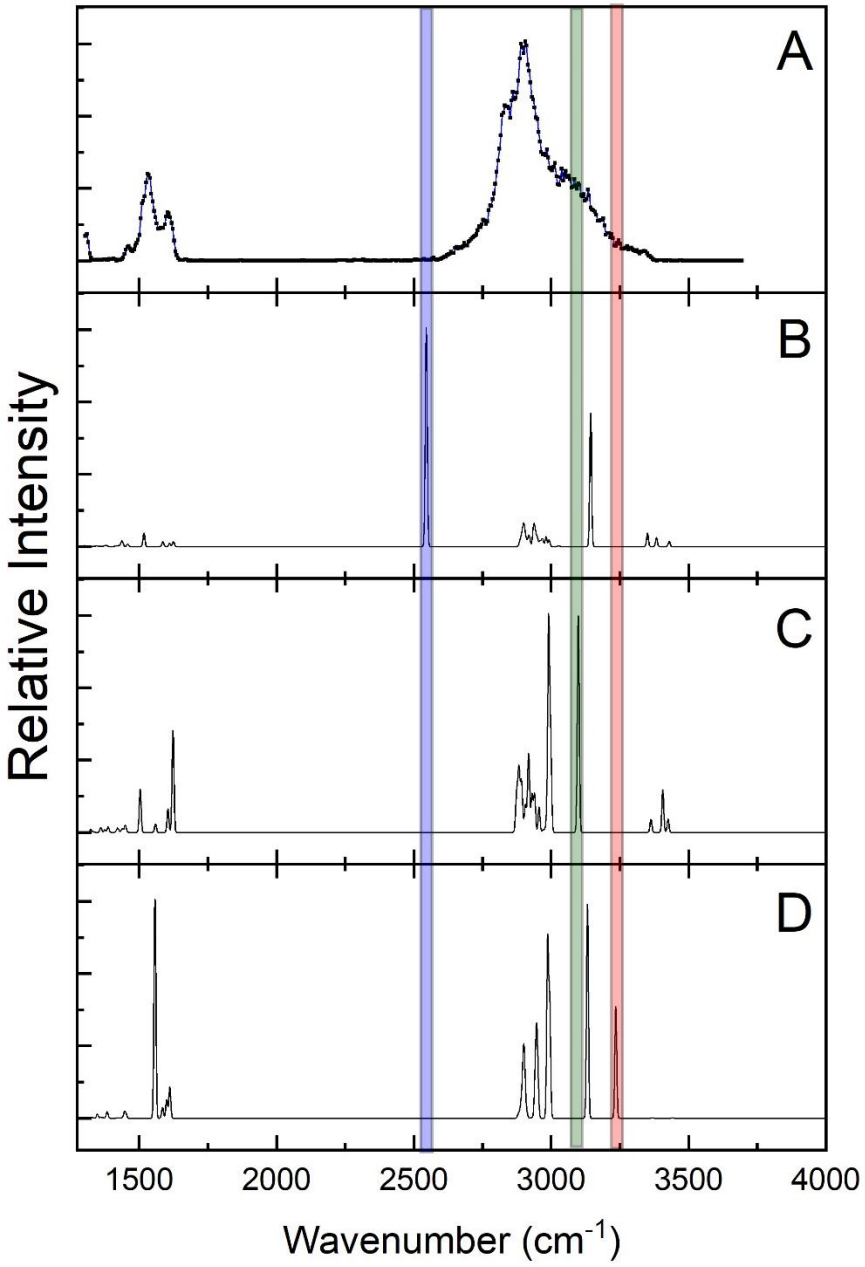


Figure B65. Comparison of the (A) experimental IRMPD spectrum of the singly charged diaminoundecane cluster, $[(B_{12}F_{12}) + H_2N(CH_2)_nNH_2 + H]^-$ (n = 11), and the computed IR spectrum of the (B) proton-sharing conformation, (C) bidentate conformation, and (D) monodentate conformation. Highlighted in (blue) is the diagnostic peak belonging to the proton-sharing conformation, (green) belongs to the bidentate conformation, and (red) belongs to the monodentate conformation.

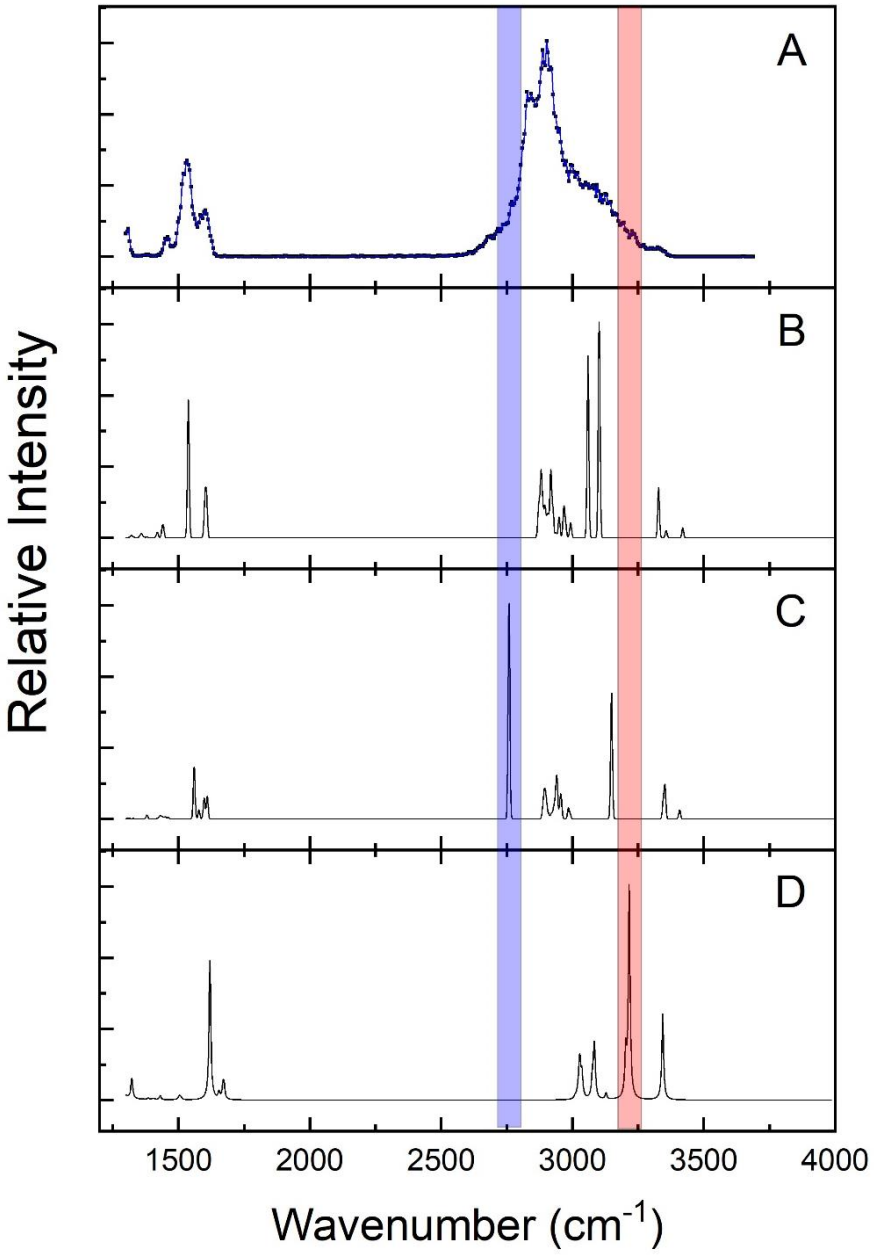


Figure B66. Comparison of the (A) experimental IRMPD spectrum of the singly charged diaminododecane cluster, $[(B_{12}F_{12}) + H_2N(CH_2)_nNH_2 + H]^-$ (n = 12), and the computed IR spectrum of the (B) proton-sharing conformation, (C) bidentate conformation, and (D) monodentate conformation. Highlighted in (blue) is the diagnostic peaks belonging to the proton-sharing conformation and (red) belongs to the monodentate conformation.

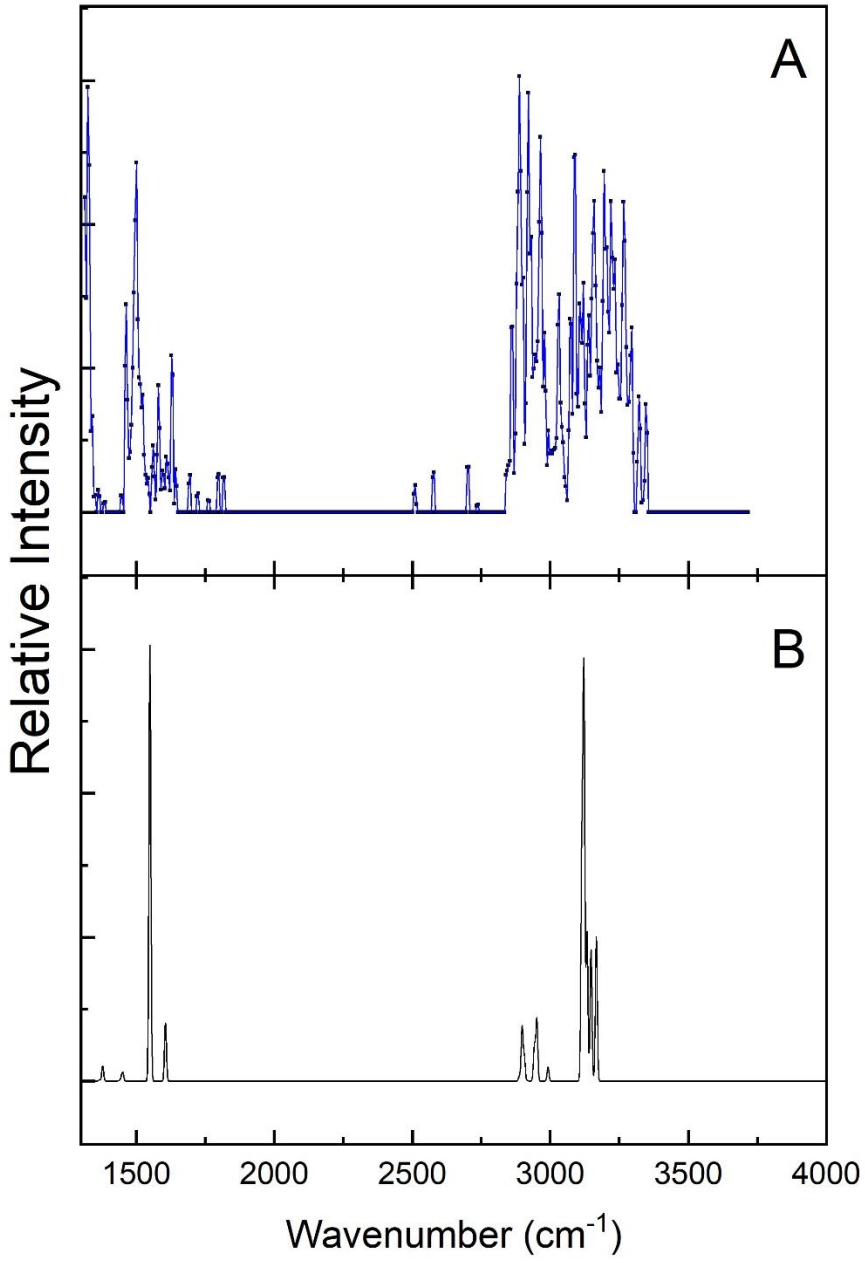


Figure B67. Comparison of the (A) experimental IRMPD spectrum of the doubly charged diaminononane cluster, $[2(B_{12}F_{12}) + H_2N(CH_2)_nNH_2 + 2H]^{2-}$ (n = 9), and (B) the computed IR spectrum.

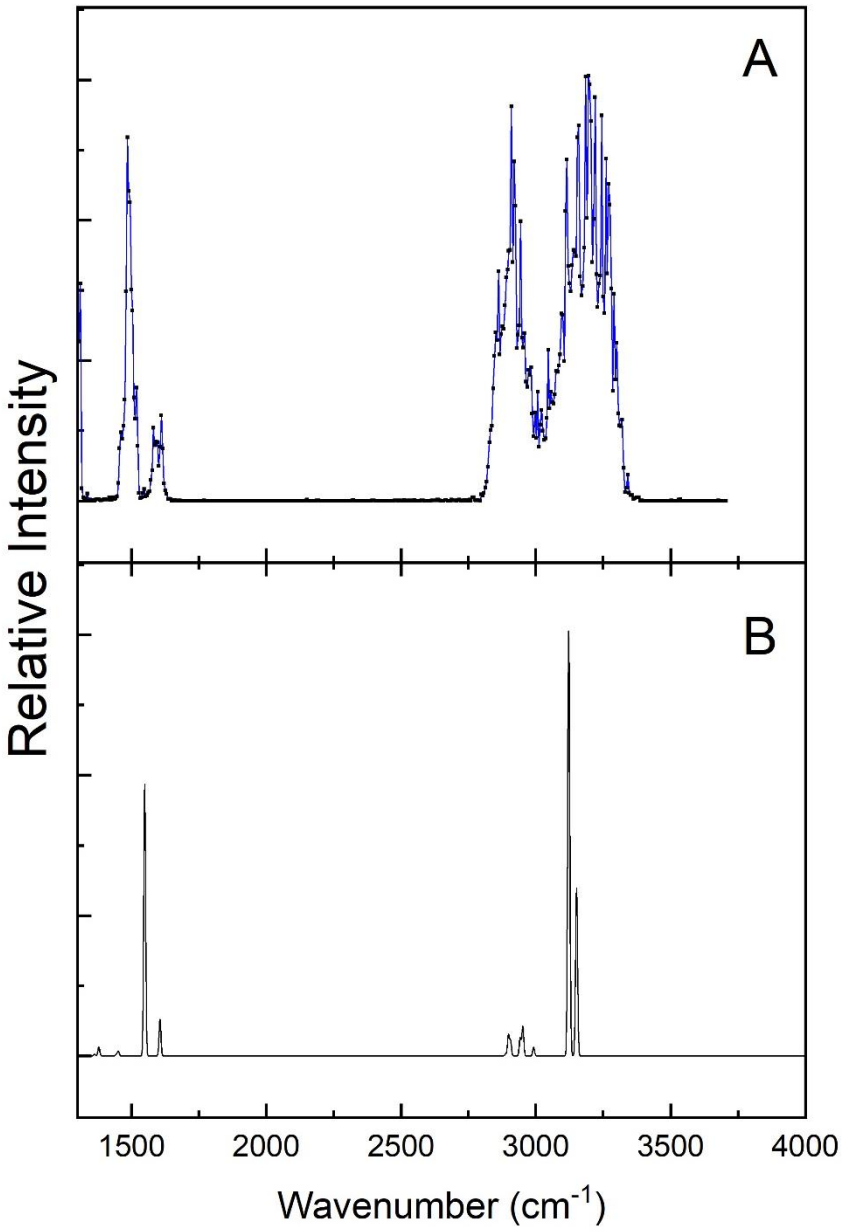


Figure B68. Comparison of the (A) experimental IRMPD spectrum of the doubly charged diaminodecane cluster, $[2(B_{12}F_{12}) + H_2N(CH_2)_nNH_2 + 2H]^{2-}$ (n = 10), and (B) the computed IR spectrum.

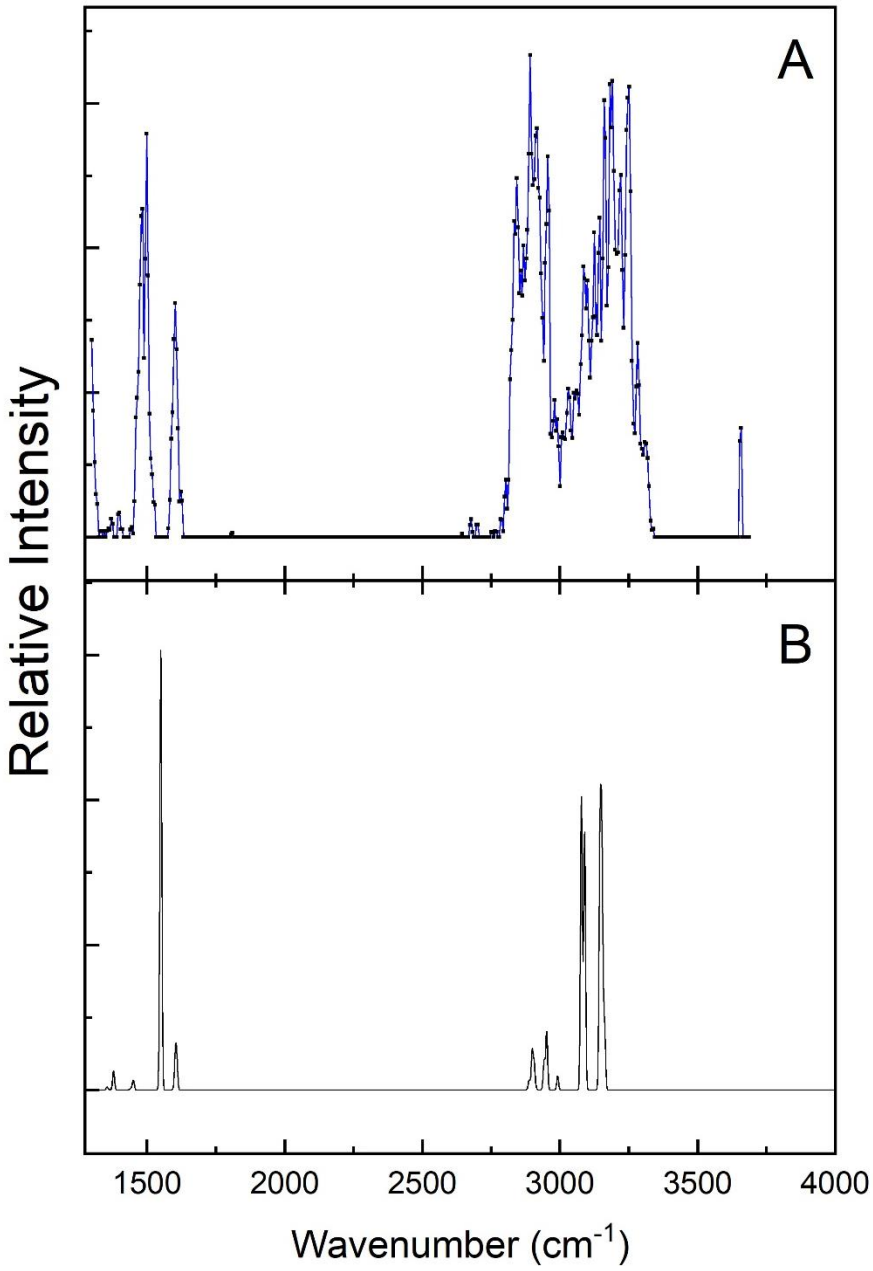


Figure B69. Comparison of the (A) experimental IRMPD spectrum of the doubly charged diaminoundecane cluster, $[2(B_{12}F_{12}) + H_2N(CH_2)_nNH_2 + 2H]^{2-}$ (n = 11), and (B) the computed IR spectrum.

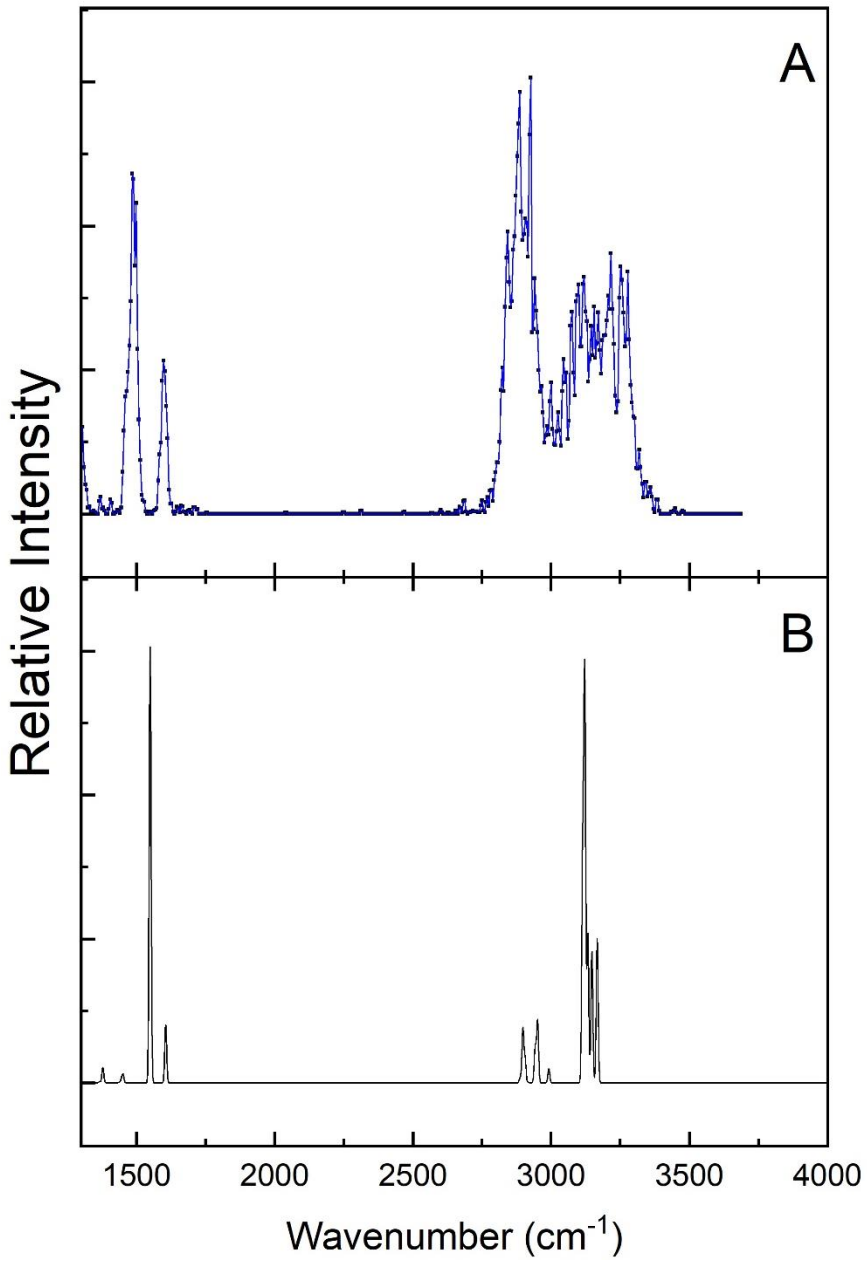


Figure B70. Comparison of the (A) experimental IRMPD spectrum of the doubly charged diaminododecane cluster, $[2(B12F12) + H_2N(CH_2)_nNH_2 + 2H]^{2-}$ (n = 12), and (B) the computed IR spectrum.

Table B14. Vibrational mode assignments for the computed bands of the singly charged diaminoalkanes clusters $[(B_{12}F_{12}) + H_2N(CH_2)_nNH_2 + H]^+$. Values in the table are reported in cm^{-1}.

Vibrational Mode	2	3	4	5	6	7	8	9	10	11	12
Boron Scissoring	1091	1096	1091	1091	1068	1098	1098	1079	1080	1083	1082
Cage Symmetric Stretch	1215	1211	1267	1267	1267	1268	1268	1268	1268	1268	1268
CH2 Twisting	1002	1044	1018	977	988	970	977	1210	1209	1232	1197
CH2 Wagging	1023	1052	1065	1032	1041	1038	1038	1040	1220	1211	1205
CH2 Scissoring	1414	1428	1493	1422	1418	1418	1416	1420	1418	1416	1415
NH3 Wagging	1477	1449	1495	1474	1548	1521	1546	1553	1549	1502	1549
NH3 Scissoring	1545	1559	1620	1596	1594	1571	1596	1597	1595	1581	1599
Proton sharing	*	2768	2628	2561	2592	2660	2607	2875	2670	2545	2759
CH2 Symmetric Stretch	2981	2931	2939	2888	2888	2882	2882	2877	2879	2879	2878
CH2 Asymmetric stretch	3031	2983	2979	2940	2917	2942	2948	2938	2946	2946	2945
NH3 Symmetric stretch	3388	3041	3045	2998	3036	2997	3053	3030	3024	2995	3054

*Not observed computationally

Geometries for chapter 5 can be found through the following link:
https://iochem-bd.bsc.es/browse/handle/100/330781